A TEMPLATE-BASED METHOD FOR SEMI-QUANTITATIVE SINGLE PHOTON EMISSION COMPUTED TOMOGRAPHY MYOCARDIAL PERFUSION IMAGING

by

Tyler John Hughes

BSc, The University of British Columbia, 2007

A THESIS SUBMITTED IN PARTIAL FULFILLMENT OF
THE REQUIREMENTS FOR THE DEGREE OF

DOCTOR OF PHILOSOPHY
in
The Faculty of Graduate Studies

(Physics)

THE UNIVERSITY OF BRITISH COLUMBIA
(Vancouver)

July 2012

Abstract

This thesis presents the template-based quantitative perfusion SPECT (TQPS) method, which is designed for the semi-quantitative analysis in SPECT myocardial perfusion imaging (MPI). Unlike traditional methods employing normal patient databases as the healthy standard when quantifying myocardial perfusion defects, the proposed method utilizes a patient-specific template for its healthy standard. In doing so, TQPS aims to overcome a number of the limitations associated with the non-patient-specific nature of normal patient databases.

The TQPS method begins with the construction of a template, which is a 3D digital model of the patient's healthy heart, using the SPECT reconstructed image. The template is then projected, reconstructed and sampled into the bulls-eye map domain. A ratio of the patient and template bulls-eye images produces a final corrected image in which a patient-specific threshold is applied to identify perfusion defects. Traditional semi-quantitative cardiac measurements, such as the summed stress score and perfusion defect extent were employed for the analysis.

This thesis presents the investigation of TQPS in three phases: method evaluation, optimization, and validation. The first two phases focused on controlled simulation studies in which the assessment was based on how well TQPS was able to quantify myocardial perfusion defects relative to the truth. In these studies, the method was able to spatially define perfusion defects with a sensitivity and specificity of 79% and 76%, respectively, while estimating the global perfusion defect size to within 3% of the truth. In the third phase, the aim was to clinically evaluate TQPS relative to an

established commercial method (QPS). TQPS exhibited improved specificity relative to the commercial method for the detection of significant coronary artery disease in the left anterior descending artery. The sensitivities for detecting 70% stenosis or greater in the LAD, LCX and RCA territories for QPS and TQPS were 60%, 82%, 75%, and 88%, 94%, 75%, respectively.

In summary, the TQPS method was able to accurately quantify myocardial perfusion defects in SPECT MPI, while exhibiting considerable advantages over a traditional normal database method, particularly in the LAD coronary territory.

Preface

The work leading to the development of the method presented in this thesis is described briefly in Chapter 3. This was published in the Journal of Nuclear Cardiology in 2010: Celler A, Shcherbinin S, and Hughes T. (2010) An investigation of potential sources of artifacts in SPECT-CT myocardial perfusion studies. J Nucl Cardiol. 17(2): 232-246. In this study, I was responsible for the analysis of the data, with particular attention paid to the cardiac applications. I was also involved in writing the manuscript.

Chapter 5 is based on the work performed at the Medical Imaging Research Group of Vancouver by Dr. Anna Celler, Dr. Sergey Shcherbinin, and Tyler Hughes. This work has been published: Hughes T**,** Shcherbinin S, and Celler A. (2011) A template-based approach to semi-quantitative SPECT myocardial perfusion imaging: Independent of normal databases. Med Phys. 38(8): 4186-4195. In this study, I worked with Dr. Celler and Dr. Shcherbinin in the design of the method, and ultimately performed all of the simulations and subsequent analysis. Additionally, I wrote the manuscript. Along with Dr. Celler, I performed the physical phantom experiments, and with Dr. Shcherbinin, I developed the necessary Matlab code.

The work presented in Chapter 6 was published: Hughes T and Celler A. (2012) Towards a practical template-based approach to semi-quantitative SPECT myocardial perfusion imaging. Med Phys. 39(3): 1374-1385. I performed all experiments and analysis in this study, along with writing the manuscript. Dr. Celler and I worked together in the methodology of this study.

A version of Chapter 7 has been submitted to the Journal of Nuclear Cardiology. Hughes T and Celler A. (2012) Clinical evaluation of a template-based method for semi-quantitative myocardial perfusion SPECT. J of Nucl Cardiol (Submitted). I was involved in obtaining all sets of data for this study, including the nuclear medicine data and coronary angiography data from VGH. The acquisition of data from SPECT and coronary angiography was granted by the UBC Research Ethics Board (ID: H11-00527). I performed all analysis and wrote the manuscript for this study.

In addition to peer-reviewed publications, the work (and versions thereof) presented in this thesis has been presented in numerous international meetings, including the 2011 Society of Nuclear Medicine meeting in San Antonio, TX (J Nucl Med, 52(supplement 1): 2041); the 2010 American Society of Nuclear Cardiology meeting in Philadelipha, PA (J Nucl Cardiol. 17(4):739), and two presentations at the 2009 IEEE Medical Imaging Conference in Orlando, FL (NSS Conf Rec. 2009: 2839-2841, NSS Conf Rec. 2009: 2839-2841).

Table of Contents

List of Tables

List of Figures

List of Abbreviations

4DM	4DM SPECT
AC	Attenuation correction
AD	Average deviation
APDI	Analytical photon distribution interpolation
AUC	Area under the curve
CABG	Coronary arterial bypass grafting
CAD	Coronary artery disease
CB	Corrected bulls-eye
CB_D	Corrected bulls-eye with the defect defined
CI	Confidence intervals
CT	Computed tomography
CTA	Computed tomography angiography
ECHO	Echocardiography
ECT	Emory Cardiac Toolbox
EXT	Perfusion defect extent
EXT-TQPS	Perfusion defect extent measured using TQPS
GE	General Electric Company
HT	Healthy threshold
LEHR	Low energy high resolution collimator
LV	Left ventricle
MPI	Myocardial perfusion imaging
MRI	Magnetic resonance imaging
NCAT	Non-uniform cardiac and torso

OSEM	Ordered subsets expectation maximization
PB	Patient bulls-eye
PCI	Percutaneous coronary intervention
PET	Positron emission tomography
PMT	Photomultiplier tube
PPD	Primary photon distribution
PVC	Partial volume correction
QPS	Quantitative Perfusion SPECT
ROC	Receiver operating characteristic
RR	Resolution recovery
SC	Scatter correction
SD	Standard deviation
SE	Standard error
SPD	Scattered photon distribution
SPECT	Single photon emission computed tomography
SSS	Summed stress score
SSS-QPS	Summed stress score measured using QPS
SSS-TQPS	Summed stress score measured using TQPS
TB	Template bulls-eye
T_{HRT}	Template with a heart compartment only
T_{HRTBKG}	Template with heart, lungs, and background compartments
T_I	Ideal template
T_P	Template projected with primary photons only
T_{PS}	Template projected with primary and scattered photons
T_s	SPECT-based template
TPD-TQPS	Total perfusion deficit measured using TQPS
TQPS	Template-based Quantitative Perfusion SPECT
VGH	Vancouver General Hospital

Acknowledgements

I offer my most sincere thanks for the continual support I have received from my PhD committee, the members of the Medical Imaging Research Group of Vancouver and the instructors in Medial Physics program at the University of British Columbia. In particular, I would like to thank Dr. Sergey Shcherbinin and Dr. Anna Celler.

Sergey, without your guidance - especially in the early days - I would not be where I am today. For your willingness to always share your seemingly endless mathematical expertise and scientific precision, I am deeply thankful.

Anna, I could not imagine a better mentor. The opportunity you gave me to join the group way back in 2007 is something I will never forget. Thank you so much for always pushing me and challenging me as an academic throughout my years at MIRG. I am forever thankful for the open arms you have provided for me every time I stepped into your office.

Finally, I would like acknowledge the University of British Columbia and the National Science and Engineering Council for funding my research over the last four years.

Dedication

To my Parents and Brother, for being there

for every equation solved,

for every homerun hit,

and every mile in between…

1 Introduction

1.1 Aim

Single photon emission computed tomography (SPECT) is a member of a relatively small class of medical imaging modalities, which have the capability of imaging human physiology and functional processes. In particular, as will be discussed in this thesis, SPECT can be used to assess the physiological impact of obstructed coronary arteries by imaging the blood perfusion within the myocardium. This technique, known as SPECT myocardial perfusion imaging (MPI), has demonstrated strong diagnostic and prognostic value for patients with known or suspected coronary artery disease (CAD). The identification of coronary artery disease, which is the leading cause of death in the western world, is the diagnostic end point for the method developed in this thesis.

The number of diagnostic tools available to cardiologists for the assessment of this pathology is extensive; though, each tool comes with its respective advantages and disadvantages. For instance, SPECT MPI is one of the most indispensable technologies available to a cardiologist; however, this modality has a number of limitations. Of particular relevance to this thesis are its limitations associated with image artifacts (false representations of the true image) and normal patient databases, which are employed by commercial software for the assessment of myocardial perfusion defects (regions with reduced perfusion).

Current commercial methods assess patients' myocardial perfusion by comparing their SPECT MPI images to a normal patient database, which is used as a healthy standard. These databases are constructed from several SPECT MPI images of healthy volunteers, which are ultimately amalgamated to create one average image of a healthy heart. However, due to this necessary averaging, the databases lack the detail of patient-specific features (including artifacts) commonly present in SPECT MPI images. For this reason, normal patient database methodologies are unable to unequivocally differentiate between myocardial perfusion defect and image artifacts in all cases.

It is hypothesized that the method presented in this thesis can improve upon the specificity of current commercial SPECT MPI techniques in the assessment of myocardial perfusion and the detection of coronary artery disease. Specifically, the proposed method is designed to overcome the aforesaid limitations through the utilization of patient-specific information. In doing so, the method is capable of correcting patient-specific image artifacts, and can therefore improve upon the specificity of SPECT MPI relative to traditional methods. With the patient-specific information coming in the form of a template, the method presented in this thesis is accordingly named the Template-based Quantitative Perfusion SPECT method, TQPS.

1.2 Highlights

- Developed a new method for the semi-quantitative assessment of myocardial perfusion with SPECT MPI, which is independent of normal patient databases.
- Developed the first template-based method where the template is constructed from nuclear medicine data, as opposed to high-resolution CT or MRI.
- Designed the first application of a template-based method for the direct measurement of myocardial perfusion in SPECT.

- Significant improvements were observed for TQPS in the detection of significant coronary artery disease relative to a leading commercial software package.
- Successful optimization of TQPS has enabled the method to perform within the clinical standards, in terms of computation time.
- The TQPS method utilizes both components of the modern SPECT-CT systems, thereby offering a new application for the CT component of these hybrid systems.

1.3 Dissertation Structure

This thesis is composed of eight chapters. The current chapter, Chapter 1, provides a high level introduction to the many aspects of the thesis along with the main objectives, highlights and overall structure.

Chapter 2 provides the necessary background for the method and its applications described in this thesis. Specifically, Chapter 2 covers both the physical and technical details of SPECT imaging as well as some of the anatomical and physiological information regarding the heart and the diagnostic assessment of coronary artery disease.

Chapter 3 describes the motivation for this thesis, together with literature describing current state of SPECT MPI. Highlighted topics include: the current state of commercial SPECT MPI software packages and their limitations, relevant image artifacts presented in SPECT MPI, as well as a review of the previously developed template-based methods.

Chapter 4 introduces the concept of the method developed in this thesis: the Template-based Quantitative Perfusion SPECT (TQPS) method. This section details each step of the method as it is used in this thesis.

The following three chapters (Chapter 5-7) of this thesis describe the studies involved in the three phases of the TQPS analysis. Each chapter is structured with sections for their respective methodologies, experiments, results, discussion, and conclusions. Chapter 5 begins this set of chapters by describing the initial evaluation of the method, which was a proof of principle study with emphasis on simulation data. Chapter 6 describes the study aimed at optimizing TQPS in terms of computation time and accuracy. Finally, Chapter 7 concludes the analysis with the clinical evaluation of TQPS using the detection of significant coronary artery disease as the diagnostic end point.

Chapter 8 states the conclusions from the studies reported in this thesis as well as the potential for future studies.

2 Background

This dissertation is multidisciplinary in nature, combining physics with cardiology. Specifically, the studies presented in this work dive deep into the technical and physical aspects of SPECT imaging, in addition to the physiological considerations regarding its application to myocardial perfusion and coronary artery disease. The following chapter will provide a comprehensive review of the background knowledge necessary to appreciate the methodologies and applications described in this thesis.

2.1 Emission Tomography

Medical imaging is a diagnostic tool that bestows a unique ability in that it allows a physician to see inside a patient's body. Behind the scenes of medical imaging resides an elaborate field of applied physics and engineering that has flourished over the last two decades, enabling medical imaging to become one of today's most prominent and influential components within the medical arena.

Emission tomography is a branch of medical imaging that comprises two principal techniques, positron emission tomography (PET) and single photon emission computed tomography (SPECT), which ultimately produce volumetric images (*tomography)* of the body's physiological properties using radiation emitted from injected radioactive materials (*emission)*. In contrast to anatomical imaging modalities, such as x-ray computed tomography (CT) and magnetic resonance imaging (MRI), PET and SPECT inherently offer functional information, depicting physiology rather than anatomy.

Whereas anatomical imaging depicts bony structures and soft tissue; functional (or physiological) imaging highlights bodily processes, such as blood perfusion or glucose metabolism (and many others). Therefore, emission tomography enables the detection of such diseased states as decreased dopamine activity related to Parkinson's disease and, in the interest of this thesis, malperfused regions of the heart muscle due to coronary artery disease.

The magic of physiological imaging lies within the tracer principle, invented in 1912 by Nobel laureate George de Hevesy who discovered that radioactive elements had identical chemical properties to their nonradioactive form and thus, could be used to trace chemical behavior in the body. In practice, SPECT and PET employ this phenomenon by injecting the patient, prior to image acquisition, with a radioactive compound known as a radiotracer (or simply, tracer), which is composed of a pharmaceutical and a radioactive isotope. Since the initial discovery of the tracer principle, there have been substantial advances in radiotracer design as a result of the immense amount of research in chemical engineering and radiopharmacy aimed at exploiting this principle. With these advances, emission tomography has rapidly evolved over the years with applications in neurology, oncology, and of course, cardiology.

Regardless of the technique, PET or SPECT, the general steps involved in the clinical imaging process are the same (see Figure 2-1), starting from the production of the radiotracer to the final image.

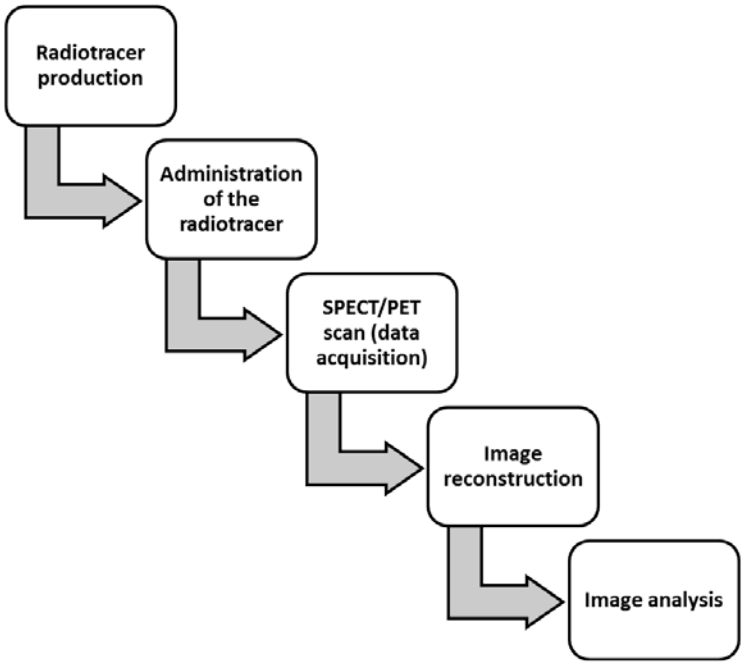

Figure 2-1 General imaging protocol for SPECT and PET imaging.

Prior to image acquisition, the appropriate radiotracer must be produced and subsequently administered to the patient. Depending on the imaging modality, study type and radiotracer, the data acquisition (often referred to as a 'scan') will begin at a predetermined time after administration. Once the data is acquired, it can then be reconstructed using a mathematical algorithm to produce a final three dimensional image, ready for the analysis by nuclear medicine physician.

Although the final images produced by PET and SPECT depict very similar information, the image acquisition process is quite different. In PET, the radiotracer is labeled with a positron emitting isotope, as where SPECT radiotracers are labeled with single photon emitters. The emitted positron from a PET tracer subsequently annihilates with an electron to produce two (roughly) collinear gamma photons, which are then detected by a ring of stationary detectors positioned around the patient. In contrast, the single

gamma photons emitted by SPECT tracers are detected by a large aperture detector, which rotates around the patient at set time intervals. Herein, the focus of this thesis will be on SPECT imaging.

2.2 SPECT

2.2.1 Basic Physics

In order to fully understand the imaging process in SPECT, it is critical to be familiar with two fundamental areas of SPECT physics: 1) nuclear emissions, and 2) photon-matter interactions. The entire scope of these two topics need not be fully explained for the purposes of this thesis; thus, this section will only provide a brief description of these two areas with focus on their relevance to this thesis.

Nuclear Emissions

Nuclear emission is the process by which the data in SPECT originates. As mentioned in the Introduction, SPECT utilizes the radiation emitted by a radiotracer, which has been administered to the patient. In the particular application of SPECT myocardial perfusion imaging, the radioisotope most commonly employed is technetium-99m (^{99m}Tc).

Congruent with nature, the nucleus of an atom has the fundamental property of evolving from higher to lower energy states. The transition of a nucleus from a higher (excited) to lower energy state results in the release of energy in the form of a gamma ray or conversion electrons. In SPECT imaging, it is the gamma photon emissions that are of interest. For instance, ^{99m}Tc decay (see Figure 2-2) results in a 140 keV gamma

photon emission, which happens to be a very favourable energy for SPECT imaging (more on this later). Specifically, in the case of ^{99m}Tc, the nucleus undergoes isomeric transition, which is the process of a gamma photon (or a conversion electron) being emitted from a nucleus in a metastable state. The term metastable refers to a nucleus in an exited state that has a lifetime longer than 10^{-12} seconds and is denoted with a superscript 'm', as in ^{99m}Tc.

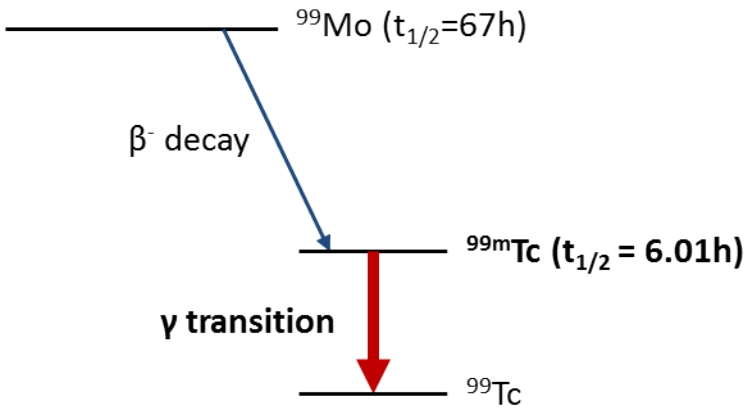

Figure 2-2 A simplified nuclear energy level diagram of the ^{99}Mo-^{99}Tc system for the generation and decay of ^{99m}Tc. The decay of interest in SPECT imaging is shown by the red arrow. The diagram is not to scale.

The activity $A(t)$ of a radioactive sample is a commonly used term in nuclear medicine, which describes number of decays per unit time:

$$A(t) = -\frac{dN}{dt} = A(0)e^{-\frac{ln2}{t_{1/2}}\cdot t} \qquad \text{Eq. 2-1}$$

where N is the number of nuclei, $A(0)$ is the initial activity, and $t_{1/2}$ is the half-life of given radioactive decay, which is the time needed to reduce the initial number of nuclei by a half. The SI unit for activity is the Becquerel (Bq), defined as the number of decays per second.

Photon-Matter Interactions

The second area of basic SPECT physics is photon-matter interactions. The phenomena that comprise photon-matter interactions are ubiquitous throughout the entire SPECT imaging process. In total, there are two types of interactions that play a significant role in SPECT: photoelectric absorption and Compton scattering.

The photoelectric effect can be described as the process of an incoming gamma photon transferring all of its energy to a bound atomic electron, which is ultimately ejected from its host atom (see Figure 2-3). The energy of the ejected electron E_e can be described as:

$$E_e = h\nu - E_b \qquad \text{Eq. 2-2}$$

where E_b is the binding energy of the electron, and $h\nu$ is the energy of the incoming photon as described by its frequency ν and Planck's constant h, $6.626 \cdot 10^{-34}\ J \cdot s$. The likelihood that a photon is absorbed via the photoelectric effect increases as Z^4, where Z is the atomic number.

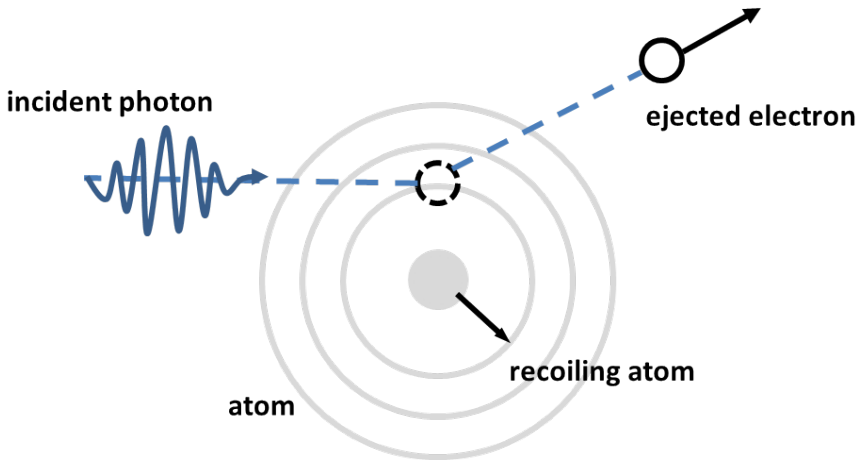

Figure 2-3 A schematic of the photoelectric effect.

Compton scattering involves the interaction of a gamma photon with an outer-atomic-shell electron (considered unbound in this model), as shown in Figure 2-4. Specifically, an incident photon with energy $h\nu$ will encounter and eject an electron with rest mass energy m_0c^2, to produce a scattered photon with energy $h\nu'$ and a scattered electron, moving at angles θ and ϕ, respectively.

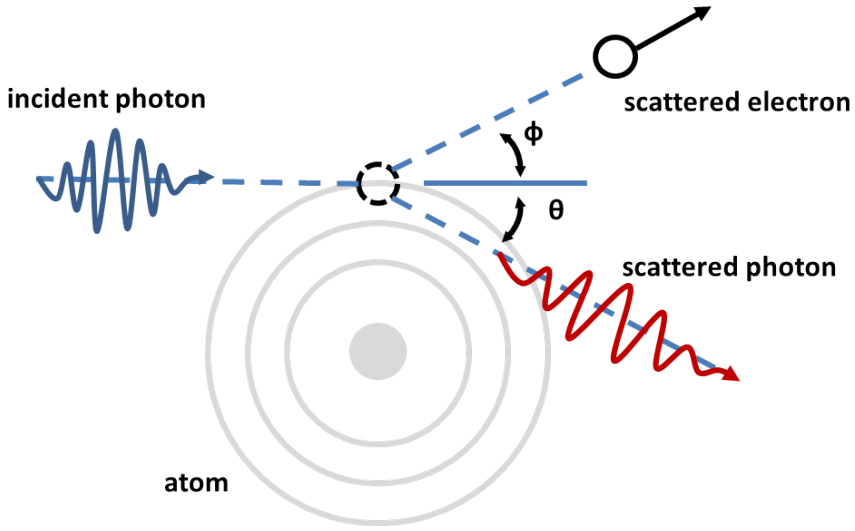

Figure 2-4 A schematic of Compton scattering.

Using the principles of conservation of energy and momentum, the final energy of the scattered photon can be expressed as follows:

$$h\nu' = \frac{h\nu}{1+(h\nu/m_0c^2)(1-\cos\theta)} \qquad \text{Eq. 2-3}$$

The angular distribution of the scattered gamma photons can be described using the Klein-Nishina formula written in terms of the differential scattering cross section:

$$\frac{d\sigma}{d\Omega} = Zr_0^2\left[\frac{1}{1+\alpha(1-\cos\theta)}\right]^2\left(\frac{1+\cos^2\theta}{2}\right)\left\{1+\frac{\alpha^2(1-\cos\theta)^2}{(1+\cos^2\theta)[1+\alpha(1-\cos\theta)]}\right\} \qquad \text{Eq. 2-4}$$

where Z is the atomic number, α is the commonly used term $h\nu/m_0c^2$, and $r_0$is the electron radius. The expression in Eq. 2-4, given in units of barns (1 barn = 10^{-24} cm^2) per steradian, describes the probability that a photon will interact with an electron as a function of the initial photon's energy and scattering angle as well as the electron density. A more intuitive representation of the Klein-Nishina cross section can be seen in Figure 2-5.

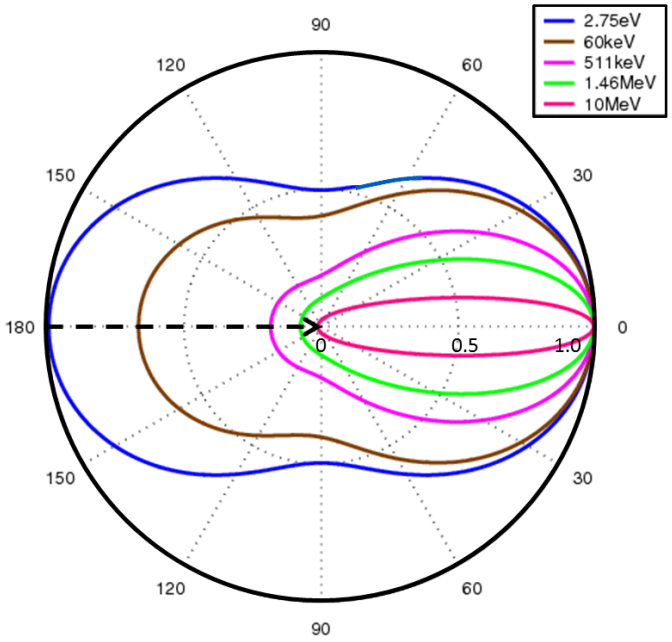

Figure 2-5 A Klein-Nishina polar plot for a number of different incident photon energies. The angles are shown on the outer ring and the amplitude, normalized for purposes of this figure, is show on the zero degree axis. The direction of the incoming photon is shown by the dashed arrow.

One important characterisitic of Compton scattering that can be interpreted from Figure 2-5 is that there is a higher probability for high energy photons to scatter at small angles (forward) than it is for lower energy photons. When considering the relevant energy range for SPECT applications (60-400 keV), it is evident from Figure 2-5 that Compton

scatter can substantially affect the direction of an emitted photon. The total probability of Compton scatter is linearly dependent on the atomic number.

2.2.2 Hardware

As alluded to already, the acquisition in SPECT involves the detection of single gamma photons emitted from a radiotracer by a large aperture gamma-detecting camera, known as the Anger camera (Figure 2-6). Since its conception in 1957 by Hal Anger, the Anger camera (also referred to as a gamma camera or scintillation camera) has been the hallmark of SPECT imaging.

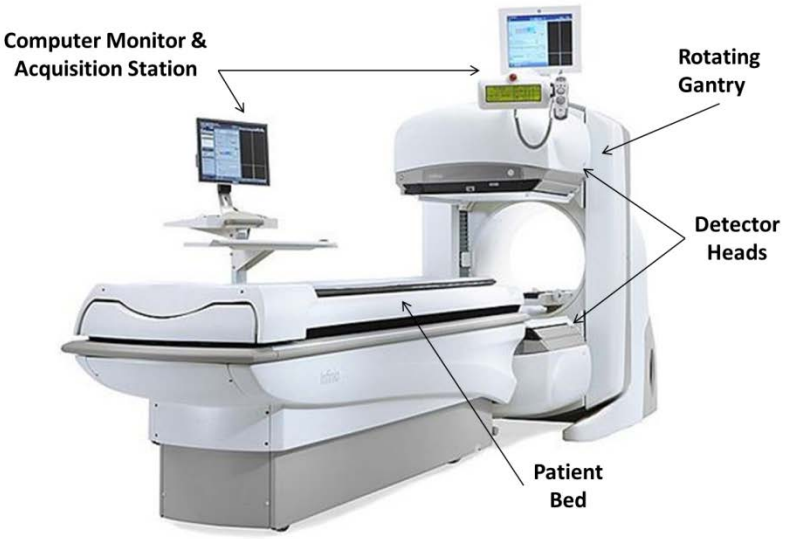

Figure 2-6 An example of a modern dual headed SPECT system: GE's Infinia™. The two detector heads (Anger camera heads) and other main components of the system are indicated and highlighted with the black arrows. Source: GE Healthcare.

As with most of the successful inventions in the world, the beauty of the Anger camera resides in its simplicity. Considering the challenges of detecting a gamma photon and

decoding its initial position and energy, one would rightfully assume an elaborate technical design for a system to achieve such a feat; however, the Anger camera can be narrowed down to just four components: 1) collimator, 2) scintillation crystal, 3) photomultiplier tubes (PMTs), and 4) energy and positioning electronics. A schematic of a generic Anger camera design can be seen in Figure 2-7 with each functional component briefly described below.

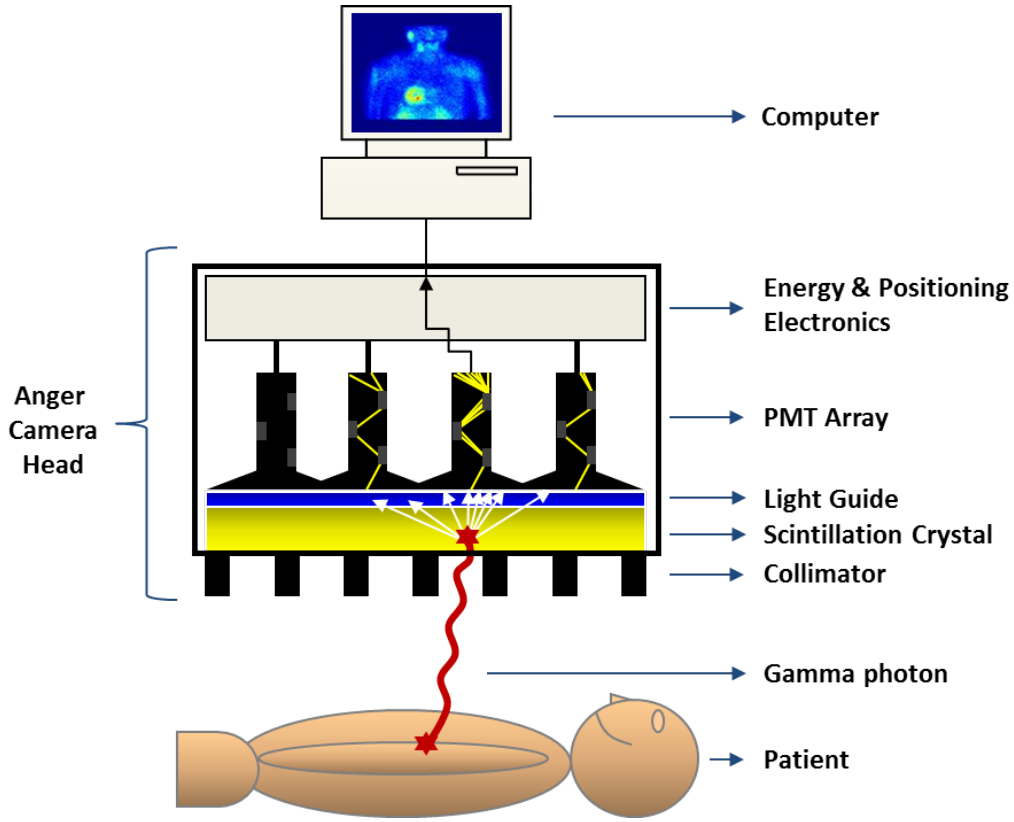

Figure 2-7 A schematic (not to scale) of a SPECT acquisition and the functioning parts of the Anger (gamma) camera at each level of the acquisition. The white arrows indicate the scintillated light generated from the scintillation crystal and the yellow lines in the photomultiplier tube (PMT) array represent the electric signal within each PMT.

Collimator

The first and very critical component of the Anger camera that an emitted gamma photon will encounter is the collimator - a thick sheet of perforated heavy material (such as lead) with long thin channels (referred to as holes). The purpose of the collimator is to define the direction of the incoming photons by allowing only these photons that pass through the collimator holes to reach the detector, while the others are being absorbed by the heavy material found between the holes (referred to as septa). Ideally, the material chosen for the collimator should satisfy two physical requirements: 1) it must have a high attenuation coefficient (μ) at the particular energy of the incoming photons in order to absorb them at the septa, and 2) it must produce relatively few secondary emissions in the interest of minimizing contamination. With regards to the latter requirement, it is desirable for the incoming photons to undergo photoelectric interactions (producing electrons and low energy secondary photons) as opposed to Compton or coherent scattering (producing high energy scattered photons). With these characteristics and other economic considerations, lead has been the most widely employed collimator material as it satisfies the aforesaid requirements for energies up to 230 keV, which covers a majority of the energies used in SPECT imaging.

The pattern and design of the holes and septa characterize the collimator and ultimately define how the images are acquired by the SPECT system. This has led to an active field of research resulting in a number of different collimator designs optimized for the various types of SPECT studies *(1-8)*.

Figure 2-8 illustrates the effects of different parallel-hole collimator designs, where the holes are oriented parallel to each other and incoming gamma photons are accepted (roughly) perpendicular to the camera face. As depicted in Figure 2-8, the characteristics of the collimator type, such as the thickness and length of the septa and

hole size influence the sensitivity (number of accepted photons) and spatial resolution of the SPECT system (width of the acceptance profile).

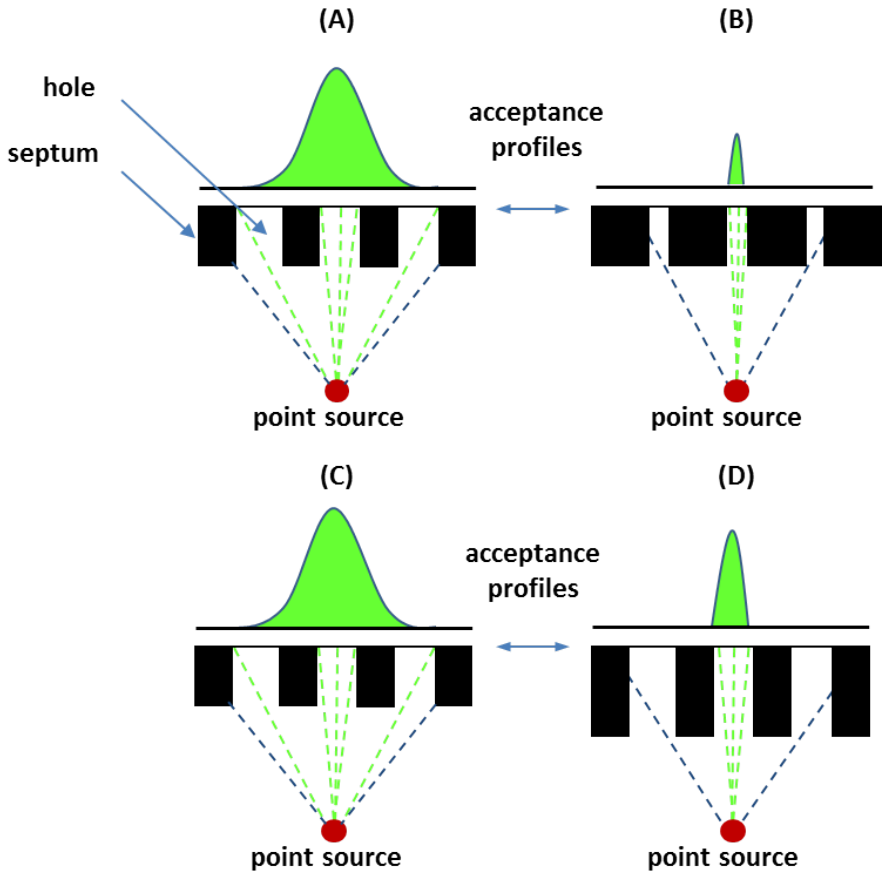

Figure 2-8 An illustration of various parallel-hole collimator designs with the corresponding acceptance profiles from a point source of activity. Comparing (A) and (B) demonstrates the effects of changing the thickness of the septa and hole size; Comparing (C) and (D) shows the effects of changing the length of the septa. The green and blue dashed lines indicate accepted and rejected photons, respectively.

Scintillation Crystal

Once past the collimator, the gamma photon will strike the scintillation crystal, which is the first component of the detection apparatus. Here, the incident energy of a gamma

photon is absorbed and subsequently re-emitted as a pulse of optical-wavelength photons (visible and ultraviolet). Both the photoelectric and Compton effect play a role in the scintillation process; however, the photoelectric effect is the more desirable interaction since the photon energy is absorbed in one interaction, as opposed to many interactions via Compton scattering. Therefore, scintillators are designed with high effective atomic numbers (Z_{eff}) to exploit the photoelectric effect's Z_{eff}^4 dependence relative to the Compton effect's linear dependence on Z_{eff}.

Another technical consideration regarding scintillator design is the crystal thickness. For instance, a thicker crystal has greater sensitivity since it has a greater probability of stopping (absorbing) the incoming gamma photons; however, this advantage comes with the trade-off of reduced spatial resolution since the increased thickness enables a greater spread of optical photons. In all, many factors must be taken into account when designing a scintillation crystal for SPECT in order to optimize the energy and spatial resolution of the system.

Due to its favourable properties, both physical and economical, thallium-activated sodium iodide crystals (NaI(Tl)) have been the scintillators of choice in SPECT. A NaI(Tl) crystal is very efficient, absorbing roughly 90% of incident photons and producing roughly 38 photons/keV at 140 keV, in addition to being relatively cheap to produce. In most clinical systems, a single large area NaI(Tl) crystal (on the scale of 40 x 50 cm^2) is used with a thickness of 0.95 cm, which is optimal for stopping gamma photons in the range of 140 keV (^{99m}Tc).

Photomultiplier Tubes

The next destination for the signal, now a pulse of optical wavelength photons, is an array of photomultiplier tubes (PMTs), which are designed to convert the incoming signal into an amplified electric signal. Typically, an Anger camera can be equipped with anywhere from 37 to 93 PMTs arranged in a hexagonal array. Schematics of a typical PMT array and the PMT design are provided in Figure 2-9. Briefly put, a PMT consists of an evacuated glass casing encompassing a photocathode and an anode as well as a number of intermediate electrodes called dynodes. The purpose of the photocathode is to absorb the incoming visible/UV photons via the photoelectric effect, which produces one photoelectron per photon absorbed. The electrons then encounter the set of dynodes, which are designed to emit secondary electrons when struck by an electron, thereby amplifying the electric signal at each dynode. The dynodes are arranged such that they increase in voltage (less negative), which facilitates the propagation of the negatively charged electrons toward the positive anode. Modern PMTs are able to achieve a gain of up to 10^6-10^7 in electric signal for a PMT with 10 dynode stages.

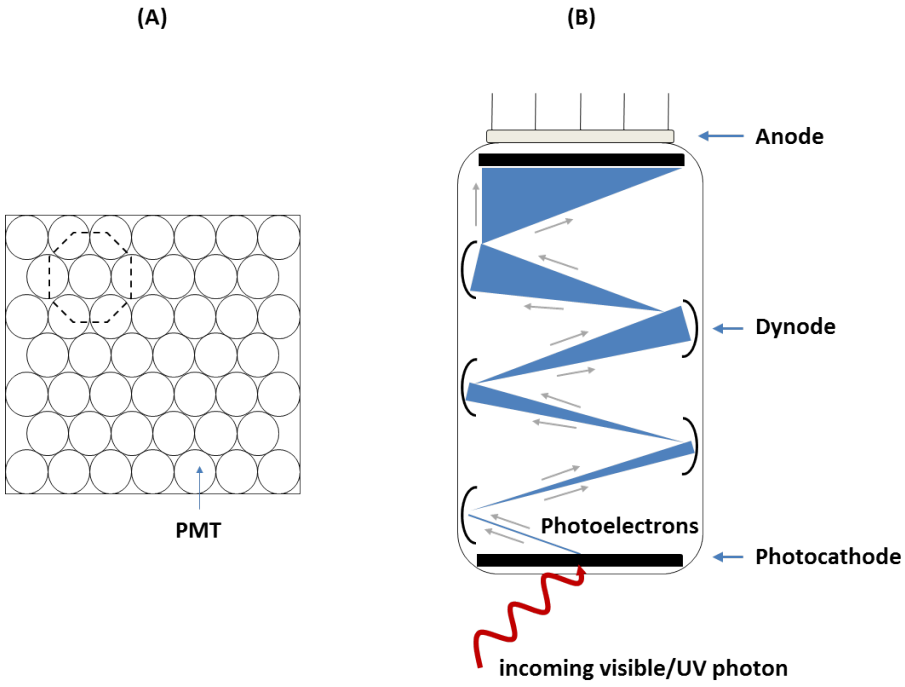

Figure 2-9 A schematic of the photomultiplier (PMT) array and design. (A) Shows a typical hexagonal array (dashed line) of circular faced PMTs as viewed from the camera face; (B) illustrates the design and general function of a standard PMT with all critical components labeled accordingly. The red curved line indicates an incoming optical photon, and the blue triangles indicate the electrical signal with the area of each shape indicating the relative size of the signal. The grey arrows indicate the directions of the electrical signal.

Energy & Positioning Electronics

Using the energy and positioning electronics, the Anger camera can process the electrical signal from the PMT array to estimate the location where the incident gamma struck the scintillator (X, Y) along with its respective energy (Z). It is important to note that when the scintillator produces its spatially broad pulse of optical photons, several PMTs will be activated resulting in a number of electrical signals reaching the energy and positioning electronics. To locate the position of an incident gamma ray, the

positioning electronics calculates the center of mass (X, Y) from all of the PMT responses:

$$X = \frac{1}{Z}\sum_{k=1}^{K} x_k a_k \qquad \text{Eq. 2-5}$$

$$Y = \frac{1}{Z}\sum_{k=1}^{K} y_k a_k \qquad \text{Eq. 2-6}$$

where (x_k, y_k) and a_k is center of and signal from the k^{th} PMT, respectively; and Z is the summed signal from all PMTs, which is proportional to the energy of the incident gamma photon.

This total signal (Z) from the PMT array is then used in the energy discrimination step. Ultimately, the Anger camera detects a wide spectrum of energies due to the many inelastic scattering events a photon can undergo in its journey from the emitting tracer atom to the detector (see Figure 2-10). In order to minimize the number of accepted scattered photons, an energy window is defined using a pulse-height analyzer, which sets a threshold for the minimum and maximum total signal (Z) to be accepted by the camera (see Figure 2-10). Typically, energy windows are set at ±7.5% to ±10% around the photopeak energy, which yields the best trade-off between sensitivity (number of accepted photons) and accuracy (number of non-interacting (photopeak) photons to interacting (scattered) photons).

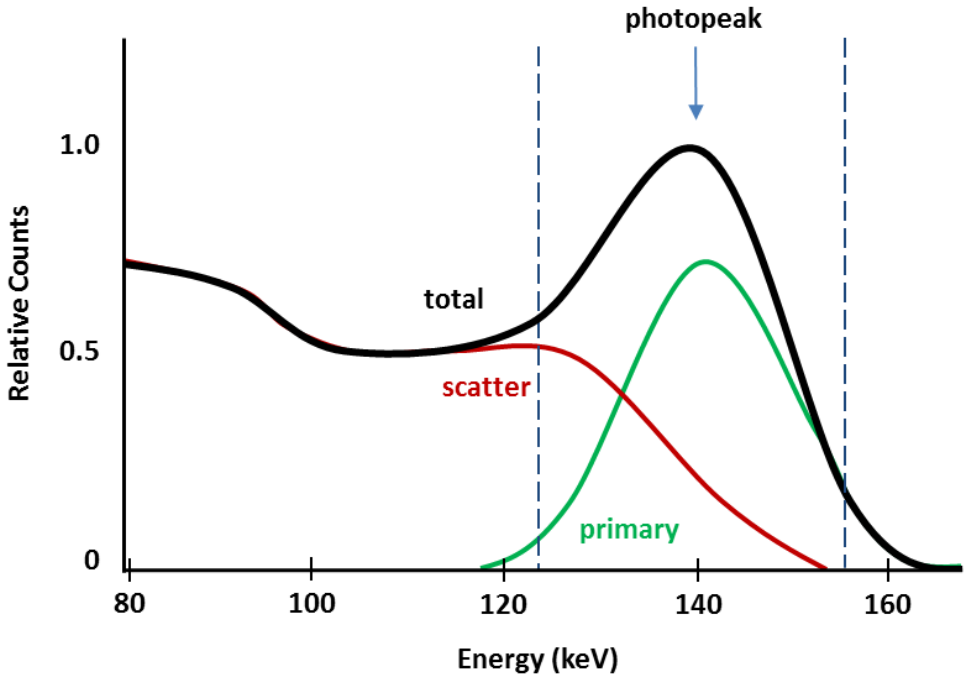

Figure 2-10 An illustration representing a ^{99m}Tc spectrum as measured by an Anger camera. The total detected energy spectrum is represented by the black line and its components, primary and scattered photons are shown by the green and red lines, respectively. The limits of an example energy window are shown by the blue dashed lines, with the photopeak indicated at 140 keV.

Computer

The final task for the Anger camera is to formulate an image. To achieve this, the camera uses computer memory to create a rectangular image matrix consisting of many storage locations. Each location, commonly referred to as a pixel, represents a fraction of the total field of view. In SPECT, data are usually acquired into matrices composed of 64x64 or 128x128 pixels, with pixel sizes of roughly 8x8 mm and 4x4 mm, respectively. Every signal accepted by the pulse-height analyzer is defined as a count, where each count is assigned to a pixel, corresponding to its position coordinates, X and Y. As the image is acquired, the counts recorded in each pixel will sum together to produce a final

two-dimensional projection (or planar) image corresponding to the activity distribution within the patient's body.

2.2.3 Acquisition

The goal of the acquisition process in SPECT is to collect sufficient data for 3D tomographic image reconstruction. To achieve this, the detector, which is mounted on a rotating gantry, will acquire a number of 2D projection images around the patient with each projection collecting data for 10-30 seconds. Typically, 60 to 128 projections are acquired at uniform angular intervals around the patient over an angular extent of 180^0 or 360^0 (see Figure 2-11). For the purposes of this thesis, only dual headed SPECT cameras will be considered although systems can be single or triple headed.

As illustrated in Figure 2-11, the detectors of a dual head SPECT system can be configured orthogonal to each other (termed "L-mode") or parallel to each other (termed "H-mode"), where the detectors will rotate to cover a total angular extent of 180^0 or 360^0, respectively. For SPECT MPI, the most common protocol adopts the "L-mode" configuration with the detectors positioned in front of the patient, since the heart resides in the anterior aspect of the human chest.

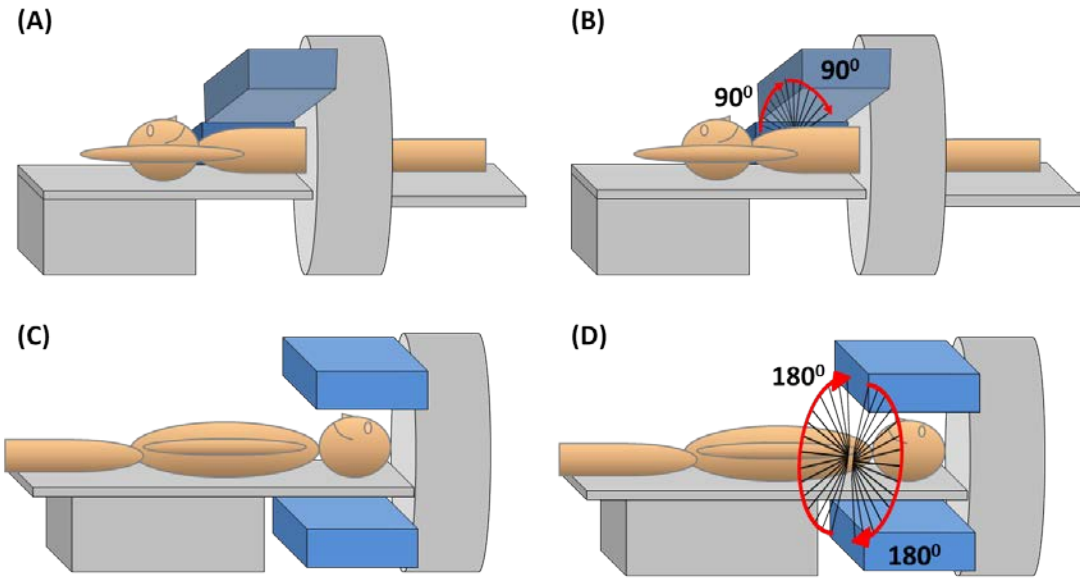

Figure 2-11 Illustrations showing basic SPECT set-ups and the corresponding acquisition processes. (A) Shows a standard 90^0 or "L-mode" set up for a typical cardiac SPECT scan with a dual head camera and (B) shows the typical 90^0 path for each detector head with such a set up (covering at total of 180^0). (C) Shows a standard 180^0 or "H-mode" set up for a typical brain study using a dual headed camera and (D) shows the typical 180^0 path for each detector head with such a set up (covering a total of 360^0). The blue boxes represent the two camera heads for each camera. The red arrows signify the overall path for the camera heads, with the black lines indicating where the cameras stops for each projection (number of projections is reduced for clarity).

2.2.4 SPECT Reconstruction

The Problem

Once the 2D projection data sets have been acquired, they can be used to mathematically construct a final 3D image via tomographic image reconstruction. By producing a 3D volumetric image, the physician is able to visualize the activity distribution inside the patient body in a slice by slice manner.

Mathematically stated, the reconstruction problem in SPECT is to find the 3D distribution of radiotracer within the patient's body x, using: 1) a set of 2D projection images y, and 2) information regarding the imaging system and possibly a statistical description of the data, all in the form of a matrix referred to as the system matrix C. Figure 2-12 illustrates the processes involved in a SPECT projection acquisition along with the data to be considered in the reconstruction. Specifically, Figure 2-12 shows the primary (non-interacting) photon, and the image degrading effects that occur during the SPECT acquisition process; namely photon scatter, photon attenuation, finite collimator resolution and statistical noise.

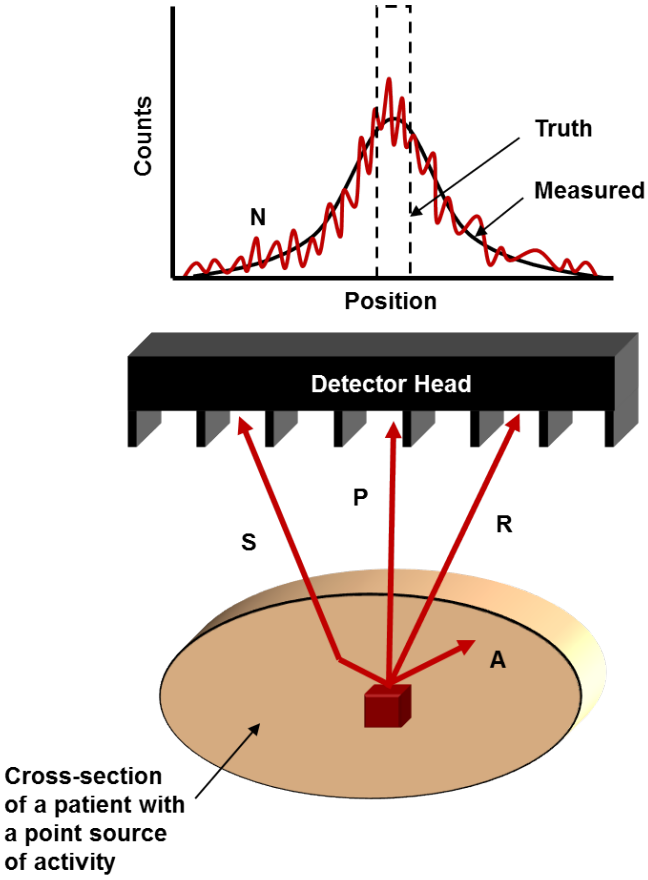

Figure 2-12 A general model of the acquisition process for a single projection in SPECT for a simple radiotracer distribution, x. The red arrows indicate the possible paths taken by photons from a point of emission to the detector face, where S is a scattered photon, P is a primary photon, R shows a photon accepted at a non-zero angle to the collimator septa (a result of the collimator's finite resolution), A is an attenuated photon, and finally N illustrates image noise. These are the processes to be modeled in the system matrix, C. The graph at the top depicts a typical final profile from the projection data, y, (red curvy line) measured relative to the truth and measured data without noise.

For computing purposes, the images are sampled to create discrete-domain functions, as illustrated in Figure 2-13. As mentioned already, the projection space is sampled into 2D elements called pixels (also referred to as bins); similarly, the image space is sampled into 3D elements, referred to as voxels.

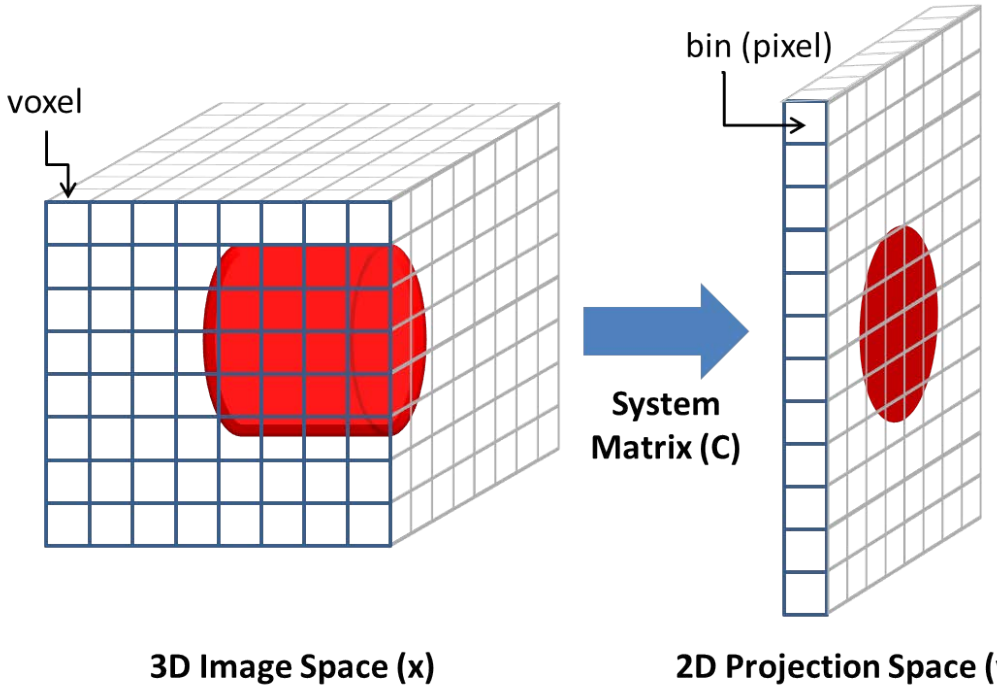

Figure 2-13 A simplified schematic of the discrete model for the image and projection spaces in SPECT. The red cylinder in the image space represents a simple activity distribution with the corresponding 2D projection in the projection space. A voxel and bin (pixel) are indicated, along with the system matrix which describes how the projection is formed from the image.

Mathematically, the reconstruction problem in SPECT is known as the inverse problem (Eq. 2-7):

$$y = Cx + n \qquad \text{Eq. 2-7}$$

where the goal is to find the object activity distribution $\boldsymbol{x}$, given a set of measured projections $\boldsymbol{y}$, information regarding the imaging system (system matrix) $\boldsymbol{C}$, and a statistical description of the measured data $\boldsymbol{n}$ (noise). Due to the immense size of the matrices presented in SPECT and image noise, the system matrix cannot be analytically inverted to solve the equation; thus, indirect approaches are adopted.

Reconstruction Algorithms

The more conventional method used to solve Eq. 2-7, which is still commonly used in most nuclear medicine departments, utilizes the idea of filtered backprojection (FBP) *(9)*. FBP is an analytical approach where the detected counts in each projection bin are evenly spread back into image space along the direction from which the photons came. This process is termed backprojection. After performing this operation for all projection bins, the line traces in image space will constructively overlap to resemble the true activity distribution. However, the backprojection operation leads to blurring of the image; thus, FBP is performed using a ramp filter applied to the projection data (in the Fourier domain) to cancel the blurring effect, which can be proven via the central slice theorem *(10, 11)*. The drawbacks of FBP, although extremely fast, include its inability to model image degrading effects such as collimator response, scatter, attenuation and noise into the algorithm.

A popular and more sophisticated method used to solve Eq. 2-7 is an iterative approach. Within this family of reconstructions, the most common techniques employed within the nuclear medicine community are based on the Maximum Likelihood-Expectation Maximization (MLEM) algorithm *(12)*. This algorithm is designed to seek the most likely distribution of activity given a set of measured projections. In its entirety, the MLEM algorithm can be written as follows:

$$x_j^{n+1} = \frac{x_j^n}{\sum_{i=1}^{N} C_{ij}} \sum_{i=1}^{N} \frac{C_{ij} y_i}{\sum_{k=1}^{M} C_{ik} x_k} \qquad \text{Eq. 2-8}$$

where y_i is the measured number of counts in projection bin i, x_j^n is the activity estimate in voxel j after the n^{th} iteration, C_{ij} is the system matrix element for projection bin i and image voxel j, and $\sum_{k=1}^{M} C_{ij} x_k$ is the forward projection step that estimates the

value of the projection bin i. The sums over M and N are over all voxels in the reconstructed object and all projection bins, respectively.

A conceptual description of the iterative reconstruction approach is provided in the flow chart in Figure 2-14. The algorithm begins with an initial image estimate – typically a uniform image – which is projected into the projection space using the system matrix. This "projection step" of the algorithm simulates what the detector would measure given the initial activity distribution. These estimated projections are then compared to the measured projections to create error projections, which are subsequently backprojected into image space to create an update image. The updated image is then used with the old estimate to form a new estimated image, concluding the first iteration. This process is repeated for a user defined number of iterations.

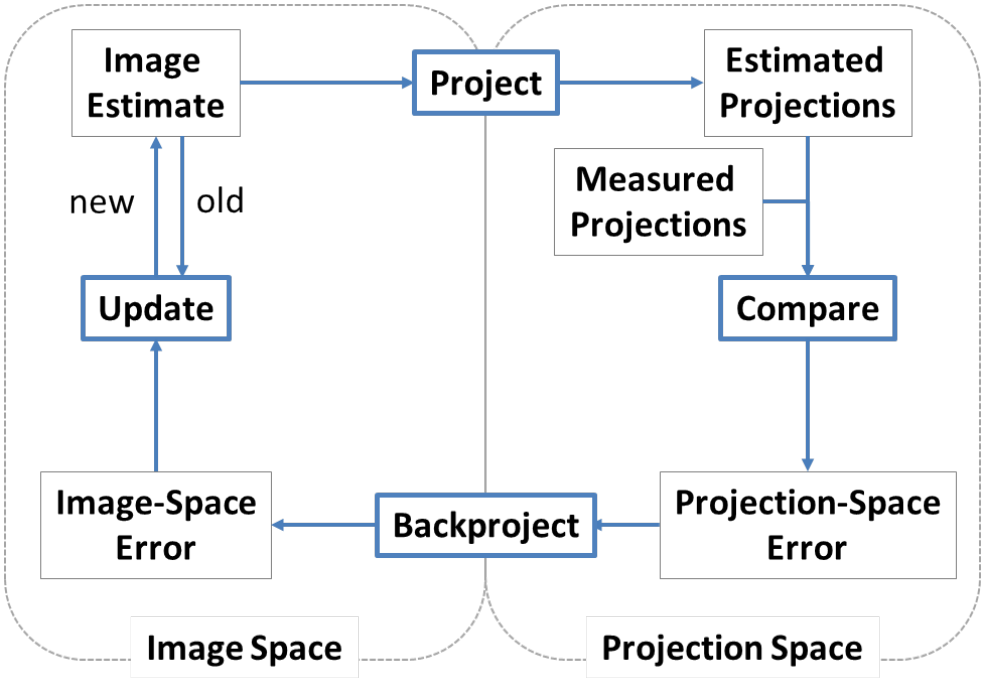

Figure 2-14 A flow chart representing the steps involved in an iterative reconstruction algorithm in SPECT.

An advantage of this algorithm (and iterative approaches, in general) relative to direct reconstructions (FBP) is that the photon emission-detection process (i.e. attenuation, scatter, etc.) can be modeled and implemented into the system matrix. Moreover, MLEM has the ability to model noise and apply constraints on the possible solutions based on *a-priori* knowledge of the activity distribution. The goal of the algorithm is to iteratively improve the estimation of the activity distribution by minimizing the difference between the estimation and measured data in projection space; however, the convergence of this algorithm is not obvious. Therefore, the optimal number of iterations is a topic of discussion since it is not known *a-priori*, but today's commercial algorithms have recommended values based on empirical studies.

Relative to filtered backprojection, MLEM is computationally intensive, especially when all corrections are implemented into the system matrix (more on this later); therefore, commercial algorithms have adopted an accelerated MLEM-based algorithm, known as Ordered Subsets Expectation Maximization (OSEM) *(13)*. The idea behind this algorithm is to group the projections into subsets, rather than processing the entire set of data as a whole, as in MLEM. Mathematically, OSEM is very similar to MLEM and can be expressed as follows:

$$x_j^{n+1} = \frac{x_j^n}{\sum_{i \epsilon S_n}^{N} C_{ij}} \sum_{i \epsilon S_n}^{N} \frac{C_{ij} y_i}{\sum_{k=1}^{M} C_{ik} x_k} \qquad \text{Eq. 2-9}$$

where the backprojections are performed only for the projections belonging to the subset S_n.

In the OSEM algorithm, the standard projection/backprojection step is applied to each of the subsets in sequence, with each resulting reconstruction used as the starting point for the next subset. Therefore, an iteration in OSEM is defined as one full pass through

all subsets. By performing the projection/backprojection step with only a subset of projections as opposed to the full set of projections, the OSEM algorithm is able to reconstruct an image much faster than MLEM. As a general rule, the number of subsets multiplied by the number of iterations in OSEM corresponds to the number of iterations in MLEM. For example, an OSEM reconstruction using 10 subsets and 10 iterations (typical values) is roughly equal to 100 iterations of MLEM, which clearly shows the increased speed of OSEM.

Image Correction Methods

The main difference between various implementations of OSEM-based reconstruction methods is in the system matrix. As depicted in Figure 2-12, there are many technical challenges and image degrading factors that must be overcome in SPECT. The goal of the system matrix as part of a reconstruction algorithm is to accurately model the probability that a photon emitted from a given voxel will end up being detected in a given projection bin; thus, models of image degrading effects are often integrated into the system matrix. There has been extensive research involving the development of algorithms devoted to modeling the four primary sources of image degradation in SPECT: photon attenuation, collimator resolution loss, photon scatter, and partial volume effects.

Attenuation Correction (AC)

The term “attenuated photons” refers to photons that have been emitted by the radiotracer but failed to reach the detector due to scattering or photoelectric absorption. Thus, the attenuation effect deceives the camera in terms of the number of

photons emitted by the radiotracer within the patient's body. Attenuation is both a depth and tissue density dependent phenomenon, thereby rendering it as a non-uniform effect throughout a SPECT image.

In order to model attenuation, one must have information regarding the spatial distribution of attenuation coefficients throughout the patient's body. The earliest approaches to attenuation correction (AC) modeled the body as a uniform water-like structure *(14)*; however, this is clearly a crude assumption, particularly in regions such as the chest where attenuation coefficients vary considerably (i.e. bone to lung). With the recent advent of hybrid SPECT-CT systems, AC techniques now utilize the detailed anatomical information obtained from the x-ray CT image *(15-21)*. Specifically, these methods convert the patient CT image into a map of attenuation coefficients, which is used to model the attenuation effects in the system matrix *(22)*. Since the x-ray CT image is computed in terms of Hounsfield units and with a finer sampling rate than SPECT, the conversion of a CT image to an attenuation map involves rescaling its values into attenuation coefficients for the energy of interest and resampling to match the SPECT image voxel size. The extent of the attenuation effect can be quantified by a parameter known as the transmitted fraction $TF(t', s', \theta)$, which describes the fraction of photons transmitted from location (t', s') through an attenuating medium at projection angle θ:

$$TF(t', s', \theta) = e^{(-\int_{s'}^{\infty} \mu(t', s) ds)} \qquad \text{Eq. 2-10}$$

where $\mu(t', s)$ is the attenuation map representing the distribution of linear attenuation coefficients as a function of location; and the integral is along the direct path from the source location s' to the detector face (shown as ∞ since all attenuation coefficients outside the body to the detector face are considered to be equal to zero). Once the

attenuation map is generated, it can then be implemented into the system matrix using the transmitted fraction.

Resolution Recovery (RR)

The image in SPECT is further degraded by the imaging system's finite spatial resolution. When imaging a source of activity, the image blurring can be characterized by two main contributions:

1. Intrinsic resolution of the camera (R_i)
2. Collimator resolution (R_c)

An important property to note here is the dependence of the collimator resolution on the source to collimator distance, which is illustrated in Figure 2-15.

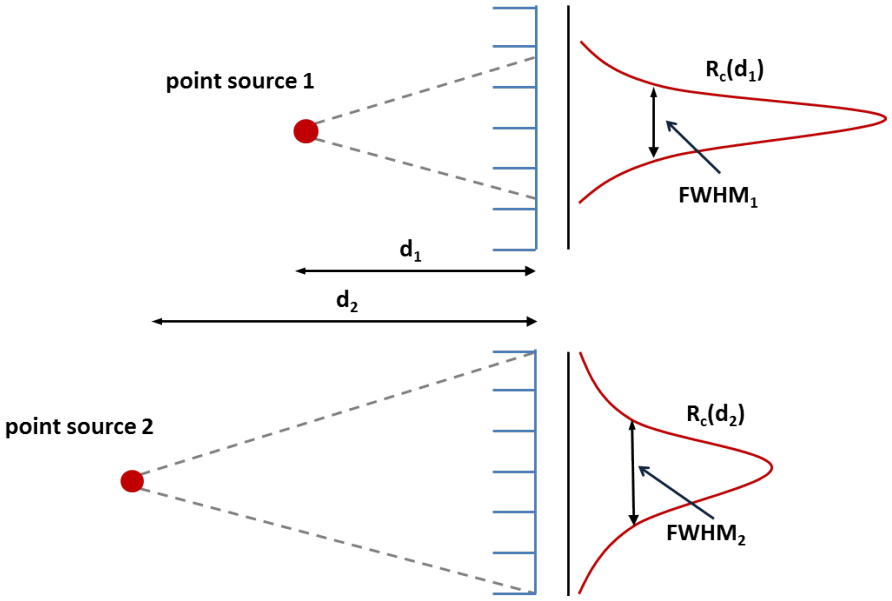

Figure 2-15 A schematic diagram illustrating the distance dependence of the collimator resolution, R_c. Two point sources of activity are shown at different distances from the collimator, d_1 and d_2, where $d_2 > d_1$. The respective responses of the collimator, $R_c(d_1)$ and $R_c(d_2)$, are shown on the right (red lines), along with their full width half maxima (FWHM), where $FWHM_2 > FWHM_1$. The horizontal axes on the response plots are the collimator responses (in counts) and vertical axes are the detector pixel positions.

In general, there are two main approaches to resolution recovery (RR): restoration filtering and spatial resolution modeling integrated into iterative reconstruction algorithms. Pre-reconstruction restoration filtering techniques are designed to recover the original image by applying the inverse of a filter that models the degradation of the original image resolution. The main issues with this approach are that it assumes spatial invariance and is subject to amplifying the noise in the image. To compensate for noise amplification, the inverse filter is usually modified with a low-pass filter in order to dampen the effects. Such filters that have been designed to restore the resolution in SPECT imaging include the Wiener and Metz filters *(23-25)*.

More advanced techniques used for resolution recovery in SPECT incorporate a depth-dependent blurring model (often called the collimator-detector response function) into the iterative reconstruction *(26-29)*. The attractive property of these methods is that the signal-to-noise ratio is maintained, as opposed to the restoration filtering techniques *(30)*. However, the one concern with this approach is the increase in computation burden resulting from modeling the collimator-detector response as it greatly reduces the sparseness of the system matrix. Consequently, there have been modifications to this approach by applying the RR model in a number of different ways. The original methods followed a "ray-driven" approach, where equiangularly spaced projection rays were propagated from each projector bin back through image space *(31)*. Ultimately, the contribution from each voxel to the projector bin was equal to the counts in the voxel multiplied by the voxel to detector distance and the collimator-detector response function at that distance. Although a fairly simple implementation, rays that missed voxels would lead to artifacts, thereby decreasing this method's utility *(32)*.

To overcome the limitations of the ray-driven approach, a so called "voxel-driven" approach was introduced, where rays are projected from each voxel in image space and summed into a projection bin. Despite being successful in avoiding missing voxel artifacts, this method tended to be computationally expensive relative to other methods *(28)*; however, a large reduction in computation time for voxel-driven approaches was realized with the use of a rotation-based system matrix *(28, 33)*. The idea behind the rotation-based system matrix was to take advantage of the fact that the collimator-detector response function is spatially invariant in planes parallel to the detector face. So, by using interpolation methods such as bilinear interpolation, the system matrix can be rotated such that the sampling grid is parallel to the detector plane. As a result, the response function can be easily implemented by convolving it with the system matrix at each plane.

Finally, modern resolution recovery techniques have exploited the fact that the collimator-detector response function, in the absence of septal penetration and septal scatter, can be approximated as a depth-dependent Gaussian function, which further accelerates the algorithm *(27, 34, 35)*. Most commercial algorithms offering RR in their reconstruction package generate this function empirically by imaging sources at various depths and measuring the systems response at each depth. The standard deviation of the Gaussian function modeling the collimator-detector response can be represented as:

$$\sigma_s = \sqrt{\sigma_i^2 + \sigma_c^2(d)} \qquad \text{Eq. 2-11}$$

where σ_s, σ_i, and $\sigma_c(d)$ are the system, intrinsic and collimator (geometrical contribution only) resolutions, respectively, and d is the source to collimator distance.

Scatter Correction (SC)

Scatter correction is one of the greatest challenges in SPECT reconstruction due to the fact that photons can scatter in all directions and undergo multiple scattering events prior to being detected. In the simplest sense, scattered photons deceive the detector regarding their origin of emission; thus, accepted scattered photons are spatially misrepresented in the final image. For instance, it has been shown in SPECT MPI that scattered photons originating from the liver can significantly influence the resulting image of the adjacent myocardium (more on this later) *(36-38)*.

Initial approaches to scatter correction expanded upon the idea of the energy window. For instance, by setting an additional energy window below the photopeak window (see Figure 2-16), one can assume that the scattered photons within lower window can be

used to estimate the scattered component within the photopeak window. This method is referred to as the dual energy window technique *(39, 40)*. The scatter correction step can be performed in two ways: (1) in image space, by subtracting a fraction of the image reconstructed using the lower window data from the image reconstructed using the photopeak window data or (2) in projection space, by subtracting a fraction of each projection image using the lower window data from the corresponding projection image using the photopeak window data. The fraction referred to here is determined via calibration experiments or simulations *(40)*. In an effort to better estimate the scatter component within the photopeak window, a third energy window set above the photopeak window has been utilized in a method known as the triple energy window technique *(41-43)*. In this method, the images from the two adjacent scatter windows are used to interpolate the scatter component within the photopeak window. The aforementioned dual and triple energy window scatter correction methods are fast and easy to implement, in addition to exhibiting improved image contrast in many studies *(37, 39-41, 43)*; thus, they have been the main technique adopted by commercial methods.

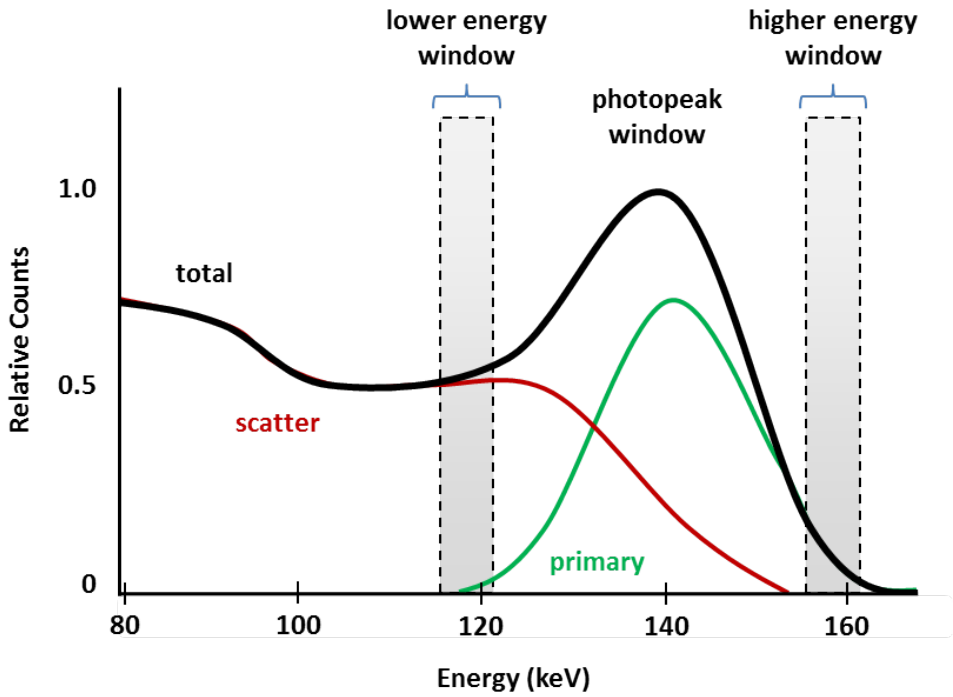

Figure 2-16 An illustration of the total, primary and scatter energy spectra with various energy windows. In the dual energy window scatter corrections, the lower energy and photopeak windows are used; in the triple energy window methods, all three windows are used as shown. The windows shown here are examples only.

More advanced scatter correction techniques used in SPECT imaging include those that generate a spatial estimation of the scatter contribution within the image *(44-46)*. In general, these methods calculate the spatial distribution of scattered photons by mapping the photons from the detector back to their point of emission. Although these methods offer advantages with regards to accuracy over energy window techniques, they are often limited by computation burden; thus, the subject of scatter correction remains in a state of development *(47)*.

Partial Volume Correction (PVC)

The final image degrading effect in SPECT is known as the partial volume effect, which in itself refers to two distinct phenomena. Firstly, the partial volume effect is a result of the discrete sampling of a SPECT image into a rectangular grid. Due to the mismatch of a discrete voxel grid and the analog contours of the real tracer distribution, a blurring effect will occur when a voxel is partially filled by activity; hence the term partial volume (see Figure 2-17).

The second type of partial volume effect is related to the finite resolution of the Anger Camera and image reconstruction, which can cause significant so called "spill-in" and "spill-out" of activities between adjacent regions (see Figure 2-18). In practice, it is generally accepted that the partial volume effect becomes significant for objects less than 2-3 times the size of the system's resolution.

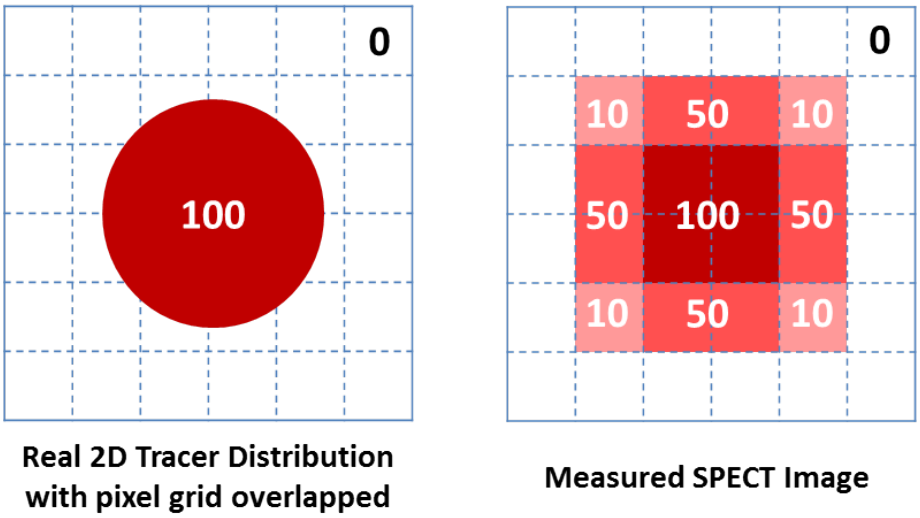

Figure 2-17 An illustration showing the partial volume effect in SPECT imaging due to sampling. The image on the left shows an example real 2D tracer distribution (red) with an arbitrary activity level of 100 and no background activity. The image on the right illustrates how the distribution would appear on a SPECT image due to the blurring of the partial volume effect.

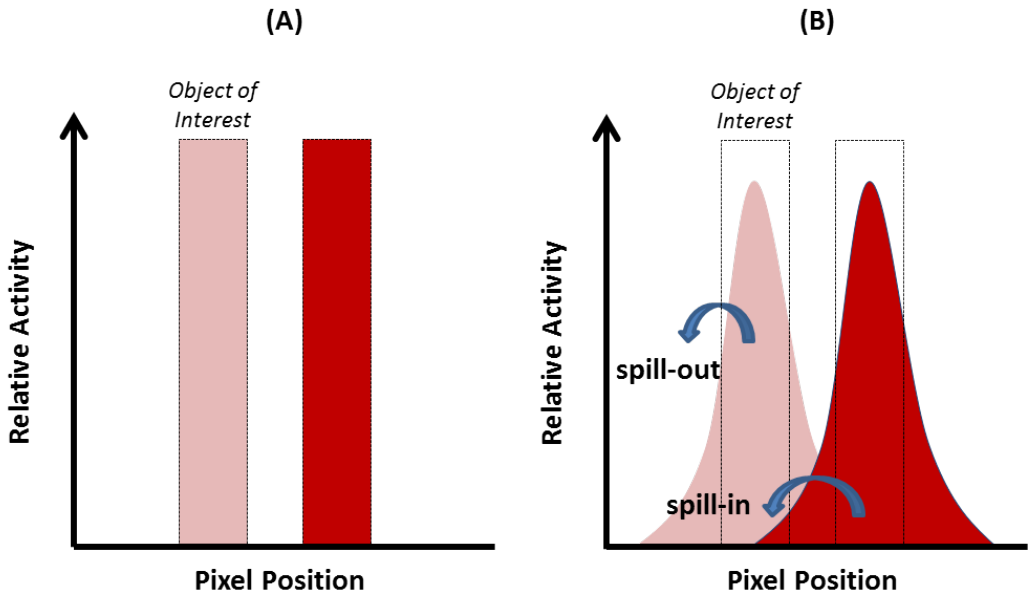

Figure 2-18 An illustration of 1D profiles through an object showing the partial volume effect due to the system's finite resolution. (A) Shows the true boundaries and relative activity for two objects (one being the object of interest); (B) illustrates the blurring effect in the SPECT image which results in activity spill-out of the object of interest and activity spill-in from the adjacent object.

Partial volume corrections comprise a relatively new field of research and have been growing in popularity as SPECT has become more and more quantitative with the advent of AC, RR and SC algorithms. At the current stage of SPECT reconstruction software, partial volume correction algorithms have become a logical and necessary next step toward SPECT quantitation (images in absolute activities), which is the holy grail of nuclear medicine. Due to its infancy, there are still many directions being experimented with and consequently none have been employed within the clinical realm.

In the interest of this thesis, it is worth mentioning that the proposed TQPS method utilizes the theory behind one of the most recent and exciting approaches to partial volume correction: the template projection-backprojection technique *(48-50)*. In general, these techniques marry anatomical information obtained via an external imaging modality with the SPECT image to recover the resolution lost due to the partial

volume effect. A full discussion of this method and latest approaches are provided in Section 3.5.

2.3 Myocardial Perfusion Imaging

In addition to the technical aspects of SPECT, this thesis will also focus on myocardial perfusion imaging (MPI) and its role in diagnosing coronary artery disease. Prior to a discussion on clinical SPECT MPI, a brief description of the relevant anatomy and physiology of the human heart is provided in the following sections.

2.3.1 Basic Anatomy & Physiology

The human heart is a muscular organ which provides the body with a continuous circulation of blood using rhythmical contractions. Situated in the chest, superior to the diaphragm, posterior to the sternum, anterior to the trachea, and medial to each lung, the heart resides roughly two thirds to the left of body midline. At about 250-300 grams in weight and roughly the size of a fist, its shape can be described as cone-like with a broad superior base and a narrowing inferior apex pointing downward and to the left. Within this cone-like structure are four chambers, two superior atria and two inferior ventricles bounded by cardiac muscle tissue, termed the myocardium (Figure 2-19).

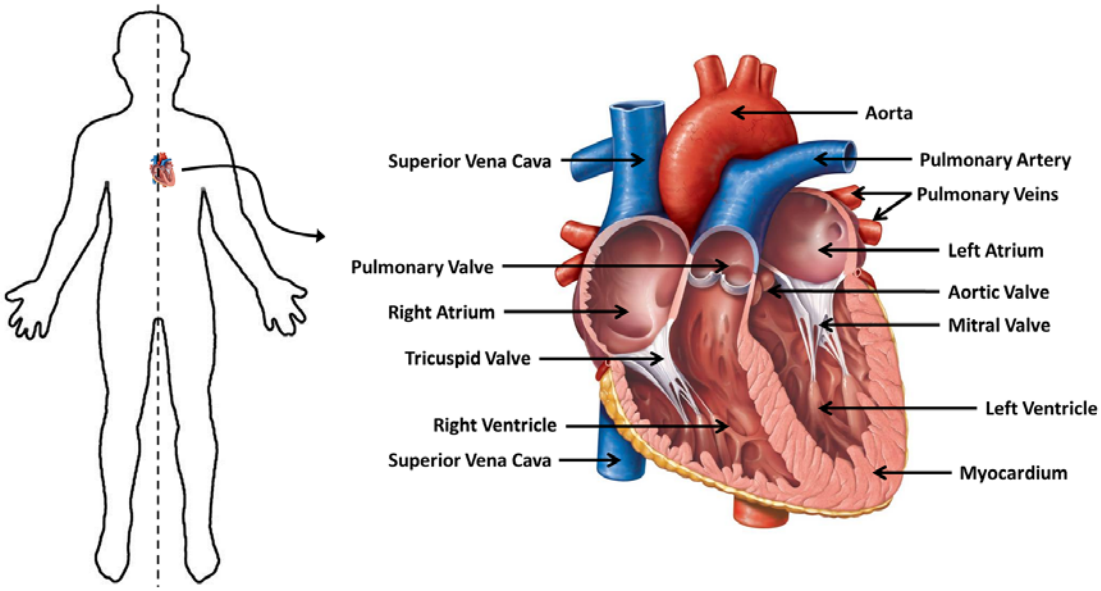

Figure 2-19 Illustrations showing the general position of the human heart (left) and its zoomed in cross section in the coronal plane (right). Blue vessels indicate deoxygenated blood carriers; red vessels indicate oxygenated blood carriers. Source: http://atlanticauctions.ca/images/human-heart-diagram-unlabeled-i4.jpg.

As mentioned, the function of the heart is to pump blood - the primary mode of transport for oxygen and nutrients - throughout the body to and from the tissues. Blood flow within the heart itself occurs in one direction, which is safeguarded by a valvular system and directed by coordinated compartmentalized myocardial contractions. In all, the mechanics of the heart can be described in one cardiac cycle (heart beat). It begins by first collecting deoxygenated blood from the tissues via the vena cava (superior and inferior) into the right atrium. The blood then travels through the tricuspid valve into the right ventricle, which subsequently contracts sending the blood through the pulmonary valve and into the lungs via the pulmonary arteries. Gas exchange occurs in the lungs where carbon dioxide is exchanged for oxygen and this now oxygenated blood is sent back to the left atrium via the pulmonary veins. Finally, the blood in the left atrium passes the mitral valve and fills the left ventricle, which contracts, sending the

oxygenated blood into the body's circulation via the aorta. The frequency of this cycle (heart rate) is set by the sinoatrial node, which is composed of impulse-generating tissue (modified cardiac myocytes, or cardiac muscle cells) situated in the right atrium. Ultimately, it is the sinoatrial node that coordinates the contractions of the chambers via electric impulses sent throughout the electric network in the heart; hence it's often referred name, the pacemaker.

Just from this very brief description of the human cardiovascular system, it is clear that this system has a number of checkpoints, which are critical to the system's success. For instance, the sinoatrial node sets the pace of the cardiac cycle and will do so in the range of 60-100 cycles per minute; however, if the sinoatrial node malfunctions, the heart rate could elevate to a level where the cardiac output (volume of blood pumped per minute) is markedly reduced due to a reduction in ventricular filling time. In this case, the tissues throughout the body would receive insufficient oxygen to function normally, which is a major health concern if not treated in time. Furthermore, the cardiovascular system can falter if the myocardium does not receive an adequate amount of oxygen. In this case, the myocardium would not be able to contract at full capacity, thereby causing a reduction in cardiac output. This particular pathology, most often caused by a blockage in the coronary arteries (the vessels that supply the myocardium with blood), happens to be the most common cause of death in the world. It is known as coronary artery disease – the pathology of interest in this thesis.

2.3.2 Coronary Artery Disease

Ischemic heart disease, the end result of CAD, led to a total of 7.3 million deaths worldwide in 2008 while accounting for roughly 14% of deaths in middle and high income countries *(51)*. In Canada, it was reported that 36,934 deaths were caused by

ischemic heart disease in 2008, which accounted for 15% of all deaths in the country *(52)*. In the United States, despite an encouraging drop of 36% in mortality rate due to CAD from 1996 to 2006, it was estimated that over 17 million adult Americans had CAD in 2006, causing roughly 1 of every 6 deaths in the country *(53)*. Although the temporal trends suggest that the CAD management has improved, it still remains the most common cause of death in the world and thus, is the basis of an enormous field of research worldwide.

As mentioned in the last section, the myocardium receives blood via a network of arteries that surround the outside of myocardium, known as the coronary arteries (see Figure 2-20). Coronary artery disease is a progressive disease in which deposits known as plaques accumulate within the artery walls causing a narrowing of the lumen and ultimately a reduction in blood supply to the myocardium. The process of plaque buildup is known as atherosclerosis, which is the underlying cause of CAD.

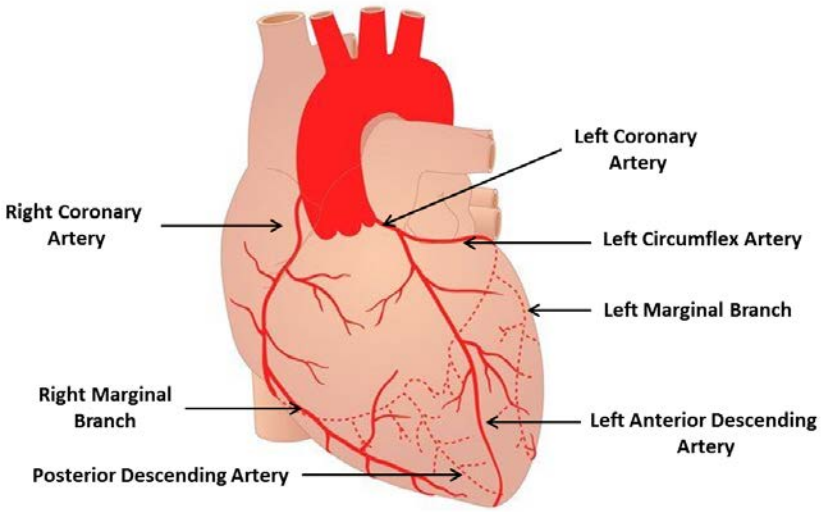

Figure 2-20 A diagram of the human heart illustrating the position of the major coronary arteries surrounding the myocardium. Source: http://www.sciencephoto.com/media/153143/enlarge.

From the early work of Ross et al, the initiation of atherosclerosis has been widely believed to be a response to an injury of the endothelial cells, which make up the inner layer of the arterial wall known as the intima *(54)*. In particular, a developing atherosclerotic plaque is hallmarked by a focal thickening of the intima, caused by a fibro-proliferative response. The injury to the endothelial cells permits the entry of lipids and various inflammatory cells into the arterial wall. With this comes the formation and accumulation of foam cells, which gives rise to the initial form of an atherosclerotic plaque known as a "fatty streak" - a slightly raised lesion composed of the aforementioned inflammatory response participants. Secondary stages of atherosclerosis occur when the disruption recruits deeper smooth muscle cells of the vessel wall, which ultimately proliferate and manufacture extracellular matrix (mainly collagen) to create what is known as a "fibrous plaque". From here, the plaque can evolve to a mature "complicated lesion", where blood vessels form within the plaques via angiogenesis and more complex structures can be formed, such as a hard fibrous outer shell, known as a "fibrous cap".

As an atherosclerotic plaque evolves and grows in size, the diameter of the vessel lumen decreases, thereby causing a reduction in blood supply to the myocardium (called ischemia). This condition will ultimately starve the myocardium of oxygen, causing short-episodes of chest pain, referred to as angina. In the worst case scenario, these unstable plaques can tear, attracting blood platelets to stick together to form blood clots and ultimately cause a complete blockage of the blood flow in the vessel. This is the most common mechanism of a myocardial infarction - often referred to as a heart attack. The second mechanism can occur when the plaque breaks apart, causing the debris to flow downstream and create a blockage in the more narrow distal arteries. A myocardial infarction causes ischemia in regions of the myocardium, which will ultimately become necrotic (cell death) if untreated. In general, necrosis due to ischemia can occur in roughly 3-4 minutes.

2.3.3 Clinical Management of Coronary Artery Disease

The management of patients with stable angina and known or suspected CAD can be broken down into four steps: diagnosis, risk stratification, treatment and patient follow-up.

One of the main challenges in the diagnosis of patients with CAD is that coronary atherosclerosis is a slowly progressive disease that can be clinically indiscernible for long periods of time *(55)*. The first clinical manifestation of this disease is most often angina, characterized by chest pain that can also radiate to the neck, jaw, shoulder, back and arm. Other symptoms can include shortness of breath, and fatigue upon exercise.

Although angina is typically a symptom of myocardial ischemia, it can also be a symptom of a number of non-cardiac conditions. Therefore, patients presenting with chest pain must first undergo a clinical examination to rule out non-cardiac conditions. Different classification schemes have been suggested for the characterization of chest pain, but it is often classified into typical, atypical or non-cardiac *(56)*. Angina can also be further classified as stable and unstable *(57)*. Stable angina is a condition where the chest pain is predictably enhanced by physical exertion and relieved upon rest; as where unstable angina can occur with minimal exertion and the intensity is typically more severe and of longer duration than in the stable case.

Subsequent to the chest pain evaluation and classification, a summary of the patient's risk factors is determined and recorded. Risk factors for CAD include: age, tobacco use, dyslipidemia, hypertension, family history, activity profile, obesity, postmenopausal status, and diabetes *(58)*. If, after the chest pain classification, risk factor summary and history report, there is suspicion of heart disease that warrants further cardiac evaluation, the physician will classify the patient via a probability estimate for the

likelihood of CAD. Using this probability estimate, the clinician must make a decision regarding the value of each of the subsequent testing options based on literature reports and personal experience/preference.

For instance, if a standard exercise test is performed, its value is significantly different for patients with a moderate probability of CAD (50%) as opposed to a high probability (90%). Specifically, for a moderate probability patient, a negative exercise test lowers the probability to 36% and a positive test raises the probability to 83% - a very valuable result in this case *(59)*. However, for a high probability patient, a negative exercise test lowers the probability to 83% and a positive test raises the probability to 98% - a less valuable test in this case *(59)*. These are the decisions that a clinician is faced with at this point of the diagnostic procedure. Although there are many more conditions and corresponding diagnostic algorithms (one example is shown in Figure 2-21), for purposes of this thesis, the focus of the following discussion will be on the condition where SPECT MPI plays a role in the testing of CAD.

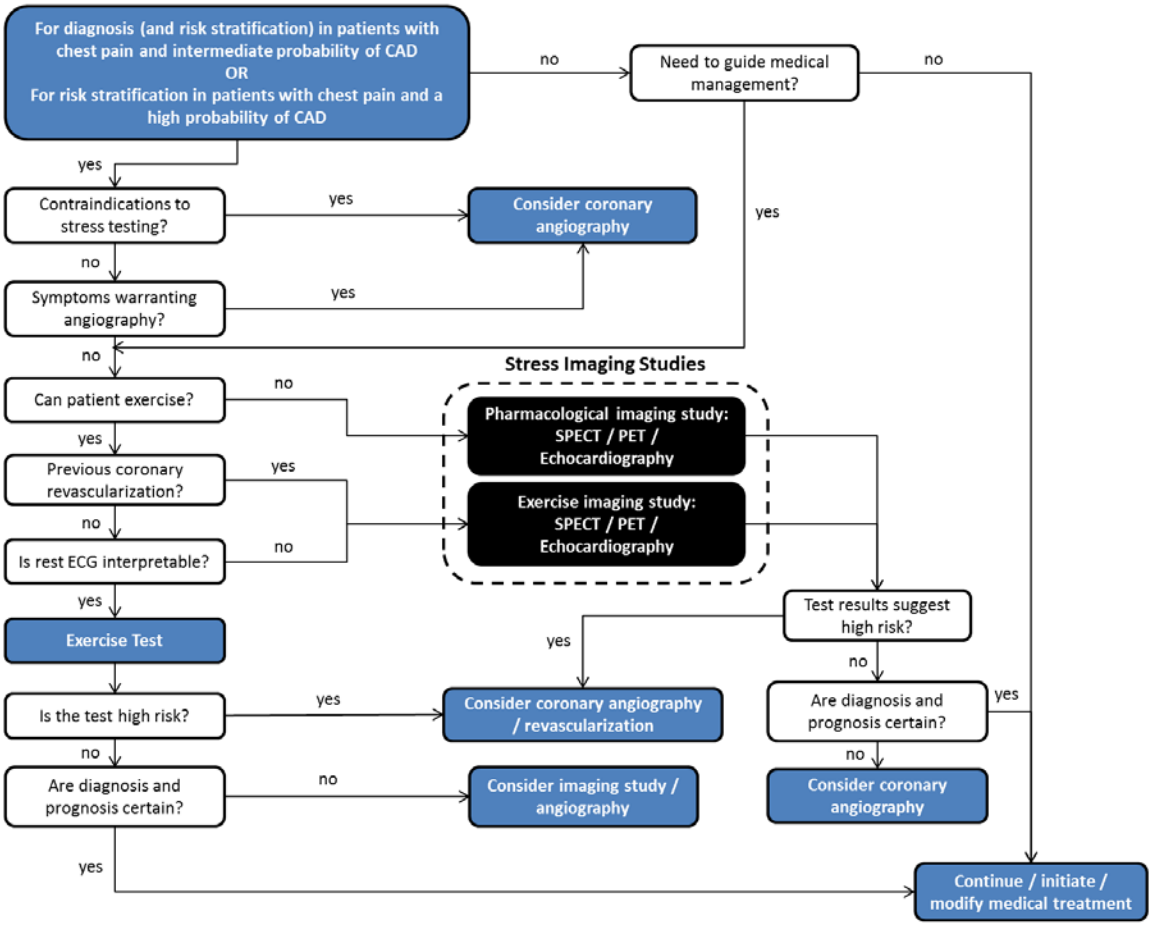

Figure 2-21 A flow chart representing the diagnostic algorithm for the diagnosis and risk stratification of patients presenting with intermediate to high probability of CAD. The blue boxes represent tests or treatments, the white boxes represent clinical questions, and the black boxes represent tests concerning the topic of this thesis, SPECT.[1]

SPECT MPI holds substantial value for the diagnosis and risk stratification of patients with an intermediate probability of CAD, and for the risk stratification for patients presenting with high probability of CAD *(59)*. Candidates for SPECT MPI include, but are

[1] Reprinted from Circulation, 99(21), Gibbons RJ et al, ACC/AHA/ACP-ASIM guidelines for the management of patients with chronic stable angina: executive summary and recommendations. A Report of the American College of Cardiology/American Heart Association Task Force on Practice Guidelines (Committee on Management of Patients with Chronic Stable Angina)., 2829-48., Copyright (1999), with permission from Elsevier.

not limited to, a) patients who are unable to exercise at a sufficient level for exercise testing and should be considered for pharmacological stress testing, and b) patients who have undergone prior revascularization, where the nature of ischemia, size and severity of lesion and myocardial viability are important questions *(60)*.

Upon successful stress imaging, the patient may be referred to coronary angiography (which is an invasive test) if the diagnosis and prognosis remain uncertain, or to surgery (revascularization) if the patient is deemed high risk, or finally to a medical therapy plan if the diagnosis and prognosis are certain. In revascularization surgeries, the goal is to increase the blood flow through the blocked region of the coronary arteries. To achieve this, there are two commonly employed techniques: 1) coronary artery bypass grafting (CABG) and 2) percutaneous coronary intervention (PCI). In CABG (commonly referred to as a "heart bypass"), segments of arteries or veins from other parts of the patient's body are grafted to the coronary arteries to bypass the atherosclerotic narrowing. In PCI, a mechanical device (a balloon) or a laser device is inserted via a catheter and used to break down the atherosclerotic plaque. Both surgeries have been proven effective, but have trade-offs. For example, PCI is generally less expensive as where CABG has demonstrated lower long term mortality rates *(61)*.

2.3.4 Myocardial Perfusion Imaging Modalities

Prior to a discussion on SPECT MPI, it is important to recognize that there are many imaging modalities regularly used in the (non-invasive) diagnosis of CAD, including: magnetic resonance imaging (MRI), x-ray computed tomography angiography (CTA), echocardiography (ECHO), electrocardiography, positron emission tomography (PET), and of course, SPECT. A summary of selected reports with quoted sensitivities and specificities for these modalities in detecting significant CAD is presented in Table 2-1.

Each modality offers specific advantages and disadvantages related to both diagnostic performance and cost/availability. For instance, PET MPI has shown great promise in overall diagnostic performance (high sensitivity), but comes with the associated economic disadvantages of PET imaging: high cost and relatively low availability. Similarly, both CT and MRI techniques have demonstrated very good diagnostic performance (high specificity) along with the unique capability of providing simultaneous anatomical and functional information; however, these modalities remain relatively expensive and also lack in the amount of supporting literature compared to the more established modalities (e.g. SPECT). Due to their technical differences and respective strengths in detecting significant CAD, the aforementioned modalities are often best used in combination to complement each other's strengths and weaknesses.

Table 2-1 A summary of reported sensitivities and specificities for detecting significant CAD for all major imaging modalities.

Imaging Modality	Sensitivity	Specificity
SPECT MPI *(62)*	86	74
PET MPI *(63)*	87	93
CT Angiography *(64-66)*	91	93
Stress Echocardiography *(67)*	79	87
Stress MRI Perfusion *(68)*	91	81
MRI Angiography *(69, 70)*	73	86
Stress Electrocardiogram *(71)*	68	77

Despite the ongoing success and proven value of SPECT MPI in CAD diagnostics, there continue to be a number of lingering pitfalls of this technology that degrade its overall performance. With new and exciting technologies continually being developed and introduced into the medical imaging market, there have been a number of meta-

analyses which provide a comprehensive analysis of the relative performance of each diagnostic modality. Table 2-2 highlights a number of these meta-analyses performed for the leading diagnostic tools employed for the detection coronary artery disease.

Table 2-2 Overall sensitivities and specificities produced by SPECT, PET, CTA, and MRI in the detection of significant CAD as reported by the indicated meta-analyses.

Modality	Investigators	Year	Combined Patient Population	Sensitivity (%)	Specificity (%)
SPECT					
	Ardle et al *(72)*	2012	12,029	83	69
	Jaarsma et al *(73)*	2011	13,462	88	60
	Underwood et al *(62)*	2004	7,318	86	74
PET					
	Ardle et al *(72)*	2012	1,164	90	88
	Jaarsma et al *(73)*	2011	1,441	85	83
	Nandalur et al *(74)*	2008	1,442	92	85
CT					
	Apfaltrer et al *(75)*	2011	1,151	96	86
MRI					
	Jaarsma et al *(73)*	2011	2,841	89	76
	Hamon et al *(76)*	2010	2,125	89	80

As can be seen by Table 2-2, SPECT remains a very sensitive modality in the detection of significant CAD; however, its specificity is substantially reduced relative to the other modalities. For this reason, the method developed in this thesis was designed to improve upon the specificity of SPECT myocardial perfusion imaging in the detection of coronary artery disease.

2.3.5 SPECT MPI

SPECT MPI is capable of assessing the coronary blood flow by depicting its physiological significance via myocardial function and viability. SPECT MPI comes with clear advantages over its competitors, particularly in terms of availability, relatively low cost and a long history of clinical validation in terms of diagnostic and prognostic accuracy for patients with intermediate to high probability of CAD. Moreover, SPECT MPI comes with the advantage over anatomical imaging modalities, such as CT and MRI, in that it has the innate ability to depict the physiological significance of CAD. Disadvantages of this technique reside with its relatively low resolution and vulnerability to image artifacts, which limits its diagnostic performance.

Protocol

SPECT MPI is performed under both rest and stress conditions. The purpose of performing both rest and stress studies is two-fold: a) to determine the reversibility of perfusion defects, and b) to increase the confidence of identifying perfusion defects and differentiating them from image artifacts. Stress is typically induced via exercise; however it can be induced pharmacologically if the patient is unable to exercise or if the exercise conditions were not met (e.g. the target heart rate of ≥85% max was not reached). Ideally, the rest and stress studies should be performed on separate days to avoid residual activity within the body from one study to the next, but this can be challenging for a variety of reasons; thus, a one-day protocol is commonly used. Figure 2-22 illustrates two typical one-day timelines for rest/stress studies using exercise and adenosine as the stressors.

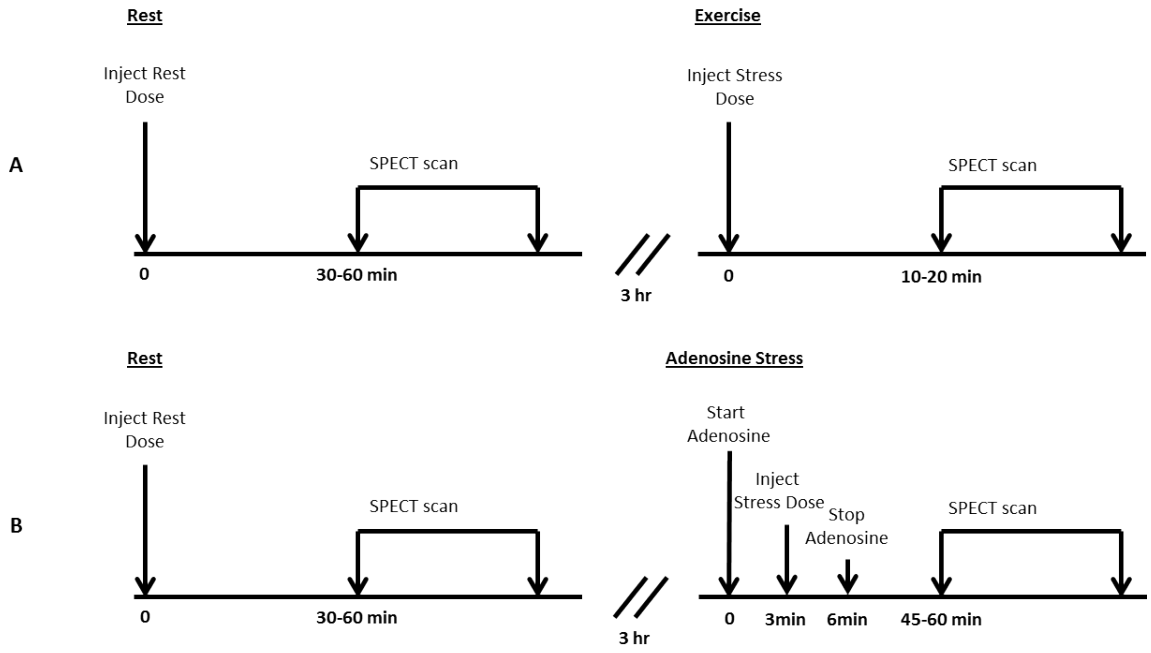

Figure 2-22 An example of a one-day ^{99m}Tc-Sestambi rest/stress protocol using (A) exercise stress and (B) adenosine stress. All times are in minutes.

Radiotracers

Images in SPECT MPI highlight the perfusion in the left ventricular myocardium, which is the compartment of the heart carrying the highest workload and thus, receives the highest uptake of radiotracer. Additionally, SPECT MPI images also show uptake in (undesirable) extra-cardiac organs and tissue, which can be highly variable depending on the patient and radiopharmaceutical used for the given study. Currently, there are three clinically employed and widely available tracers for SPECT MPI (also see Table 2-3):

1. Thallium (^{201}Tl) Chloride
2. Technetium (^{99m}Tc) Sestamibi
3. Technetium (^{99m}Tc) Tetrofosmin

A full discussion of the biokinetics for each aforementioned tracer is out of the scope of the thesis; however, a brief description of the mechanisms involved with ^{99m}Tc-Sestamibi (collectively referred to as MIBI) uptake in the myocardium will be provided as this is the most commonly used tracer and it is also the tracer adopted for the studies performed in this thesis. A brief comparison of the three tracers is presented in Table 2-3.

Table 2-3 Advantages and disadvantages of the most commonly used SPECT MPI radiotracers.

Property	^{201}Tl – Chloride	^{99m}Tc – Sestamibi	^{99m}Tc – Tetrofosmin
Clinical Approval Date	1980	1990	1995
Gamma Energy (keV)	75-80	140	140
Radioisotope Half-Life (h)	73.1	6.0	6.0
First Pass Extraction (%)	85	65	54
Typical MPI Injection (MBq)	74-111	370-925	370-925
Whole Body Effective Dose with Typical MPI Injection (mSv)	16-24	3.3-8.3	2.8-7.0
Dominant Clearance Mechanism	Urinary/GI	Hepatobiliary	Hepatobiliary

The MIBI tracer is a lipophilic cationic complex which is extracted from the coronary circulation to viable myocardium in proportion to the coronary blood flow. During its first pass, roughly 65% of the MIBI tracer will be extracted to the myocardium from the

coronary circulation, which is markedly lower than ^{201}Tl (85%) *(77)*. The MIBI complex passively enters the mitochondria of the myocardium (since it is lipophilic), while the negative membrane potential maintained by healthy mitochondria sequesters MIBI within the organelle via electrostatic interactions (since it is cationic) *(78)*. Since the MIBI tracer is trapped within the mitochondria of the myocardium, unlike ^{201}Tl which redistributes, it is well suited for long acquisition times and enables great flexibility in clinical scheduling. The myocardial uptake typically results in roughly 1.2%-1.5% of the injected dose *(79)*. Ultimately, the major pathway for the excretion of MIBI is the hepatobiliary system, which leads to high uptake in the liver and gallbladder. At one hour post-injection, MIBI shows the highest uptake in the gallbladder, followed by the heart, liver, spleen and lung (see Figure 2-23). In some situations, substantial extra-cardiac uptake can negatively influence the quality of the myocardial perfusion image via scattering, partial volume effects, and color display normalization.

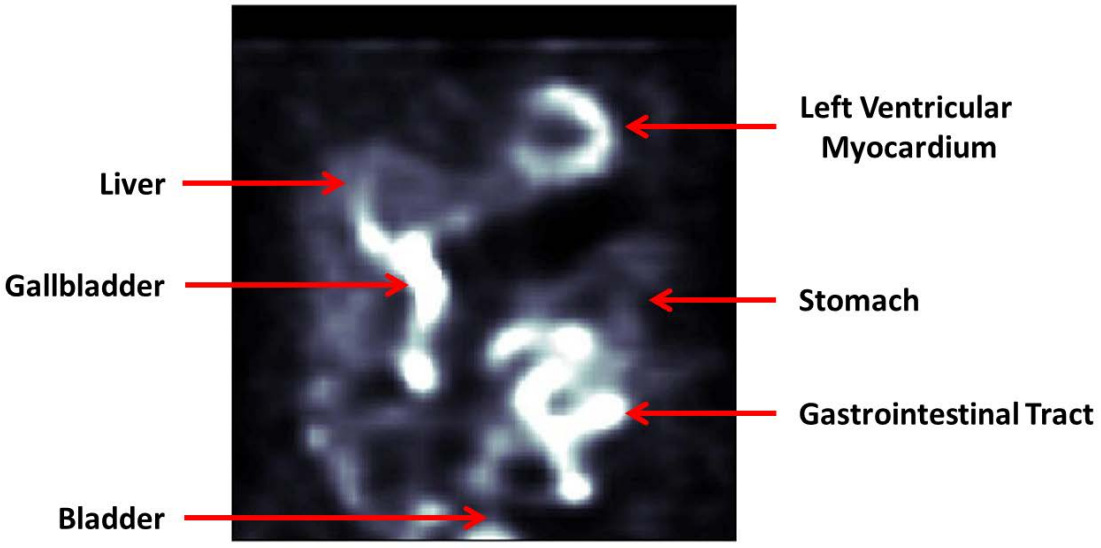

Figure 2-23 An example coronal slice of a patient SPECT MPI reconstructed image using ^{99m}Tc-Sestamibi. The visible organs with uptake are labeled.

Image Display

The images acquired in SPECT MPI are presented to the physician in a number of ways. First, due to the oblique orientation of the heart in the chest, the reconstructed images are reoriented from the traditional imaging axes (coronal, sagittal and transverse) into the cardiac axes: short axis, horizontal long axis and vertical long axis (see Figure 2-24). A typical visual assessment of a patient's myocardial perfusion involves a physician scrolling through slices of the heart in each of cardiac axes.

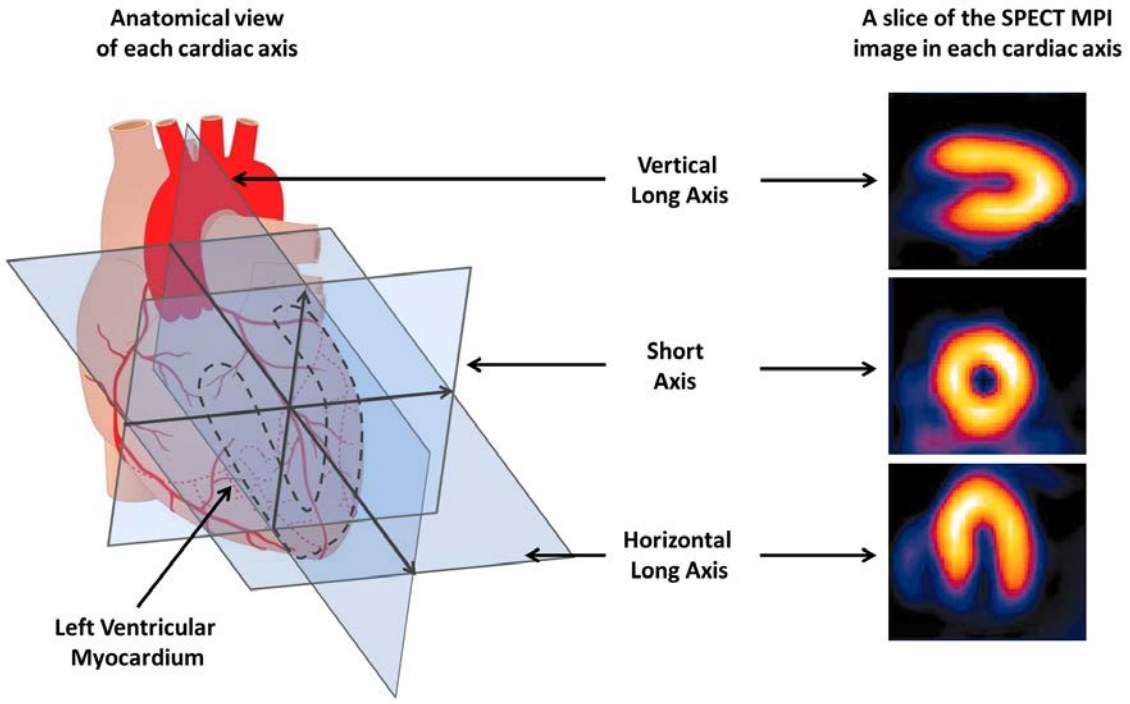

Figure 2-24 A representation of the cardiac axes: vertical long axis, short axis, and horizontal long axis. The left image shows the axes overlaid on a heart, with the left ventricular myocardium indicated by the black dashed line. The images on the right show an example slice of a SPECT MPI image reoriented into each of the cardiac axes.

The second way to present the information in SPECT MPI images is known as a bulls-eye map (or polar map). Introduced in the late 1980s by DePasquale et al *(80)*, a bulls-eye

map is a parameterization of the entire 3D set of short axis slices into a single 2D image. The basic steps involved in the construction of a bulls-eye map are shown in Figure 2-25.

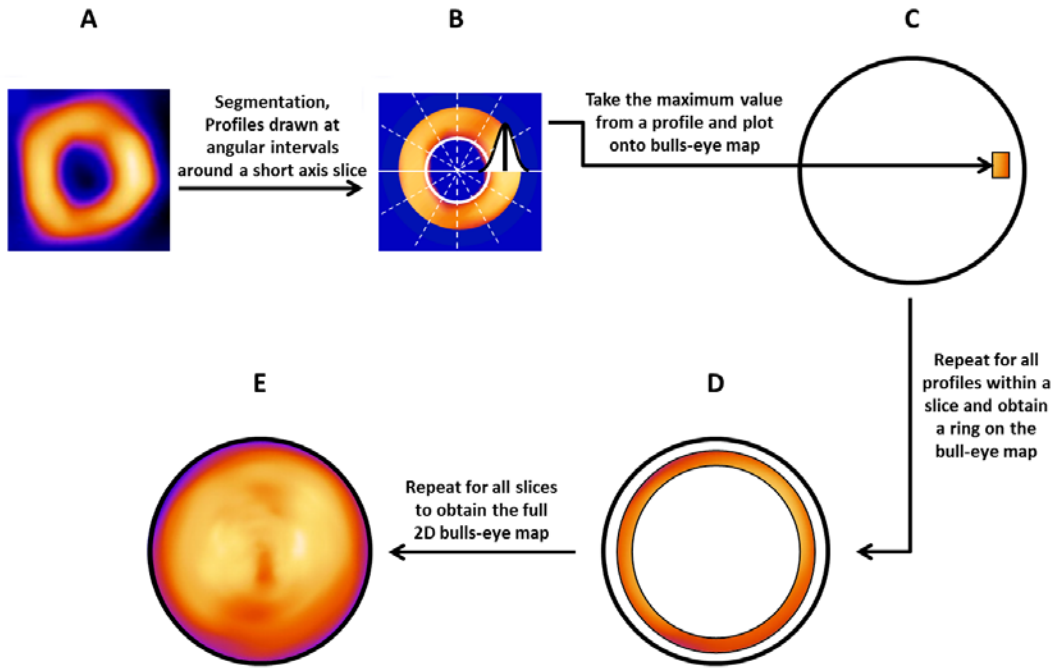

Figure 2-25 An illustration of the step involved when constructing a bulls-eye map. A is an example short axis slice of the left ventricle; B shows the orientation of the circumferential profile drawn around the myocardium with an example profile shown in the lateral wall; C shows the parameterization step by taking the maximum of the example profile in B and mapping that data point as an element of the bulls-eye map; D shows the resulting ring of the bulls-eye map after performing the circumferential profiles for an single slice; E shows the final bulls-eye map after performing the profiles for all slices and all angles.

An important element in constructing a bulls-eye map is the segmentation the left ventricle within the SPECT MPI image. The delineation of the left ventricle has been a heavily researched topic since the introduction of semi-quantitative SPECT MPI. Over the years, there have been many approaches aimed at finding the true anatomical boundaries of the left ventricle (and other objects) using the information provided in a SPECT MPI image *(81, 81-89)*. The main challenge of delineating the left ventricle in a SPECT image is related to the fact that SPECT provides a physiological representation of

the heart, and not a truly anatomical one. As a result, particularly challenging situations can occur when a patient presents with a large myocardial perfusion defect, thus rendering the left ventricle discontinuous within a SPECT image, as shown in Figure 2-26.

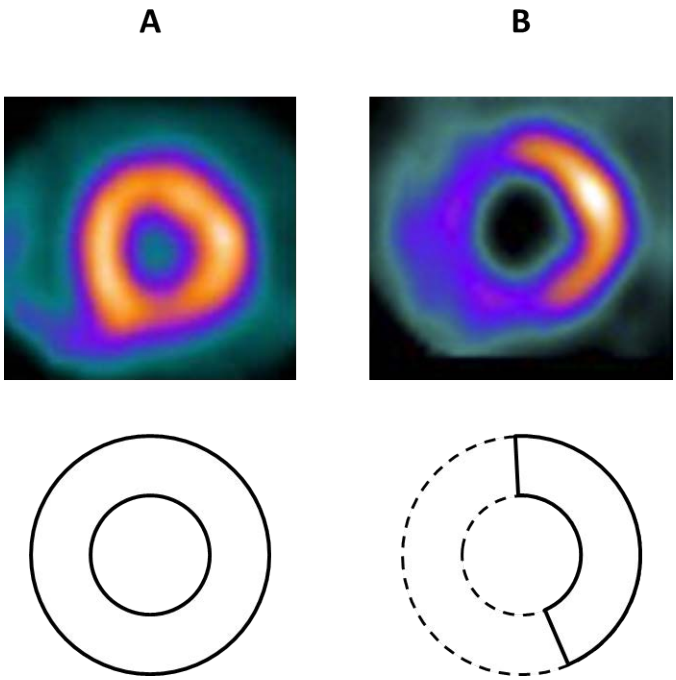

Figure 2-26 The basic segmentation problem in SPECT MPI, shown using slice in the short axis view of the left ventricle. The top row illustrates example SPECT images of a healthy myocardium and a myocardium with a large perfusion defect (in the septal wall) in column A and B, respectively. The bottom row illustrates a crude representation of the boundaries of the healthy myocardium in each case. The difference here is that a healthy heart will present as the true "donut" shape of the left ventricle in the short axis, as where a heart presenting with a large defect will only appear as an incomplete "donut" shape; thus making it difficult to delineate remainder of the left ventricle (dashed black lines) using this image.

In the case where there is a severe and large perfusion defect (see Figure 2-26-B), the segmentation software used to delineate the heart must make an assumption, or use a priori knowledge of heart anatomy to interpret the true boundaries in the defect region

(dashed black lines in Figure 2-26). To cope with this issue, many approaches have been adopted, which range from simple assumptions of uniform myocardial thickness *(82-84, 90)* to more sophisticated approaches integrating databases of measurements acquired via anatomical imaging modalities, such as MRI *(91, 92)*. In most commercial software, more simplistic approaches have been adopted in the interest of minimizing computational burden and thus, increasing patient throughput.

In general, commercial segmentation software methods (left ventricle delineation techniques) begin by defining the center of the left ventricle followed by a search for the middle of the myocardial wall for each slice in the short axis view. A uniform myocardial thickness is then assumed, which is used to place a boundary for the endocardium and epicardium on either side of the midmural line. There are obvious limitations in this approach as a true human heart does not have a uniform myocardial wall thickness *(93)*.

Following segmentation, profiles can be drawn at angular intervals around each short axis slice of the left ventricular myocardium (Figure 2-25-B). For each of these profiles, the maximum count along the given angular profile is recorded and mapped to the bulls-eye map as a single element corresponding to the slice and angle of the profile. This process is repeated for all angles of that slice (typically 40-60), which ultimately results in a ring of data on the bulls-eye map corresponding to the position of the slice within the short axis data set. Finally, this procedure is performed for all slices to create a full bulls-eye map representing the entire 3D short axis data set as a single 2D image.

With respect to bulls-eye map nomenclature, there are a number of systems used to describe regions of a bulls-eye map, as shown in Figure 2-27. The reason for segmenting regions of the bulls-eye map is to standardize the reporting methods for perfusion defects *(94)*. For instance, clinicians will report perfusion defects in terms of myocardial

wall position (i.e. Figure 2-27-A) in conjunction with the likely culprit coronary artery (i.e. Figure 2-27-B). The nomenclature shown in Figure 2-27-C and -D illustrates the 17- and 20-segment models, which are primarily used for semi-quantitative measurements of myocardial perfusion performed by commercial software.

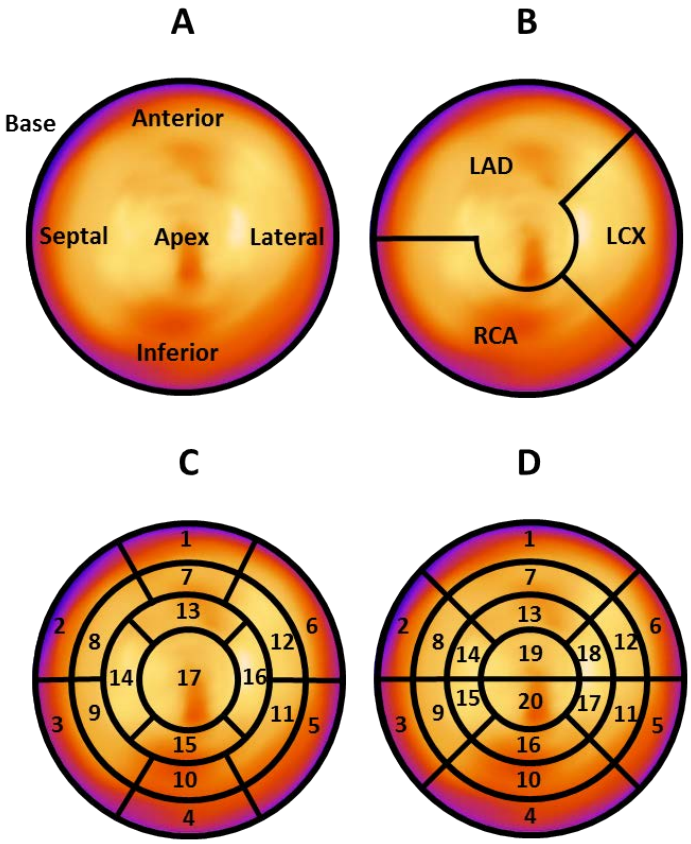

Figure 2-27 Common nomenclature for bulls-eye maps used in SPECT MPI. A indicates the regions of the myocardial walls; B shows the major coronary territories; C and D show the 17- and 20-myocardial segment models.

Image Assessment and Semi-Quantitation

In addition to a qualitative/visual assessment of the images, the major utility of SPECT MPI is its ability to quantify the extent and severity of malperfused regions within the myocardium.

With the recent advent of sophisticated semi-quantitative image analysis software along with advancements in camera hardware, SPECT MPI now offers a number of metrics aimed at quantifying myocardial perfusion and providing reliable insight on ischemic heart disease. In order to identify regions of reduced perfusion, the patient's SPECT image must be compared to a healthy standard, which is most commonly represented by a normal patient database (see Section 3.1 for more detail). For instance, a 5-point scoring system (Table 2-4) describing the degree of reduced perfusion relative to such a healthy standard has enabled a number of useful semi-quantitative measurements, such as the summed rest and stress scores.

Table 2-4 The five-point scoring system used in conventional semi-quantitative measurements in SPECT MPI.

Category	Score
Normal perfusion	0
Mild reduction in counts – not definitely abnormal	1
Moderate reduction in counts – definitely abnormal	2
Severe reduction in counts	3
Absent uptake	4

Specifically, these summed scores provide an overall grade of the perfusion for a given patient by summing all of the scores assigned to each segment of the myocardium. The summed stress score has demonstrated significant prognostic power and is used in all

commercially available software *(95)*. As an extension to the summed score methodology, the group at Cedars Sinai has recently introduced a new parameter called the total perfusion deficit, which combines the size of the perfusion defect with the aforementioned scoring system *(96)*. Although the literature is limited with the use of the total perfusion deficit, it has shown promise with regards to the detection of significant CAD *(96, 97)*. A list of cardiac measurements commonly performed in SPECT MPI is shown in Table 2-5, and a more detailed look at a select number of these measurements will be provided as they are introduced in the studies performed in this thesis.

Beyond the semi-quantitative measures listed in Table 2-5, SPECT MPI also has the capability of measuring left ventricular function via electrocardiographic gating. In gated SPECT MPI, projections are binned in-sync with the cardiac cycle via electrocardiography, resulting in typically 8 to 16 gates per projection. Ultimately, the final reconstruction of a gated study will comprise 8 to 16 images corresponding to particular states of the cardiac cycle (e.g. end-diastolic). Despite being outside the scope of this thesis, it is important to note that gated SPECT MPI can provide even further insight to the overall status of the patient's heart and has shown great value in diagnosis *(98, 99)*, risk and prognostic assessment *(100, 101)*, determination of myocardial viability *(102, 103)*, and post-operative evaluation *(104)* for patients with known or suspected CAD.

Table 2-5 A list of common quantitative measurements used in SPECT MPI with a brief description of each.

Semi-Quantitative Measurement	Common Acronym	Description
Perfusion Defect Extent	EXT	• A measure of the size of the perfusion defect as a percentage of the entire myocardium
Perfusion Defect Severity	SEV	• A measure describing the degree of perfusion reduction in malperfused regions relative to a healthy standard, which is suggestive of the severity of the coronary occlusion. Usually expressed as a percentage.
Summed Stress Score and Summed Rest Score	SSS and SRS	• An index obtained by summing the individual 5-point scores from each myocardial segment over each coronary territory or the entire patient heart.
Summed Difference Score	SDS	• The difference between the SSS and SRS to indicate the reversibility of the perfusion defect.
Total Perfusion Deficit	TPD	• A combined measure of size and severity of the perfusion defect using the 5-point scoring system. Expressed as percentage.

3 Motivation

With coronary artery disease continuing to be the number one cause of death in the world, the motivation for improving any component of CAD diagnostics, such as SPECT MPI, is very clear.

The TQPS method developed in this thesis aims to improve upon the current commercial methods used for semi-quantitative SPECT MPI analysis. Specifically, the TQPS method was designed to overcome limitations associated with the normal patient database approach, which is considered the gold standard methodology in SPECT MPI analysis. Thus, a review of the leading software packages, normal patient databases, and their respective limitations will be provided in the following chapter.

In addition to improving upon commercial software methodology, the objective of this project was to improve the specificity of SPECT MPI by way of image artifact correction. Therefore, this chapter will provide a review of the different types of image artifacts presented in SPECT MPI, as they pertain to this thesis.

Finally, the last section of this chapter will provide a review of the template-based methods previously designed for SPECT imaging.

3.1 Commercial SPECT MPI Software

Traditional visual interpretation of SPECT MPI images is a subjective process and is inherently dependent on the observer and his or her expertise *(105)*. For this reason, several semi-quantitative software packages have been developed over the last two decades in an effort to reduce the inter-observer variability and improve the diagnostic performance of SPECT MPI *(81, 83, 84, 90)*. Besides several research-based methods devoted to semi-quantitative SPECT MPI, there are three leading commercial software packages used in clinics today: 1) Cedars-Sinai Medical Center's Quantitative Perfusion SPECT (QPS) *(83)*, 2) University of Michigan's Corridor4D-MSPECT (4DM) *(81)*, 3) Emory University's Emory Cardiac Toolbox (ECT) *(84)*.

These software packages have been subject to continuous refinement over the last two decades with each company developing their own proprietary software in order to perform their respective analysis. Recently, Wolak et al *(106)* reported a number of significant differences in a variety of cardiac parameters obtained from the three leading software packages. For instance, QPS exhibited higher sensitivity than 4DM (87% versus 80%, respectively), and a higher specificity than ECT (71% versus 49%, respectively). Although it has been shown that each package can produce significantly different results, all commercial SPECT MPI software packages employ the same general framework in their analyses - the normal patient database methodology.

3.1.1 Normal Patient Database Methodology

The general approach adopted by each of the leading commercial SPECT MPI software packages is to compare a patient's myocardial perfusion image to an average healthy standard, thereby enabling the software to differentiate between normal and abnormal

perfusion within the patient's image. This healthy standard is known as a normal patient database (normal database for short). The data flow in traditional normal patient database analysis can be broken into three main sections, as shown in Figure 3-1: the patient study, the normal patient database construction, and the semi-quantitative measurements.

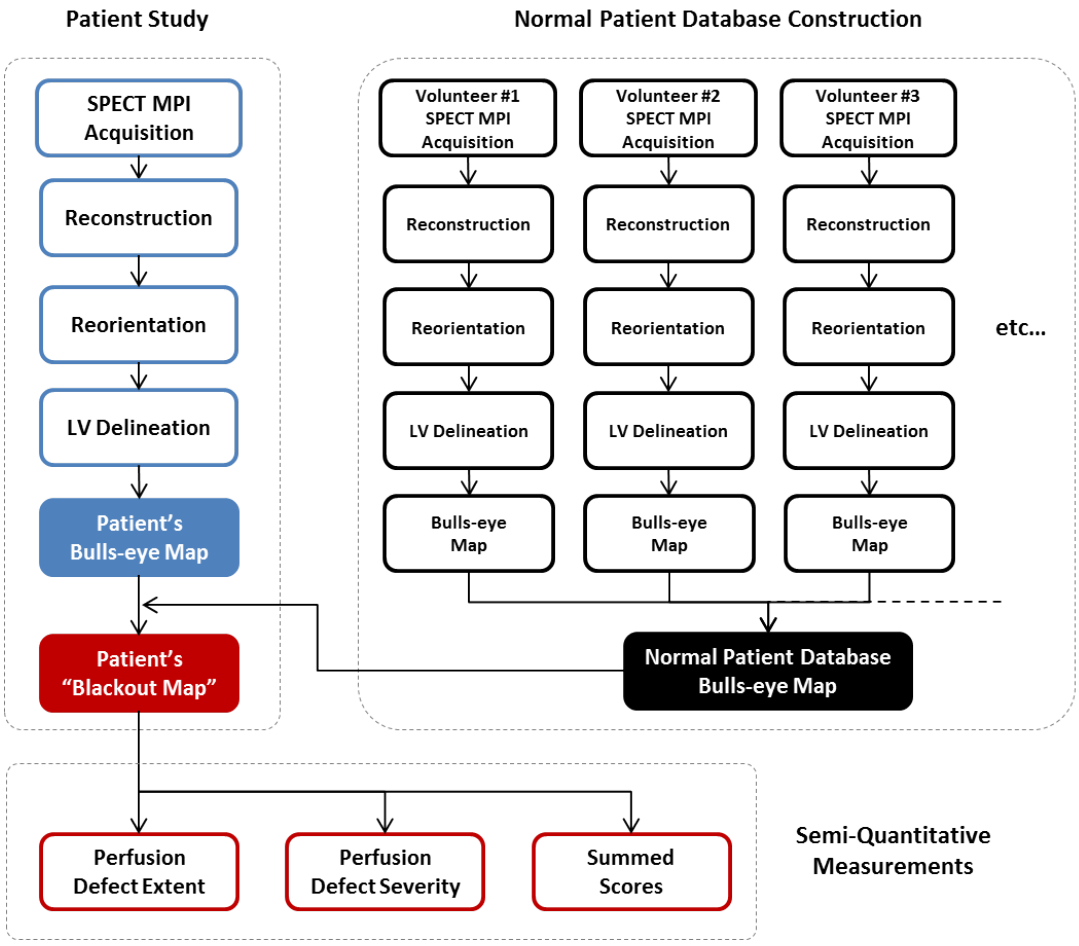

Figure 3-1 A generalized flow chart showing the processing steps from the SPECT acquisition to the final measurements adopted by the leading commercial software packages.

Normal patient databases are constructed by first acquiring SPECT MPI studies for a number of healthy volunteers (typically 15-50), who have been pre-evaluated as having

less than 5% likelihood of having CAD. These SPECT MPI studies are then reconstructed, reoriented, delineated with respect to the left ventricle, and mapped into bulls-eye images, all in accordance to the protocol employed at the given institution. The bulls-eye maps are then resampled (to accommodate for inter-patient variability in heart geometry) and averaged to produce a single bulls-eye map image, where each bulls-eye pixel ultimately represents the average healthy perfusion along with its respective standard deviations. The patient bulls-eye image can then be directly compared to this average healthy bulls-eye image in order to assess the patient's myocardial perfusion.

It is important to note that normal patient databases are typically generated by the software providers; however, if desired, they can also be constructed and customized by the host institution. In either case, the database is created once, and not for each study. Since the patient study is ultimately compared to the normal patient database, it is critical that these two images are acquired and processed under the same protocol (e.g. reconstructed with the same algorithm) to avoid inconsistencies.

Once the patient and normal database images have been compared, all commercial software packages create what is called a "blackout map". In most cases, if the patient's perfusion for a given bulls-eye pixel value is less than an empirically derived number of standard deviations (typically 2.5) relative to the normal database, then that pixel is deemed to be part of a malperfused region of the myocardium *(82-84, 90)*. With this, the information can then be presented to the viewing physician as a blackout map, where all malperfused regions are indicated as "blackout" pixels (see Figure 3-2).

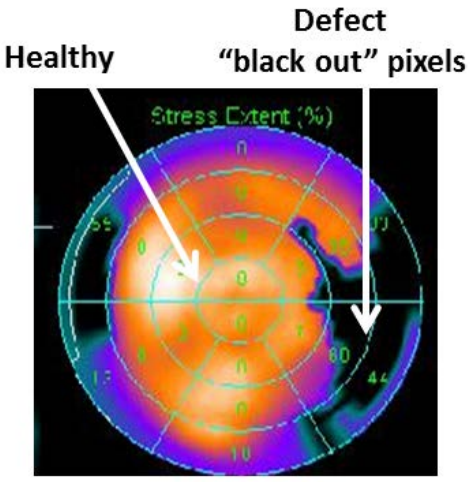

Figure 3-2 An example bulls-eye map from Cedars-Sinai's QPS software showing both healthy regions and regions determined to be perfusion defects ("black out" pixels). The grid overlaid on the image is the 20-segment model, with the numbers inside each segment representing semi-quantitative scores regarding the perfusion within each segment (0 = healthy, 100 = no perfusion).

The utilization of normal patient databases to define perfusion defects in SPECT MPI has become a widely accepted concept within the nuclear medicine community. Along with the advancements made in image reconstruction and modern quantitative analysis software, the exploitation of normal patient databases has contributed to SPECT's well-established footprint in the prognosis and diagnosis of CAD *(81-84, 90, 95, 97, 107-110)*.

3.1.2 Limitations of Commercial SPECT MPI Software

Despite the widespread use of the database approach, a number of shortcomings related to this methodology have been recognized, which continue to impair the specificity of SPECT MPI with respect to perfusion defect quantitation *(96)*. Table 3-1 presents three recent investigations regarding the diagnostic performance of SPECT MPI using each of the three of the leading commercial software packages with coronary

angiography as the gold standard for detecting significant CAD. From these studies a mean sensitivity and specificity of 77% and 67% was achieved, respectively, demonstrating SPECT MPI's poor specificity. Additionally, with significant differences reported between the results obtained from the three software packages, it is important to recognize the potential differences introduced by different normal patient database techniques.

Table 3-1 Recent literature comparing the diagnostic performance of the three leading commercial software packages in SPECT MPI using coronary angiography as the gold standard (stenosis ≥50%).

Authors	Year	Study Size (normal)	Software	Sensitivity (%)	Specificity (%)
Wolak et al *(106)*	2008	143 (45)	4DM	80*	67
			Emory	86	49†
			QPS	87*	71†
Guner et al *(111)*	2010	114 (169)	4DM	74	63
			Emory	82	62
			QPS	76	64
Johansson et al *(112)*	2011	318 (734)	4DM	78	80‡#
			Emory	76	61‡Π
			QPS	75	73#Π
			Overall Mean	77	67

Matching pairs of *,†, ,‡, #, or Π for a given study and measure indicates a significant difference (p<0.05).

Shortcomings of the normal database methodology can be attributed to the fact that two healthy SPECT MPI images can look very diffserent from one another, depending on several factors ranging from the patient's left ventricular anatomy to the image acquisition and reconstruction parameters. Due to this variability of SPECT images,

multiple databases are commonly generated to account for the generic anatomical differences between men and woman, as well as for differences caused by camera, acquisition and processing protocols *(96, 107, 110, 113)*. Moreover, Li et al recently suggested the addition of databases based on ethnicity, such as for Chinese populations due to their relatively small mean heart size and body mass index as compared to Western populations *(114)*. Similarly, Cuberas-Buros et al demonstrated significant differences between North American and Spanish databases, thereby suggesting the utility in including Spanish populated databases in clinics *(115)*. Lastly, Nakajima et al *(116)* have shown the value of employing population specific and acquisition specific normal patient databases. Specifically, they reported significant differences between using Japanese and American normal patient databases for a Japanese population, as well as for 180^0 and 360^0 SPECT MPI acquisitions *(116)*. In summary, it would be optimal to have a normal patient database for every acquisition, reconstruction and patient condition in order to accurately represent the respective healthy heart for each case. However, this is clearly impractical in the clinical arena and thus, normal database will always be limited to particular situations.

Further concerns regarding normal databases are related to inter-institutional variability. When an institution purchases a commercial software package for their clinic, they must choose whether to use the pre-installed databases provided by the software manufacturer, or to construct the databases themselves. The problem with institutions independently developing their respective databases is that different criteria may be implemented, such as the number of volunteers and/or volunteer characteristics *(116)*. For instance, databases constructed with a greater number of volunteers will tend to have tighter standard deviations for each bulls-eye element. As a result, the standard threshold of 2.5 standard deviations below the mean can be quite different for a database constructed from 50 volunteers relative to a database constructed with only 15 volunteers.

Additionally, clinics will construct their databases using different populations of healthy volunteers. For instance, one clinic may restrict healthy volunteers to be within a certain body mass index range in hopes to construct a database that is representative of a typical patient presenting with ischemic heart disease (i.e. high body mass index); as where another clinic may construct their databases using young healthy volunteers (non-representative of the average CAD patient). These types of differences in the healthy patient characteristics can further add to the variability between different normal patient databases. Even more, some clinics will construct more databases (e.g. gender-based, ethnicity-based) than other clinics. Although the generation of multiple databases has improved the performance of methods that rely on them, the inability to unequivocally differentiate between image artifact and abnormal perfusion in all cases persists as a limitation of the database approach. By eliminating the use of normal databases, the proposed template-based semi-quantitative SPECT MPI method was designed to overcome the aforesaid limitations associated with the traditional methodology.

3.2 Artifacts in SPECT MPI

The TQPS method introduced in this thesis was designed to correct for image artifacts presented in SPECT MPI and therefore improve upon the modality's diagnostic performance. Traditionally, image artifacts are defined as any false representation of the true image. With regards to this thesis (and the following discussion), a much broader definition is used where an artifact is defined as any effect that causes the normal patient database to not accurately represent the patient's healthy myocardial perfusion. Ultimately, image artifacts can prevent a normal database from accurately

differentiating between healthy and abnormal perfusion in a SPECT MPI study, thereby leading to a reduction in diagnostic accuracy.

Although there are many different types of image artifacts that can occur in SPECT imaging, the following section provides a discussion only of the artifacts in which the TQPS method is designed to address. Specifically, these artifacts can be grouped into two categories: partial volume artifacts (caused by the partial volume effect), which are related to patient anatomy, and software-related artifacts, which are related image processing.

3.2.1 Partial Volume Artifacts

In SPECT MPI, it has been well documented over the years that patient-related artifacts can negatively influence the modality's diagnostic accuracy *(36, 38, 98, 117-124)*. Of the many patient-related artifacts investigated in the aforementioned studies (e.g. breast attenuation, upward creep of the heart, etc.), it is the artifacts caused by the partial volume effect that are of particular interest for the method developed in this thesis and thus, will be discussed in more detail.

In general, partial volume artifacts presented in a SPECT MPI image are directly related to the patient's specific cardiac anatomy. As described in Section 2.2.4, partial volume effects become significant for small objects, specifically for objects less than 2-3 times the system's resolution. In the case of SPECT MPI, the resolution of a reconstructed image for modern systems is on the order of the average human myocardial wall thickness (1-2 cm); thus, the partial volume effect plays a large role in SPECT MPI *(125)*. In particular, relatively thin regions of a patient's myocardial wall will appear to have reduced perfusion compared to thicker regions of the myocardial wall despite having

uniform blood perfusion. Moreover, the degree of perfusion non-uniformities can vary considerably from patient to patient, thereby rendering it difficult to differentiate between what non-uniformities are caused by true reduced perfusion or by the partial volume effect. In a traditional semi-quantitative analysis, if the normal patient database does not exhibit the same patterns of non-uniform wall thickness as the investigated patient, then the software can be vulnerable to falsely identifying a partial volume artifact as a perfusion defect. The following sections will discuss four sources of partial volume artifacts in SPECT MPI:

1) Non-uniform myocardial wall thickness
2) Apical thinning
3) Regional myocardial hypertrophy
4) Liver uptake.

Non-Uniform Myocardial Wall Thickness

Non-uniform myocardial wall thickness has long been recognized as a culprit for false positives diagnoses in SPECT MPI *(126)*. Through the early work of Clausen et al *(93)*, it is well known that there are normal variants in human myocardial wall thickness and thus, there are normal variants in the way healthy myocardial perfusion can appear in SPECT MPI due to the partial volume effect. For instance, it has been shown that there are discernible increases in left ventricular myocardial wall thickness at the anterior and posterior junctions with the right ventricle, as well as in the papillary muscle region; whereas distinct minima were observed, particularly in the basal aspect of the septum *(93)*. Although many wall thickness non-uniformities have been shown to be normal variants and thus, should be well represented in a normal patient databases (since this ultimately represents the “average” patient), there will always be patients who have

myocardial wall thicknesses beyond the standard deviations of the normal variants. For this reason, non-uniform myocardial wall thickness, although a normal variant, can provide challenges for normal database methodologies in extreme cases.

Apical Thinning

One of the most common presentations of the partial volume effect in SPECT MPI is the appearance of irreversible apical defects caused by apical thinning (a specific case of non-uniform myocardial wall thickness) *(127, 128)*. Links et al has shown that apical thinning can be present in up to 87% and 71% of patients with abnormal and normal perfusion, respectively, with up to 30% of these cases considered to be moderate to severe apical thinning *(128)*. Despite the fact that ischemic myocardium has been associated with the thinning of myocardial walls, Johnson et al showed that thinning myocardial walls can be a normal variant, particularly in the apex *(127)*. It has been speculated whether this effect has a physiological influence in the apparent reduced blood flow to the apex; however, it is most certainly in part related to the partial volume effect caused by the physical thinning of the myocardial wall at the apex *(93, 124, 127, 128)*. Again, for patients who lie outside of the normal variants of apical thinning, normal patient databases will not accurately represent the perfusion in the apex for these patients and can ultimately lead to false diagnoses.

Regional Myocardial Hypertrophy

Another common partial volume artifact presented in SPECT MPI is the appearance of fixed perfusion defects due to pathological regional thickening of the myocardial wall known as regional myocardial hypertrophy *(125)*. Unlike apical thinning described

above, myocardial hypertrophy is not a normal variant. This condition can be caused by a number of conditions, including systemic hypertension and pressure overload via valvular heart disease. Common presentation of regional myocardial hypertrophy in SPECT MPI is an increase in count density in the septal regions, thus creating the appearance of a perfusion defect in the lateral region *(129)*. Interestingly, it has been shown that false-positive perfusion defects can be present in up to 33% of studies in young male athletes *(130)*. In these cases, myocardial hypertrophy is induced by substantial exercise, as opposed to pathology. Despite the definite presence of the partial volume effect in all of the aforementioned cases, it is a topic of debate whether alterations in regional blood flow and/or metabolism associated with this pathology contribute to the apparent reduced uptake in non-hypertrophic regions in SPECT MPI *(131-133)*. Current methods used to deal with patients with myocardial hypertrophy are limited to an assessment of the patient's history and the use of gated SPECT MPI images, which can identify wall motion abnormalities in the suspected hypertrophied regions of the myocardium.

Liver Uptake Artifact

Finally, one partial volume artifact unrelated to myocardial wall thickness is known as the liver uptake artifact (or liver scatter, or liver spill-in, or simply the liver artifact). Despite the ability of the MIBI tracer to be sequestered in the myocardium, at 60 minutes post injection, the uptake in the heart accounts for roughly 1-2% of the injected dose, whereas the bladder, liver, gallbladder and kidneys can account for roughly 3-6% each *(134)*. Due to the proximity of the liver to the inferior wall of the heart (within 5mm in some cases, or roughly a single SPECT pixel length), this organ can dramatically influence the appearance of the count distribution within the heart *(36, 38, 49, 119, 135-137)*. Specifically, the presence of a hot liver adjacent to the inferior wall of the

heart can contribute counts to this portion of the myocardium via partial volume ("spill-in") and scattering effects, thus creating an artificially hot inferior wall. This effect has been shown to be dependent on both the proximity of the liver to the heart, as well as the liver to heart activity ratio *(138)*. A practical method of reducing this artifact is to have the patient drink (typically water or milk) or have a fatty meal just before the acquisition, which stimulates liver clearance *(137)*. More sophisticated methods of correcting for the liver artifact include scatter correction *(139-142)* and partial volume correction techniques *(49, 143-145)*.

3.2.2 Software-Related Artifacts

Artifacts in SPECT MPI can also be generated from the image processing software. In particular, these artifacts can be caused by the inconsistencies between how the normal patient database and the investigated patient study are processed. From the acquisition of the data to the final image, there are a number of image processing steps that must be performed and not all steps are trivial. Although this list is not comprehensive, this thesis will focus on a few of the potential sources of artifacts as they pertain to the TQPS method:

1) Reorientation
2) Apex and Base Selection
3) Reconstruction

Reorientation

As mentioned already, the heart resides obliquely in the chest which makes it necessary for the imaging software to reorient the images into the cardiac axes in order to generate a bulls-eye map. Since the orientation of the heart can vary from patient to patient, the reorientation step is patient-specific and must be performed separately for every study. The reorientation parameters selected by the user can have a large influence on the spatial distribution of the perfusion within the final bulls-eye image *(146)*. Figure 3-3 illustrates how two different reorientations of the same heart can affect the resulting bulls-eye maps.

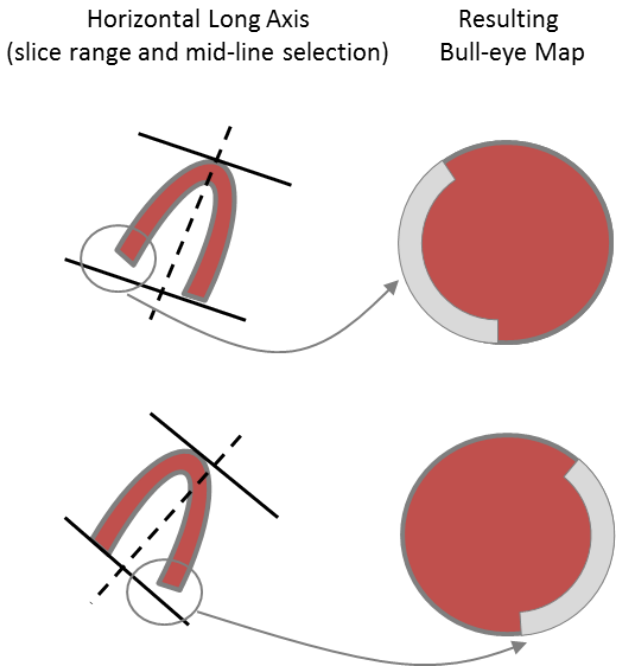

Figure 3-3 An illustration of showing the influence of orientation on the final bulls-eye map for a healthy heart. The top left image shows a correct selection of the base and apex slice (solid black lines) as well as the mid-line (dashed black line) of the left ventricle. The corresponding bulls-eye map is shown in the top right, with the normal reduction in perfusion due to (light grey) due to the shorter septal wall. The bottom row shows a case where the mid-line and basal slice has been incorrectly chosen. Here, the bulls-eye map depicts reduced perfusion in the lateral wall, which is not a typical representation of a healthy heart and maybe interpreted as a false positive as a result.

In a clinical situation, image reorientation can cause an artifact if the patient's heart is reoriented inconsistently with normal patient database. For instance, a healthy bulls-eye map will show reduced perfusion in the basal-septal wall due to the shortening of the septal wall (due to the aortic outflow tract) relative to the lateral wall (top row of Figure 3-3). This area is typically designated in a bulls-eye map as the aortic outflow tract and is not considered as a perfusion defect. However, if the patient study is reoriented incorrectly, the position of the aortic outflow tract may be displaced relative to the normal patient database (compare bulls-eye maps in Figure 3-1). In this particular example, the incorrect reorientation can cause an artifact in the bulls-eye image, which could lead to a false-positive diagnosis.

In addition to the case where the patient study is compared to a normal patient database, reorientation effects can also play a significant role when a patient's rest and stress studies are being compared for reversibility analysis. In this case, if the rest and stress studies are inconsistently reoriented, a false representation of reversible and irreversible defect can be created.

Apex and Base Slice Selection

In addition to reorientation effects, the correct identification of the apex and base of a patient's heart will also have a significant effect on the final perfusion estimate depicted in the bulls-eye image *(146)*. The identification of apex and base is part of the segmentation process of the left ventricle with the SPECT MPI image prior to the bulls-eye map construction. If the most basal slice is selected too far from the patient's true base, then there is a possibility of introducing false perfusion defects in the basal aspect of the bulls-eye map. Conversely, if the limits of the apex and base are selected too tightly, then the semi-quantitative analysis is at risk of underestimating the size of the

defect as a result of underestimating the size of the left ventricle. Although the selection of the apex and base is robust in most modern commercial software, there remain challenging cases when true perfusion defects reside in the base or apex, making it difficult to accurately choose the limits in these cases.

Image Reconstruction

Image reconstruction in SPECT is a complex process, which often involves a number of approximations. Despite the success of OSEM-based methods, there are many well-known artifacts that can be produced when corrections are integrated into the algorithms as well as by the algorithm itself. For instance, the integration of CT-based attenuation correction has been a topic of debate since the conception of the first commercial SPECT-CT system in 1999 by General Electric (GE) Healthcare. The basis of the debate is not whether or not accurate attenuation correction can improve SPECT MPI images, but more if the correction can be done without technical complications *(147)*. The most common complication is the misregistration of the SPECT and CT data which can cause severe artifacts in SPECT MPI *(121, 147, 148)*. In fact, a recent study by Goetze et al reported severe SPECT MPI artifacts caused by SPECT-CT misregistration in 42% of their study population *(149)*. Despite these challenges, every major manufacturer of SPECT machines offer at least one SPECT-CT system (with co-registration software) in their nuclear medicine portfolio *(147)*, indicating that the community remains optimistic with respect to SPECT-CT systems.

Additionally, OSEM has the potential to introduce false perfusion defects in SPECT MPI for complex reconstruction cases *(148)*. For instance, it has been shown that false perfusion artifacts are more prominent in cases with highly non-uniform distribution of attenuation coefficients, increased matrix size (128 x 128 versus 64 x 64) and increased

patient body size. In these difficult cases, the OSEM algorithm may require more iterations to converge. In traditional SPECT MPI analysis, however, the patient's image is always reconstructed using the same protocol as used to reconstruct the normal patient database; thus, if an obese patient is to be analysed, the reconstructed image for this patient may be insufficiently processed and be inconsistent with that of the normal database where a lower number of iterations was sufficient.

3.3 Template-Based Methods

The TQPS method utilizes a patient-specific template as its healthy standard for semi-quantitative SPECT MPI analysis, as opposed to an averaged heart used in the traditional normal database approaches. In doing so, the proposed method can overcome some of the aforementioned limitations of the normal database approach.

The idea of a template was adopted from previously developed "template-based methods", which have been traditionally designed for partial volume correction in both PET and SPECT imaging *(48-50, 143-145, 150-157)*. The original applications of the template idea were in PET brain studies *(151-153, 157)*; however, there has been growing interest in partial volume correction within the SPECT community as the modality continues to evolve. In particular, template-based partial volume correction methods have now been investigated in neurology, oncology *(50, 150, 156)* and cardiology *(49)*.

In general, the aforementioned template-based methods utilize the information from an external high-resolution anatomical imaging modality (e.g. MRI or CT) to model the boundaries of particular organs of interest and correct for the partial volume effect present in the SPECT image (see Figure 3-4).

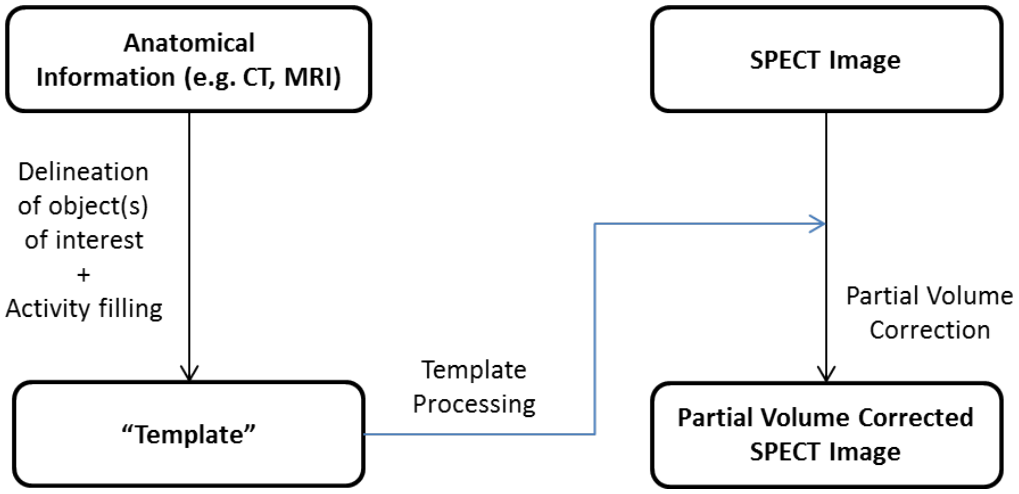

Figure 3-4 A simplified flow chart describing the general template-based method for partial volume correction.

Since its introduction in 1992 by Muller-Gartner et al *(153)*, there have been a number of variations in this approach; however, all methods begin with the construction of the "template". In nuclear medicine, the goal of the template is to create a digital representation of tracer distribution within the patient's body (or an object of interest); thus, the true anatomical boundaries must be defined. In order to achieve this, previous methods have utilized CT and MRI images to manually delineate objects of interest necessary for the construction of the template *(49, 50, 144, 154, 158)*. Once the boundaries have been defined, each object of interest (often referred to by template-based methods as a compartment) can be filled with digital activity. One way to fill the compartments with activity is by using a binary system, where the object of interest's activity is set to one and the background is set to zero *(144)*. More sophisticated methods include estimations of the activities in both the object of interest and background compartments *(50)*. The template-based methods can be broken down to two main categories: compartment-based *(158-161)* and voxel-based methods *(49, 50,*

143, 144, 150, 151, 153, 155, 157). The two categories differ on how the partial volume correction is applied. The compartment-based methods correct the image while assuming uniform activity within each compartment *(162)*, whereas the voxel-based methods perform the partial volume correction on a voxel-by-voxel basis, thereby providing a much more detailed correction and without the assumption of uniform activities within each compartment *(50)*.

The TQPS method developed in this thesis adopts the voxel-based approach, known as the template projection-backprojection technique, which was initially proposed by Muller-Gartner et al *(153)*. In general, this technique begins by first creating projections of the template using a projector, which simulates the acquisition process in SPECT. The template projections are then backprojected (reconstructed) to create a template image. This template image, which ultimately represents the image degradation due to the partial volume effect, is then used to correct the original SPECT image.

Along with challenges associated with constructing the template, the template projection-backprojection method must also implement an accurate and computationally efficient projector (simulating SPECT acquisition) in order to properly model the partial volume effect.

3.3.1 Limitations of Current Template-Based Methods

The primary limitation of current template-based methods is their dependence on high resolution CT or MRI images for the construction of the template. Although an anatomical image is ideal for delineating the boundaries of template compartments, this

approach comes with several technical challenges. First, there are substantial differences in image resolution between SPECT and diagnostic quality CT or MRI *(143, 162)*. In practice, this resolution difference can be as low as 2 fold and as high as 8 fold, depending on the SPECT and CT systems employed for the study. Therefore, when creating a template from these anatomical images, the high-resolution information is inevitably lost as these images must be down-sampled to match the SPECT image. Further technical complications are introduced in the co-registration process between the two imaging systems. Since most hybrid SPECT-CT systems do not yet yield diagnostic quality CT images (i.e. the myocardial boundaries are not visible without the aid of a contrast agent)[2] and clinical hybrid SPECT-MRI systems are in their infancy stages; all anatomical images used in the aforementioned template-based studies have to come from separate imaging systems *(48, 48, 144, 144, 156, 157, 163, 164)*. Ultimately, the use of separate imaging systems translates into a challenging co-registration process, which can introduce many additional artifacts within the "corrected" images. Finally, SPECT and diagnostic quality CT or MRI studies for the same patient are not always available, especially for cardiac studies. Although current template-based methods offer an accurate method for partial volume correction, there remain many challenges that must be overcome prior to clinical implementation.

In cardiology, two groups have attempted to tackle the template-based partial volume correction in SPECT MPI studies. These were: Bruce Hasegawa's group in the University of California at Berkeley *(48, 144)*, and Michael King's group in the University of Massachusetts *(49, 155, 165)*. To date, both groups have focused the application of this technique on the absolute quantitation of activity in SPECT MPI, aiming to quantify the

[2] Most manufacturers do, in fact, offer 4 to 16 slice CT's onboard their high-end SPECT-CT systems with diagnostic capability; however, they are rarely used at full capacity (reduced tube current and without contrast) for routine SPECT-CT studies in the interest of minimizing patient dose.

blood flow to the myocardium (termed coronary flow reserve). For instance, Da Silva et al *(144)* found that their template-based method could recover the myocardial activity in a porcine model to within 10% of the true value, as compared to 42% for their uncorrected images. With the exception of the porcine model used by Da Silva et al, the literature regarding the template-based approach to SPECT MPI has been limited to simulation and phantom studies only. The TQPS method described in this thesis not only introduces a new application and design of the template projection-backprojection technique, but it also investigates the performance of the method in a clinical setting with a true diagnostic end point - the detection of coronary artery disease.

4 The Method

This chapter introduces the concept of the TQPS method, a new software-based image processing technique designed for the semi-quantitative assessment of SPECT myocardial perfusion imaging. The primary objective of this technique is to overcome the limitations of the normal patient database methodology adopted by current commercial software, thereby improving the diagnostic accuracy of SPECT MPI in the detection of coronary artery disease. The TQPS method offers a unique approach to SPECT MPI analysis in that it utilizes a template-based method to create a patient-specific model of his/her healthy myocardium, which essentially replaces the use of traditional normal patient databases. The following sections of this chapter will describe TQPS in its entirety, beginning with an overview and subsequently stepping through the method with a full description of each step.

4.1 Overview

The method begins with the construction of a numerical template, which represents a 3D digital version of the activity distribution within the patient's heart as if it were healthy. The template is then analytically projected using a truthful model of the clinical SPECT acquisition process, and subsequently reconstructed using the same algorithm as was used for the patient study. By processing the template data in the same manner as the patient data, it is hypothesized that both images will exhibit the same image artifacts created via image processing, thereby enabling the differentiation of the true activity distribution from the artifacts within the patient image. In contrast, the normal

patient database methodology employs an “average heart” as its reference, rendering it incapable of recognizing distinct patient-specific artifacts (e.g. severe apical thinning). In order to assist in the diagnosis, an artifact corrected image is generated by taking the ratio of the template and patient bulls-eye map images. Finally, an empirically designed threshold is implemented to identify potential perfusion defects within the corrected image. With that said, the TQPS method is best described in a step-wise fashion with the following key procedures:

Step 1: Template construction
Step 2: Template projection
Step 3: Reconstruction
Step 4: Artifact correction
Step 5: Defect definition

Figure 4-1 illustrates the method in its entirety and the indicated steps (highlighted by grey circles) will be discussed in the following sections.

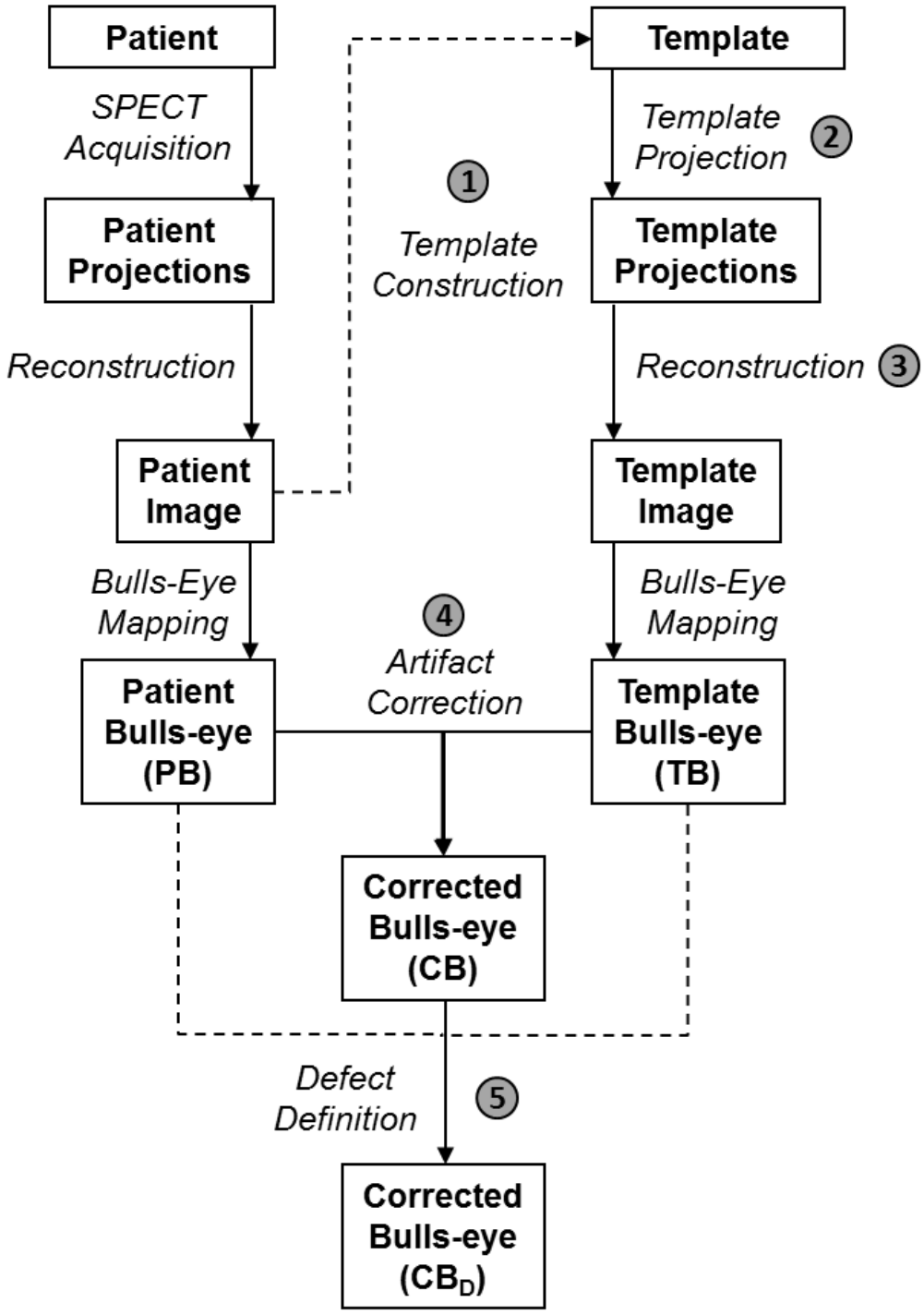

Figure 4-1 A flow chart representing the TQPS method for (clinical) SPECT MPI. The steps indicated by the grey circles correspond to the steps discussed in the Sections 4.2-4.6.

4.2 Step 1: Template Construction

The first step of TQPS involves the construction of the template. The primary challenge in this aspect of the method is to accurately define the endo- and epicardial boundaries of the patient's left ventricular myocardium.

In previous template-based methods designed for SPECT and PET applications, the construction of such templates have adopted CT or MRI images *(48, 49, 143, 166, 167)*. Although CT (or MRI) is an ideal modality for template construction as it provides relatively accurate anatomical information, it is very difficult to implement in practice for a number of reasons (described in detail in Section 3.3.1). One of the aims of this thesis was to design not only an accurate method for SPECT MPI analysis, but also a pragmatic method with future clinical applications in mind. Therefore, TQPS utilizes the readily-available SPECT data of the investigated patient for the template construction thereby enabling it to be performed for any SPECT MPI study.

4.2.1 Template Boundaries

Left Ventricle Segmentation

To delineate the endo- and epicardial boundaries of the left ventricle within a SPECT image, the method described in this thesis employed the segmentation technique developed by Heiberg et al and integrated into the freely available research software, Segment - version 1.8 R1145 (http://segment.heiberg.se) *(92, 168)*. This segmentation software package is semi-automatic in that it requires minimal user input. Only a brief

overview of the segmentation process is provided in this section (please refer to Soneson et al *(92)* and Appendix A for further operational details).

One of the highlights of the Segment approach is its incorporation of anatomical information, obtained from a training set of MRI images, into the segmentation process. This anatomical information is used to enforce limits on the myocardial boundaries detected within the SPECT image, thereby preserving anatomical validity. Specifically, these limits are used to ensure that the segmented left ventricular myocardium is within the anatomical limits in terms of length (apex to base), mass and thickness. This database of anatomical information obtained via MRI data can play an important role in the segmentation process, particularly in cases where there is substantial adjacent extra-cardiac uptake, which can highly influence the delineation process. It is worthy to note that this anatomical information is used merely to keep the segmented left ventricle within reasonable anatomical bounds; thereby enabling the program to uniquely delineate the left ventricle for each patient (preserving patient specificity). In particular, these MRI databases are *not* to be confused with the normal patient databases used in commercial SPECT MPI analysis, as they are employed for completely different purposes.

After uploading a reconstructed dataset into the Segment program, the user must first choose the range of short axis slices encompassing the left ventricular myocardium. This step is performed to provide a rough definition of the volume of interest and to exclude extra-cardiac uptake (liver, gallbladder, etc.), thus helping the algorithm to locate the left ventricle within the data set. The algorithm subsequently defines the most basal and apical slices with the assistance of the database of anatomical information. For instance, the most basal aspect of the patient's heart is defined as the first short axis slice to have a group of pixels, defined as having an area greater than 75 mm^2, with intensities greater than 30% of the maximum intensity within that area *(92)*.

The most apical slice is detected in a similar manner, but with different thresholds defined by the MRI-based anatomical database.

The next operation performed by Segment involves the calculation of the midline of the left ventricle, as shown in Figure 4-2. Here, the program finds the center of the left ventricle for each short axis slice using an iterative optimization algorithm (Figure 4-2-A-D). The midline of the entire left ventricle is then calculated via a least-squares method using the center points calculated for each short axis slice (Figure 4-2-E-G).

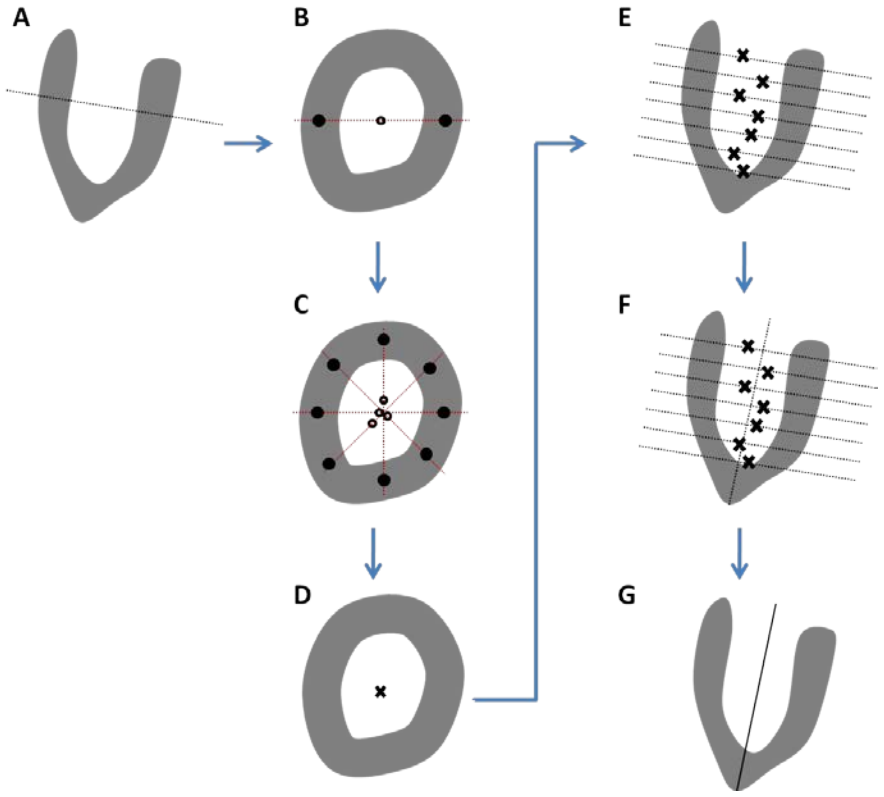

Figure 4-2 The steps used in Segment for the calculation of the left ventricle midline. Image (A) begins with the selection of a short axis slice (shown here in the horizontal long axis view); (B) shows a single radial profile (red dashed line) drawn for the selected short axis slice with the two midmural points (black filled circles) and calculated the midpoint (black outlined circle); (C) shows the same as image as (B) but with multiple radial profiles; (D) shows the eventual selection of the midpoint for this slice; (E) shows the midpoints for each of the other slices in the horizontal long axis; (F) shows the least-squares fit for the midline of the entire left ventricle, and (G) shows the final result.

The determination of the midline for the entire left ventricle enables the algorithm to perform its next step, which is to calculate the mean myocardial wall thickness and the mean radius for the short axis slice with the highest total intensity (i.e. assumed to be the healthiest slice). In order to calculate these parameters, the short axis image is first resampled from its spatial coordinates into a set of radial profiles (default number of profiles is 40) defined at each radial angle (see Figure 4-3). Once resampled, Segment then finds the midmural line (midline of the myocardial wall) using an optimization algorithm known as Djikstra's algorithm *(92)*. In this application, the algorithm essentially seeks the midmural line by assigning low cost to pixels with high intensity values and high cost to high gradients in the resampled short axis slice. With the middle of the myocardial wall defined, the mean radius can then be calculated as the mean value from the center point of the slice to the midmural line at each radial angle. To calculate the mean wall thickness, the endo- and epicardial boundaries are defined in a two-step process. First, the pixel with maximum intensity is defined for each radial profile at angle (θ) within 7 mm on either side of the midmural line. Second, the first pixels with a value less than or equal to 85% of the maximal intensity on either side of the midline are defined as the endo- and epicardial edges for each radial angle *(92)*. The mean myocardial wall thickness is calculated as the mean distance from the endo- and epicardial points defined at each radial angle, θ.

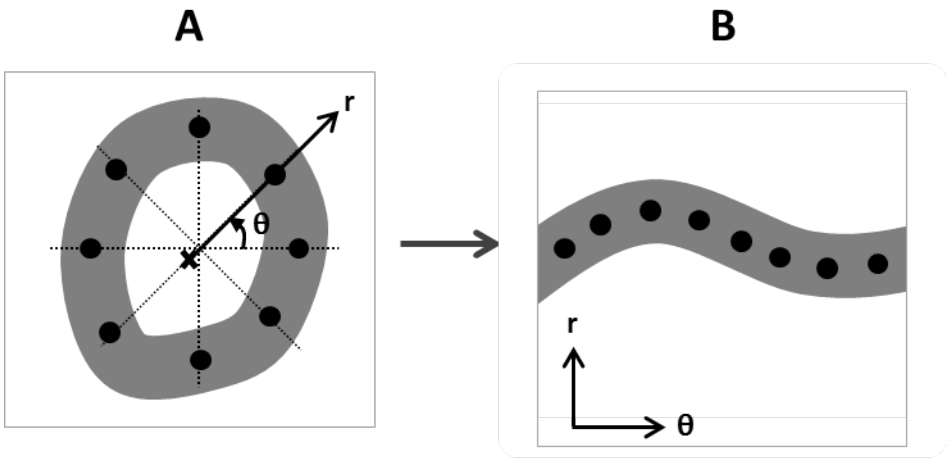

Figure 4-3 A representation of the resampling process in Segment. Image (A) shows a short axis slice with a number of radial profiles drawn with parameters r and θ; image (B) shows the resampled image where each radial profile is plotted with the radial profile intensities along the vertical axis at each angle θ, plotted on the horizontal axis.

Once the mean radius and thickness are calculated for the slice with maximum total intensity, the algorithm uses this information as starting points for finding the endo- and epicardial edges in the remaining short axis slices. In this search, the radii for the subsequent slices are bounded to be within 70-130% of the calculated mean radius, which ensures that the radii do not migrate too far from the mean and thus, preserving anatomical validity. Additionally, the pre-calculated mean thickness is used as a starting point for each of the subsequent endo- and epicardial boundary definitions. In this case, a simple search for the pixel closest to 85% of the maximum intensity for the given radial profile is performed in the neighborhood of these starting points to define the wall boundaries for the remaining slices. In all, these steps take advantage of the fact that the left ventricular myocardium has fairly predictable gross shape parameters (e.g. radius and thickness) and thus, can be used to guide the delineation to within such geometry and accelerate the segmentation process.

Specifics on how the algorithm handles the delineation of the more peculiar aspects of the left ventricular myocardium, such as the aortic outflow tract (where the blood in the left ventricle is ejected via the aorta) and the apex, and other details are described by Soneson et al *(92)*. Figure 4-4 shows the end result of a segmentation using Segment for an example patient SPECT MPI dataset. It is these boundaries that are used for the left ventricular myocardium compartment of the template in the TQPS method. Herein, this compartment will be referred to as the heart compartment.

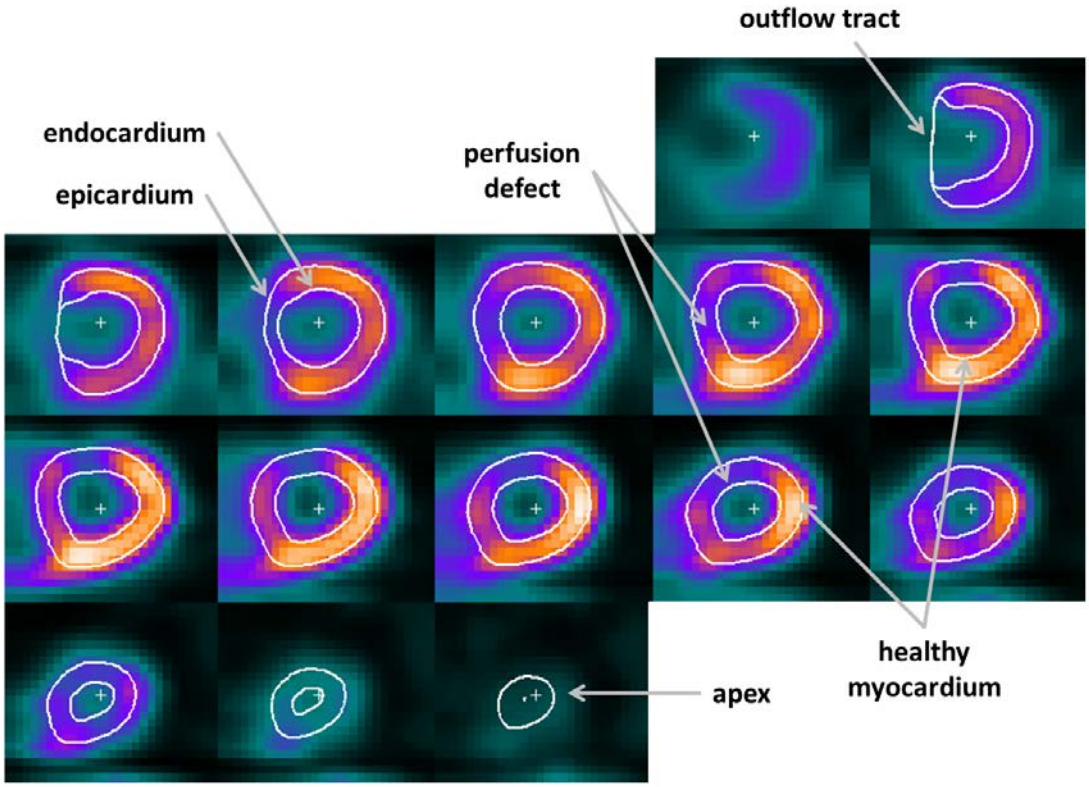

Figure 4-4 An example left ventricular myocardium segmentation of a patient SPECT MPI study (shown as short axis slices) using the Segment program. The resulting segmentation is represented by the white lines. A number of features of the segmentation and patient data are labeled on the figure: endocardium, epicardium, outflow tract, apex, perfusion defect, and healthy myocardium.

Extra-Cardiac Organ Segmentation

In order to investigate the performance of the TQPS method when using different templates, this thesis introduced two more template compartments, in addition to the heart as described above. The two compartments were defined as: the background and the lungs. Under this definition, all bodily tissues excluding the heart and lungs were generalized as one template compartment, referred to as "background". Unlike in SPECT MPI images, the boundaries of the lungs and background are readily visible on any standard attenuation map - even those generated from low dose CT images acquired on hybrid SPECT-CT systems. As shown in Figure 4-5, standard attenuation maps from SPECT-CT systems exhibit good contrast between the lungs and background tissue; however, the boundaries of the left ventricular myocardium and other specific soft tissues are not reliably discernible in these images. For these reasons, the SPECT MPI image is used to construct the heart compartment, and the attenuation map is used to generate the lung and background compartments of the template.

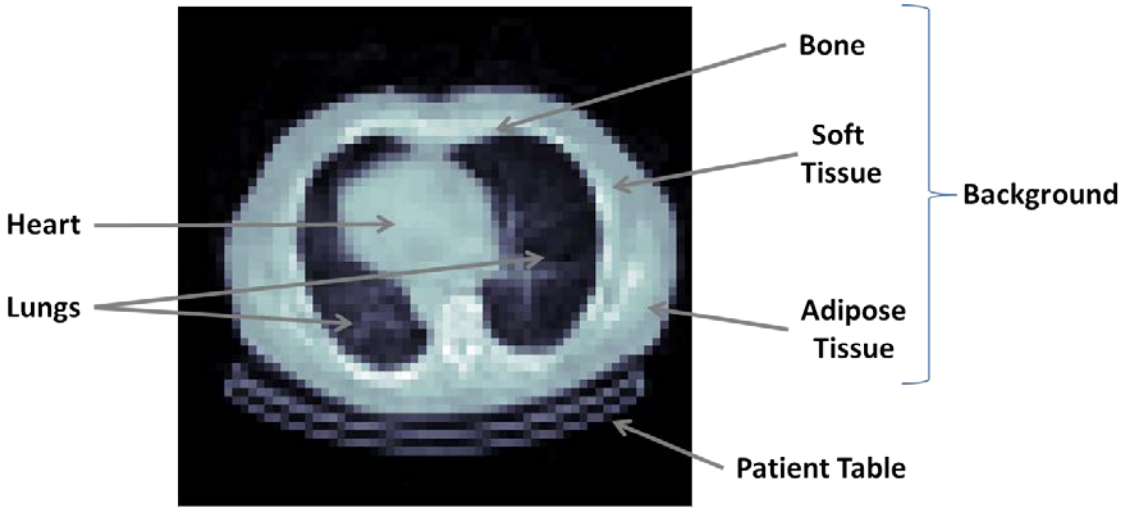

Figure 4-5 An example transaxial slice of an attenuation map obtained on a standard SPECT-CT system. All main tissue types are indicated by the arrows in addition to the patient table.

The first step in defining the two non-cardiac compartments of the template is to delineate the lungs. To achieve this, a threshold derived from the linear attenuation coefficient of lung tissue is applied within the attenuation map image. In this case, the employed threshold need not be of high precision due to the relatively large difference between the linear attenuation coefficients of the lungs (0.043 cm^{-1}) and background (0.142 cm^{-1} in its lowest limit – adipose tissue). Once the lungs are defined, the background can then be defined as all tissue not included within the boundaries of the lungs and the heart (corresponding to co-registered SPECT-defined left ventricular myocardium). Figure 4-6 illustrates the key steps involved in defining the template boundaries for all compartments: heart, lungs, and background.

4.2.2 Template Activities

With the boundaries of the template compartments defined, the next step is to fill these compartments with appropriate activity ratios. It worth it to note here that since the projection of the template is performed without modeling statistical noise (more on this in Section 4.3), it is the activity ratios, as opposed to the absolute activity values that are of concern in this step of the template construction.

The activity ratios of the background and lungs relative to the heart were estimated using the counts from the reconstructed SPECT image (Figure 4-6). Within the lung and background compartments, the mean of the total SPECT counts were calculated. For the heart compartment, only the top 40^{th} percentile of counts within the heart boundaries was used to calculate the mean value. The reason for this approach was to avoid the influence of perfusion defects and partial volume effects within the heart, which can artificially reduce the value of the mean for this compartment. Using the mean counts calculated for each compartment, the estimated activity ratios were obtained. Thus, the

final template included regions defined as the heart, lungs, and background, each filled with uniform activity with ratios corresponding to the relative uptake in these regions estimated from the SPECT image (as shown in Figure 4-6).

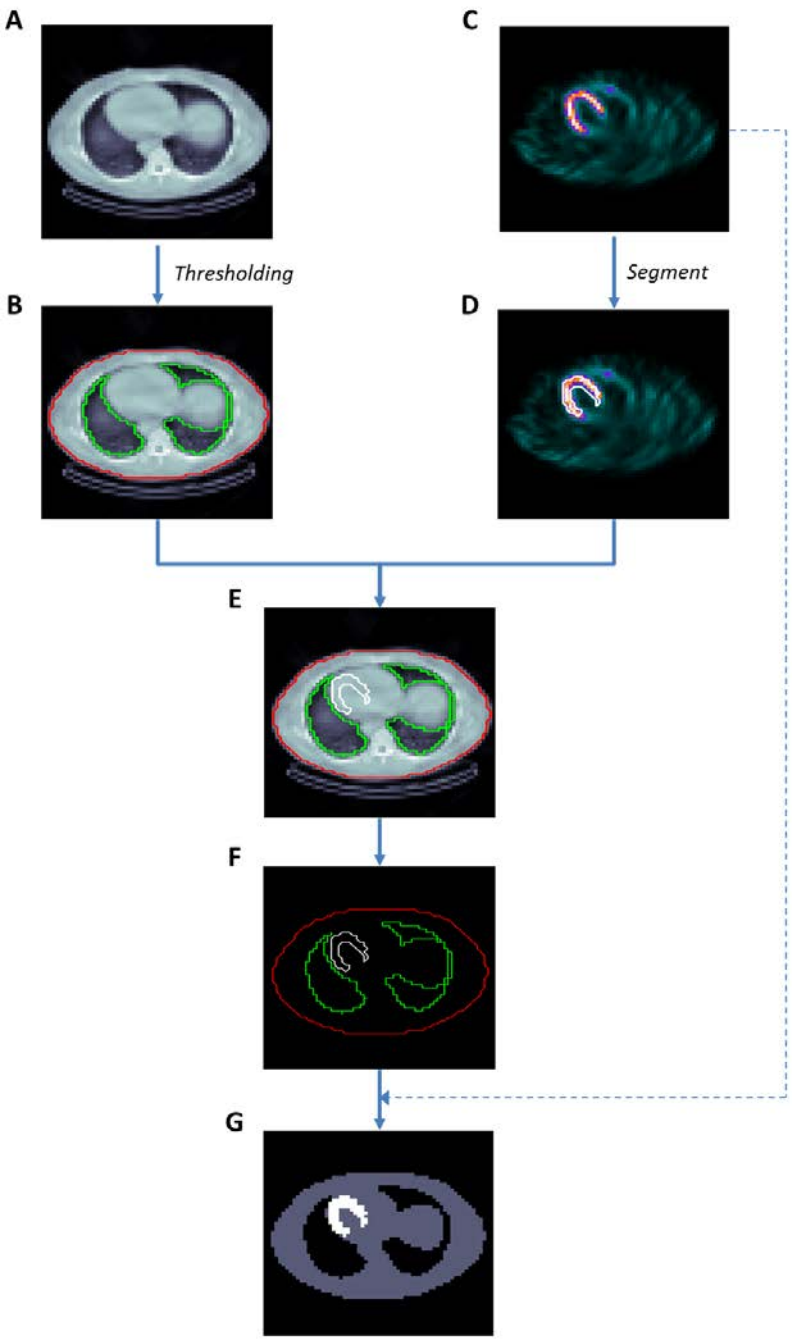

Figure 4-6 A flow chart describing the template construction process. Images (A) and (B) show the segmentation of the lungs (green outline) and background (red outline) using thresholding of the attenuation map. Images (C) and (D) show the segmentation of the left ventricular myocardium (white outline) using the Segment program and the reconstructed image. Images (E) and (F) show the delineations of the three compartments overlaid on the attenuation map and on their own, respectively. Finally, image (G) shows the resulting template with each compartment filled with uniform activity ratios as determined by the reconstructed image (C).

4.2.3 Template Variations

In the evaluation (Chapter 5) and optimization (Chapter 6) stages of the TQPS analysis, the performance of different template models was investigated. Specifically, two different template compartment configurations and two template construction methods were studied.

The two templates differing in compartment configurations can be described as follows:

1. Template Compartment Configuration I: *Heart Only*
2. Template Compartment Configuration II: *Heart + Lungs + Background*

Herein, these templates will be referred to as T_{HRT} and T_{HRTBKG}, respectively. The T_{HRT} template contained the heart compartment without the lung or background compartments. Therefore, the T_{HRT} template activities were binary in that the heart activity was set to one with the rest of the image set to zero. The second configuration was simply the full three-compartment template with activity ratios defined for the heart, lungs, and background.

The two templates construction methods can be described as follows:

1. Template Construction I: *SPECT-based*
2. Template Construction II: *Ideal* (Phantom-based or CT-based)

Herein, these templates will be referred to as T_S and T_I, respectively. The difference between these two templates was in how the boundaries and activity ratios for each compartment were determined. For T_S, the boundaries and activity ratios were obtained from the SPECT image and associated attenuation map (as described in the

previous sections), whereas T_I was an idealized version of the template, where the true boundaries and activity ratios were employed. Although it was not possible to create the *Ideal* template for clinical studies, such templates were created for the simulation and physical phantom studies where information regarding the true organ configurations and their activities could be extracted.

4.3 Step 2: Template Projection

The second step in the TQPS method is the projection of the template, where the goal is to accurately model the acquisition processes for the given patient and SPECT system. To achieve this, an in-house algorithm was employed, known as the Analytical Photon Distribution Interpolation (APDI) method *(44, 45)*.

The APDI method calculates noiseless SPECT projections using an activity distribution, attenuation map and imaging system parameters as input. For the TQPS application, the template is used as the input for the activity distribution, which enables APDI to generate a set of projections of the template as if it was scanned on a given SPECT imaging system. One of the advantages of this technique over other analytical methods is that it utilizes pre-calculations for patient independent parameters, such as the Klein-Nishina cross sections, geometry of the imaging system, and acquisition parameters, and stores them as look-up tables, which substantially reduces the computational burden of the method *(44, 45)*.

The method computes the distribution of primary, first-order, and second-order Compton scattered photons. The primary distribution calculation is a relatively simple task. Using the activity distribution, attenuation map and acceptance angle of the

collimator, the primary photon distribution is a two dimensional integration of the photon detection probability function over the detector surface as shown in Eq. 4-1.

$$PPD(\lambda, \overrightarrow{n_i}) = \sum_{j=1}^{J} \lambda_j P_E(0) \exp\left(-\int_{\overrightarrow{s_j}}^{\overrightarrow{n_i}} \mu(x)dx\right) \int_{A_i} F(\xi) \frac{\cos(\xi)}{4\pi r_{ns_j}^2} d^2n \qquad \text{Eq. 4-1}$$

where $\overrightarrow{s_j}$ and $\overrightarrow{n_i}$ are the vector coordinates describing the centre of voxel j and detector pixel i, respectively; λ_j is the activity in voxel j; $P_E(0)$ is the probability that an emitted photon will be accepted within the defined energy window; $\mu(x)$ is the attenuation coefficient as a function of distance along the photon path; A_i is the area of a detector pixel centered at n_i; $F(\xi)$ describes the probability that a photon reaching the collimator surface at an angle ξ will reach the detector; r_{ns_j} is the distance between vectors $\vec{n}$ and $\overrightarrow{s_j}$; and finally $\frac{\cos(\xi)}{4\pi r_{ns_j}^2} d^2n$ is the solid angle of a sphere centred at $\overrightarrow{s_j}$ and subtended by a detector pixel element d^2n.

In contrast, the scattered photon distribution is a much more involved calculation as the integration must be performed over the entire 3D scattering medium. A scattered photon distribution (SPD) is calculated for each template voxel containing activity. The SPD is the 2D distribution of Compton scattered photons emitted from a given source voxel and ultimately detected in a given detector bin. In order to calculate this distribution, APDI utilizes the activity distribution (template), attenuation map, Klein-Nishina formula and collimator geometry to model photon transport through the body (including 1st and 2nd order Compton scattered photons) and to the detector. The SPD can be summarized as follows *(45)*:

$$SPD(\lambda,\overrightarrow{n_i}) = \sum_{j=1}^{J}\lambda_j \sum_{k=1}^{K}\rho_e\left(\overrightarrow{t_k}\right)\cdot\left[K^{(1)}_{s_j t_k n_i} + \frac{13}{12}K^{(2)}_{s_j t_k n_i}\int_{\overrightarrow{s_j}}^{\overrightarrow{t_k}}\mu(x)dx\right]\cdot$$
$$exp\left[-\int_{\overrightarrow{s_j}}^{\overrightarrow{t_k}}\mu(x)dx - \int_{\overrightarrow{t_k}}^{\overrightarrow{n_i}}\mu(x,E(\theta))dx\right] \quad \text{Eq. 4-2}$$

where λ_j is the activity in voxel j; $\rho\left(\overrightarrow{t_k}\right)$ indicates the electron density at the location of the scattering event t_k; $\mu(x)$ is the linear attenuation coefficient at position x; and $\overrightarrow{s_j}$ and $\overrightarrow{n_i}$ are the vector coordinates describing the centre of voxel j and detector pixel i. The term $\mu(x,E(\theta))$ indicates the linear attenuation coefficient at x and energy $E(\theta)$, which is the energy of the photon after undergoing Compton scatter at a scattering angle of θ. The terms $K^{(1)}_{s_j t_k n_i}$ and $K^{(2)}_{s_j t_k n_i}$ are the aforementioned pre-calculated look up tables for 1st and 2nd order Compton scatter, respectively. The summations over J and K are over all voxels containing activity and over all voxels containing scattering material, respectively. A full description of these tables can be found in the original paper by Wells et al *(44)*.

Once the scatter point spread function is calculated, the template projections $TP(\lambda,\overrightarrow{n_i})$ can be obtained by adding the scatter and primary photon distributions:

$$TP(\lambda,\overrightarrow{n_i}) = PPD(\lambda,\overrightarrow{n_i}) + SPD(\lambda,\overrightarrow{n_i}) \quad \text{Eq. 4-3}$$

Figure 4-7 provides an illustration showing the possible photon paths from a source voxel to a detector bin as they pertain to the variables introduced in Eq. 4-1 and Eq. 4-2.

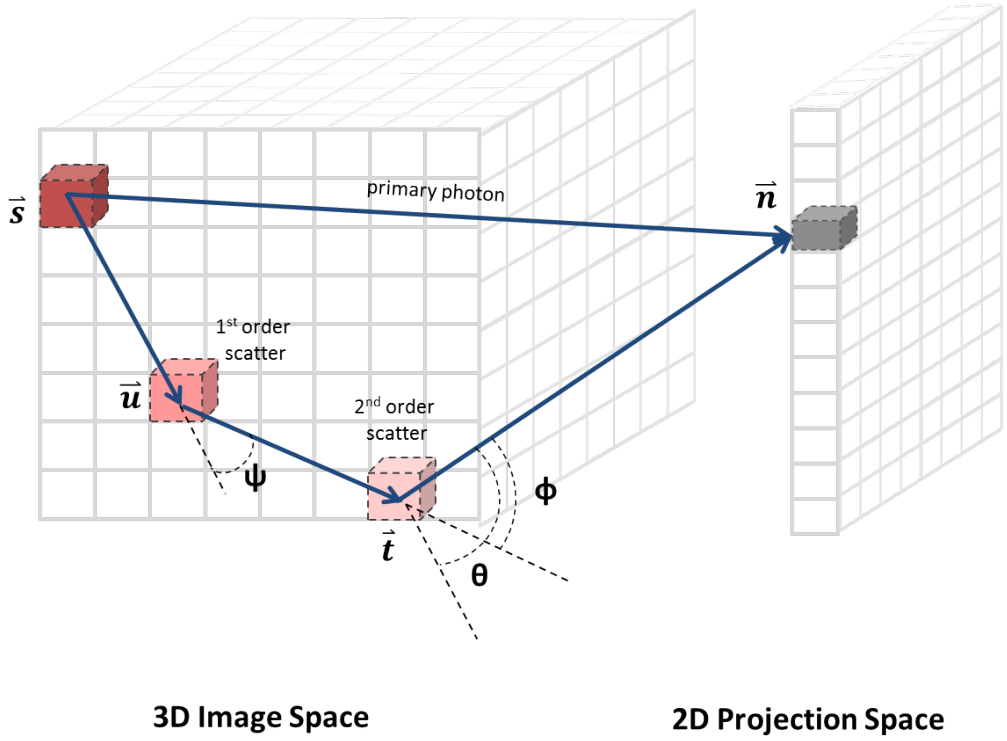

Figure 4-7 An illustration showing the possible photon paths from a source voxel $\vec{s}$ to a detector bin $\vec{n}$. The direct path $\vec{s}$ to $\vec{n}$ shows the path of a primary photon; the path $\vec{s}$ to $\vec{u}$ to $\vec{t}$ to $\vec{n}$ represents the path of a scattered photon with scattering angles ψ, θ, and ϕ.

4.4 Step 3: Reconstruction

Once the set of template projections is generated via APDI, they can be reconstructed. One of the most important aspects of the TQPS method is that the patient and template projections are reconstructed with the same algorithm and with the same parameters. This ensures that all artifacts related to image-processing will be exhibited in both the patient and template images, thereby enabling an artifact correction step, which will be explained in the next section. One of the benefits of the TQPS algorithm is that it is not restricted to any particular reconstruction algorithm, and thus can be implemented with any reconstruction software offered by commercial SPECT systems.

Reconstructions employed for the studies in this thesis included both an in-house algorithm and a commercial algorithm offered by GE. The in-house algorithm was developed by the Medical Imaging Research Group of Vancouver. This reconstruction method is based on the OSEM algorithm with the option of implementing depth-dependent resolution recovery and/or attenuation correction *(34, 169)*. When attenuation was included in the reconstruction algorithm, the CT-based maps with broad beam attenuation coefficients were used.

The Evolution for Cardiac™ reconstruction software from GE was also employed for some of the patient studies *(30, 170-172)*. This algorithm is also OSEM-based and comes integrated with resolution recovery and the capability of implementing attenuation correction (although no attenuation correction was used for the studies in this thesis when employing this algorithm). Further details regarding the reconstruction algorithms and reconstruction parameters are provided in the sections describing each of the respective studies.

4.5 Step 4: Artifact Correction

Subsequent to the reconstruction step, the patient and template reconstructed images were reoriented into the short axis view, which enabled the generation of the two bulls-eye maps: patient bulls-eye (PB) and template bulls-eye (TB), respectively (see Figure 4-1). All reorientations and bulls-eye map constructions were performed using in-house code developed on the Matlab™ (version 7.8.0 R2009a) platform.

Prior to the artifact correction step, it was necessary to normalize the PB and TB images since the template was generated using activity ratios and not absolute activity values.

The normalization technique adopted in the TQPS method was similar to that used in commercial algorithms when normalizing rest and stress SPECT MPI bulls-eye map images *(97, 173)*. The template bulls-eye was normalized to the healthy regions of the patient bulls-eye image. Specifically, the mean of all counts greater than 80% of the maximum count (i.e. "healthy") found within the PB image was calculated and used to normalize the PB image. Using this information, the mean of the homologous pixels within the TB image was used to normalize the template bulls-eye image. Here, homologous pixels refer to pixels in the TB image in the same locations as those pixels in the PB image which were found to be greater than 80% of the maximum value in the PB image. By choosing homologous healthy pixels to normalize the images, the method assumes that regions of healthy myocardium in the PB image correspond to healthy regions in the TB image. Lastly, it is important to note that the TQPS method is semi-quantitative in its analysis; thus, only the relative count distribution in the images is of concern.

With the images normalized, the method then calculates an artifact corrected bulls-eye (CB) image:

$$CB = \frac{PB}{TB} \qquad \text{Eq. 4-4}$$

The theory of the artifact correction in CB is based upon the characteristics of PB and TB. In this regard, one can think of the activity distribution in PB as an image with areas including healthy perfusion (H), potential perfusion defects (D), and potential artifacts (A). Likewise, TB can be thought of as containing areas of H and A, but not exhibiting perfusion defects since the template is healthy, by definition. As a result, CB will preserve H and D regions, since the ratio of PB and TB will correct for the artifactual information present in both images. Therefore, CB can be considered as an artifact corrected image.

4.6 Step 5: Defect Definition

The final step of the TQPS approach involves the differentiation between normal and abnormal perfusion within CB. As opposed to the traditional "normal limits" strategy obtained from normal patient databases, TQPS implements a "healthy heart threshold" (HT) *(91)* based on the means and average deviations (AD) found within TB, PB and CB. HT was defined as follows:

$$HT = (\overline{CB} - x \cdot AD_{CB}) + (\overline{TB} - x \cdot AD_{TB}) - (\overline{PB} - x \cdot AD_{PB}) \qquad \text{Eq. 4-5}$$

where the means ($\overline{CB}$, $\overline{TB}$, $\overline{PB}$) were calculated over entire bulls-eye images and the number of average deviations is represented by x. The average deviation was defined as the mean of the absolute deviations, which were measured as the absolute differences between each value and the mean. The optimization of the number of average deviations x was performed in the evaluation and optimization phases of this thesis and will be discussed in more detail in the Chapters 5 and 6.

Eq. 4-5 was developed based on the image characteristics described in the Section 4.5. We can rewrite the equation (ignoring the average deviation terms, for now) by substituting the image terms (CB, TB, PB) with their respective image characteristics ($H + D, H + A, H + A + D$) and get:

$$HT \stackrel{\text{def}}{=} (H + D) + (H + A) - (H + D + A) = H \qquad \text{Eq. 4-6}$$

From Eq. 4-6, it can be seen that HT roughly represents the value of a healthy region (H).

The purpose of including the average deviation terms in Eq. 4-5 was to ensure that the healthy threshold represented the minimum healthy perfusion value for the investigated patient. Therefore, by applying the healthy threshold to CB, all pixels with counts less than HT (minimum healthy value) could be considered defect. Pixels below HT were presented as blackout pixels in CB_D, which could then be used to perform a number of semi-quantitative cardiac measurements, including perfusion defect extent, summed stress score, and total perfusion deficit.

4.7 Conclusions

In this chapter, the concept of the TQPS method was introduced with detailed descriptions regarding each of its critical steps: Step 1) Template Construction, Step 2) Template Projection, Step 3) Reconstruction, Step 4) Artifact Correction, and Step 5) Defect Definition. As with any model-based technique, TQPS requires a number of approximations, particularly in the template construction (Step 1) and template projection (Step 2) steps. Although these approximations are reasonable in theory, it was necessary to evaluate the overall performance of the method – which will be described in the next chapter (Chapter 5).

5 Method Evaluation

With the concept of the TQPS method introduced in the last chapter (Chapter 4), the next step of the project was to assess the performance of the method by using a variety of simulation, phantom and clinical experiments. Specifically, using these experiments, the aim of this assessment was to see how accurately TQPS could define myocardial perfusion defects and ultimately detect significant coronary artery disease. In all, the analysis of the TQPS method was organized into three phases, which will be described in their entirety in the following three chapters:

1) Method Evaluation (Chapter 5)
2) Method Optimization (Chapter 6)
3) Method Validation (Chapter 7)

The first phase, Method Evaluation (Chapter 5), provides the initial assessment of TQPS with a focus on the template construction and projection steps of the method. The second phase the analysis, Method Optimization (Chapter 6), is dedicated to the optimization of TQPS in terms of computation time and accuracy by investigating a number of simplified variations of the method. Finally, the Method Validation phase (Chapter 7) provides an evaluation of the technique in the clinical domain using a true diagnostic end point – the detection of significant coronary artery disease.

The following chapter describes the evaluation phase of TQPS, which is organized into eight sections. First, the Methodology section is included to introduce the objective of

the study as well as the justification for the experimental design. The Experiments section lists the experiments performed in this phase of the analysis including the simulations, physical phantoms and patient studies. A section on Image Processing includes all relevant processing parameters used in the study. The Figures of Merit and Statistical Analysis sections describe the measurements and subsequent statistics employed in the analysis of these aforesaid studies, respectively. Finally, the chapter concludes with the Results, Discussion and Conclusion sections, which highlight the major findings and their respective significance for the evaluation phase of the TQPS method.

It is worth noting that a number of studies and applications of the TQPS method were developed prior to the final version presented in this thesis. The results of these studies were presented at international meetings including: one abstract at the Canadian Organization of Medical Physicists meeting in 2009 *(174)*, two abstracts at the lEEE Medical Imaging Conference in 2010 *(175, 176)*, and finally one presentation at the American Society of Nuclear Cardiology meeting in 2010 *(177)*. Although many of these studies contributed to the end product of TQPS, not all were included in this thesis.

5.1 Methodology

The general objective of the study presented in this chapter was to evaluate the TQPS method. Beyond a proof of concept, this study aimed to specifically assess the performance of the TQPS method with regards to two of its key steps: 1) template construction, and 2) template projection. As mentioned, the software used in these two steps make a number of approximations, thus it was essential to evaluate the effects of these approximations on TQPS' overall ability to define myocardial perfusion defects.

Simulation data was employed in this study. Unlike patient data where the true activity distribution is unknown, simulated data enables an evaluation of the semi-quantitative measurements made with TQPS relative to the truth, since the true activity distribution is known and controlled by the investigator. As a note: in simulation studies, digital models of patients are generated using software programs; thus, "patients" created in simulated studies are referred to as "phantoms".

The experimental design employed in the following study is best described by highlighting the first three steps of the TQPS method as two parallel processes: 1) phantom data processing and 2) template data processing. This is shown in Figure 5-1.

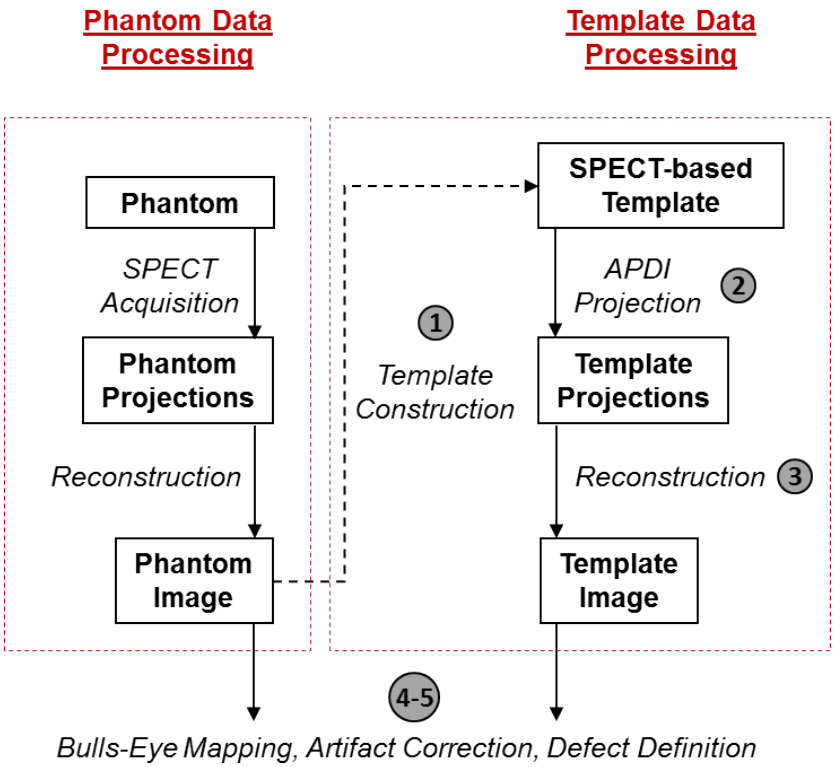

Figure 5-1 A flow chart of the TQPS method highlighting the two parallel processing streams (phantom and template) for the first three steps of the method.

The ultimate goal of TQPS with regards to these two data streams is for the template data processing (template construction, projection, and reconstruction) to accurately model that of the phantom data. In doing so, the method can accurately correct for image processing artifacts in the phantom image (Step 4 of the TQPS method). The reconstruction step, which is defined and controlled by the user, must be identical for both the template and phantom. Therefore, the only potential inconsistencies between these two parallel processes may occur if: 1) the *SPECT-based* template (template construction) does not accurately model the true healthy phantom, and 2) the APDI projector (template projection) does not accurately model the SPECT acquisition process. These two steps were the primary focus of the study presented in this chapter.

In terms of experimental design, the template construction and projection steps were strategically isolated by making controlled changes to the TQPS method. In the first series of experiments, the performance of TQPS when using the *SPECT-based* template (T_S) was investigated by comparing these results to those obtained when employing an *Ideal* template (T_I) - as described in Section 4.2.3. Since the only difference between the two methods using this experimental design is in the template construction step (see Figure 5-2), any difference between the results obtained from the two methods can be attributed to the template construction only.

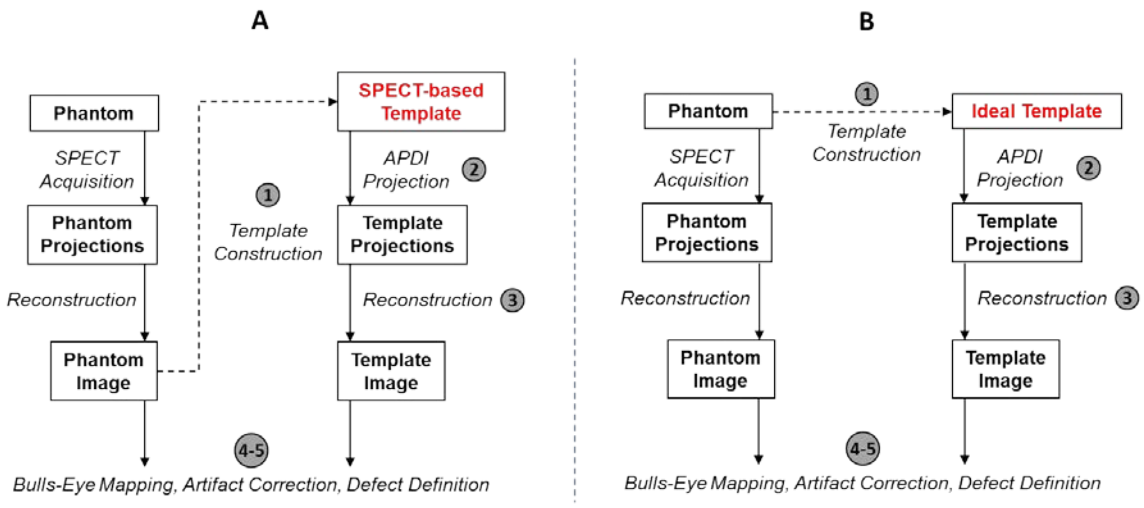

Figure 5-2 Two variations of the TQPS method used to investigate the performance of the *SPECT-based* template. (A) Illustrates the true TQPS method using T_S; and (B) shows the modified method when employing the *Ideal* template (T_I). The red font is used to show the differences between the two TQPS methods.

Next, to analyze the performance of the two template projection methods, namely (a) the analytical projector (APDI) and (b) the SPECT acquisition process, the *Ideal* template (T_I) method was used, as shown in Figure 5-3. By isolating the projection step in this analysis (the only difference between the template and phantom data streams), it was possible to investigate the performance of the APDI projector. In the simulation studies, the SPECT acquisition process was modeled using a clinically validated Monte Carlo simulation code (more on this in Section 5.2.1).

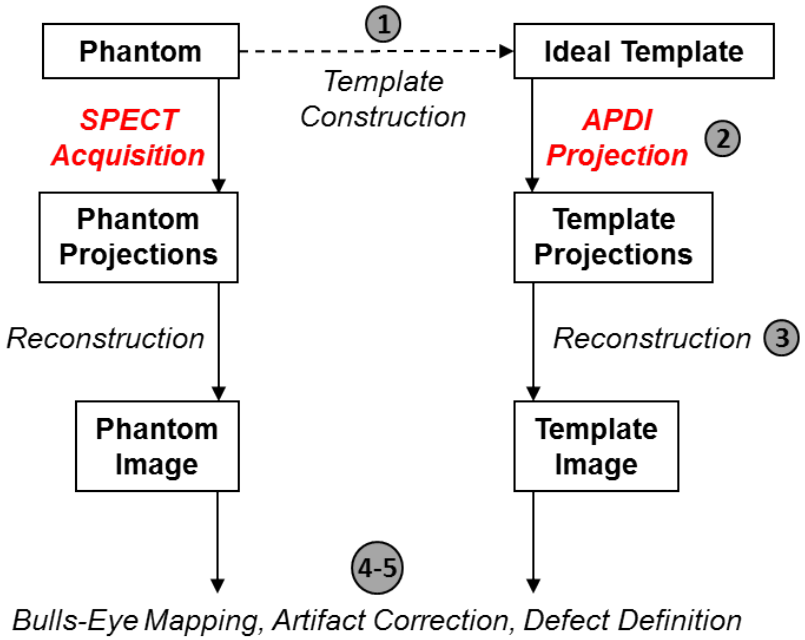

Figure 5-3 The experimental design used to investigate the performance of the APDI projector.

The next step of the evaluation phase was to test the TQPS method using physical phantom experiments. Similar to simulation studies, the true activity distribution within a physical phantom is controlled and known but not as precisely as it is when using simulations. However, physical phantom studies come with the advantage over simulations in that they involve real acquisitions with a physical SPECT camera, therefore the data are subjected to several effects that are not usually modelled in simulations (collimator septal penetration, photon scatter in the camera, etc.). Since, in the phantom studies, the true activities were known and a physical analog of the *Ideal* template could be created using the CT image acquired on-board the SPECT-CT system, the isolation schemes illustrated in Figure 5-2 and Figure 5-3 were used for the physical phantom studies as well.

Finally, the evaluation phase of the TQPS method was concluded with a preliminary proof of concept in the clinical domain. In this case, patient data was used and commercial software was employed as the gold standard in the analysis.

5.2 Experiments

5.2.1 Simulations

For all simulation studies in this thesis, the non-uniform cardiac and torso (NCAT) phantom *(178)* was employed. The NCAT phantom is a digital representation of a patient body. Analogous to patient studies, different organs can be filled with activity and nearly all physical dimensions and activity distribution parameters can be defined by the user. In this study presented in this chapter, both male and female phantoms were created. Both phantoms contained an average sized heart and body as defined by NCAT. Respiratory and cardiac motions were not simulated and the heart was set to end-diastole. For each phantom, 10 different heart activity distributions were generated: one healthy and nine with perfusion defects in the inferior wall (severity was set to 50% relative to the healthy myocardium) ranging in extent from 4% to 64% of the total myocardium. Activities in the phantoms were distributed to yield healthy heart to background and healthy heart to liver ratios of 5:1 and 1:1, respectively. No activity was placed in the lungs. The phantom details are summarized in Table 5-1.

Table 5-1 A summary of the NCAT phantoms included for the evaluation phase of TQPS. Defect extent is expressed as a percentage of the total left ventricle myocardium.

Phantom number	Phantom	Defect location	Defect Extent (%)	Adjacent liver uptake?
1-10	Average Male	n/a	Healthy (0%)	Yes
		Inferior	4%, 9%, 17%, 22%, 35%, 42%, 49%, 57%, 64%	Yes
11-20	Average Female	n/a	Healthy (0%)	Yes
		Inferior	4%, 9%, 17%, 22%, 35%, 42%, 49%, 57%, 64%	Yes

All 20 phantoms (10 heart activity distributions x 2 phantom genders) were projected using the Monte Carlo simulation code SimSET *(179, 180)* following a standard Tc-99m cardiac protocol: the simulated projection data were acquired over an 180^0 angular arc, at a 3^0 interval to yield a total of 60 projections, while using an energy window set at 126-154 keV. The simulated number of counts corresponded to the statistics found in clinical stress Sestamibi Tc-99m SPECT scans following a 740 MBq injection. Two different matrix sample sizes were investigated in this phase of the analysis: a 64x64 matrix with a 6.80mm pixels size, and a 128x128 matrix with a 4.42mm pixel size. In summary, 20 phantoms were created, which were subsequently projected with SimSET using two protocols differing in matrix size to yield a total of 40 simulation experiments.

5.2.2 Physical Phantoms

As mentioned, physical phantom experiments were included in this study as a second level of validation for the TQPS method, where the true activity distribution was known and the data was acquired by a physical SPECT camera. In these studies, the thorax phantom (Data Spectrum Corp.) was used, which included two lungs filled with Styrofoam® beads (no activity), a spine and a plastic insert representing the left ventricle of the myocardium (120mL). The phantom thorax (7000mL) and heart were filled with 184.4 MBq and 17.6 MBq of ^{99m}Tc solution, respectively, to yield a heart to background ratio of roughly 6:1. A small insert (7mL, 6% extent, 100% severity (i.e. no activity)) was used within the phantom heart to simulate perfusion defects in four different locations: inferior wall, anterior wall, lateral wall and septal wall. Additionally, an experiment was performed without the use of the defect insert, thus representing a healthy phantom. In total, five experiments were acquired using GE's Infinia Hawkeye SPECT-CT camera located at Vancouver General Hospital (VGH). The camera was equipped with a low energy high resolution collimator (LEHR) with acquisition parameters set to a 128x128 matrix size, 60 projections over a 180^0 arc, 4.42mm pixel size and an energy window range of 126-154 keV.

5.2.3 Patients

Finally, the method was tested on patient data, which were randomly and retrospectively selected from routine MPI studies performed in the nuclear medicine department at VGH. The use of fully anonymized patient data for software development projects was approved by the Clinical Research Ethics Board at the University of British Columbia. A group of seven patient studies were acquired on the GE Infinia Hawkeye SPECT-CT camera using standard clinical cardiac protocol: Tc-99m Sestamibi with a LEHR

collimator, 180^0 arc, 60 projections (25 and 20 seconds per projection for rest and stress, respectively), 64x64 matrix and a 6.80mm pixel size. In total, 5 male and 2 female patients were scanned with an average age ± SD of 69 ± 8 y. Both rest and stress scans were acquired and analyzed for each patient.

Semi-quantitative results were obtained from the GE Xeleris Workstation operating Cedars Sinai's QPS Software *(83)*. The QPS procedure was performed by an expert operator following standard protocol at our institution, using gender matched non-attenuation corrected (NC) normal patient databases. Of the 14 studies acquired (7 patients x 2 rest/stress studies), 6 were considered healthy (<4% perfusion defect extent) by QPS and the remaining 8 studies exhibited perfusion defect sizes ranging from 5% to 52% of the total myocardium with an average of 12%.

5.3 Image Processing

For this evaluation phase of the TQPS method, the T_{HRT} template was employed for all analyses, as described in Section 4.2.3. The reason for not using the T_{HRTBKG} template at this point of the evaluation was to simplify the method, in addition to the fact that the benefit of including background in the template design was still uncertain. It was not until the optimizing phase (Chapter 6) where the T_{HRTBKG} template was investigated.

Additionally, this phase of the analysis defined the healthy threshold (HT) using the number of average deviations (x) set to 1.5:

$$HT = (\overline{CB} - 1.5 \cdot AD_{CB}) + (\overline{TB} - 1.5 \cdot AD_{TB}) - (\overline{PB} - 1.5 \cdot AD_{PB}) \quad \text{Eq. 5-1}$$

At this stage, the value of 1.5 was determined empirically using a training set of phantom studies as yielding the most accurate estimates of the myocardial perfusion defect size. Subsequently, a much more comprehensive training set and figures of merit for establishing parameter x was performed and the results are presented in the next chapter (Chapter 6).

Reconstructions for all experimental and template data were performed using the in-house software employing the ordered subset expectation maximization (OSEM) algorithm with a CT-based attenuation correction (rescaled to broad beam attenuation coefficients) and depth-dependent resolution recovery. For these reconstructions, 10 subsets and 4 iterations were used with a 5^{th} order Butterworth (0.6 cycles/cm cut-off frequency) post-reconstruction filter.

In the clinical studies, additional reconstructions were performed for the patient and template data using the GE's Evolution for Cardiac^{TM} reconstruction software available on the camera. These reconstructions included its resolution recovery algorithm but without attenuation correction, while using 10 subsets and 4 iterations with a 10^{th} order Butterworth post-reconstruction filter (cut-off frequency of 0.4 cycles/cm).

5.4 Figures of Merit

The performance of the TQPS method was assessed by performing all measurements on the bulls-eye map images. The primary measurement of interest for this study was the extent (EXT) of the myocardial perfusion defect as defined within each investigated image. The EXT was defined as the volume of the perfusion defect expressed as a percentage of the entire myocardium. The mean errors in EXT were calculated for each experiment type (simulations, physical phantoms, and patients) by taking the absolute

difference between the measured EXT value and the true EXT value and subsequently averaging these values for all experiments in each study type. For the patient studies, the EXT values were obtained from the QPS software, which were chosen to be the reference standard in this phase of the analysis.

The EXT is an important metric in SPECT MPI, but it does not provide specific information as to how well the defect was defined in terms of its spatial distribution within the myocardium (i.e. shape and location). The spatial distribution of a perfusion defect is *very* important in a clinical situation as this is the information required to identify specific obstructed coronary arteries; thus, guiding revascularization surgery. For this reason, we introduce a group of "spatial measurements" to provide more insight as to how accurately the perfusion defect was identified by TQPS. Since the true spatial characteristics of the defects were required for these measurements, they could only be performed for the simulation experiments. The spatial measurements can be summarized as follows:

1. Dice Coefficient (DC)

$$DC = \frac{2TP}{FP+2TP+FN} \quad \text{Eq. 5-2}$$

2. Sensitivity (SN)

$$SN = \frac{TP}{TP+FN} \quad \text{Eq. 5-3}$$

3. Specificity (SP)

$$SP = \frac{TN}{TN+FP} \quad \text{Eq. 5-4}$$

4. Positive Predictive Value (PV)

$$PV = \frac{TP}{TP+FP} \quad \text{Eq. 5-5}$$

5. Negative Predictive Value (NV)

$$NV = \frac{TN}{TN+FN} \quad \text{Eq. 5-6}$$

6. Total Performance Score (TS)

$$TS = \frac{DC+SN+SP+PV+NV}{5} \quad \text{Eq. 5-7}$$

where TN, FN, TP, and FP represent the number of pixels considered to be true negative, false negative, true positive and false positive, with regards to the true phantom distribution, respectively. It is important to note here that specificity, sensitivity, positive predictive value, and negative predictive value are all defined on a pixel by pixel basis as opposed to their traditional patient by patient basis; thus providing a much more in-depth assessment. The dice coefficient is a measure representative of the amount of overlap between the estimation and the truth. The total performance score is simply an average of all spatial measurements, and has been added to this study to provide an overall index on how well the defect was spatially defined.

5.5 Statistical Analysis

In this phase of the thesis, all continuous variables were expressed as mean ± standard deviation (SD). Student's *t*-test was used to compare differences in paired continuous data. All tests were two-tailed and a threshold of $P < 0.05$ was considered significant. Bland-Altman plots were used to assess the agreement between two clinical measurement methods.

5.6 Results

5.6.1 Simulations

Overall, segmentations of the left ventricle for all NCAT phantoms produced a mean error of 8.1 ± 2.0% from the true volume, which was similar to results recently published by Soneson et al. *(85)*

In all simulated cases, TQPS was able to correctly identify the presence and location of the perfusion defects. Examples of the template bulls-eye (TB) and corrected bulls-eye (CB_D) maps for the *Ideal* template (T_I) and *SPECT-based* template (T_S) methods using a one of the simulated female data sets (64x64 matrix, EXT = 21%) can be seen in Figure 5-4 along with the respective phantom and true NCAT bulls-eye images.

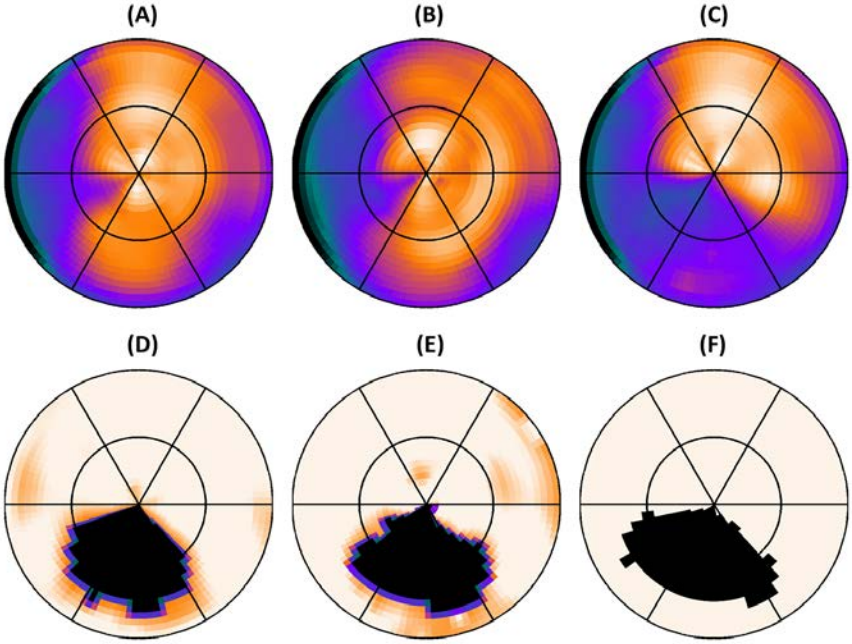

Figure 5-4 Bulls-eye maps for a selected female phantom simulation (EXT=21%) with the 64x64 matrix protocol. Images (A) and (B) are the template bulls-eyes created using T_I and T_S, respectively; image (C) is the phantom bulls-eye; images (D) and (E) are the corrected bulls-eye images created using the T_I and T_S method, respectively; and finally, image (F) is the true distribution with the black pixels representing the true defect.

Qualitatively, it is evident after a comparison between the true distribution (Figure 5-4-F) and the phantom bulls-eye image (Figure 5-4-C) that there is an artifact, appearing as reduced perfusion in the relatively thin septal wall of the myocardium caused by the partial volume effect. In agreement with the theory of TQPS, the template bulls-eye image (using T_I) in Figure 5-4-A also portrays this artifact leading to an effective correction in CB_D (Figure 5-4-D). The same results can be seen for the T_S method (Figure 5-4-B and -E), which is in agreement with our hypothesis that both templates produce equivalent results.

Figure 5-5 shows the circumferential profiles for the same female simulation experiment (64x64 matrix, EXT = 21%) as shown in Figure 5-4, which shows a large perfusion defect

in the inferior wall. The profiles are constructed using a slice within the mid-ventricular region for the template (TB), phantom (PB) and corrected (CB) bulls-eyes and the true distribution obtained using the T_S template. Again, the artifact caused by the partial volume effect is visible in the septal region (partially in the true defect region) for the template and patient profiles, with the corrected image showing a much improved representation of the true distribution.

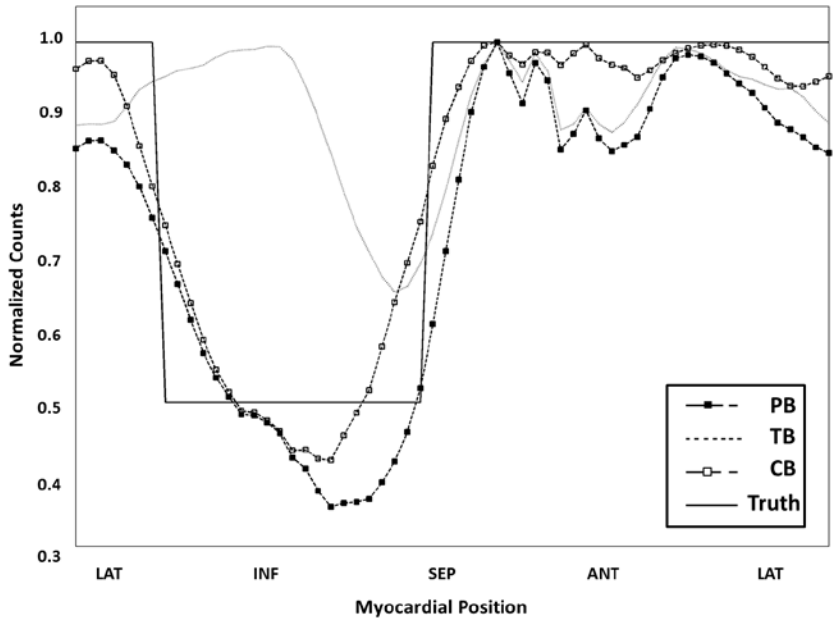

Figure 5-5 Circumferential profiles of slice within the mid-ventricular region for the same female phantom simulation as presented in Figure 5-4 which shows a large perfusion defect in the inferior wall (EXT=21%). The data was acquired using the 64x64 matrix protocol. The T_S template was used with a 64x64 matrix. The horizontal axis labels LAT, INF, SEP, and ANT indicate the lateral, inferior, septal and anterior wall positions along the myocardium sampled in the short axis view, respectively. All profiles are normalized to the maximum value with the selected profile.

Correlation and residual plots are presented in Figure 5-6 for the T_I and T_s template EXT measures using the simulation data with a 64x64 matrix. The correlation coefficients were 0.996 for T_I and 0.992 for T_S (*P* = not significant). The regression equations for T_I

and T_S as functions of the true EXT were $y = 1.08x + 0.40\%$ (SE=1.8%) and $y = 0.90x - 0.27\%$ (SE=2.2%), respectively. Similarly, Figure 5-6-C and Figure 5-6-D display the correlations and residuals for the 128x128 matrix studies, with the correlation coefficients being 0.998 and 0.996 for T_I and T_S, respectively (*P* = not significant). The regression equations were $y = 0.98x + 0.43\%$ (SE=1.3%) for T_I and $y = 0.99x + 1.28\%$ (SE=1.9%) for T_S. Table 5-2 displays the mean EXT errors for each simulation protocol. No significant differences were found in these measurements between the T_I and T_S methods.

Table 5-2 Mean absolute error in perfusion defect extent measurements for all simulation and phantom experiments using the *Ideal* (T_I) and *SPECT-based* (T_S) template methods.

Study (matrix)	Mean EXT Error (%)		*P* value
	T_I	T_S	
Simulations (64x64)	1.96 ± 2.10	2.68 ± 2.43	*P* = NS
Simulations (128x128)	1.22 ± 1.31	1.53 ± 1.27	*P* = NS
Physical Phantoms (128x128)	0.46 ± 0.56	0.85 ± 0.53	*P* = NS

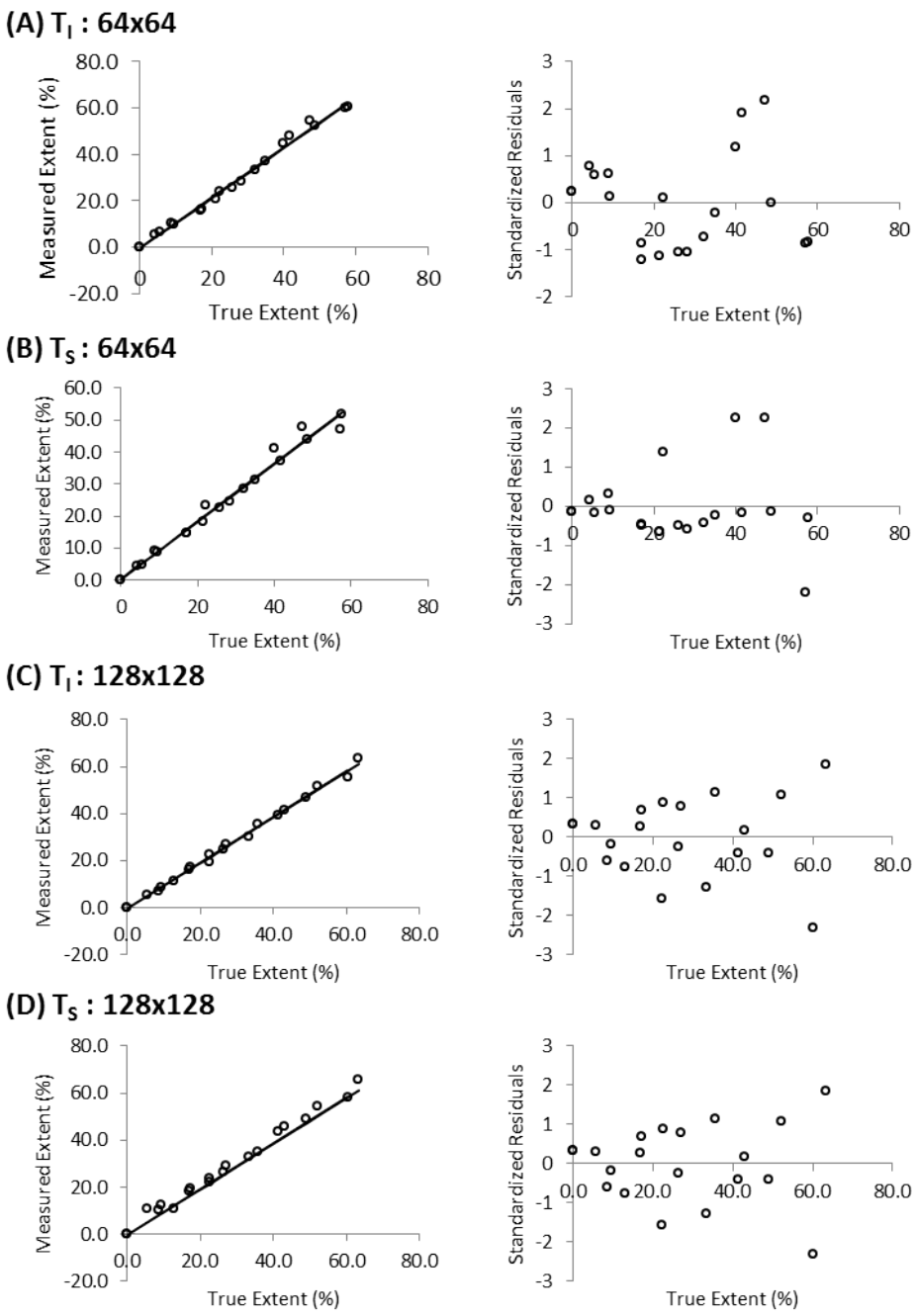

Figure 5-6 Measured extent (%) vs. true extent (%) (*n* = 20) for the simulation studies: 64x64 (rows A and B) and 128x128 (rows C and D). Vertical distance between individual observations and fitted regression line is shown on regression residual plot in units of standard deviations (standardized residuals). Plots A and C are linear regression and regression residual plots for the T_I measure vs. the truth. Plots B and D are linear regression and regression residual plots for the T_S measure vs. the truth.

Additionally, Bland-Altman plots were included to assess the agreement between the *Ideal* and *SPECT-based* template methods (Figure 5-7). In both cases, a slight bias was observed. For example, the bias observed between the two methods when using the 64x64 matrix was -3.9 ± 0.82%. For both matrices, the bias introduced between the two methods was minimal with regards to clinically significant perfusion defect extent.

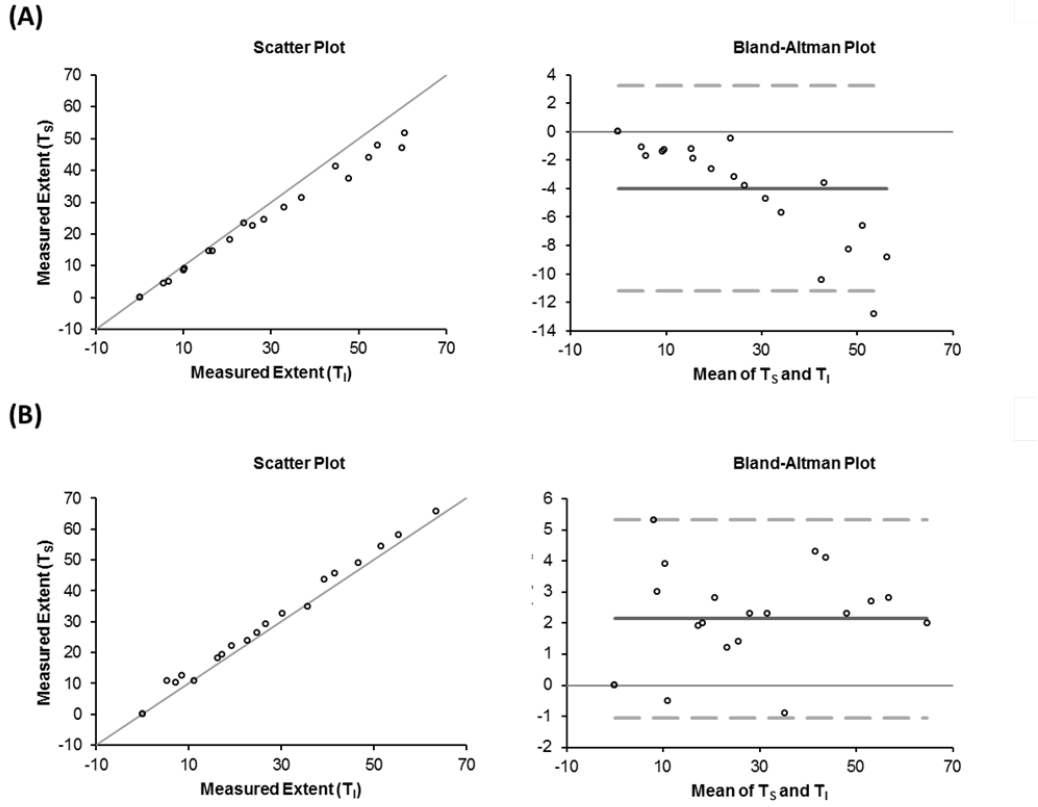

Figure 5-7 Scatter and Bland-Altman plots for the agreement between the T_I and T_S methods for the (A) 64x64 and (B) 128x128 matrices. Lines of identity are shown by the light grey solid line in the scatter plots and the bias (thick solid line) and 95% limits of agreement (dashed lines) are shown in the Bland-Altman plots.

The results regarding the spatial quality of the measured perfusion defects in the 64x64 and 128x128 simulation studies can be seen in Figure 5-8-A and Figure 5-8-B, respectively. In all cases, no significant differences were found between the spatial

measurements for T_I and T_S, with the exception of the sensitivity measure for the 64x64 protocol (T_I: SN = 0.88 ± 0.04, T_S: SN = 0.74 ± 0.06, P<0.05).

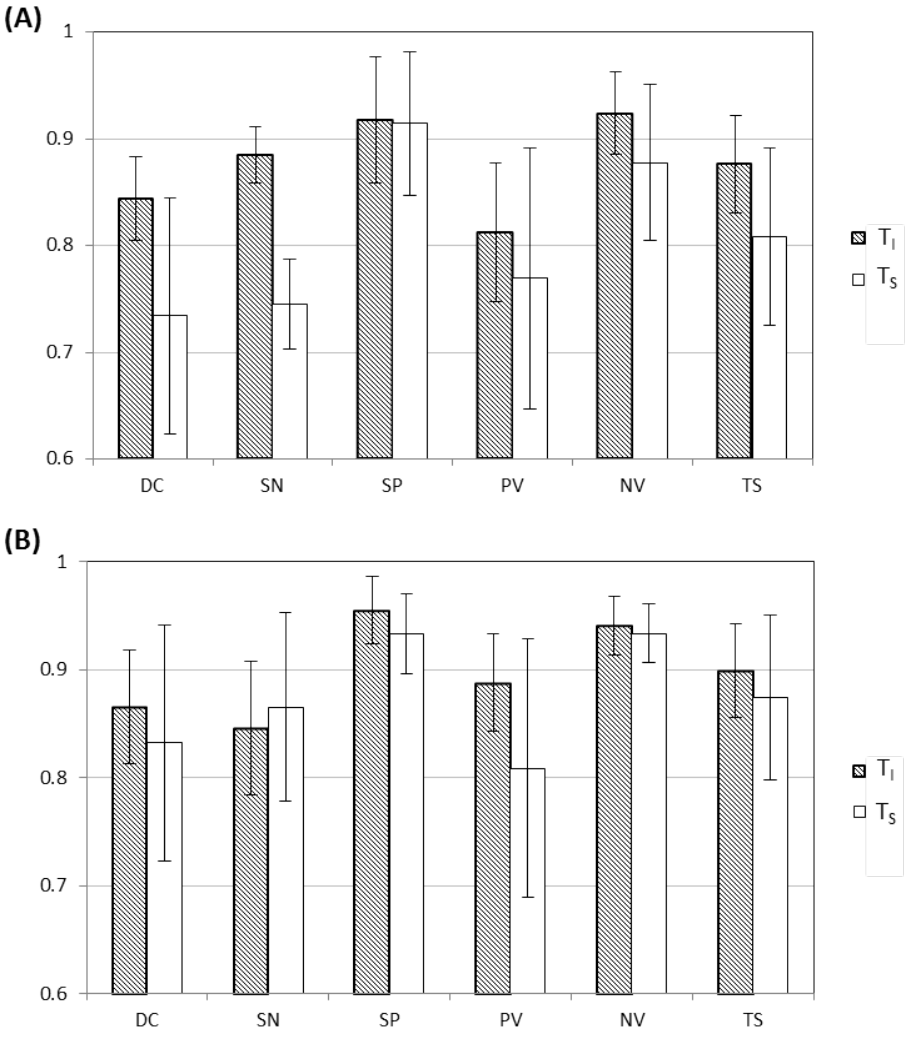

Figure 5-8 The mean value for each of spatial measurements made for the simulation studies: (A) 64x64 matrix and (B) 128x128 matrix. The results for the T_I and T_S template methods are shown as the dashed and solid bars, respectively. The error bars represent 95% confidence intervals.

5.6.2 Physical Phantoms

As in the case of the simulation studies, no significant differences were found in the mean EXT errors for the physical phantom experiment between the two templates, T_I and T_S (see Table 5-2). Images for one of the phantom experiments with a defect in the lateral wall (EXT=6%) are shown in Figure 5-9.

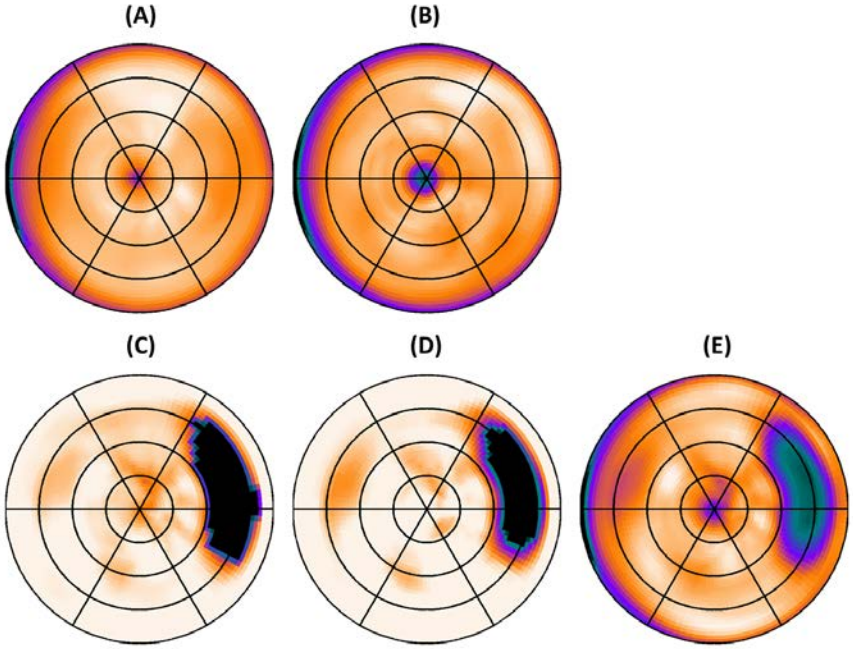

Figure 5-9 Bulls-eye maps for a selected physical phantom experiment (EXT=6%). Images A and B are the TB images created using T_I and T_S, respectively; images C and D are the CB_D images created using the T_I and T_S method, respectively; and finally, image E is the phantom image PB.

5.6.3 Patients

Out of the fourteen patient studies, six studies were identified by the QPS software as having a perfusion defect extent of less than 4% (considered clinically normal perfusion) *(97)*. The template method was able to correctly identify 6/6 and 4/6 of these studies using the in-house (with AC) and GE (without AC) reconstruction software, respectively.

Correlation and residual plots of the measured extent versus QPS extent (obtained via NC normal patient databases) are presented in Figure 5-10 when using the in-house (Figure 5-10-A) and GE reconstruction software (Figure 5-10-B). The correlation coefficients were 0.981 and 0.989 for the in-house and GE software, respectively (*P* = not significant). The regression equations for the in-house and GE software as functions of the QPS extent were $y = 0.91x - 0.45\%$ (SE=3.1%) and $y = 0.99x - 0.85\%$ (SE=2.6%), respectively.

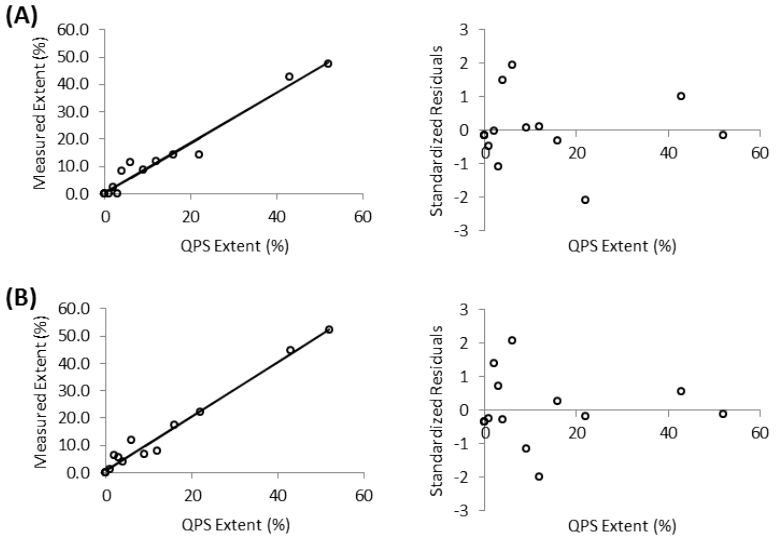

Figure 5-10 Measured extent (%) vs. QPS extent (%) (*n* = 14) for the patient studies. (A) Linear regression and regression residual plots for the in-house reconstruction EXT measures vs. QPS. (B) Linear regression and regression residual plots for the GE reconstruction EXT measures vs. QPS.

Finally, the mean EXT error results (as compared to the QPS measurements) for the patient studies were 2.20 ± 2.64% and 1.98 ± 2.66% (*P* = not significant) for the in-house and GE reconstructions, respectively. An example patient study (QPS extent = 43%) with images reconstructed using the GE reconstruction software is shown in Figure 5-11. Note that the QPS analysis was performed using the reorientation software provided on the camera workstation.

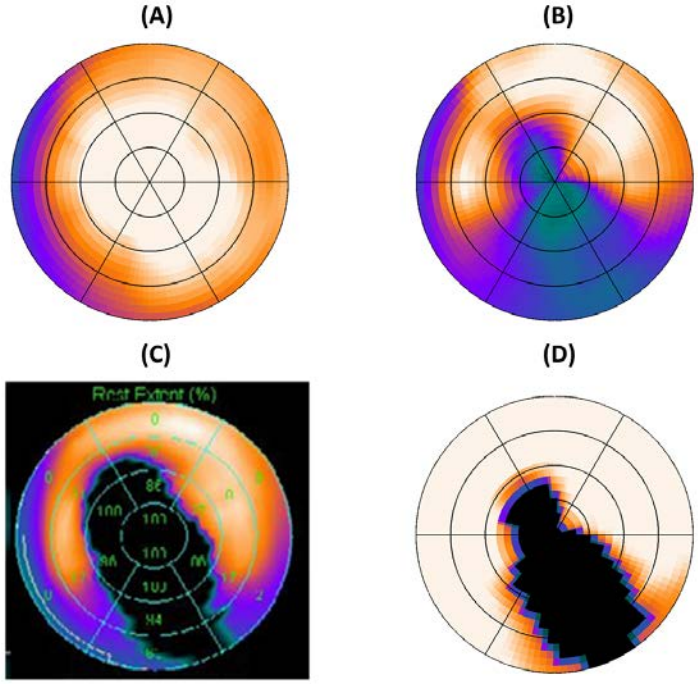

Figure 5-11 Bulls-eye maps for a selected patient study (EXT=43%) using the T_S template with the GE reconstruction software. In the top row: (A) and (B) represent TB and PB, respectively; in the bottom row: (C) and (D) are the QPS results and CB_D image, respectively.

5.7 Discussion

In this evaluation phase of the TQPS method, it was shown that the method is capable of providing an accurate assessment of myocardial perfusion, while enabling a correction for reconstruction-related artifacts.

In order to assess the performance of the *SPECT-based* template relative to an *Ideal* CT-based approach; the measurements obtained from the T_S (*SPECT-based*) and T_I (*Ideal*) templates were compared. Both methods showed excellent agreement with the true EXT values for all simulation and physical phantom experiments. The correlation coefficient values for T_I and T_S with the true EXT were greater than 0.98 in all cases with no significant differences found for any of the investigated experiments. The mean EXT errors for T_I and T_S were also in good agreement in all cases. From these experiments, it can be seen that a *SPECT-based* template can perform just as well as a CT-based (*Ideal*) template with regards to defect extent-type measurements.

The projection step of TQPS constitutes a second aspect of the approach which deserved attention. Recall that when using T_I in the simulation studies, the only difference between obtaining the final template and phantom bulls-eye images was in the projection step, thus the performance of APDI could be investigated using these experiments (refer to Figure 5-3). As mentioned, the correlation coefficient values for all T_I studies were very high (≥0.98) demonstrating excellent agreement between EXT measurements and the truth. Furthermore, from Figure 5-6 it can be seen that all measurements regarding the spatial quality of the perfusion defects defined by the T_I method in the simulation studies were high (≥0.81 for 64x64 matrix and ≥0.85 for the 128x128 matrix). Although these values were high considering that they were defined on a pixel by pixel basis, they were not equal to 1.0, suggesting that APDI performed very well in modeling the acquisition, but not perfectly. A potential cause for this effect

is image noise, which was the only difference between the experimental projections and template projections generated by SimSET (with noise) and APDI (analytical, thus noiseless), respectively. While Poisson noise could be added to the template projections generated by the APDI code, it would unnecessarily alter the distribution of the photons and ultimately reduce the accuracy of the analytically calculated distribution. Furthermore, it has been suggested that the inclusion of Poisson noise in the template projections for the purposes of general SPECT partial volume correction can be detrimental to the quantitative accuracy of the final image *(143)*. For these reasons, noise was not added to the template projections.

The performance of the TQPS method with respect to artifact correction is best highlighted in Figure 5-4. For instance, Figure 5-4-C exemplifies the artifact in the septal wall caused by a severe reduction in counts in this region; however this artifact is visibly corrected in CB_D (compare Figure 5-4-D and Figure 5-4-E). Although commercial methodologies compensate for the presence of common artifacts by generating multiple databases corresponding to particular groups of patients (e.g. breast attenuation artifact for female databases) and by using myocardial segment modeled normal limits, they are unable to unequivocally differentiate between perfusion defects and image artifacts in all cases *(181)*. The main artifact presented in these simulation studies was the decrease in contrast exhibited in the basal aspect of the NCAT septal wall of the myocardium. This loss of contrast was caused by inadequate sampling of the relatively thin basal aspect of the septal wall in combination with a decrease in resolution recovery compared to the rest of the myocardium (i.e. the partial volume effect). The proposed correction method is not limited to this artifact, as it can also correct for other common partial volume effects in SPECT MPI such as asymmetrical left ventricle hypertrophy and apical thinning. Moreover, this method could correct for image processing artifacts, such as non-optimal iteration number effects created by the convergence behavior of maximum likelihood based algorithms *(141, 148, 182)*.

The robustness of the template method was demonstrated in the patient study when analyzing the patient data reconstructed with our in-house algorithm and with GE`s clinical reconstruction software. Despite the difference in the reconstruction algorithms (attenuation corrected versus no attenuation correction), no significant differences were observed between the correlation coefficients from the in-house and GE template methods and the EXT results from QPS.

Although the truth was unknown for the patient studies, the comparative analysis of the TQPS method relative to the most widely used commercial software package (QPS) provided a preliminary evaluation for the method in the clinical realm. The EXT measurements resulting from TQPS correlated very well with the QPS results, with reported correlation coefficients of 0.981 and 0.989 for the in-house and GE software reconstructions, respectively. Moreover, the mean EXT errors (relative to QPS) for the in-house and GE software were 2.20 ± 2.64% and 1.98 ± 2.66% (*P* = not significant), respectively, suggesting very good agreement in both cases. However, when looking at individual cases, the EXT measured by TQPS can be both substantially over- and underestimated relative to QPS. For instance, 2 of the 14 patient studies the TQPS EXT measurements were over- or underestimated by >5% using the in-house software with the maximum error being 7.6%. A potential cause for these differences could be due to the fact that the in-house reconstruction algorithm included attenuation correction, as where the results obtained via QPS utilized NC reconstructions. Despite the strong overall correlation in perfusion defect extent measurements between the TQPS and QPS software within this patient group, it is important to note that on a patient by patient basis, there were substantial differences between the two methods.

At this point of the evaluation of TQPS, there were a number of issues that still needed to be addressed. First, the computation time for the projection step using APDI was not

yet within clinical acceptability (on the order of an hour for 64x64 matrix and 60 projections); thus, more clinically acceptable projection methods needed to be investigated, which was the main objective of the optimization phase of this theses (Chapter 6). Secondly, a more thorough clinical validation of the template methodology still needed to be addressed, which was the theme of the third and final phase of the analysis.

5.8 Conclusions

The template-based method for semi-quantitative SPECT MPI offers an approach that is independent of normal databases and provides semi-quantitative patient-specific measurements of the myocardial perfusion defects. The ability to provide artifact corrected images enables the differentiation between healthy and perfusion defect regions within the myocardium, thereby offering an accurate definition of the defect region. The preliminary results obtained from these aforementioned studies were very encouraging.

Despite the encouraging results presented in this phase of the analysis, the TQPS method required long processing times. One of the goals of this thesis was to develop pragmatic template-based method for semi-quantitative SPECT MPI; thus, the next chapter (Chapter 6) provides a detailed study aimed at optimizing the TQPS method in terms of computation time and accuracy.

6 Method Optimization

The second phase of the analysis involved the optimization of TQPS in terms of computation time and diagnostic accuracy. In particular, the extensive processing times of the template projection step reported in the previous chapter (Chapter 5) could be considered the major issue preventing clinical use of the TQPS method. Therefore, different approximations within the template projection step of TQPS were proposed in this chapter and their performances were investigated. In addition, the previous study (Chapter 5) was limited to the use of a simple one compartment template (T_{HRT}) where only the heart was considered. In this phase of the project, the influence of extra-cardiac uptake was investigated by including the three compartment template (T_{HRTBKG}) as described in Section 4.2.3. In summary, the objective of this phase of the thesis was to optimize the TQPS method in the two major areas of its functionality: 1) template construction and 2) template projection. The work performed in this chapter was presented at the annual meeting for the Society of Nuclear Medicine in 2011 *(183)* and published as an original article in Medical Physics *(184)*.

The following chapter describes the optimization phase of TQPS, which is organized into seven sections. First, a Methodology section describes the studies performed in this chapter, including the objective and justification of the experimental design. The Experiments section lists the experiments performed in this phase of the thesis including the simulations and patient studies. The Figures of Merit and Statistical Analysis sections describe the measurements and subsequent statistics employed in this study, respectively. Finally, the chapter concludes with the Results, Discussion and Conclusion

sections, which highlight the major findings and their respective significance for the optimization of the TQPS method.

6.1 Methodology

As alluded to already, the following studies address important issues regarding the optimization of the TQPS method. With respect to template construction, a comparison is provided between the performances of TQPS when using the template with activity in the heart only (T_{HRT}) relative to that when using the template modeling activity in the heart, lungs and background (T_{HRTBKG}). The details of the construction for these two templates are described in Section 4.2.3. With regards to template projection, the performance of TQPS when projecting the template modeled as if it would emit primary photons only (T_P) was investigated relative to projecting with primary and scattered photons (T_{PS}). In all, these aforementioned variations can be combined and summarized as four template generation methods (Table 6-1), which were investigated in terms of relative processing time and diagnostic performance.

Table 6-1. List of each TQPS template generation method analyzed in the optimization phase of this thesis and their referenced names herein. Methods are listed in increasing complexity from top to bottom.

Template projection method	Template construction method	Template generation method
Primary (T_P)	Heart (T_{HRT})	$T_{P\text{-}HRT}$
Primary + Scatter (T_{PS})	Heart (T_{HRT})	$T_{PS\text{-}HRT}$
Primary (T_P)	Heart + Background (T_{HRTBKG})	$T_{P\text{-}HRTBKG}$
Primary + Scatter (T_{PS})	Heart + Background (T_{HRTBKG})	$T_{PS\text{-}HRTBKG}$

As in the evaluation phase, the analysis presented in this chapter incorporated the idea of the *Ideal* template, where the template was derived from the true activity distribution as defined by the NCAT phantoms in the simulation studies. Again, the *Ideal* template could not be employed for the patient studies as the true activity distribution in these cases is unknown. The four template generation methods presented in Table 6-1 were investigated for both the *Ideal* and *SPECT-based* templates. Please note that in this chapter, the templates shown above are referred to as *SPECT-based* or *Ideal* – and not T_S and T_I as in the previous chapter - in the interest of minimizing abbreviations in this chapter.

Prior to addressing the various template generation methods, this study began with a more in-depth analysis regarding the optimization of the healthy threshold, in terms of the number of average deviations (x), as described in Eq. 4-5. In this case, careful attention was paid not only to the sample size of the training set used to establish the optimal number of average deviations, but also on the realistic nature of the phantoms by including respiratory and cardiac motion.

6.2 Experiments

6.2.1 Simulations

Two sets of phantoms were generated for this study. The first was a training set, Group A (n=48), which was used to establish the optimal number of average deviations (x) for the healthy threshold (Eq. 4-5). The second set, Group B (n=48), was used for the analysis of the various template generation methods, using the thresholds established in the Group A study. In all simulations, the NCAT phantom *(178)* was used to generate a

number of different phantoms and variations of activity distributions within each phantom. The details of the phantoms are shown in Table 6-2.

All phantoms were simulated with a normal breathing cycle (5 seconds per respiratory cycle), and a normal beating heart (1 second per cardiac cycle). With regards to activity distribution, a clinically representative 5:1 heart to soft tissue activity ratio was used, with defect severity set to 50% of the normally perfused myocardium. In select cases (as indicated in Table 6-2), liver uptake was modeled with the liver positioned adjacent to the heart (within 2 pixels or roughly 1.3 cm from the inferior aspect of the heart) using a 1:1 liver to healthy heart activity ratio, in order to represent clinically challenging cases. Four different defect sizes (9%, 21%, 32%, and 47% of the total myocardial volume) were generated for each defect location (anterior, inferior, lateral, and septal walls). Each phantom contained only a single defect.

For all phantoms, acquisitions were simulated using the Monte Carlo simulation code SimSET *(179)*. The simulated number of counts corresponded to the statistics found in clinical stress Sestamibi Tc-99m SPECT scans following a 740 MBq injection. The SPECT camera was modeled after the GE Hawkeye SPECT system with a LEHR collimator. Standard cardiac protocol was used: the projection data were acquired into a 64x64 matrix at a 3^0 angular interval over an 180^0 angular arc to yield a total of 60 projections. The energy window was set to 126-154keV, and pixel sizes were 6.80mm.

Table 6-2 A summary of the two NCAT phantom groups included for the threshold establishment and TQPS optimization studies. Defect extent is expressed as a percentage of the total left ventricle myocardium.

Phantom group	Phantom number	Phantom	Defect location	Defect extent	Adjacent liver uptake?
A					
	1-16	Average Male	Anterior	9%, 21%, 32%, 47%	No
			Inferior	9%, 21%, 32%, 47%	No
			Lateral	9%, 21%, 32%, 47%	No
			Septal	9%, 21%, 32%, 47%	No
	17-32	Average Male	Anterior	9%, 21%, 32%, 47%	Yes
			Inferior	9%, 21%, 32%, 47%	Yes
			Lateral	9%, 21%, 32%, 47%	Yes
			Septal	9%, 21%, 32%, 47%	Yes
	33-48	Obese Female	Anterior	9%, 21%, 32%, 47%	No
			Inferior	9%, 21%, 32%, 47%	No
			Lateral	9%, 21%, 32%, 47%	No
			Septal	9%, 21%, 32%, 47%	No
B					
	49-64	Average Female	Anterior	9%, 21%, 32%, 47%	No
			Inferior	9%, 21%, 32%, 47%	No
			Lateral	9%, 21%, 32%, 47%	No
			Septal	9%, 21%, 32%, 47%	No
	65-80	Average Female	Anterior	9%, 21%, 32%, 47%	Yes
			Inferior	9%, 21%, 32%, 47%	Yes
			Lateral	9%, 21%, 32%, 47%	Yes
			Septal	9%, 21%, 32%, 47%	Yes

Phantom group	Phantom number	Phantom	Defect location	Defect extent	Adjacent liver uptake?
	81-96	Obese Male	Anterior	9%, 21%, 32%, 47%	No
			Inferior	9%, 21%, 32%, 47%	No
			Lateral	9%, 21%, 32%, 47%	No
			Septal	9%, 21%, 32%, 47%	No

6.2.2 Patients

In addition to the simulation studies, the TQPS optimization analysis was also performed on a patient population. Twenty-one patients were retrospectively and randomly selected from routine stress SPECT MPI studies performed in the nuclear medicine department at VGH. The use of fully anonymized patient data for software development projects was approved by the Ethics Board of the University of British Columbia. Only studies without visually detectable attenuation map to SPECT data misregistration were subsequently processed and analyzed. The stress studies were acquired on the GE Infinia Hawkeye SPECT-CT camera using clinical cardiac protocol, including: Tc-99m Sestamibi (1110 MBq injected intravenously) with a LEHR collimator, 180^0 arc, 60 projections (20 seconds per projection), 64x64 matrix and a 6.80mm pixel size. In total, 13 male and 8 female patients were included in this study with an average age ± SD of 71 ± 7 y. Of the 21 studies acquired, 3 were healthy (< 4% perfusion defect extent) as determined by the commercial quantitative software onboard the camera. In the remaining 18 datasets, perfusion defect extents ranged from 0% to 52% of the total myocardium with a mean extent of 20 ± 15%.

6.3 Figures of Merit

As in Chapter 5, a group of spatial measurements was included in the analysis to assess the quality of the perfusion defect (shape and location) defined by each method:

1. Sensitivity (SP)

$$SP = \frac{TP}{TP+FN} \quad \text{Eq. 6-1}$$

2. Specificity (SN)

$$SN = \frac{TN}{TN+FP} \quad \text{Eq. 6-2}$$

3. Accuracy (AC)

$$AC = \frac{TP+TN}{TP+FP+TN+FN} \quad \text{Eq. 6-3}$$

where TN, FN, TP, and FP represent the total number of pixels considered to be true negative, false negative, true positive and false positive, respectively, as defined by the gold standard for the analysis. For the analysis of the simulation data, the true NCAT phantom distribution was considered to be the gold standard; whereas in the patient studies, the gold standard was considered to be the $T_{PS\text{-}HRTBKG}$ (most comprehensive TQPS template generation method), since the truth was unknown in clinical studies.

For the patient and simulation studies, the perfusion defect extent (EXT) was included in the analysis. The EXT was again defined as the volume of the defect region (perfusion less than the healthy threshold) expressed as a percentage of the total left ventricle myocardial volume. For the simulation studies, where the true perfusion defect extent was known, the mean extent difference (EXT_{md}) was calculated for each template generation method as:

$$EXT_{md} = \frac{1}{N}\sum_{i=1}^{N}(EXT_i^{measured} - EXT_i^{truth}) \quad \text{Eq. 6-4}$$

where $EX_i^{measured}$ and EX_i^{truth} are the measured and true perfusion defect extents for phantom i, respectively; and N is the total number of phantom studies included in the measurement.

6.4 Determination of the Optimal Threshold Value (x)

In order to quantify the myocardial perfusion defects in each study, it was necessary to define the defect within the corrected bulls-eye image (i.e. differentiate between normal and abnormal perfusion). As alluded to in Chapter 4 (Section 4.6), TQPS implements a healthy heart threshold based on a variable x, which defines the number of average deviations to be subtracted from the each of the average values found within TB, PB and CB (recall Eq. 4-5). To determine the optimal threshold value (x) for each template, receiver operating characteristic (ROC) analysis was performed using code developed with MATLAB 7.8.0 (R2009a). ROC curves were created by varying the number of user defined average deviations x as in Eq. 4-5, from 0 to 5 in intervals of 0.25 (a total of 21 operating points). Area under the curve (AUC) measurements were reported with standard error (SE) and 95% confidence intervals. The optimal operating point for each method was chosen as the minimum distance from the (0, 1) point in the ROC curve:

$$Optimal\ Operating\ Point = \min[\sqrt{(1 - SN_x)^2 + (1 - SP_x)^2}] \quad \text{Eq. 6-5}$$

where SN_x and SP_x are the sensitivities and specificities at a given value of parameter x, respectively.

6.5 Statistical Analysis

All continuous variables were compared using a two-tailed Student's t-test with a threshold of $P < 0.05$ considered significant. Mean EXT measurements were reported as mean ± 95% confidence intervals (C.I.).

6.6 Results

6.6.1 Threshold Establishment

For the ROC analysis, Figure 6-1 highlights the results for the four TQPS template generation methods analyzed in this study using the *Ideal* template (Figure 6-1-A) and *SPECT-based* template (Figure 6-1-B). Each data point in these plots represents the mean sensitivity and (1-specificity) over the entire Group A phantom population at a given value of parameter x, which defines the number of average deviations used in Eq. 4-5. The AUCs, standard errors and 95% confidence intervals measured for each investigated method are reported in Table 6-3.

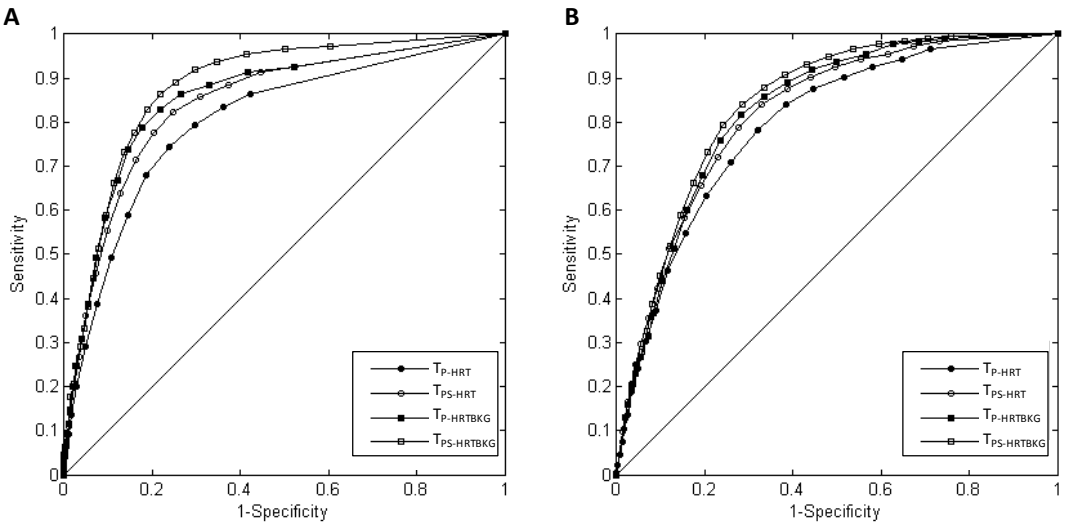

Figure 6-1 ROC curves for the detection of abnormal perfusion in the Group A (n=48) simulation study for the four template generation methods: $T_{P\text{-}HRT}$, $T_{PS\text{-}HRT}$, $T_{P\text{-}BKGHRT}$, $T_{PS\text{-}BKGHRT}$. Plots A and B show the results comparing sets of methods using the *Ideal* and *SPECT-based* templates, respectively.

Table 6-3 AUC results from the ROC analysis using the Group A (n=48) simulation study and each of the four template generation methods for the *Ideal* and *SPECT-based* templates.

Template	Template generation method	AUC	SE	95% C.I.
Ideal				
	$T_{P\text{-}HRT}$	0.80*	0.02	0.76-0.85
	$T_{PS\text{-}HRT}$	0.84	0.02	0.80-0.88
	$T_{P\text{-}HRTBKG}$	0.86	0.02	0.82-0.89
	$T_{PS\text{-}HRTBKG}$	0.88*	0.02	0.85-0.91
SPECT-based				
	$T_{P\text{-}HRT}$	0.80	0.02	0.75-0.82
	$T_{PS\text{-}HRT}$	0.82	0.02	0.78-0.86
	$T_{P\text{-}HRTBKG}$	0.83	0.02	0.79-0.87
	$T_{PS\text{-}HRTBKG}$	0.84	0.02	0.80-0.88

*significant differences found $P<0.05$.

There were no significant differences in AUC's across all methods, with the exception of $T_{P\text{-}HRT}$ and $T_{PS\text{-}HRTBKG}$ using the *Ideal* templates (0.80 ± 0.02 versus 0.88 ± 0.02, P<0.05). In general, all template generation methods analyzed in this part of the study exhibited AUC measurements ranging from 0.80 to 0.88, suggesting a good test in each case.

The optimal operating points (in terms of the number of average deviations x) determined by the ROC analysis for each template generation method are shown in Table 6-4 along with the corresponding sensitivity, specificity, and accuracy measured at those particular points.

Table 6-4 Optimal number of average deviations (x) to be set in the healthy threshold as determined by the Group A (n=48) ROC analysis. Sensitivities, specificities and accuracies at each respective operating point are presented.

Template	Template generation method	Optimal no. average deviations (x)	Sensitivity (%)	Specificity (%)	Accuracy (%)
Ideal					
	$T_{P\text{-}HRT}$	0.75	82	75	79
	$T_{PS\text{-}HRT}$	1.00	78	80	82
	$T_{P\text{-}HRTBKG}$	1.25	79	82	84
	$T_{PS\text{-}HRTBKG}$	1.75	83	81	84
SPECT-based					
	$T_{P\text{-}HRT}$	1.50	78	68	72
	$T_{PS\text{-}HRT}$	2.00	79	72	75
	$T_{P\text{-}HRTBKG}$	2.25	76	76	77
	$T_{PS\text{-}HRTBKG}$	2.50	79	76	78

In all cases, the $T_{PS\text{-}HRTBKG}$ method exhibited the highest sensitivity, specificity and accuracy for each template method, *Ideal* and *SPECT-based*, with the exception of $T_{P\text{-}HRTBKG}$ having a slightly higher specificity than $T_{PS\text{-}HRTBKG}$ for the *Ideal* template (82% versus 81%, respectively).

6.6.2 TQPS Template Generation Analysis

Figure 6-2 illustrates the simulation study results for the Group B phantom population using the optimal operating points determined from Group A. For the *Ideal* template methods, a significant difference was found between $T_{P\text{-}HRT}$ and $T_{PS\text{-}HRTBKG}$ in sensitivity (83 ± 4% vs. 88 ± 3%, P = 0.0472). Similarly, $T_{P\text{-}HRT}$ and $T_{PS\text{-}HRTBKG}$ were found to have a significant difference in specificity when using the *SPECT-based* template (77 ± 3% vs. 82 ± 3%, P = 0.0284). Figure 6-3 highlights the differences between the template generation methods and the truth for a selected female phantom with an adjacent liver and a perfusion defect in the anterior wall.

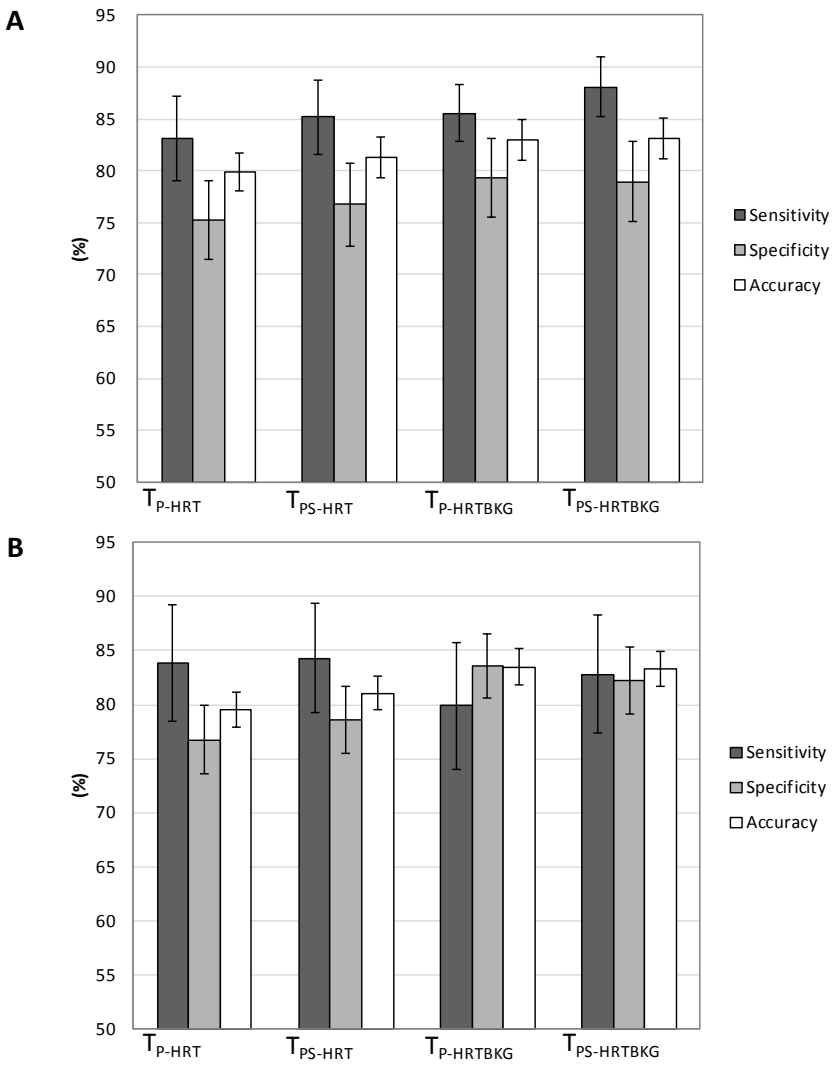

Figure 6-2 Mean sensitivity, specificity and accuracy results for the Group B phantom population (n=48) using the *Ideal* and *SPECT-based* templates, shown in A and B, respectively. Each template generation method is indicated on the horizontal axis. Error bars represent 95% confidence intervals.

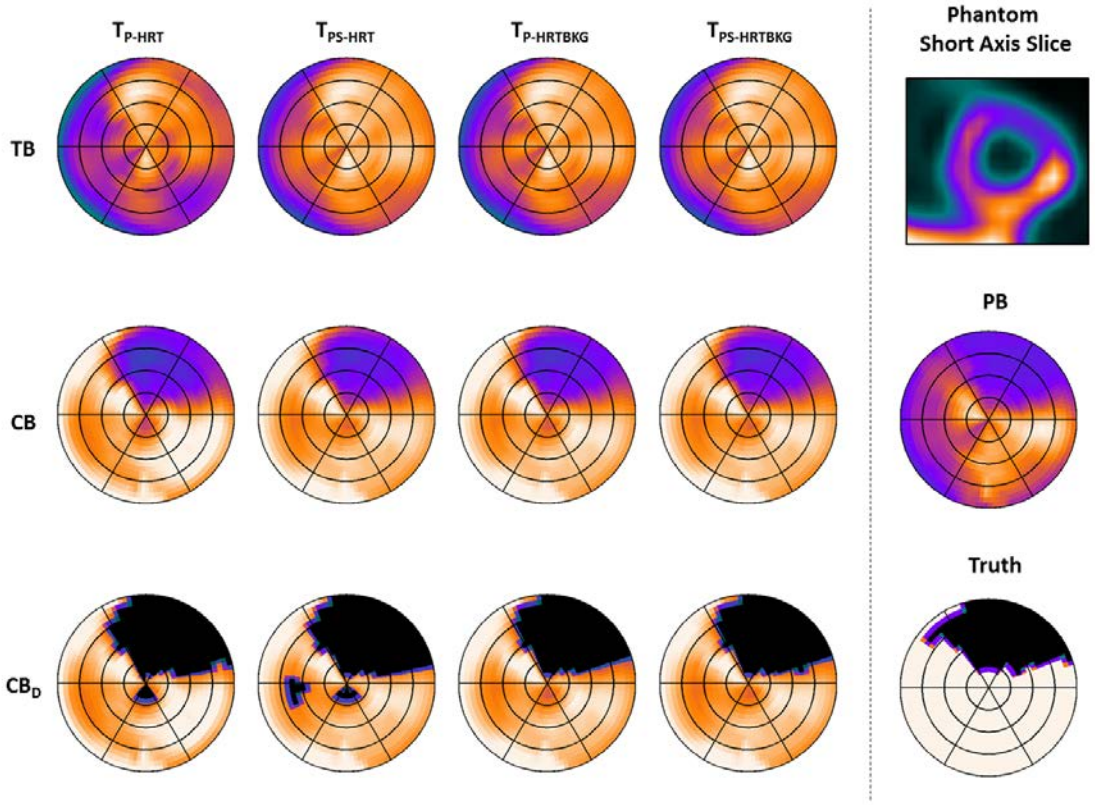

Figure 6-3 Images generated for an example phantom case (female, adjacent liver, 21% perfusion defect extent in the anterior wall). The first 4 columns, from left to right, represent images generated from the $T_{P\text{-}HRT}$, $T_{PS\text{-}HRT}$, $T_{P\text{-}HRTBKG}$, and $T_{PS\text{-}HRTBKG}$ templates using the *SPECT-based* method. The rows from top to bottom (for the first 4 columns left of the vertical line) show the images TB, CB and CB_D. The black pixels in the bottom row (CB_D) represent pixels defined as abnormal perfusion by HT. The right most column shows: a mid-ventricular short axis slice from the patient image (top), the patient bulls-eye image (middle), and the true NCAT generated bulls-eye distribution with the black pixels representing abnormal perfusion (bottom).

For the Group B phantom population, the mean extent differences (EXT_{md}) were calculated as a global measure of how well the perfusion defects were defined. For $T_{P\text{-}HRT}$, $T_{PS\text{-}HRT}$, $T_{P\text{-}HRTBKG}$ and $T_{PS\text{-}HRTBKG}$, the EXT_{md} measurements using the *SPECT-based* template were 9.4 ± 3.2%, 8.3 ± 3.1%, 3.6 ± 3.3%, and 5.4 ± 3.3%, respectively. No

significant differences were recorded between any of the template generation methods using this metric. Similar trends were observed for the *Ideal* template methods.

As in the case of the simulation studies, the sensitivity, specificity and accuracy of the perfusion defects defined by each template generation method were measured for the patient study (using the optimal operating points determined for the *SPECT-based* methods). In this case, since the truth was unknown, the results were compared to the most complex TQPS method, $T_{PS\text{-}HRTBKG}$ (considered to be the "gold standard" in this analysis). Figure 6-4 shows the results from this study. The sensitivities, specificities and accuracies for the investigated methods ranged from 69-97%, 97-98%, and 89-98%, respectively, with $T_{P\text{-}HRTBKG}$ exhibiting the best results in each category. Both $T_{P\text{-}HRT}$ and $T_{PS\text{-}HRT}$ exhibited significant reductions in sensitivity and accuracy relative to $T_{P\text{-}HRTBKG}$ ($P < 0.01$ in all cases).

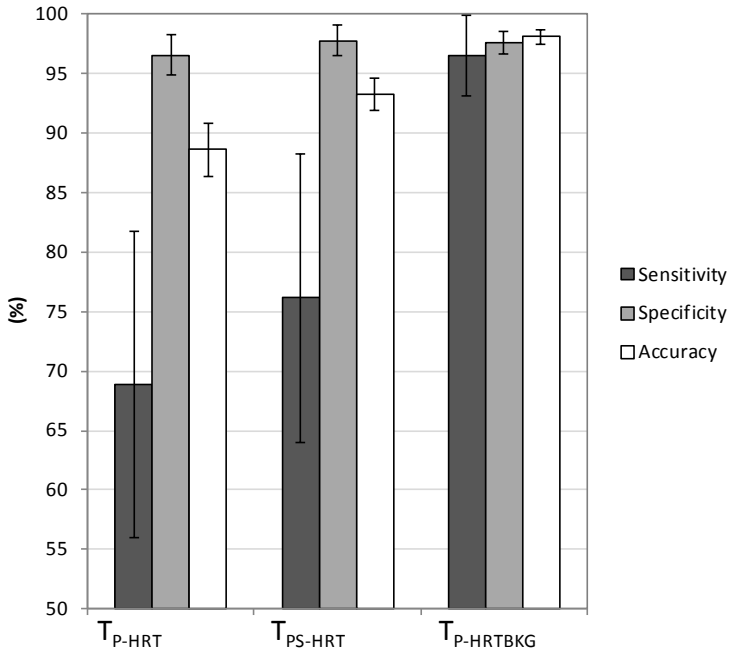

Figure 6-4 Mean sensitivity, specificity and accuracy results for the patient population comparing each template generation method to the most complex method, $T_{PS\text{-}HRTBKG}$. Error bars represent 95% confidence intervals.

Figure 6-5 presents the linear regression and regression residual plots for the EXT measures performed for each template generation method versus the most complex method, $T_{PS\text{-}HRTBKG}$. The regression equations for the $T_{P\text{-}HRT}$, $T_{PS\text{-}HRT}$ and $T_{P\text{-}HRTBKG}$ EXT as functions of the $T_{PS\text{-}HRTBKG}$ EXT were $y = 0.92x + 9.23\%$ (SE = 6.4%), $y = 0.96x + 4.75\%$ (SE = 4.3%), and $y = 1.00x - 0.71\%$ (SE = 1.6%), respectively. All three comparisons demonstrated very high correlation, with Pearson correlation coefficients of 0.96, 0.98 and 1.00, respectively. Figure 6-6 displays bulls-eye images generated by each method for a selected patient.

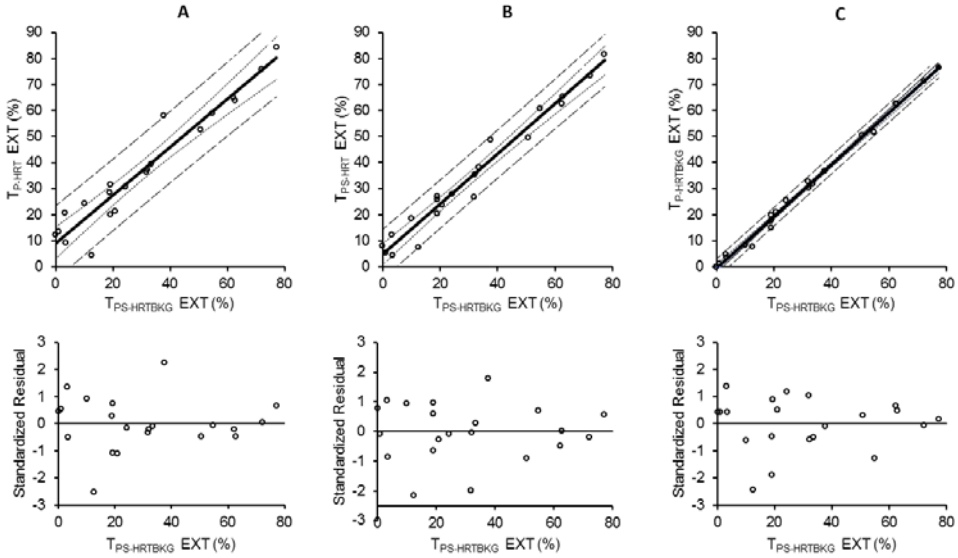

Figure 6-5 Linear regression plots (top row) and standardized residual plots (bottom row) for the patient study comparing EXT (%) measures using each investigated template generation method. Columns A, B and C show the results for $T_{P\text{-}HRT}$, $T_{PS\text{-}HRT}$, and $T_{P\text{-}HRTBKG}$ versus $T_{PS\text{-}HRTBKG}$, respectively.

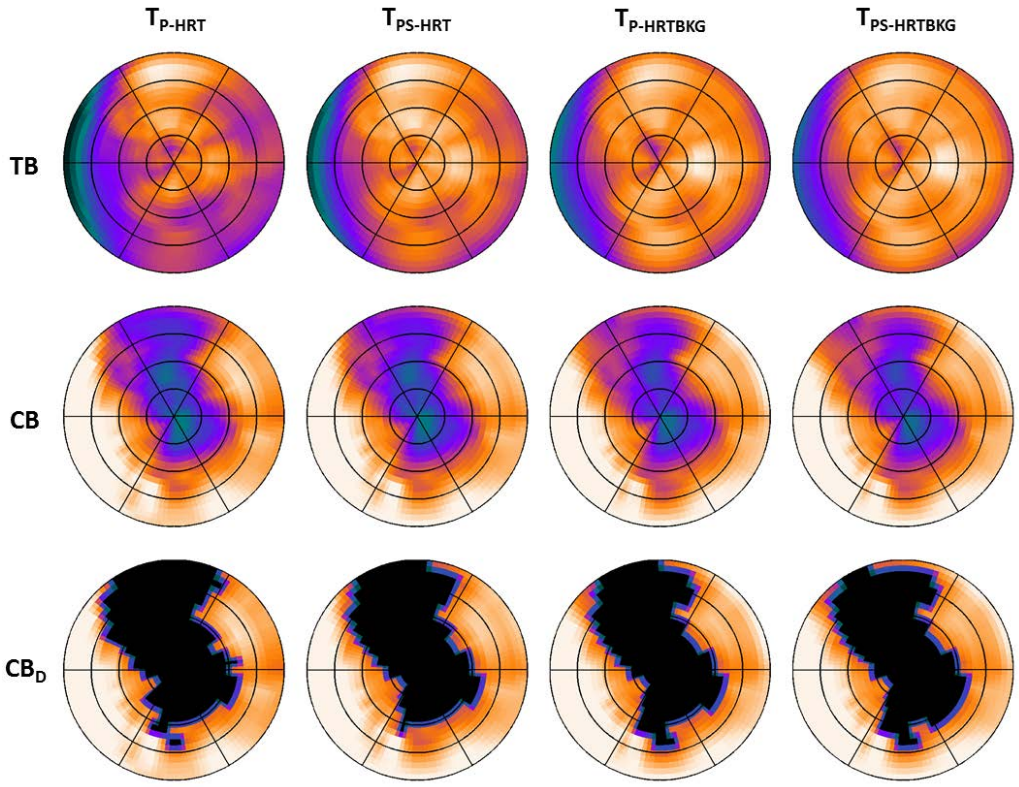

Figure 6-6 Bulls-eye images for a selected patient case. The columns, from left to right, represent images generated from the $T_{P\text{-}HRT}$, $T_{PS\text{-}HRT}$, $T_{P\text{-}HRTBKG}$, and $T_{PS\text{-}HRTBKG}$. The rows, from top to bottom, show the template (TB), corrected bulls-eye map (CB) and corrected bulls-eye map with defect defined (CB_D) using the appropriate thresholds defined from the threshold establishment study. The black pixels in the bottom row (CB_D) represent abnormal pixels as defined by the healthy threshold, HT.

With regards to computation time for the template generation methods, significant reductions were observed when using the T_{HRT} and T_P methods relative to T_{HRTBKG} and T_{PS}, respectively. The approximate processing times for $T_{P\text{-}HRT}$, $T_{PS\text{-}HRT}$, $T_{P\text{-}HRTBKG}$, and $T_{PS\text{-}HRTBKG}$ are shown in Table 6-5. All calculations were performed using an Intel® Duo Core™ 3.00 GHz processor with 3.22 GB RAM.

Table 6-5 Approximate processing times for each investigate template generation method using TQPS.

TQPS Template generation method	Approx. processing time (minutes)
$T_{P\text{-}HRT}$	< 1
$T_{PS\text{-}HRT}$	60-90
$T_{P\text{-}HRTBKG}$	~1
$T_{PS\text{-}HRTBKG}$	180-240

6.7 Discussion

In this phase of the thesis, four template generation methods were evaluated for use with the proposed TQPS method. In the study presented in the previous chapter, it was demonstrated that the initial version of the method performed well, with the accuracy of perfusion defect extent estimates within 5% of the truth; however, the TQPS version used in these studies was not optimized in terms of processing time *(91)*. This study addressed this issue by investigating four specific template generation methods differing in the complexity of the template construction and projection methods.

Prior to the analysis of the four aforementioned template methods for TQPS, it was necessary to establish the optimal threshold for each method, which would be used to most accurately define abnormal perfusion within a given myocardial perfusion image. For the *SPECT-based* template methods, it was found that the optimal thresholds (in terms of parameter x in Eq. 4-5) ranged from x =1.5 for $T_{P\text{-}HRT}$ to x =2.5 for $T_{PS\text{-}HRTBKG}$. Similar trends were observed for the *Ideal* template. The cause for this range in optimal thresholds could be attributed to the variability in count distribution between the template bulls-eye images produced by each method, as seen in Figure 6-6 (top row).

For instance, the $T_{P\text{-}HRT}$ template tended to underestimate the activity in the basal regions of the heart due to the absence of spill-in activity from the background; thus, causing an overestimation of this region in the corrected (CB) image. With this, it was necessary to have a higher healthy threshold (lower x value) to accommodate for such effects and maintain optimal sensitivity. This procedure is analogous to what is used in commercial software such as Cedars Sinai's QPS software *(173, 185)*, where different thresholds (in terms of standard deviations) are employed for each myocardial segment to account for the variable distribution found in the normal heart database. For both methods, TQPS and QPS, determining an optimal healthy threshold was necessary in order to achieve the maximum specificities and sensitivities.

The *Ideal* template was again utilized to assess the performance of the *SPECT-based* methods. This template was chosen to represent the potential scenario where a template could be constructed from an anatomical imaging source (e.g. CT or MRI). To date, template methods have been primarily limited to simulation studies and designed with the assumption that a diagnostic quality anatomical image is available *(49, 143, 165-167)*. However, the ability to create a template of the heart via an anatomical imaging modality remains a challenge due to the limited availability of diagnostic quality CT systems onboard hybrid SPECT-CT systems and the increased radiation risks associated with such systems. This was the primary motivation for the *SPECT-based* template construction employed in the TQPS method.

From the results presented in Figure 6-2, it was found that there were no significant differences in specificity, sensitivity or accuracy for corresponding template generation methods when using the *Ideal* template versus the *SPECT-based* templates, with the lone exception of $T_{P\text{-}HRTBKG}$. Here, the specificities with *Ideal* and *SPECT-based* templates using the $T_{P\text{-}HRTBKG}$ method were 84 ± 3% and 79 ± 4% (P=0.0378), respectively. In general, these results suggest that small errors are introduced by the *SPECT-based*

template segmentation process; however, it should be recognized that throughout the measurements (as highlighted in Table 6-4) there was an overall trend of improved results in favor of the *Ideal* methods despite significance not being reached. As mentioned previously, the segmentation software adopted in this study, Segment *(92, 168)*, has the advantage over many of the commercially available segmentation methods in that it does not assume uniform myocardial wall thickness, thereby enabling it to better represent a true myocardium. Moreover, the algorithm has proven to be robust even in challenging situations where there are defects in the 40-70% extent range. These results confirm that the TQPS method offers a pragmatic template-based approach to semi-quantitative MPI analysis in that it does not require hardware beyond what is commercially available.

In the template generation analysis, the objective was to find the best combination of template construction and template projection for the TQPS method, with respect to computation time and the quality of perfusion defect definition. When using the *Ideal* method, which is independent of potential error introduced in the SPECT segmentation process, it was found that only the $T_{P\text{-}HRT}$ method underperformed with a sensitivity and accuracy significantly lower than the gold standard $T_{PS\text{-}HRTBKG}$. In the *SPECT-based* template case, the same trends were found as the $T_{P\text{-}HRT}$ method proved to have significantly lower specificity and accuracy relative to both $T_{P\text{-}HRTBKG}$ and $T_{PS\text{-}HRTBKG}$. Interestingly, there were no differences in the perfusion defect definition quality when projecting the same template with primary photons only versus primary and scattered photons.

Looking at all aspects of the four template generation methods, it was found that the addition of lung and background activity to the heart template had a significantly greater effect on the results of the defect analysis relative to changing the projection method, thereby suggesting that it is beneficial to construct the template with heart,

lung and background activity (i.e. T_{HRTBKG}). These findings can be explained considering the partial volume effects related to activity spill-in and spill-out. In the case where background was not modeled in the template (i.e. T_{HRT}), the spill-in effect was completely ignored since there was no background activity to spill-in to the myocardium. As a result of excluding the spill-in effects, a significant loss in the accuracy of perfusion defect definition was observed when using the T_{HRT} template relative to T_{HRTBKG} (where background activity was included). With regards to the template projection method, it is important to note that activity spill-in and spill-out effects are related to both limited resolution and scatter, which suggests that some spill-in and spill-out effects can still be present even when scatter is disregarded. Thus, for the $T_{P\text{-}HRTBKG}$ template method, spill-in and spill-out effects were still partly accounted for by modeling the finite resolution of the imaging system, even though scatter was not incorporated into the projection step. This idea is in agreement with our observations that there were no significant losses in the quality of the defect definition when using the $T_{P\text{-}HRTBKG}$ method relative to $T_{PS\text{-}HRTBKG}$. Overall, the results of this study were consistent with the literature suggesting that partial volume effects related to activity spill-in and spill-out play a large role in the quality of myocardial perfusion imaging.*(49, 165, 165)*

An additional reason for the minimal influence observed in the perfusion defect analysis when neglecting scatter in the template projection could be related to the nature of bulls-eye sampling. As illustrated in Figure 4-1, the artifact correction step is performed using the bulls-eye images, which essentially correspond to a collection of circumferential profiles of the myocardium. Scatter (with Tc-99m) has a relatively smooth spatial distribution and accounts for roughly 20% of the accepted photons in SPECT MPI; therefore, it would take an extremely hot source adjacent to the heart wall to significantly affect the circumferential profile within a short axis slice of the heart. In our simulation studies, phantoms were designed with a liver less than two pixels

(roughly 1.3 cm) from the inferior aspect of heart with a 1:1 heart to liver activity ratio, and still, no significant differences were observed relative to the results obtained from phantoms without liver uptake. Moreover, there were no significant differences in performance between $T_{P\text{-}HRTBKG}$ and $T_{PS\text{-}HRTBKG}$ for the *Ideal* templates (where the liver was modeled into the background), indicating that influence of liver scatter and spill-in was not significant for these studies. Due to the rather insensitive nature of the bulls-eye sampling with respect to scattered photons, it proved satisfactory to neglect scatter from the template projection in the interest of reducing processing time to a more clinically acceptable range.

In the patient study, each template generation method was evaluated relative to the gold standard method, $T_{PS\text{-}HRTBKG}$. Again, it was found that the $T_{P\text{-}HRT}$ method underperformed in both sensitivity (69%) and accuracy (89%) relative to the other two methods, $T_{PS\text{-}HRT}$ and $T_{P\text{-}HRTBKG}$. With regards to the EXT correlation results, $T_{P\text{-}HRT}$ produced a y-intercept of 9.37% resulting from the linear regression, suggesting a substantial bias toward overestimating the size of the perfusion defects. Conversely, $T_{P\text{-}HRTBKG}$ exhibited the most promising results with a sensitivity, specificity, and accuracy of 97%, 98%, and 98% to go along with an EXT correlation coefficient and y-intercept of 1.00 and -0.71%, respectively. From the performances demonstrated by each method in terms of the perfusion defect analysis, in conjunction with the dramatic reduction in computation time for the T_P methods relative to T_{PS}, and only slightly lower for the T_{HRT} methods relative to the T_{HRTBKG} methods (due to fewer photons being projected), it was concluded that the $T_{P\text{-}HRTBKG}$ method is optimal for TQPS.

Beyond the improved performance reported in this study for the $T_{P\text{-}HRTBKG}$ method, additional benefit could be realized if scatter correction is implemented into the patient reconstruction algorithm. When using any of the T_P methods, the primary difference between the patient and template images is the scattered photon distribution within

the patient image. This difference could be minimized if scatter was corrected in the patient reconstruction step; however, this is not a trivial process. For instance, one difficulty in this approach could be the uncertainty (mismatch in the data) introduced by an unsophisticated and inaccurate scatter correction technique. Furthermore, a more advanced scatter correction technique could be highly beneficial in terms of accuracy (for the T_P methods), but at the cost of additional processing time. At this point, clinical scatter correction algorithms are relatively unsophisticated due to computational burden associated with more advanced scatter correction methods. Nonetheless, the potential value of various scatter corrections techniques with the T_P methods could be a future development for the TQPS method.

6.8 Conclusions

Four modifications of the TQPS method were evaluated in this chapter, with the objective of reducing processing time to within a clinically acceptable range. It was determined that the template should model the heart, lung, and background activity (i.e. T_{HRTBKG}), with the results indicating that such a comprehensive template model improves the accuracy of perfusion defect definition. Interestingly, the template projected using primary photons only, without scatter, proved to be optimal in terms of the trade-off between processing time and diagnostic accuracy.

With its ability to correct for image processing artifacts and accurately perform semi-quantitative SPECT MPI within a clinically acceptable processing timeframe, TQPS can add valuable information to routine SPECT MPI analysis. Therefore, the next phase of this thesis was aimed at evaluating TQPS relative to commercial software while using an external gold standard and true diagnostic end point – the detection of coronary artery disease.

7 Method Validation

The final phase of this thesis involved the validation of TQPS in the clinical domain. As opposed to using commercial SPECT MPI software (QPS) as the reference standard (Chapter 5); this phase of the analysis provides an objective evaluation of TQPS relative to QPS by using an external gold standard – coronary angiography. The work presented in this chapter of the thesis has been submitted to the Journal of Nuclear Cardiology.

The following chapter is organized into eight sections. First, a Methodology section is included to highlight the main objectives of the studies performed in this chapter. The Experiments section presents the details of the studies together with the patient demographics and protocol used in the SPECT MPI and coronary angiography procedures. A section on Image Processing includes all relevant processing parameters used in the study. The Figures of Merit and Statistical Analysis sections describe the measurements and subsequent statistics, respectively. Finally, the chapter concludes with the Results, Discussion and Conclusion sections, which highlight the major findings and their respective significance for the clinical validation phase of the TQPS method.

7.1 Methodology

As alluded to already, the methodology adopted in this phase of the thesis was designed with a clinical focus. Specifically, this phase of the analysis was aimed at providing an objective comparison between the clinical performances of TQPS relative to that of the

leading commercial SPECT MPI quantitative analysis software, Cedars Sinai's QPS. In order to determine the presence of coronary artery disease, an external assessment of the coronary arteries was made using coronary angiography.

Prior to the direct comparison between TQPS and QPS, an additional analysis was implemented in this study to assess the performance of TQPS when using two different reconstruction algorithms. Specifically, the results obtained with TQPS when using the in-house reconstruction software with attenuation correction (AC) and without attenuation correction (NC) were compared. The objective was to test the robustness of TQPS with respect to using different processing algorithms, which is a practical concern in a true clinical setting.

Furthermore, the following study also provided a confirmation of the conclusions drawn from the optimization phase by comparing the performance of TQPS when using the $T_{P\text{-}HRTBKG}$ template generation method relative to $T_{PS\text{-}HRTBKG}$. Recall from Chapter 6 that the $T_{P\text{-}HRTBKG}$ template generation method was determined to be the most efficient version of TQPS with respect to diagnostic accuracy and computation time (i.e. a template with heart and background, and projected with primary photons only). Whereas the previous studies used the definition of perfusion defects as the primary metric for the assessment, this phase of the thesis provides a similar analysis, but with a true diagnostic end point for the assessment of the $T_{P\text{-}HRTBKG}$ and $T_{PS\text{-}HRTBKG}$ methods.

Overall, the results for this phase of the thesis were broken into three parts:

1) TQPS Reconstruction Study: AC vs. NC
2) TQPS Template Generation Method Study: $T_{P\text{-}HRTBKG}$ vs. $T_{PS\text{-}HRTBKG}$
3) TQPS Validation Study: TQPS vs. QPS

7.2 Experiments

7.2.1 Patients

In this retrospective study, a patient population of 42 MPI rest-stress studies performed at VGH were obtained. The use of fully anonymized patient data for software analysis was approved by the Clinical Research Ethics Board at the University of British Columbia. All patients underwent exercise or pharmacologically (adenosine or dipyridamole) induced stress ^{99m}Tc-Sestamibi SPECT MPI, followed by catheter coronary angiography within 90 days of the SPECT MPI study.

Table 7-1 summarizes all patient characteristics and reported conditions. Only studies without visually detectable attenuation map to SPECT data misregistration were subsequently processed and analyzed. In total, two datasets were rejected due to misregistration.

Table 7-1 Patient population characteristics for the validation phase.

Parameter	Patient Population (n=42)
Age ± SD (years)	68 ± 11
Gender: Male	23 (55%)
Hypertension	20 (48%)
Diabetes	13 (31%)
Hypercholesterolemia	17 (40%)
Atypical Angina / Chest Pain	15 (36%)
Typical Angina	8 (19%)
Dyspnea	6 (14%)

7.2.2 Coronary Angiography

All patients underwent catheter coronary angiography, which was performed using the Judkins left and right catheters as a first choice. Modified catheters were employed depending on the specific anatomy of the patient. The images were read by a single physician at the time of the study with stenoses visually graded as a percentage (in deciles) of luminal narrowing. Additional descriptors (focal, diffuse, calcific, etc.) were recorded to describe the nature of a particular stenosis. For this study, two grades of stenosis were considered significant: ≥50% and ≥70% stenosis. A summary of the coronary angiography findings for the patient population can be seen in Table 7-2.

Table 7-2 Angiographic Data Characteristics in the Patient Population (n=42)

Parameter	No. of patients (% of total population)	
	≥50% Stenosis	≥70% Stenosis
Normal	5 (12%)	6 (14%)
Single vessel	9 (21%)	18 (43%)
Double vessel	13 (31%)	10 (24%)
Triple vessel	15 (36%)	8 (19%)
LAD territory*	32 (76%)	25 (60%)
LCX territory*	26 (62%)	17 (40%)
RCA territory*	23 (55%)	20 (48%)

* Main Coronary Artery Acronyms: Left Anterior Descending, LAD; Left Circumflex, LCX; Right Coronary Artery, RCA.

7.2.3 Image Acquisition

The ^{99m}Tc-Sestamibi SPECT MPI studies were acquired on GE's Infinia Hawkeye hybrid SPECT-CT (GE Healthcare, Haifa, Israel) camera equipped with a LEHR collimator using the standard clinical protocol adopted at our institution. The acquisitions were performed using a 180^0 camera rotation with a non-circular, body contoured orbit with 60 projections (3^0 angular intervals) set at 25 and 20 seconds per projection for the rest and stress studies, respectively. The acquisition matrix size was set to 64x64 resulting in a 6.80 mm pixel size, with 20% energy windows set on the 140 keV photopeak. Studies followed a one-day protocol with 370Bq and 1110MBq injected intravenously for the rest and stress study, respectively. The CT scan was performed after each of the SPECT acquisitions.

7.3 Image Processing

Cedars-Sinai's QPS

As alluded to already, the QPS approach (Cedars-Sinai Medical Center, Los Angeles, CA) to semi-quantitative SPECT MPI has been very well documented over the last decade *(83, 96, 97, 173, 185, 186)*. In this study, QPS (Version 2.0) was utilized with normal databases specific to the SPECT MPI acquisition and processing protocol used at the Nuclear Medicine Department in VGH. Specifically, gender-matched non-attenuation-corrected (NC) normal databases were employed. The influences of age and body mass index were not accounted for in the databases. The databases were reconstructed using GE's OSEM-based Evolution for Cardiac^{TM} algorithm with resolution recovery using 10 subsets and 4 iterations and a 5th order Butterworth post-filter (0.52 cycles/cm cut-off frequency). As a result, to match this particular database, all patient analysis using the QPS software employed the Evolution for Cardiac^{TM} algorithm.

TQPS

For the reconstruction step in TQPS, the in-house OSEM-based software was utilized. For the comparative analysis between TQPS and QPS, the in-house reconstructions were performed to match the clinical reconstructions (see Appendix B for a brief comparison between the two algorithms). Specifically, the algorithm included resolution recovery without attenuation correction (NC), using 10 subsets and 4 iterations of the OSEM-based algorithm with a 5th order Butterworth post-reconstruction filter (0.52 cycles/cm cut-off frequency). In addition to these reconstructions, a second set of TQPS results were obtained with the inclusion of CT-based attenuation correction (AC) into the in-

house algorithm for the reconstruction step. This was done for the purpose of comparing TQPS when using NC relative to AC reconstructions.

In terms of template generation methods, both the $T_{P\text{-}HRTBKG}$ and $T_{PS\text{-}HRTBKG}$ were employed for this study using the optimized number of average deviations x for the healthy thresholds established in the optimization phase of the analysis (see Table 6-4).

7.4 Figures of Merit

The semi-quantitative analysis of the SPECT MPI images using TQPS and QPS involved a number of measurements specific to each method. In each case, the specific measurements were calculated for each main coronary territory (n = 42 patients x 3 territories/patient = 126 territories). The three main coronary territories included the left anterior descending (LAD), left circumflex (LCX), and the right coronary artery (RCA). The territories were defined for each analyzed bulls-eye map using the 20 segment model (Figure 2-27).

7.4.1 TQPS Measurements

Three measurements were made using the TQPS method:

1. Perfusion Defect Extent (EXT-TQPS)
2. Summed Stress Score (SSS-TQPS)
3. Total Perfusion Deficit (TPD-TQPS).

EXT-TQPS

As in the previous two phases of this thesis, the measure of perfusion defect extent (EXT-TQPS) was included. The EXT-TQPS was defined as the volume of the defect region (perfusion less than the healthy threshold) expressed as percentage of the total left ventricle myocardial volume.

SSS-TQPS

The second metric used to assess the left ventricular myocardial perfusion in TQPS was the summed stress score, which accounts for the severity of the perfusion defect. The overall definition of this measurement is similar to that employed in commercial software packages *(81, 83, 84, 90)*. The SSS-TQPS measurements for each coronary territory were calculated in three steps. First, all pixels with values less than the healthy threshold for the given study were defined as abnormal pixels. From there, the intensity values of the abnormal pixel values were calculated as a percentage of the healthy threshold (% HT):

$$\%HT_i = \frac{C_i}{HT} \times 100 \qquad \text{Eq. 7-1}$$

where HT is the healthy threshold for the given study, C_i is the pixel intensity (counts) in bulls-eye pixel i, and $\%HT_i$ is the value of bulls-eye pixel i as a percentage of the healthy threshold. Once defined as a percentage of the healthy threshold (as shown in Eq. 7-1), the bulls-eye pixel values were then scored on a 5-point scale with the following distribution:

- Score 0-1 for pixels ≥ 100% HT
- Score 2 for pixels 70-99% HT
- Score 3 for pixels 40-69% HT
- Score 4 for pixels ≤ 39% HT.

Finally, segmental scores (using the 20-segment model – see Figure 2-26) were calculated as the mean scores rounded to the nearest integer for all pixels within a given myocardial segment. Using the segmental score, the SSS-TQPS value for each coronary territory was defined as the sum of the segmental scores within each respective territory.

TPD-TQPS

The last metric used to describe the myocardial perfusion for the patient studies was based on the total perfusion deficit introduced by Slomka et al *(97)*. The idea of total perfusion deficit, TPD-TQPS, was to combine the extent and summed stress scores into one parameter. The TPD-TQPS was defined as follows:

$$TPD\text{-}TQPS = 100\% \cdot \sum_{i=0}^{i<K} \sum_{\theta=0}^{\theta<M} \frac{score(i,\theta)}{4 \cdot K \cdot M} \qquad \text{Eq. 7-2}$$

where i and θ were the polar coordinates of the bulls-eye map and *K* and *M* were the maximum number of elements in each dimension, respectively; $score(i,\theta)$ was defined as the score for each pixel (i,θ), as described in the SSS-TQPS section above. Under this definition, a healthy heart would have a TPD-TQPS value of 0%, as where a heart without uptake would have a value of 100%. The TPD-TQPS value for each coronary territory was defined as the mean TPD-TQPS value for all pixels within each territory.

7.4.2 QPS Measurements

Segmental summed stress scores for QPS (SSS-QPS), as described by Slomka et al *(97)*, were the output measurements offered by the QPS software employed in this study, and thus, were used as the figures of merit for QPS. The methodology behind this metric is similar to that used in the SSS-TQPS score; however, the QPS method employs normal patient databases to establish "normal limits" in the scoring process. The SSS-QPS score for a given coronary territory was calculated as the sum of the segment scores (again, using the 20-segment model) contained within each coronary territory, as defined by the QPS software. Segmental perfusion defect extent and total perfusion deficit measurements QPS were not available at the workstations used for this study.

7.5 Statistical Analysis

Receiver operating characteristic (ROC) curves were constructed for each measurement using the results from the angiography studies as the reference standard (≥50% and ≥70% stenosis). These ROCs were generated and analyzed using the Analyse-It software (version 2.24; Analyse-It Software Ltd, Leeds, United Kingdom). With this approach, a paired comparison of ROC curves was achieved using the method proposed by Hanley and McNeil *(187)*. Area-under-the-curve (AUC) results were expressed as AUC ± SE, where SE is the standard error. A threshold of $P<0.05$ was considered significant for all analysis. The optimal sensitivity, specificity and accuracy for a given ROC curve were chosen as the values at the optimal operating point, defined as the point that yields the minimum value for $(1 - \text{sensitivity})^2 + 0.95 \times (1 - \text{specificity})^2$, given that sensitivity > specificity *(97)*.

7.6 Results

7.6.1 TQPS Reconstruction Study: NC vs. AC

The performance of TQPS using two different reconstruction algorithms in the reconstruction step of the method was compared. Table 7-3 presents the AUC results for the two in-house reconstruction methods, NC and AC, and two levels of significant stenosis (≥50% and ≥70%), using each of the aforesaid figures of merit: SSS-TQPS, TPD-TQPS, and EXT-TQPS. Note that all results presented in this section employed the $T_{PS\text{-}HRTBKG}$ template generation method in TQPS. No significant differences were found between the results for AC and NC when using the same figure of merit, with all AUC measurements above 0.80, indicating a good test in each case.

Table 7-3 Areas under the ROC curve for the detection ≥50% and ≥70% stenosis using each figure of merit, SSS-TQPS, TPD-TQPS, and EXT-TQPS. The $T_{PS\text{-}HRTBKG}$ template generation method was used for TQPS using AC and NC reconstruction methods as shown (n=126).

Figure of Merit	Reconstruction Method	ROC area under curve (±SE)	
		≥50% Stenosis	≥70% Stenosis
SSS-TQPS	NC	0.86 ± 0.03	0.87 ± 0.03
SSS-TQPS	AC	0.85 ± 0.04	0.84 ± 0.04
TPD-TQPS	NC	0.84 ± 0.04	0.85 ± 0.04
TPD-TQPS	AC	0.83 ± 0.04	0.81 ± 0.04
EXT-TQPS	NC	0.83 ± 0.04	0.85 ± 0.04
EXT-TQPS	AC	0.83 ± 0.04	0.80 ± 0.04

Figure 7-1 presents the results, in terms of sensitivity, specificity and accuracy, for TQPS when using the AC and NC reconstructions. Confidence limits for the AC sensitivities

were between ±7% and ±11%, and between ±11% and ±16% for the specificities. For the NC results, the confidence limits were between ±6% and ±10% for sensitivities, and ±11% and ±15% for specificities. In all, no significant differences were found when using the two algorithms for any of the figures of merit, although it is evident that there was a slight trend in favour of the NC performance, particularly for the detection of ≥70% stenosis.

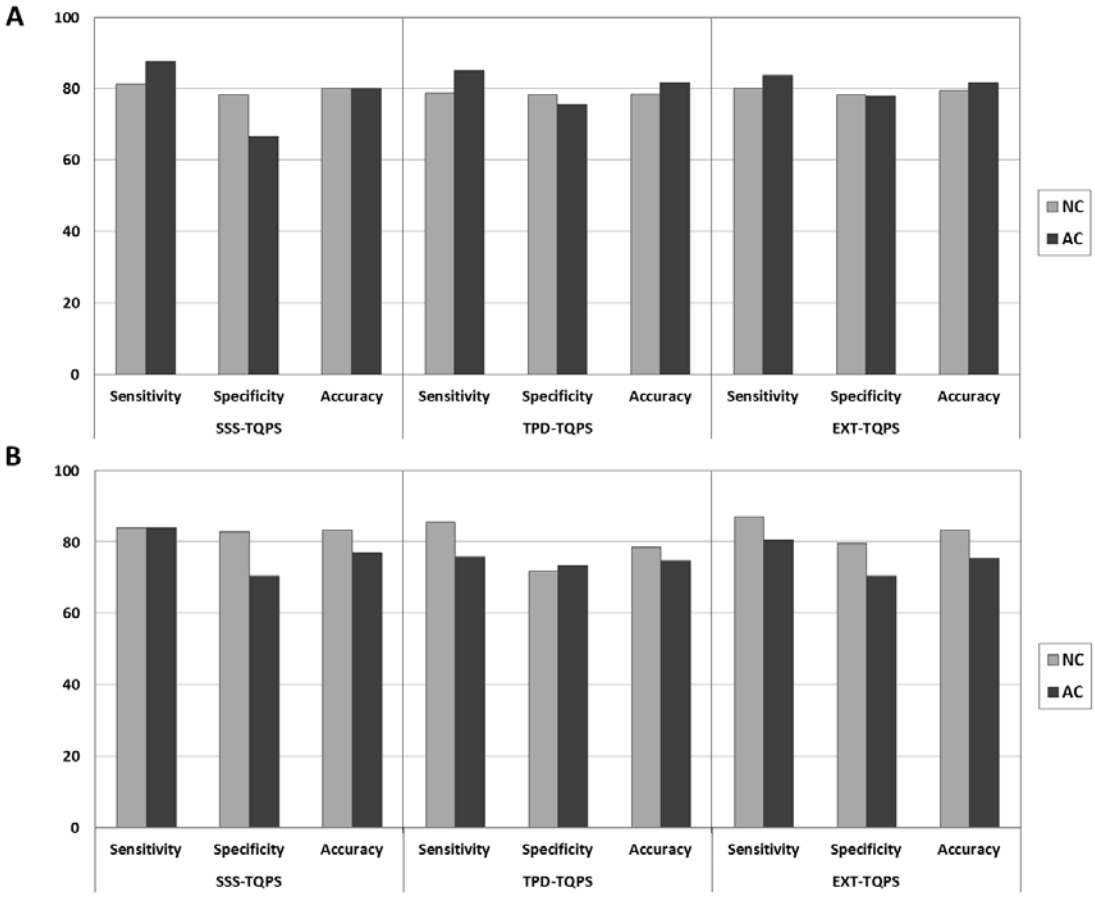

Figure 7-1 Sensitivities, specificities, and accuracies for each figure of merit (SSS, TPD and EXT) when using the in-house AC and NC in-house reconstruction algorithms for TQPS. Here, TQPS with the $T_{PS\text{-}HRTBKG}$ template generation method was used. Images (A) and (B) show the results for the detection of ≥50% and ≥70% stenosis for all coronary territories (n=126), respectively.

Figure 7-2 illustrates the images produced during the TQPS process using the AC and NC in-house reconstruction methods. In this case, the (male) patient presented with a significant stenosis (≥70%) in the left anterior descending coronary artery. The patient bulls-eye image using the NC reconstruction method (Figure 7-2-A) highlights the attenuation artifact in the inferior region of the myocardium as compared to the attenuation corrected image (Figure 7-2-B), which did not exhibit this artifact. The value of the TQPS method can be particularly observed by comparing the artifact corrected images, CB, as shown in Figure 7-2-A and Figure 7-2-B. Specifically, it can be seen that resulting corrected images in both methods appear very similar from a qualitative standpoint, thus confirming the correction/removal of the attenuation artifact. The ability of the template images to portray this artifact can be seen in the TB image in Figure 7-2-A.

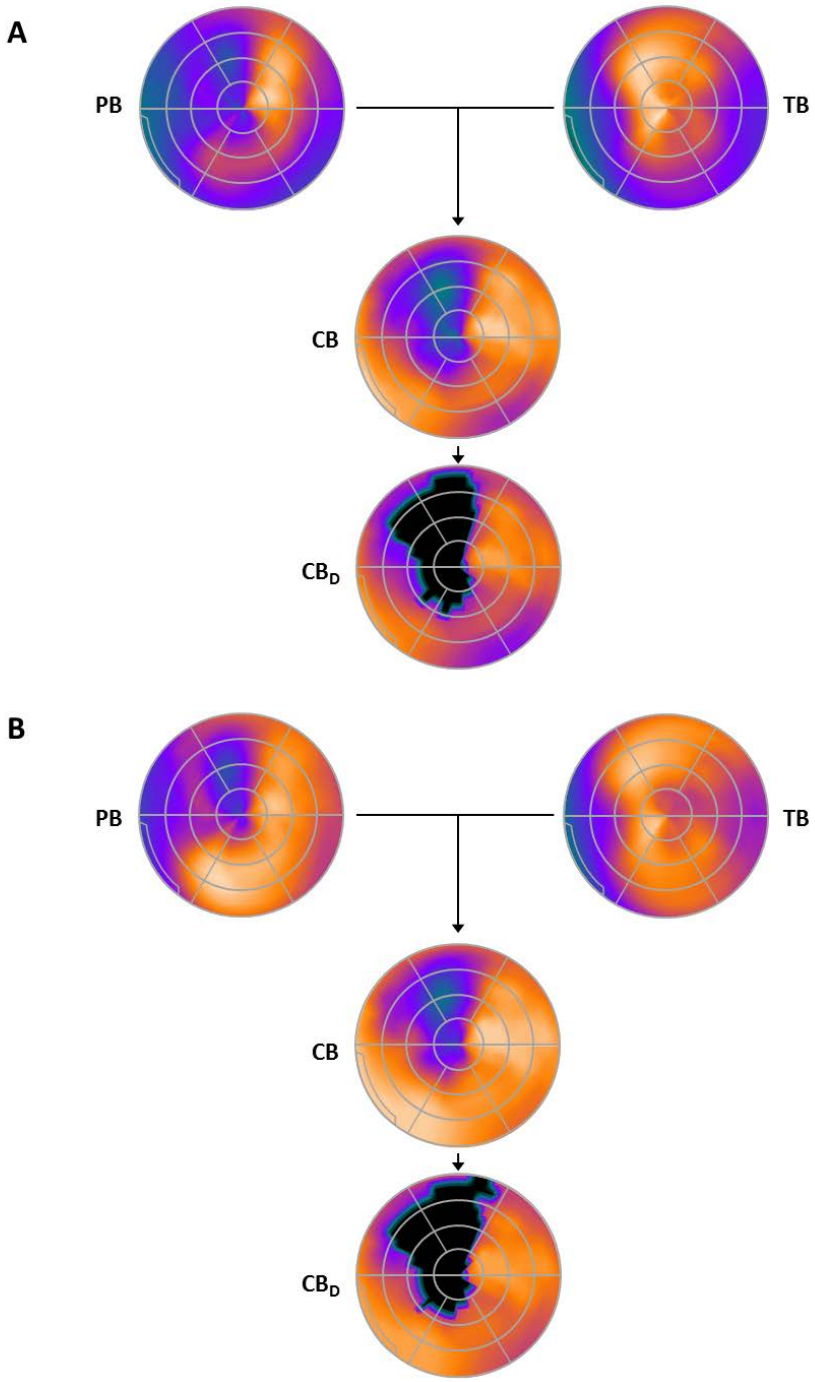

Figure 7-2 Two example flow charts of images produced at selected key steps of the TQPS method when using the (A) NC and (B) AC in-house reconstruction algorithms. For each figure, the patient bulls-eye (PB), template bulls-eye (TB), corrected bulls-eye (CB) and corrected bulls-eye with the defect defined (CB_D) images are shown with the arrows indicating how they are created. The 20-segment model is overlaid on each image (light grey lines).

7.6.2 TQPS Template Generation Study: $T_{P\text{-}HRTBKG}$ vs. $T_{PS\text{-}HRTBKG}$

In addition to testing TQPS using two different reconstruction algorithms, it was also analyzed in terms of two template generation methods. Specifically, the $T_{P\text{-}HRTBKG}$ and $T_{PS\text{-}HRTBKG}$ methods were included in this study. All reconstructions in this section were performed with the in-house NC algorithm.

Table 7-4 presents the AUC results for the two aforementioned template generation methods at two levels of significant stenosis (≥50% and ≥70%), using SSS-TQPS, TPD-TQPS, and EXT-TQPS as figures of merit. Here, no significant differences were found between the results for two template generation methods. For instance, the areas under the curve for $T_{P\text{-}HRTBKG}$ and $T_{PS\text{-}HRTBKG}$ using TPD-TQPS were 0.84±0.03 and 0.83±0.03, respectively, yielding P=0.88. Again, all AUC measurements were reported to be above 0.80, indicating a good test in each case.

Table 7-4 Areas under the ROC curve for the detection ≥50% and ≥70% stenosis using each figure of merit, SSS-QPS, SSS-TQPS, TPD-TQPS, and EXT-TQPS. The NC reconstruction method was used for TQPS with the $T_{P\text{-}HRTBKG}$ and $T_{PS\text{-}HRTBKG}$ template generation methods, as shown (n=126).

Figure of Merit	Template Generation Method	ROC area under curve (±SE)	
		≥50% Stenosis	≥70% Stenosis
SSS-TQPS	$T_{PS\text{-}HRTBKG}$	0.86 ± 0.03	0.87 ± 0.03
SSS-TQPS	$T_{P\text{-}HRTBKG}$	0.84 ± 0.04	0.87 ± 0.03
TPD-TQPS	$T_{PS\text{-}HRTBKG}$	0.84 ± 0.04	0.85 ± 0.04
TPD-TQPS	$T_{P\text{-}HRTBKG}$	0.86 ± 0.03	0.85 ± 0.04
EXT-TQPS	$T_{PS\text{-}HRTBKG}$	0.83 ± 0.04	0.85 ± 0.04
EXT-TQPS	$T_{P\text{-}HRTBKG}$	0.83 ± 0.04	0.86 ± 0.04

Figure 7-3 presents the results, in terms of sensitivity, specificity and accuracy, for TQPS when using the $T_{P\text{-}HRTBKG}$ and $T_{PS\text{-}HRTBKG}$ methods. Confidence limits for the $T_{P\text{-}HRTBKG}$ sensitivities were between ±8% and ±11%, and between ±11% and ±15% for the specificities. For the $T_{PS\text{-}HRTBKG}$ results, the confidence limits were between ±8% and ±11% for sensitivities, and ±11% and ±15% for specificities. In all, no significant differences were found when using the two techniques for any of the figures of merit.

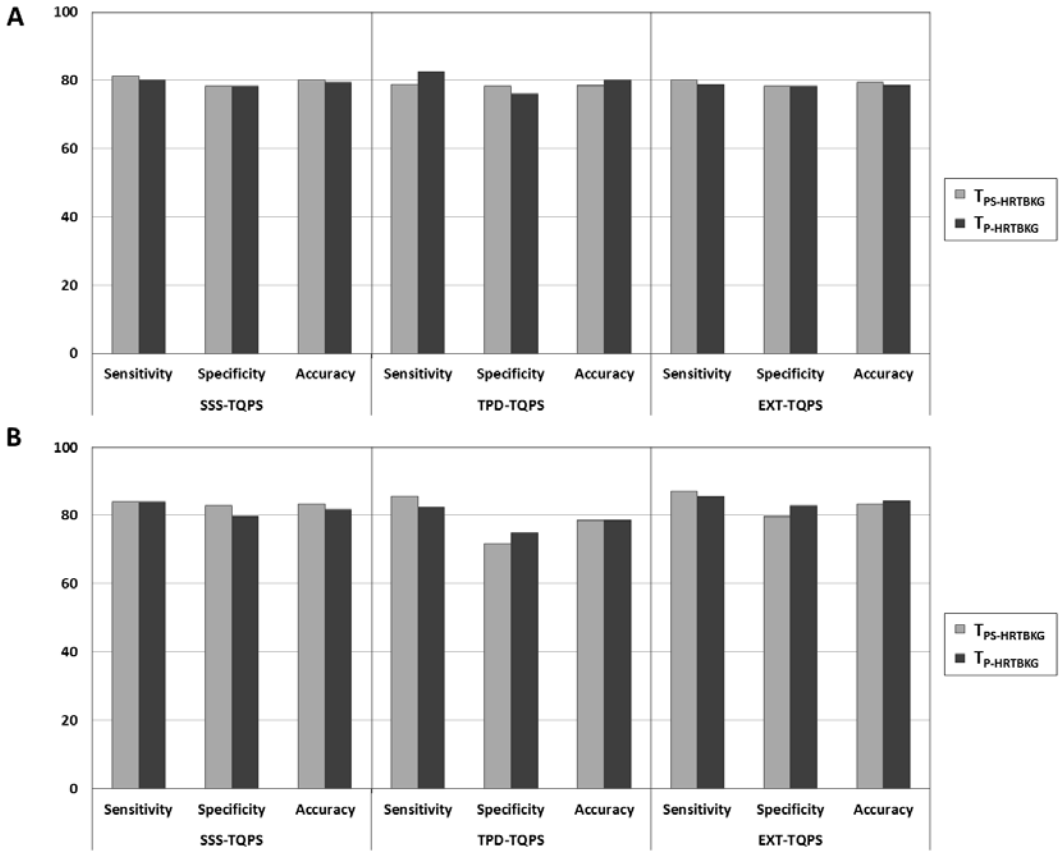

Figure 7-3 Sensitivities, specificities, and accuracies for each figure of merit (SSS, TPD and EXT) when using the $T_{PS\text{-}HRTBKG}$ and $T_{P\text{-}HRTBKG}$ template generation methods for TQPS. The NC reconstruction algorithm was applied. Images (A) and (B) show the results for the detection of ≥50% and ≥70% stenosis for all coronary territories (n=126), respectively.

7.6.3 TQPS Validation Study: TQPS vs. QPS

With the robustness of the TQPS algorithm tested and confirmed in the previous two sections, the final aspect of this phase of the analysis involved comparing the proposed TQPS method against the leading commercial method, QPS. To note, all reconstructions in this section employed the NC algorithms, since QPS was not equipped with AC databases, as noted in Section 7.2.4.

Figure 7-4-A illustrates the images generated during the TQPS process using the $T_{P\text{-}HRTBKG}$ method for a challenging patient presenting with a reported 90% stenosis in both the LAD and RCA arteries. Figure 7-4-B displays the images obtained for the same patient using QPS with sample tomographic reconstruction slices and the final "blackout map", where the perfusion defect (black pixels) was defined using the normal databases. In this example, both methods were able to detect significant coronary artery disease in the LAD and RCA territories using their respective summed stress score methodologies.

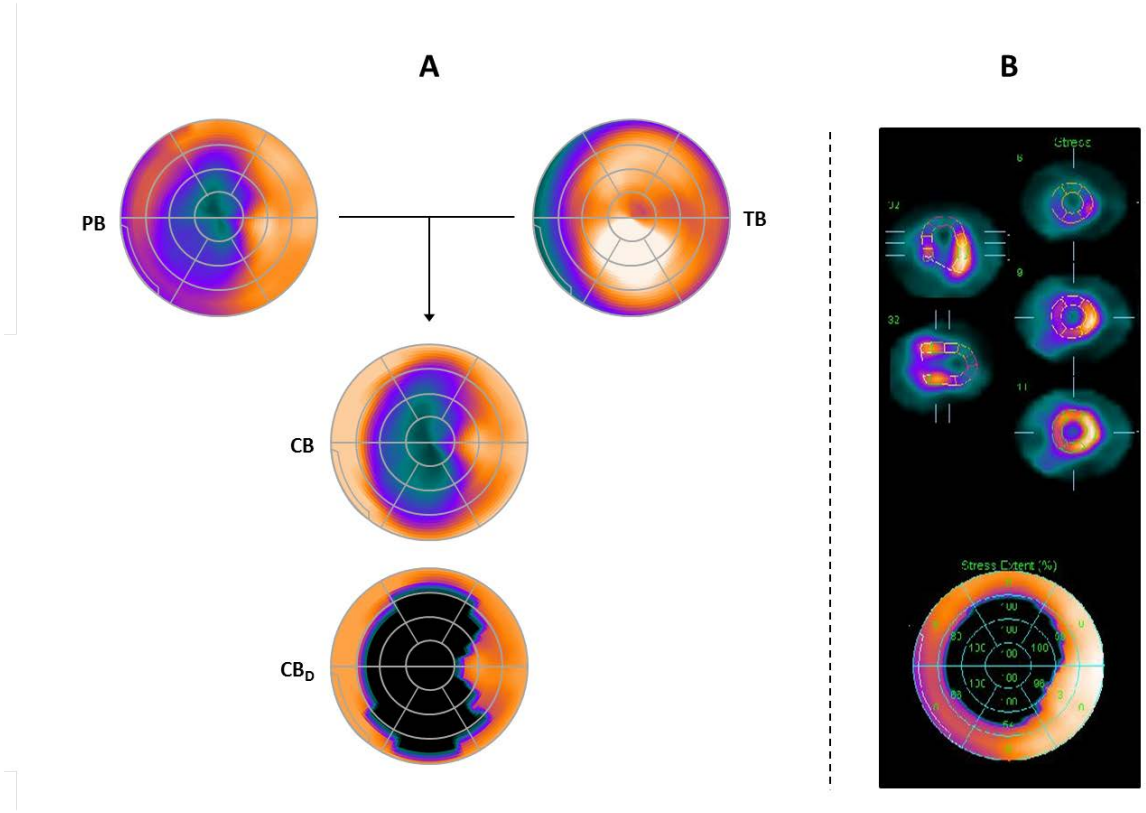

Figure 7-4 Example images created in the TQPS and QPS processes for a patient study presenting with a ≥70% stenosis (reported as 90%) in the LAD and RCA coronary arteries. Here, TQPS is performed with $T_{P\text{-}HRTBKG}$. In column (A) the patient (PB) and template (TB) bulls-eye images are shown in the top row. The arrows in the figure indicate the flow of how the images were created in the TQPS method (as suggested in Figure 4-1). The corrected bulls-eye (CB) is shown in the middle with the perfusion defect (black pixels) defined by the healthy threshold shown at the bottom (CB_D). In column B (right), sample slices of the tomographic reconstruction are shown as displayed in QPS, as well as the final bulls-eye image at the bottom with the perfusion defect (black pixels) defined by the normal databases.

Figure 7-5-A displays the ROC curves obtained for QPS and the two TQPS template generation methods using their respective summed stress scores. The respective sensitivities and specificities calculated at the optimal operating points (obtained from the ROC curves) are shown in Figure 7-5-B. The 95% confidence intervals were between ±7% and ±13% for the sensitivity measurements and ±8% and ±15% for specificities. Optimal operating points (for a given coronary territory) were determined

to be 2 for SSS-QPS, and 9 for SSS-TQPS, 24% for TPD-TQPS and 41% for EXT-TQPS when using the $T_{PS\text{-}HRTBKG}$ method (detecting stenoses of 50% or greater). The greatest improvements in the $T_{PS\text{-}HRTBKG}$ SSS-TQPS measurements relative to the SSS-QPS were observed in specificity: 78% vs. 57% when detecting 50% stenosis or greater, respectively. The same trends were observed for the $T_{P\text{-}HRTBKG}$ method.

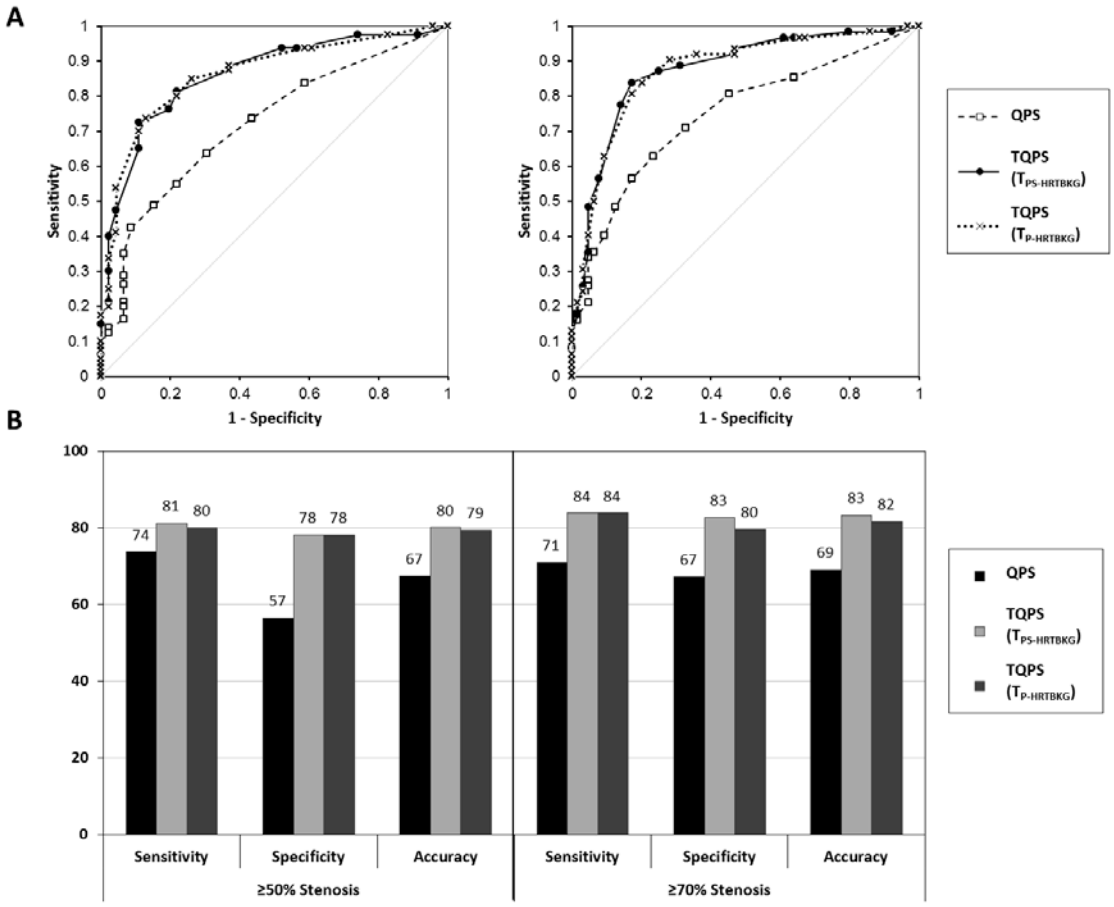

Figure 7-5 (A) ROC curves for the detection of ≥50% and ≥70% stenosis for all coronary territories (n=126) using QPS, and the $T_{PS\text{-}HRTBKG}$ and $T_{P\text{-}HRTBKG}$ TQPS methods. (B) Optimal sensitivities, specificities, and accuracies for QPS, and the $T_{PS\text{-}HRTBKG}$ and $T_{P\text{-}HRTBKG}$ TQPS methods for the detection of ≥50% and ≥70% stenosis for all coronary territories (n=126). All results are shown using the SSS-QPS and SSS-TQPS figures of merit for the QPS and TQPS methods, respectively.

The areas under the ROC curves corresponding to Figure 7-5-A are summarized in Table 7-5. All AUC measurements were significantly improved for each TQPS measurement relative to QPS, suggesting a better test in each case. The greatest improvement (relative to the other figure of merit) was observed between SSS-QPS and SSS-TQPS ($T_{PS-HRTBKG}$): 0.72 ± 0.05 vs. 0.86 ± 0.03 (*P*=0.001) when detecting 50% stenosis or greater and 0.75 ± 0.04 vs. 0.87 ± 0.03 (*P*=0.004) when detecting 70% stenosis or greater. Again, similar trends were observed for the $T_{P-HRTBKG}$ method.

Table 7-5 Areas under the ROC curve for the detection ≥50% and ≥70% stenosis by SSS-QPS, SSS-TQPS, TPD-TQPS, and EXT-TQPS (n=126). The results for both TQPS template generation methods, $T_{PS-HRTBKG}$ and $T_{P-HRTBKG}$ are shown.

Method	Template Generation Method	ROC area under curve (±SE)	
		≥50% Stenosis	≥70% Stenosis
SSS-QPS	n/a	0.72 ± 0.05	0.75 ± 0.04
SSS-TQPS	$T_{PS-HRTBKG}$	0.86 ± 0.03*	0.87 ± 0.03*
TPD-TQPS	$T_{PS-HRTBKG}$	0.84 ± 0.04*	0.85 ± 0.04*
EXT-TQPS	$T_{PS-HRTBKG}$	0.83 ± 0.04*	0.85 ± 0.04*
SSS-TQPS	$T_{P-HRTBKG}$	0.84 ± 0.04*	0.87 ± 0.03*
TPD-TQPS	$T_{P-HRTBKG}$	0.86 ± 0.03*	0.85 ± 0.04*
EXT-TQPS	$T_{P-HRTBKG}$	0.83 ± 0.04*	0.86 ± 0.04*

* Significantly better ($P < 0.05$) than SSS-QPS for the indicated degree of stenosis

Table 7-6 displays the results from the ROC analysis for the male and female subgroups of the main patient population. Significant differences were observed for each figure of merit and each template generation method relative to SSS-QPS in the detection of 50% stenosis or greater in the female population. For instance, when detecting a 50%

stenosis or greater in the female population, the AUCs measured for SSS-QPS and SSS-TQPS ($T_{P\text{-}HRTBKG}$) were 0.66 ± 0.07 vs. 0.82 ± 0.06 (*P*=0.02), respectively. With regards to the female subgroup and the detection of 70% stenosis or greater, no differences were observed between all methods and figures of merit.

Table 7-6 Areas under the ROC curve for the detection ≥50% and ≥70% stenosis by SSS-QPS, SSS-TQPS, TPD-TQPS, and EXT-TQPS in male (n=69) and female (n=57) populations.

Method	Template Generation Method	ROC area under curve (±SE)			
		≥50% Stenosis		≥70% Stenosis	
		Males	Females	Males	Females
SSS-QPS	n/a	0.77 ± 0.06	0.66 ± 0.07	0.75 ± 0.06	0.72 ± 0.08
SSS-TQPS	$T_{PS\text{-}HRTBKG}$	0.90 ± 0.04*	0.80 ± 0.06*	0.92 ± 0.04*	0.80 ± 0.06
TPD-TQPS	$T_{PS\text{-}HRTBKG}$	0.81 ± 0.06	0.83 ± 0.06*	0.89 ± 0.04*	0.79 ± 0.07
EXT-TQPS	$T_{PS\text{-}HRTBKG}$	0.79 ± 0.07	0.82 ± 0.06*	0.88 ± 0.05	0.80 ± 0.07
SSS-TQPS	$T_{P\text{-}HRTBKG}$	0.90 ± 0.04*	0.82 ± 0.06*	0.91 ± 0.04*	0.82 ± 0.06
TPD-TQPS	$T_{P\text{-}HRTBKG}$	0.83 ± 0.06	0.83 ± 0.06*	0.89 ± 0.04*	0.79 ± 0.06
EXT-TQPS	$T_{P\text{-}HRTBKG}$	0.81 ± 0.06	0.83 ± 0.06*	0.88 ± 0.04	0.81 ± 0.06

* Significantly better ($P < 0.05$) than SSS-QPS for the indicated gender population and degree of stenosis.

The respective sensitivities, specificities and accuracies calculated at the optimal operating points for each gender population are shown in Figure 7-6. For the male population and the detection of 50% stenosis or greater, the 95% confidence intervals were between ±8% and ±14% for the sensitivity measurements and ±12% and ±25% for specificities. For the female population and the detection of 50% stenosis or greater, the 95% confidence intervals were between ±11% and ±19% for the sensitivity

measurements and ±13% and ±21% for specificities. Optimal operating points were determined to be 2 for SSS-QPS, 10 for SSS-TQPS, 23% for TPD-TQPS and 41% for EXT-TQPS when detecting stenoses of 50% or greater for the male population.

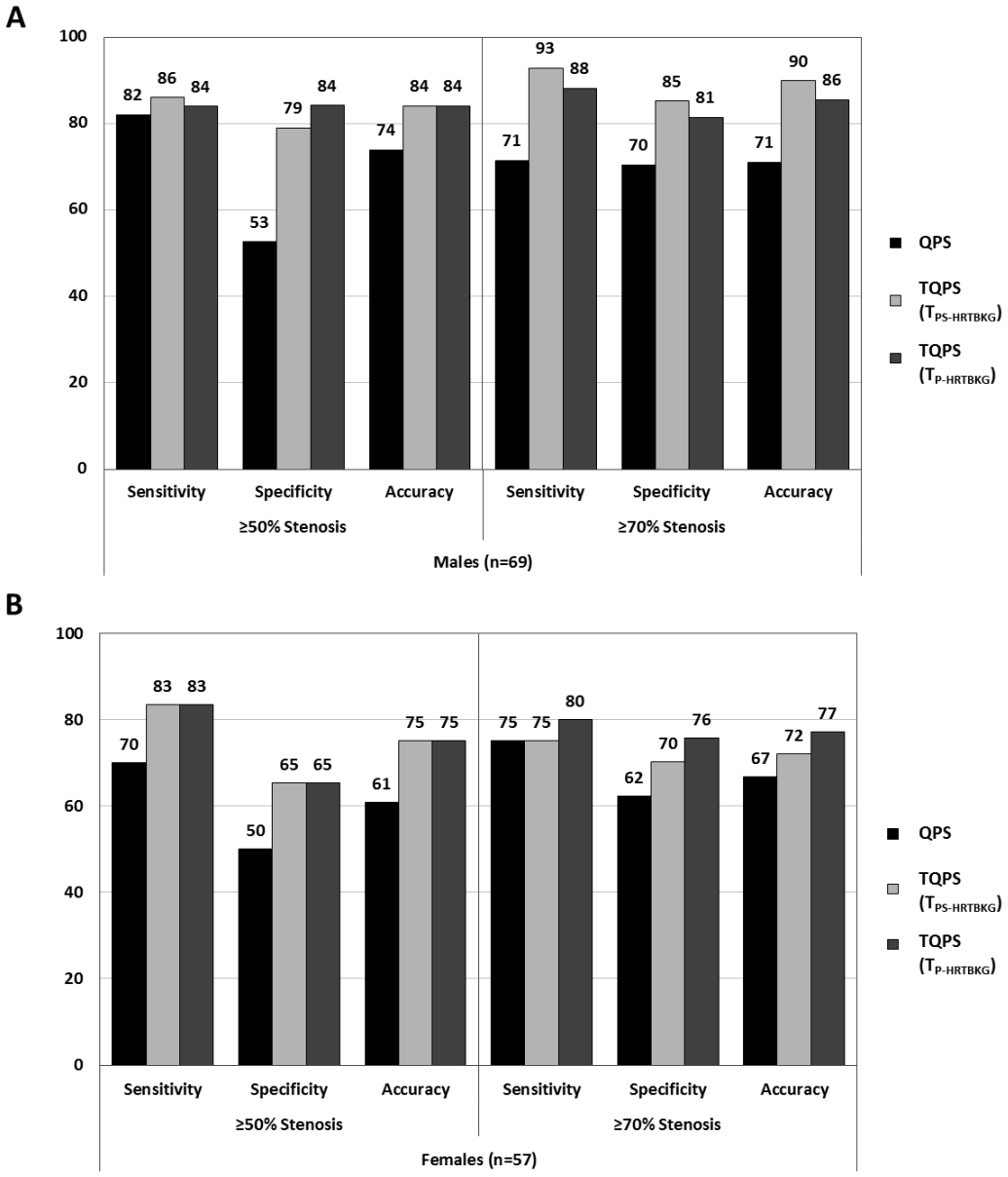

Figure 7-6 Optimal sensitivities, specificities, and accuracies for QPS, and both TQPS template generation methods, $T_{PS-HRTBKG}$ and $T_{P-HRTBKG}$, using their respective SSS figures of merit in the detection of ≥50% and ≥70% stenosis. Images (A) and (B) show the results for the male (n=69) and female populations (n=57), respectively.

The results for each individual coronary territory, LAD, LCX and RCA, can be seen in Figure 7-7 and Figure 7-8. Specifically, these figures provide a review of the results for each figure of merit when using the $T_{PS\text{-}HRTBKG}$ and $T_{P\text{-}HRTBKG}$ method, respectively, relative to QPS. In general, the greatest differences between the QPS and TQPS measurements were observed in the LAD territory. For instance, the differences in sensitivity measurements between SSS-QPS and SSS-TQPS ($T_{PS\text{-}HRTBKG}$) measurements for the LAD, LCX, and RCA territories were 38%, 0% and 13% (each in favour of SSS-TQPS), respectively when detecting a 50% stenosis or greater. Similar trends were observed for the specificity and accuracy measurements. The 95% confidence intervals were between ±9% and ±22% for the sensitivities, and ±10% and ±36% for the specificities when detecting a stenosis of 50% or greater.

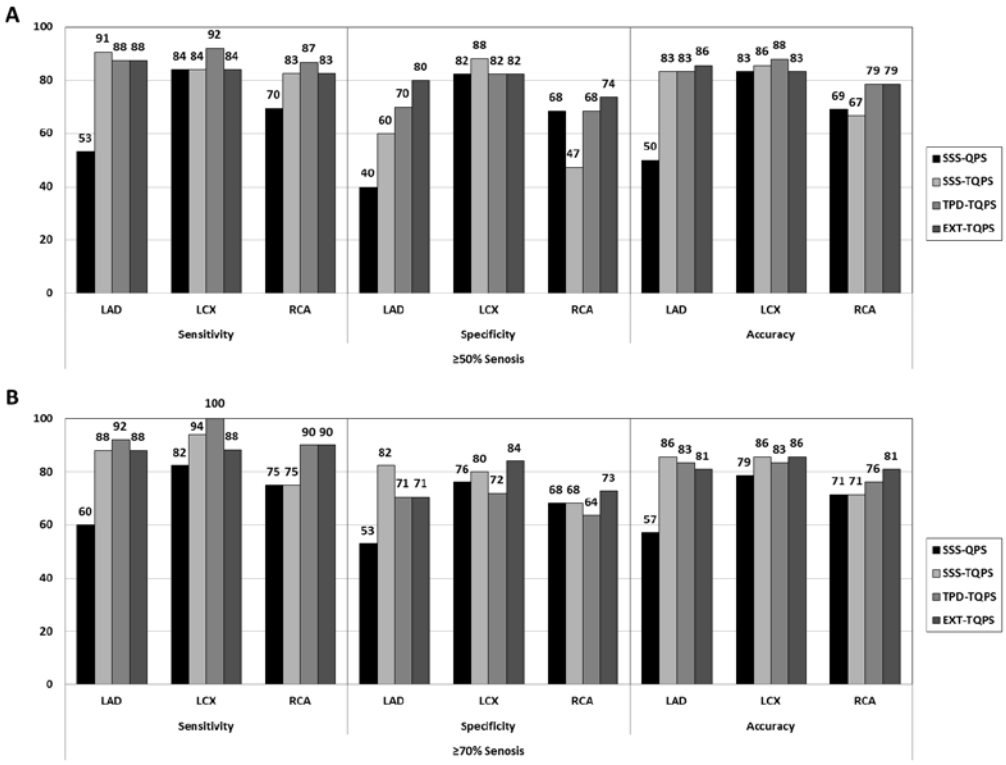

Figure 7-7 Optimal sensitivities, specificities and accuracies for the detection of (A) ≥50% and (B) ≥70% stenosis in specific vessels (LAD, LCX and RCA) using SSS-QPS, SSS-TQPS, TPD-TQPS, and EXT-TQPS (n=42, for each vessel). The $T_{PS\text{-}HRTBKG}$ TQPS method was employed in these results.

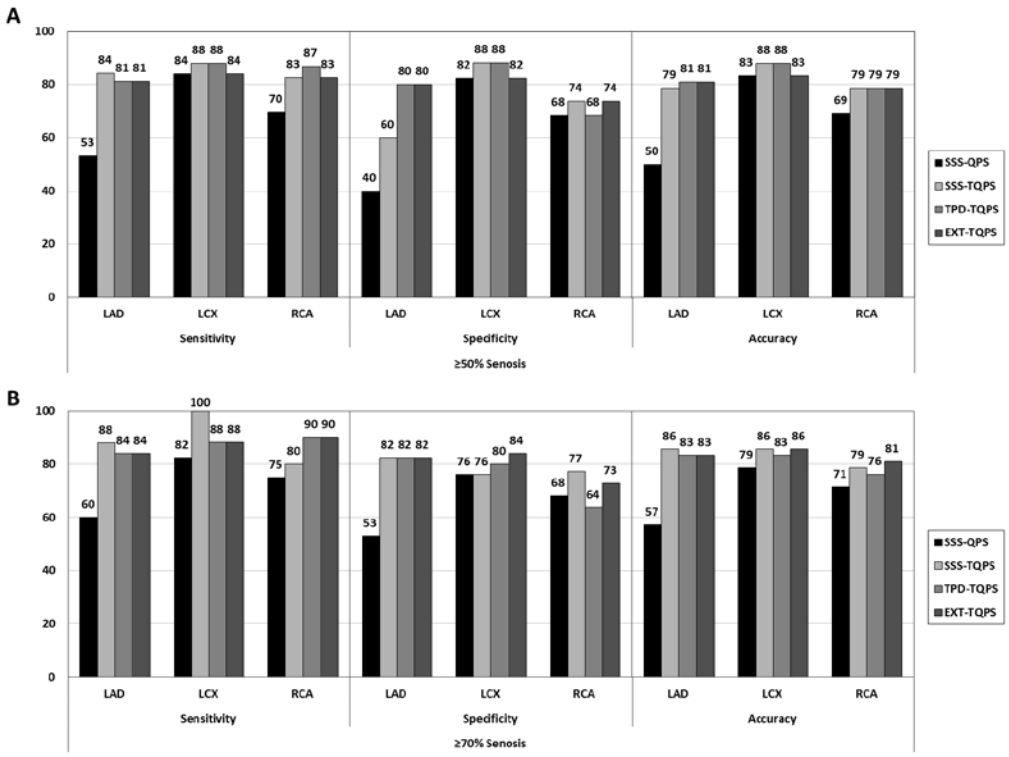

Figure 7-8 Optimal sensitivities, specificities and accuracies for the detection of (A) ≥50% and (B) ≥70% stenosis in specific vessels (LAD, LCX and RCA) using SSS-QPS, SSS-TQPS, TPD-TQPS, and EXT-TQPS (n=42, for each vessel). The $T_{P\text{-}HRTBKG}$ TQPS method was employed in these results.

Table 7-7 and Table 7-8 show the AUC measurements obtained from the ROC curves for each vessel when detecting 50% and 70% stenosis of greater, respectively. In each case, significant differences were observed for the LAD territory for each figure of merit and each TQPS methods, relative to the SSS-QPS method. When detecting a 50% stenosis or greater in the LAD territory, the AUC for SSS-QPS was 0.57 ± 0.10 compared to 0.86 ± 0.06 (P = 0.0033) and 0.87 ± 0.05 (P = 0.0027) for SSS-TQPS using $T_{PS\text{-}HRTBKG}$ and $T_{P\text{-}HRTBKG}$, respectively. No significant differences were observed between the methods for the RCA and LCX territories.

Table 7-7 Areas under the ROC curve for the detection ≥50% stenosis using SSS-QPS, SSS-TQPS, TPD-TQPS, and EXT-TQPS in specific vessels (LAD, LCX and RCA).

Method	Template Generation Method	ROC area under curve (±SE)		
		≥50% Stenosis		
		LAD	LCX	RCA
SSS-QPS	n/a	0.57 ± 0.10	0.85 ± 0.07	0.71 ± 0.08
SSS-TQPS	$T_{PS\text{-}HRTBKG}$	0.86 ± 0.06*	0.88 ± 0.06	0.83 ± 0.06
TPD-TQPS	$T_{PS\text{-}HRTBKG}$	0.86 ± 0.06*	0.86 ± 0.06	0.80 ± 0.07
EXT-TQPS	$T_{PS\text{-}HRTBKG}$	0.87 ± 0.06*	0.87 ± 0.06	0.77 ± 0.08
SSS-TQPS	$T_{P\text{-}HRTBKG}$	0.87 ± 0.05*	0.89 ± 0.06	0.83 ± 0.06
TPD-TQPS	$T_{P\text{-}HRTBKG}$	0.87 ± 0.05*	0.88 ± 0.06	0.81 ± 0.07
EXT-TQPS	$T_{P\text{-}HRTBKG}$	0.87 ± 0.06*	0.88 ± 0.06	0.77 ± 0.08

* Significantly better ($P < 0.05$) than SSS-QPS for the indicated degree of stenosis.

Table 7-8 Areas under the ROC curve for the detection ≥70% stenosis using SSS-QPS, SSS-TQPS, TPD-TQPS, and EXT-TQPS in specific vessels (LAD, LCX and RCA).

Method	Template Generation Method	ROC area under curve (±SE)		
		≥70% Stenosis		
		LAD	LCX	RCA
SSS-QPS	n/a	0.68 ± 0.08	0.88 ± 0.06	0.71 ± 0.08
SSS-TQPS	$T_{PS\text{-}HRTBKG}$	0.91 ± 0.05*	0.85 ± 0.06	0.81 ± 0.07
TPD-TQPS	$T_{PS\text{-}HRTBKG}$	0.87 ± 0.06*	0.88 ± 0.05	0.79 ± 0.07
EXT-TQPS	$T_{PS\text{-}HRTBKG}$	0.86 ± 0.07	0.90 ± 0.05	0.80 ± 0.07
SSS-TQPS	$T_{P\text{-}HRTBKG}$	0.92 ± 0.04*	0.87 ± 0.06	0.81 ± 0.07
TPD-TQPS	$T_{P\text{-}HRTBKG}$	0.88 ± 0.06*	0.89 ± 0.05	0.80 ± 0.07
EXT-TQPS	$T_{P\text{-}HRTBKG}$	0.86 ± 0.07	0.89 ± 0.05	0.80 ± 0.07

* Significantly better ($P < 0.05$) than SSS-QPS for the indicated degree of stenosis.

Figure 7-9 presents bulls-eye images for the TQPS ($T_{PS\text{-}HRTBKG}$) and QPS methods for a patient presenting with significant CAD (80% stenosis in the RCA). Here, SSS-QPS was determined to be 3 in the RCA territory (below the optimal operating point = insignificant CAD) as where SSS-TQPS was 11 (above the optimal operating point = significant CAD).

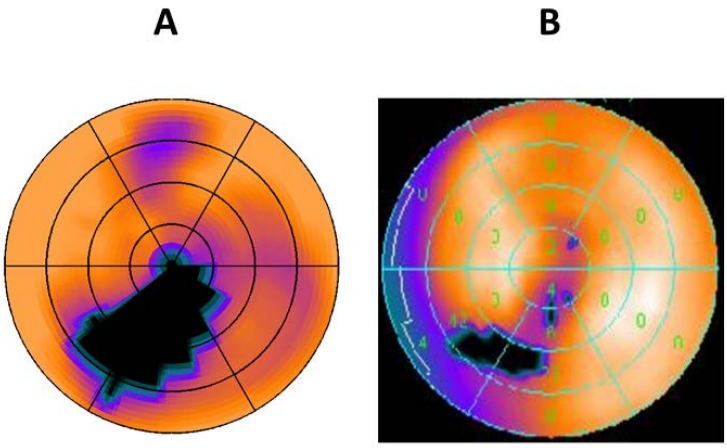

Figure 7-9 An example patient study illustrating a large difference between the results from TQPS (A) and QPS (B). According to the angiography results, this patient presented with a ≥70% stenosis (reported as 80%) in the proximal RCA.

7.7 Discussion

Prior to the clinical evaluation of TQPS relative to the commercial QPS software, two aspects of the TQPS method were tested as an extension of the optimization study presented in Chapter 6.

First, the influence of different reconstruction algorithms used in the TQPS method was investigated. When comparing the performance of TQPS using the attenuation corrected reconstruction algorithm versus no attenuation correction, no significant differences were observed for each figure of merit and each degree of significant stenosis. These results confirm the ability of the method to correct for artifacts generated by the image processing algorithm. This effect was best illustrated in Figure 7-2, where the left hemidiaphragm attenuation artifact is clearly visible in the inferior aspect of the patient bulls-eye (PB) image and nearly fully absent in the corrected bulls-eye image (CB). As a result, the artifact did not influence the determination of the

defect and the method was able to correctly identify the perfusion defect in the LAD territory using both the AC and NC reconstruction methods.

Secondly, the relative difference in performance between the $T_{P\text{-}HRTBKG}$ and $T_{PS\text{-}HRTBKG}$ template generation methods was analyzed. When comparing the results obtained using the two template generation methods, no significant differences were observed for each figure of merit and each level of significant stenosis. Although this was demonstrated in the optimization phase of this thesis (Chapter 6), it was important to further confirm these results by using patient studies and the diagnostic end point adopted in this chapter – the detection of significant coronary artery disease. By showing that $T_{P\text{-}HRTBKG}$ can provide accurate results along with a dramatic reduction in processing time relative to $T_{PS\text{-}HRTBKG}$, it reconfirmed that $T_{P\text{-}HRTBKG}$ is the optimal version of the TQPS method.

The primary objective in this phase of the thesis was to evaluate the proposed TQPS method relative to the leading commercial software, QPS, using the diagnostic end point obtained via coronary angiography. The main advantage of the TQPS methodology is the ability to differentiate between patient-specific artifacts (e.g. partial volume effects) and abnormal perfusion. In doing so, it was hypothesized that the TQPS method should be able to reduce the number of false positive diagnoses, thereby improving the specificity relative to standard normal patient database methods.

When analyzing all 126 coronary territories for detecting stenoses of 50% or greater in the investigated patient population, the SSS-TQPS measurements using the $T_{PS\text{-}HRTBKG}$ method yielded a sensitivity, specificity and accuracy of 81%, 78%, and 80%, respectively; whereas the SSS-QPS method yielded measurements of 74%, 57%, and 67%, respectively. Most notably, the specificity was improved by 21%. Moreover, a

consistent and substantial trend toward improved specificity was observed for each figure of merit and each TQPS method ($T_{PS\text{-}HRTBKG}$ and $T_{P\text{-}HRTBKG}$) throughout the analysis.

Previous studies regarding the performance of detecting significant CAD with the QPS software have quoted sensitivities and specificities, on a per patient basis, ranging from 80% to 89% and 71% to 73%, respectively *(96, 97, 106)*. However, since the measurements were performed on a per coronary territory basis, which is a more precise measurement relative to a per patient basis, it is understandable that the QPS results quoted in this study were slightly lower than those previously reported. Moreover, the aforementioned studies used much more restricted patient populations, which could artificially enhance the performance of the software in the cases where non-optimal studies were rejected. For instance, patients presenting with cardiomyopathies, significant valvular disease, left bundle branch block, paced rhythm, as well as SPECT images presenting with insufficient quality, such as those with significant extra-cardiac uptake were excluded from those studies *(96, 97)*. In contrast, this study restricted the population only to acceptable attenuation map quality (absence of visually detectable misregistration artifacts), which was also an exclusion criterion for the aforesaid studies. With this said, it is likely that the marked reduction in QPS results relative to those previously reported and the significant improvement in TQPS performance was related to the nature of the measurements and the exclusion criteria for the patient population.

Without the inclusion of attenuation correction in the reconstruction algorithms, attenuation was the most notable artifact present in the images analyzed in this study. Although the TQPS method requires an attenuation map (as it is necessary for template projection step to model data acquisition process), and would likely be used with attenuation correction in a clinical setting, AC-databases were not available for QPS; thus, AC was not included in the reconstructions. Attenuation artifacts have been

reported to reduce the overall specificity of SPECT MPI when using catheter coronary angiography as the gold standard for detecting significant CAD *(123)*. Specifically, attenuation artifacts presented in male and female populations are very different in both presentation and frequency. For example, left hemidiaphragm attenuation artifacts in the RCA territory can occur in males up to 25% *(188)* of cases, whereas breast attenuation artifacts in female studies can present in the LAD or LCX in up to 40% of cases *(189)*. For the male and female populations investigated in this study, we found that there were no significant differences in AUC measurements between the populations for the SSS-TQPS $T_{P\text{-}HRTBKG}$ method (0.90 ± 0.04 vs. 0.82 ± 0.06; $P > 0.05$) and SSS-QPS (0.77 ± 0.06 vs. 0.66 ± 0.07; $P > 0.05$). These results indicate that both methods were able to perform consistently, irrespective of patient gender. This has been previously demonstrated with the QPS software when using gender-matched databases *(97)*; however, it confirms that the proposed TQPS was able to maintain its performance without the aid of normal databases, specifically in populations characterized by different artifacts, such as males and females.

With respect to the per vessel analysis, significant differences in AUC measurements between SSS-QPS and SSS-TQPS were found in the LAD territory (e.g. 0.57 ± 0.10 vs. 0.86 ± 0.06 for detecting a 50% stenosis or greater, respectively using $T_{PS\text{-}HRTBKG}$). With respect to the LCX and RCA territory, there were no significant differences between the two methods. Specifically, in the LAD territory it was found that QPS produced 8 of 42 (19%) false positives when detecting a 70% stenosis or greater, as where the TQPS ($T_{PS\text{-}HRTBKG}$) method only produced 2 of 42 (4%). From a qualitative standpoint, it was observed that 5 of the 8 (63%) false positives produced by QPS in the LAD region were associated with the apical region, suggesting the potential influence of apical thinning on the diagnosis – although there was no access to high resolution anatomical images (e.g. CT, MRI) to confirm the presence of such a condition. It has been well documented that apical thinning is a common effect (albeit, more so with AC reconstructions), which

hinders the performance of SPECT MPI *(124, 128)*. Specifically, it has been reported that apical thinning in non-attenuation-corrected SPECT MPI can be present in as much as 87% and 71% in abnormal and normal patient cases, respectively *(128)*. Although it can be speculated whether this effect has a physiological influence in the reduced blood flow to the apex, it is most certainly, in part, related to the relatively enhanced partial volume effect caused by the physical thinning of the myocardial wall at the apex *(124, 127, 128)*. With the primary advantage of the TQPS method being that it utilizes patient-specific information via the template, it is understandable that this method performed better in cases where a patient-specific artifact (apical thinning) was prominent.

Beyond the fact that apical thinning can be present in as much as 87% of SPECT MPI cases, with over a third of these cases resulting in moderate to severe false perfusion defects due to partial volume effects, non-uniformities in wall thickness can occur throughout the entire myocardium *(93, 125)*. For instance, Clausen et al found that there are discernible increases in left ventricle myocardial wall thickness at the anterior and posterior junctions with the right ventricle, as well as in the papillary muscle region; whereas distinct minima were observed, particularly in the septum *(93)*. In this study, these effects are illustrated in Figure 7-4, where the distribution produced by the template bulls-eye image is markedly non-uniform. With the template constructed with uniform activity (by definition), the only source for the non-uniform distribution shown in this figure can be related to non-uniform thickness in the segmented myocardium and another forms of artifact, such as attenuation effects. In particular, the basal aspect of the septum in Figure 7-4 shows significant reduction in intensity in both the TB and PB images, which is likely congruent with the findings from Clausen et al, especially adjacent to the aortic outflow tract. Although the most important result of the present study was the statistically significant improvement in the detection of significant CAD in the LAD coronary artery using the TQPS method, it is worth noting that the particular

cases where TQPS can be advantageous by accounting for the artifacts caused by patient-specific anatomical variability.

Beyond diagnostic performance, there were substantial differences in the processing time between the $T_{PS\text{-}HRTBKG}$ TQPS method (~2-4 h) and QPS (~1 min). As quoted by Slomka et al, the processing time for the QPS algorithm is on the order of seconds, which is easily within what is considered clinically acceptable *(96)*. On the other hand, the processing time for the $T_{PS\text{-}HRTBKG}$ TQPS method is currently on the order of 2-4 hours due to the template projection using primary and scattered photons. However, by excluding scatter from the template projection as in the $T_{P\text{-}HRTBKG}$ method, the processing time is reduced from hours down to minutes. For this reason, the results for the $T_{P\text{-}HRTBKG}$ method were provided, which had a processing time comparable to QPS.

Additional advantages of the TQPS algorithm related to the software caused artifacts described in Chapter 3 (Section 3.3.2) are not as clearly illustrated by the presented results as the partial volume artifacts. First, potential artifacts introduced by an inconsistency between the reorientation of the patient image and the normal patient database image are eliminated with the use of TQPS. The cause of these artifacts is due to the fact that the reorientation of the heart is patient specific and can vary significantly between patients (e.g. if the patient's heart is dextrorotated). Even more, additional mismatches between the normal database and patient reorientations can be introduced via inter-operator variability of the software program since this is a manual process. In the case of TQPS, the template heart is always reoriented in the same manner as the patient's heart, since it is constructed from the patient data. In doing so, reorientation artifacts are non-existent in the TQPS methodology.

The limitations of this study were related to the image processing software. First, NC reconstructions were used in this study since only NC databases were available for the

QPS software at VGH. For this reason, NC reconstructions we employed for the TQPS algorithm. Secondly, the workstations at VGH institution did not provide total perfusion deficit as an output for QPS, which has been reported as a more accurate measure for detecting significant CAD using QPS, relative to their standard summed stress score *(97)*. Finally, although the best efforts were made to match the image processing for each method, it is important to recognize that these operations were performed using different software, which could lead to variability in the results, although it is not suspected that this would be a major source of discrepancy between the investigated methods.

Potential future clinical implementation of TQPS would require a number of careful considerations. First, the introduction of new images (e.g. corrected bulls-eye map) to the clinical staff would require careful training in image interpretation. Due to the removal of artifacts in the corrected images in TQPS, the myocardial perfusion distribution presented in these images would be significantly different than those used in traditional methods. Thus, training would be required to read these new images appropriately. Second, software optimization and graphical user interface development would be necessary to enable easy operation of the method. With these considerations and further clinical validation, TQPS could certainly be considered as a useful application in nuclear medicine departments around the world.

7.8 Conclusions

In this final phase of the thesis, the proposed template-based method for semi-quantitative SPECT MPI was compared to a leading commercial software package with respect to the detection of significant coronary artery disease. By utilizing patient-specific information from the SPECT reconstructed image and attenuation map, the

TQPS method was able to accurately differentiate between artifact and abnormal perfusion better than the commercial QPS software employing normal database method, particularly in the LAD coronary territory.

8 Conclusions

This thesis presented a new approach to semi-quantitative SPECT myocardial perfusion analysis. This final chapter will first summarize the work presented in this thesis with a focus on the highlights of each phase of the analysis. Secondly, a section devoted to potential future directions of this work will be presented followed by a final word by the author.

8.1 Summary of Work

A new software-based technique was introduced in this thesis for the analysis of SPECT myocardial perfusion images. Unlike traditional methods employing normal patient databases as the healthy standard when quantifying myocardial perfusion defects, the proposed TQPS method utilizes a template to provide a patient-specific healthy standard. In doing so, TQPS was designed to overcome a number of the limitations associated with normal databases. The highlights of the work presented in this thesis can be summarized as follows:

- First and foremost, a proof-of-principle study was performed which demonstrated TQPS' ability to successfully identify and locate myocardial perfusion defect presented in SPECT MPI images. This was performed using simulation, physical phantom and clinical data.

- The method was then rigorously investigated with regards to two of its critical steps: template construction and template projection.
    - By comparing the performance of TQPS when using a *SPECT-based* template to that when using an *Ideal* template, no significant differences were observed in the ability to define myocardial perfusion defects. This confirmed the feasibility of creating the template with the SPECT data, which is a key differentiation from previously developed template-based methods that have adopted high resolution CT or MRI images in their respective template constructions.
    - With regards to the template projection step, the performance of TQPS using the analytical photon distribution interpolation (APDI) technique was compared to that when using clinically validated SPECT simulation algorithm. No significant differences were observed in the performance of TQPS when using the two projection algorithms, thus confirming the validity of using the APDI algorithm as a template projector for TQPS.

- Four versions of the TQPS method were then evaluated with the objective of reducing processing time while maintaining accuracy. Specifically, the versions included two template construction techniques and two template projection techniques, which combined to produce four different "template generation techniques": $T_{PS\text{-}HRTBKG}$, $T_{P\text{-}HRTBKG}$, $T_{PS\text{-}HRT}$, $T_{P\text{-}HRT}$. It was found that the template constructed with the heart, lungs and background compartments and projected using primary photons only (i.e. $T_{P\text{-}HRTBKG}$) produced optimal results.

- In this final phase of the thesis, the proposed template-based method for semi-quantitative SPECT MPI was compared in its performance to a leading commercial software package, QPS, with respect to the detection of significant coronary artery disease. It was found that the TQPS method was able to accurately differentiate

between artifact and abnormal perfusion in more cases than the commercial normal database method, particularly in the LAD coronary territory. As per the hypothesis stated in this thesis, the TQPS method was able to improve the specificity of SPECT MPI in detecting significant coronary disease on a per vessel basis from 57% (using the QPS) method to 78% (using TQPS).

8.2 Future Directions

The work presented in this thesis provided a full description of the analysis involved from taking the proposed method from concept to clinical evaluation. Nevertheless, there is always work that could be done to improve and further test the method. This work could include an investigation of respiratory and/or cardiac gated SPECT, the possibility of using new diagnostic quality CT onboard modern SPECT-CT systems, and also further software development.

With regards to gating applications, it would be interesting to investigate the possibility of applying the TQPS method in cardiac gated SPECT MPI. Although the computational burden would increase 8 or 16 fold depending on the number of gates used in the acquisition, the optimized TQPS method ($T_{P\text{-}HRTBKG}$) could still perform the task within a clinically acceptable timeframe. By performing TQPS on gated studies, there would be a potential of improving upon gated analysis, and thus providing a greater insight on ischemic heart disease. Secondly, although respiratory gating is not yet performed or required under standard SPECT MPI protocol, it could be beneficial to the TQPS method. In respiratory gating the SPECT image is acquired in the same way as in cardiac gating, but synced to the respiratory cycle as opposed to the cardiac cycle. With the gated SPECT images being nearly independent (minimized) of respiratory motion, the TQPS method could be performed without the concern potential artifact created by such a

motion. Despite the results in this thesis suggesting a minimal influence of respiratory (and cardiac) motion on its performance, improvements could be realized with the implementation of such a technique.

The method described in this thesis was aimed toward the development of a pragmatic software-based SPECT MPI analysis. As a result, the method adopted a template-based technique using the SPECT data, as opposed to data obtained from a high resolution anatomical imaging device. Despite the proven success of this method, it is important to look forward and explore the true potential of this method beyond "practical" applications. With that said, it would be interesting to investigate TQPS using the most recent hybrid SPECT-CT systems, where a diagnostic quality CT is onboard the system. For these systems, it would be possible to construct the heart compartment of the template using the co-registered high resolution CT image (with the aid of a contrast agent). These are exciting new imaging systems introduce a variety of potential applications, and an investigation of TQPS as one of these new applications could be very interesting.

Finally, the TQPS method as described in this thesis is currently in a research state, with regards to software and usability. For this method to be operated by non-experienced users, a full software integration and graphical user interface development would be necessary.

8.3 Final Words

Although further clinical validation is required prior to clinical implementation or commercialization, the TQPS method could readily serve as a source of supplemental information for cases in which the normal database methodology fails. Myocardial

perfusion imaging with SPECT is a very well established modality; however, the author would argue that it is approaching a dangerous state of stagnancy relative to the upcoming modalities, such as CT and MRI. Innovation is necessary in the modern world of technology, and it is hoped that the TQPS method can offer a much needed fresh perspective in the field of semi-quantitative SPECT myocardial perfusion imaging.

Bibliography

1. Heller SL, Goodwin PN. SPECT instrumentation: Performance, lesion detection, and recent innovations. Semin Nucl Med. 1987 7;17(3):184-99.

2. Gullberg GT, et al. Review of convergent beam tomography in single photon emission computed tomography. Phys Med Biol. 1992;37(3):507.

3. Frey EC, et al. Improved estimation of the detector response function for converging beam collimators. Phys Med Biol. 1998;43(4):941.

4. Jaszczak RJ, Greer KL, Floyd CE, Manglos SH, Coleman RE. Imaging characteristics of a high resolution cone beam collimator. Nuclear Science, IEEE Transactions on. 1988;35(1):644-8.

5. Koole M, D'Asseler Y, Vandenberghe S, Van de Walle R, Van Laere K, Versijpt J, et al. In: Modeling of the sensitivity of fan-beam collimation in SPECT imaging. Engineering in medicine and biology society, 2001. proceedings of the 23rd annual international conference of the IEEE; ; 2001. p. 2375,2378 vol.3.

6. Metzler SD, Accorsi R, Ayan AS, Jaszczak RJ. Slit-slat and multi-slit-slat collimator design and experimentally acquired phantom images from a rotating prototype. Nuclear Science, IEEE Transactions on. 2010;57(1):125-34.

7. Moore SC, Kouris K, Cullum I. Collimator design for single photon emission tomography. European Journal of Nuclear Medicine and Molecular Imaging. 1992;19(2):138-50.

8. Strand S, Ivanovic M, Erlandsson K, Weber DA, Franceschi D, Button T, et al. High resolution pinhole spect for tumor imaging. Acta Oncol. 1993 01/01; 2011/10;32(7-8):861-7.

9. Ramachandran GN, Lakshminarayanan AV. Three-dimensional reconstruction from radiographs and electron micrographs: Application of convolutions instead of fourier transforms. Proceedings of the National Academy of Sciences. 1971 09/01;68(9):2236-40.

10. Galt JR, Hise HL, Garcia EV, Nowak DJ. Filtering in frequency space. 1986;14(3):152-60.

11. Zubal I, Wisniewski G. Understanding fourier space and filter selection. Journal of Nuclear Cardiology. 1997 -05-01;4(3):234-43.

12. Shepp LA, Vardi Y. Maximum likelihood reconstruction for emission tomography. Medical Imaging, IEEE Transactions on. 1982;1; 1(2):113-22.

13. Hudson HM, Larkin RS. Accelerated image reconstruction using ordered subsets of projection data. IEEE Trans Med Imaging. 1994;13(4):601-9.

14. Chang L. A method for attenuation correction in radionuclide computed tomography. Nuclear Science, IEEE Transactions on. 1978;25(1):638-43.

15. Goetze S, Brown TL, Lavely WC, Zhang Z, Bengel FM. Attenuation correction in myocardial perfusion SPECT/CT: Effects of misregistration and value of reregistration. Journal of Nuclear Medicine. July 2007 July 2007;48(7):1090-5.

16. Hendel RC, Corbett JR, Cullom SJ, DePuey EG, Garcia EV, Bateman TM. The value and practice of attenuation correction for myocardial perfusion SPECT imaging: A joint position statement from the american society of nuclear cardiology and the society of nuclear medicine. Journal of Nuclear Cardiology. 2002 1;9(1):135-43.

17. Kojima A, Tomiguchi S, Kawanaka K, Utsunomiya D, Shiraishi S, Nakaura T, et al. Attenuation correction using asymmetric fanbeam transmission CT on two-head SPECT system. Ann Nucl Med. 2004;18(4):315-22.

18. Pazhenkottil AP, Ghadri J, Nkoulou RN, Wolfrum M, Buechel RR, Küest SM, et al. Improved outcome prediction by SPECT myocardial perfusion imaging after CT attenuation correction. Journal of Nuclear Medicine. 2011 February 01;52(2):196-200.

19. Tonge CM, Manoharan M, Lawson RS, Shields RA, Prescott MC. Attenuation correction of myocardial SPECT studies using low resolution computed tomography images. Nucl Med Commun. 2005;26(3).

20. Utsunomiya D, Tomiguchi S, Shiraishi S, Yamada K, Honda T, Kawanaka K, et al. Initial experience with X-ray ct based attenuation correction in myocardial perfusion spect imaging using a combined spect/ct system. Ann Nucl Med. 2005;19(6):485-9.

21. Wakabayashi Y, Imai K, Morozumi K, Takahashi Y, Shibasaki M. Evaluation of 99mTc-myocardial perfusion SPECT attenuation correction by hybrid SPECT/CT-examination by quantitative analysis-. Japanese Journal of Radiological Technology. 2010;66(4):371-8.

22. Blankespoor SC, Xu X, Kaiki K, Brown JK, Tang HR, Cann CE, Hasegawa BH. Attenuation correction of SPECT using X-ray CT on an emission-transmission CT system: Myocardial perfusion assessment. IEEE Trans Nucl Sci. 1996 aug;43:2263-74.

23. Penney BC, Glick SJ, King MA. Relative importance of the error sources in wiener restoration of scintigrams. Medical Imaging, IEEE Transactions on. 1990;9(1):60-70.

24. King M. A wiener filter for nuclear medicine images. Med Phys. 1983 1983-11-01;10(6):876-5.

25. King M. Activity quantitation in SPECT: A study of prereconstruction metz filtering and use of the scatter degradation factor. Med Phys. 1991 1991-03-01;18(2):184-6.

26. Kamphuis C, Beekman FJ, Viergever MA. Evaluation of OS-EM vs. ML-EM for 1D, 2D and fully 3D SPECT reconstruction. Nuclear Science, IEEE Transactions on. 1996;43(3):2018-24.

27. Beekman FJ, Eijkman EGJ, Viergever MA, Borm GF, Slijpen ETP. Object shape dependent PSF model for SPECT imaging. Nuclear Science, IEEE Transactions on. 1993;40(1; valid to a high accuracy at Δ<e1>E</e1>=15%, for a large range):31-9.

28. Zeng GL, Gullberg GT. Frequency domain implementation of the three-dimensional geometric point response correction in SPECT imaging. Nuclear Science, IEEE Transactions on. 1992;39(5):1444-53.

29. Penney BC, King MA, Knesaurek K. A projector, backprojector pair which accounts for the two-dimensional depth and distance dependent blurring in SPECT. Nuclear Science, IEEE Transactions on. 1990;37(2):681-6.

30. Tsui BMW, et al. The importance and implementation of accurate 3D compensation methods for quantitative SPECT. Phys Med Biol. 1994;39(3):509.

31. Tsui BMW, Hu H, Gilland DR, Gullberg GT. Implementation of simultaneous attenuation and detector response correction in SPECT. Nuclear Science, IEEE Transactions on. 1988;35(1):778-83.

32. Frey EC, Tsui BMW. Collimator-detector response compensation in SPECT. In: Zaidi H, editor. Quantitative Analysis in Clinical Nuclear Medicine Imaging. Geneva, Switzerland: Springer; 2006. p. 141-66.

33. McCarthy AW, Miller MI. Maximum likelihood SPECT in clinical computation times using mesh-connected parallel computers. Medical Imaging, IEEE Transactions on. 1991;10(3):426-36.

34. Blinder S, Celler A, Wells RG, Thomson D, Harrop R. Experimental verification of 3D detector response compensation using the OSEM reconstruction method. Nuclear Science Symposium Conference Record, 2001 IEEE. 2001;4; 4:2174-8.

35. Vandana Kohli ea. Comparison of frequency-distance relationship and gaussian-diffusion-based methods of compensation for distance-dependent spatial resolution in SPECT imaging. Phys Med Biol. 1998;43(4):1025.

36. King MA, Xia W, deVries DJ, Pan T, Villegas BJ, Dahlberg S, et al. A monte carlo investigation of artifacts caused by liver uptake in single-photon emission computed tomography perfusion imaging with technetium 99m-labeled agents. Journal of Nuclear Cardiology. 1996 2;3(1):18-29.

37. Gur YS, Farncombe TH, Pretorius PH, Gifford HC, Narayanan MV, Frey EC, et al. Comparison of scatter compensation strategies for myocardial perfusion imaging

using tc-99m labeled sestamibi. Nuclear Science, IEEE Transactions on. 2002;49(5):2309-14.

38. Marendic B, Yongyi Yang, King M, Pretorius PH, Wernick MN, Brankov JG. In: Imaging in sitting position may reduce liver artifact in myocardium perfusion imaging. Nuclear science symposium conference record (NSS/MIC), 2009 IEEE; ; 2009. p. 3984-7.

39. Koral KF, Swailem FM, Buchbinder S, Clinthorne NH, Rogers WL, Tsui BMW. SPECT dual-energy-window compton correction: Scatter multiplier required for quantification. J Nucl Med. 1990 January 1;31(1):90-8.

40. Jaszczak RJ, Greer KL, Floyd CE, Harris CC, Coleman RE. Improved SPECT quantification using compensation for scattered photons. Journal of Nuclear Medicine. 1984 August 01;25(8):893-900.

41. Dewaraja Y, Jia Li, Koral K. Quantitative ^{131}I SPECT with triple energy window compton scatter correction. Nuclear Science, IEEE Transactions on. 1998;45(6; a pixel by pixel correction where the scatter fraction in the photopeak window is estimated by linear interpolation between two adjacent narrow sub-windows. For the phantom measurements performed in this work the TEW estimate of scattered cou(TRUNCATED)):3109-14.

42. T. I. Compton scatter compensation using the triple-energy window method for single-and dual-isotope SPECT. J Nucl Med. 1993;34:2216-21.

43. Ogawa K. Simulation study of triple-energy-window scatter correction in combined tl-201, tc-99m SPECT. Ann Nucl Med. 1994;8(4):277-81.

44. Wells RG, Celler A. Analytical calculation of scatter distributions in SPECT projections. Nuclear Science Symposium and Medical Imaging Conference Record, 1995 , 1995 IEEE. 1995;2; 2:1087,1091 vol.2.

45. Vandervoort E, Celler A, Wells G, Blinder S, Dixon K, Yanxin Pang. Implementation of an analytically based scatter correction in SPECT reconstructions. Nuclear Science, IEEE Transactions on. 2005;52(3):645-53.

46. Riauka T. Photon propagation and detection in single?photon emission computed tomography?an analytical approach. Med Phys. 1994 1994-08-01;21(8):1311-11.

47. Freek J Beekman and Johan M den Harder and Max A Viergever and Peter,P.van Rijk. SPECT scatter modelling in non-uniform attenuating objects. Phys Med Biol. 1997;42(6):1133.

48. Da Silva AJ, Tang HR, Wu MC, Hasegawa BH. Absolute quantitation of myocardial activity in phantoms. Nuclear Science, IEEE Transactions on. 1999;46(3):659-66.

49. Pretorius PH, King MA. Diminishing the impact of the partial volume effect in cardiac SPECT perfusion imaging. Med Phys. 2009 Jan;36(1):105-15.

50. Shcherbinin S, Celler A. Assessment of the severity of partial volume effects and the performance of two template-based correction methods in a SPECT/CT phantom experiment. Phys Med Biol. 2011;56(16):5355.

51. Leading top 10 causes of death by broad income group (2008) [Internet]. [updated June 2011. Available from: http://www.who.int/mediacentre/factsheets/fs310/en/index.html. Accessed February 21, 2012.

52. Statistics Canada. Mortality, summary list of causes. Available from: http://www.statcan.gc.ca/pub/84f0209x/2008000/t001-eng.htm. Accessed March 10, 2012.

53. Lloyd-Jones D, Adams RJ, Brown TM, Carnethon M, Dai S, et al. Heart disease and stroke Statistics—2010 update. Circulation. 2010 February 23;121(7):e46-e215.

54. Ross R, Glomset J, Harker L. Response to injury and atherogenesis. Am J Pathol. 1977;86(3):675-84.

55. Weiner DA, Ryan TJ, Parsons L, Fisher LD, Chaitman BR, Sheffield LT, et al. Prevalence and prognostic significance of silent and symptomatic ischemia after coronary bypass surgery: A report from the coronary artery surgery study (CASS) randomized population. J Am Coll Cardiol. 1991 8;18(2):343-8.

56. Diamond GA. A clinically relevant classification of chest discomfort. J Am Coll Cardiol. 1983 Feb;1(2 Pt 1):574-5.

57. Braunwald E, Antman EM, Beasley JW, Califf RM, Cheitlin MD, et al. ACC/AHA guideline update for the management of patients with unstable angina and Non–ST-segment elevation myocardial Infarction—2002: Summary article. Circulation. 2002 October 01;106(14):1893-900.

58. Califf R, Armstrong P, Carver J, D'Agostino R, Strauss W. 27th bethesda conference: Matching the intensity of risk factor management with the hazard for coronary disease events. task force 5. stratification of patients into high, medium and low risk subgroups for purposes of risk factor management. J Am Coll Cardiol. 1996 04;27(5):1007-19.

59. Gibbons RJ, Abrams J, Chatterjee K, Daley J, Deedwania PC, Douglas JS, et al. ACC/AHA 2002 guideline update for the management of patients with chronic stable angina--summary article: A report of the american college of Cardiology/American heart association task force on practice guidelines (committee on the management of patients with chronic stable angina). J Am Coll Cardiol. 2003 Jan 1;41(1):159-68.

60. Gibbons RJ, Balady GJ, Timothy Bricker J, Chaitman BR, Fletcher GF, et al. ACC/AHA 2002 guideline update for exercise testing: Summary article. Circulation. 2002 October 01;106(14):1883-92.

61. Hannan EL, Wu C, Walford G, Culliford AT, Gold JP, Smith CR, et al. Drug-eluting stents vs. coronary-artery bypass grafting in multivessel coronary disease. N Engl J Med. 2008 01/24; 2011/11;358(4):331-41.

62. Underwood SR, Anagnostopoulos C, Cerqueira M, Ell PJ, Flint EJ, Harbinson M, et al. Myocardial perfusion scintigraphy: The evidence. Eur J Nucl Med Mol Imaging. 2004 Feb;31(2):261-91.

63. Bateman TM, Heller GV, McGhie AI, Friedman JD, Case JA, Bryngelson JR, et al. Diagnostic accuracy of rest/stress ECG-gated rb-82 myocardial perfusion PET: Comparison with ECG-gated tc-99m sestamibi SPECT. J Nucl Cardiol. 2006 Jan-Feb;13(1):24-33.

64. Chow BJW, Wells GA, Chen L, Yam Y, Galiwango P, Abraham A, et al. Prognostic value of 64-slice cardiac computed tomography: Severity of coronary artery disease, coronary atherosclerosis, and left ventricular ejection fraction. J Am Coll Cardiol. 2010 March 9;55(10):1017-28.

65. Abdulla J, Abildstrom SZ, Gotzsche O, Christensen E, Kober L, Torp-Pedersen C. 64-multislice detector computed tomography coronary angiography as potential alternative to conventional coronary angiography: A systematic review and meta-analysis. European Heart Journal. 2007 December 01;28(24):3042-50.

66. Lau GT, Ridley LJ, Schieb MC, Brieger DB, Freedman SB, Wong LA, et al. Coronary artery stenoses: Detection with calcium scoring, CT angiography, and both methods Combined1. Radiology. 2005 May 01;235(2):415-22.

67. Fleischmann KE, Hunink MG, Kuntz KM, Douglas PS. Exercise echocardiography or exercise SPECT imaging? A meta-analysis of diagnostic test performance. JAMA. 1998 Sep 9;280(10):913-20.

68. Nandalur KR, Dwamena BA, Choudhri AF, Nandalur MR, Carlos RC. Diagnostic performance of stress cardiac magnetic resonance imaging in the detection of coronary artery disease: A meta-analysis. J Am Coll Cardiol. 2007 10/2;50(14):1343-53.

69. Berman DS, Hachamovitch R, Shaw LJ, Friedman JD, Hayes SW, Thomson LE, et al. Roles of nuclear cardiology, cardiac computed tomography, and cardiac magnetic resonance: Assessment of patients with suspected coronary artery disease. J Nucl Med. 2006 Jan;47(1):74-82.

70. Schuijf JD, Bax JJ, Shaw LJ, de Roos A, Lamb HJ, van der Wall EE, et al. Meta-analysis of comparative diagnostic performance of magnetic resonance imaging and multislice computed tomography for noninvasive coronary angiography. Am Heart J. 2006 Feb;151(2):404-11.

71. Gianrossi R, Detrano R, Mulvihill D, Lehmann K, Dubach P, Colombo A, et al. Exercise-induced ST depression in the diagnosis of coronary artery disease. A meta-analysis. Circulation. 1989 July 01;80(1):87-98.

72. Ardle B, Dowsley T, Wells G, deKemp R, Beanlands R. Systematic review of the diagnostic utility of rubidium-82 positron emission tomography perfusion imaging in comparison to single photon emission tomography. J Am Coll Cardiol. 2012;59:E1318-.

73. Jaarsma C, Leiner T, Bekkers S, Crijns H, Wildberger J, Nagel E, et al. Diagnostic performance of PET, SPECT and CMR perfusion imaging for the detection of significant coronary artery disease - a meta-analysis. Journal of Cardiovascular Magnetic Resonance. 2011;13(0):1-.

74. Nandalur KR, Dwamena BA, Choudhri AF, Nandalur SR, Reddy P, Carlos RC. Diagnostic performance of positron emission tomography in the detection of coronary artery disease: A meta-analysis. Acad Radiol. 2008 4;15(4):444-51.

75. Apfaltrer P, Schoepf UJ, Vliegenthart R, Rowe GW, Spears JR, Fink C, et al. Coronary computed tomography--present status and future directions. Int J Clin Pract Suppl. 2011 Oct;65(173):3-13.

76. Hamon M, Fau G, Née G, Ehtisham J, Morello R, Hamon M. Meta-analysis of the diagnostic performance of stress perfusion cardiovascular magnetic resonance for detection of coronary artery disease. Journal of Cardiovascular Magnetic Resonance. 2010;12(1):1-10.

77. Husain SS. Myocardial perfusion imaging protocols: Is there an ideal protocol? Journal of Nuclear Medicine Technology. March 2007 March 2007;35(1):3-9.

78. Piwnica-Worms D, Kronauge J, Chiu M. Uptake and retention of hexakis (2-methoxyisobutyl isonitrile) technetium(I) in cultured chick myocardial cells. mitochondrial and plasma membrane potential dependence. Circulation. 1990 November 01;82(5):1826-38.

79. Baggish AL, Boucher CA. Radiopharmaceutical agents for myocardial perfusion imaging. Circulation. 2008 October 14;118(16):1668-74.

80. DePasquale E, Nody A, DePuey E, Garcia E, Pilcher G, Bredlau C, et al. Quantitative rotational thallium-201 tomography for identifying and localizing coronary artery disease. Circulation. 1988 February 01;77(2):316-27.

81. Ficaro EP, Lee BC, Kritzman JN, Corbett JR. Corridor4DM: The michigan method for quantitative nuclear cardiology. J Nucl Cardiol. 2007 Jul;14(4):455-65.

82. Watson DD, Smith WH,2nd. The role of quantitation in clinical nuclear cardiology: The university of virginia approach. J Nucl Cardiol. 2007 Jul;14(4):466-82.

83. Germano G, Kavanagh PB, Slomka PJ, Van Kriekinge SD, Pollard G, Berman DS. Quantitation in gated perfusion SPECT imaging: The cedars-sinai approach. J Nucl Cardiol. 2007 Jul;14(4):433-54.

84. Garcia EV, Faber TL, Cooke CD, Folks RD, Chen J, Santana C. The increasing role of quantification in clinical nuclear cardiology: The emory approach. Journal of Nuclear Cardiology. 2007 7;14(4):420-32.

85. Soneson H, Ubachs JFA, Ugander M, Arheden H, Heiberg E. An improved method for automatic segmentation of the left ventricle in myocardial perfusion SPECT. Journal of Nuclear Medicine. February 2009 February 2009;50(2):205-13.

86. Nuyts J, Mortelmans L, Suetens P, Oosterlinck A, de Rou M. Model-based quantification of myocardial perfusion images from SPECT. J Nucl Med. 1989 Dec;30(12):1992-2001.

87. Suri JS. Computer vision, pattern recognition and image processing in left ventricle segmentation: The last 50 years. Pattern Analysis & Applications. 2000;3(3):209-42.

88. Montagnat J, Delingette H. 4D deformable models with temporal constraints: Application to 4D cardiac image segmentation. Med Image Anal. 2005 2;9(1):87-100.

89. Tan W, Besar R. Segmentation of the left ventricle in myocardial perfusion SPECT using active shape model. In: Badioze Zaman H, Robinson P, Petrou M, Olivier P, Schröder H, Shih T, editors. Visual Informatics: Bridging Research and Practice. Springer Berlin / Heidelberg; 2009. p. 38-49.

90. Liu YH. Quantification of nuclear cardiac images: The yale approach. J Nucl Cardiol. 2007 Jul;14(4):483-91.

91. Hughes T, Shcherbinin S, Celler A. A template-based approach to semi-quantitative SPECT myocardial perfusion imaging: Independent of normal databases. Med Phys. 2011 July 2011;38(7):4186-95.

92. Soneson H, Ubachs JFA, Ugander M, Arheden H, Heiberg E. An improved method for automatic segmentation of the left ventricle in myocardial perfusion SPECT. J Nucl Med. 2009 February 1;50(2):205-13.

93. Clausen M, Civelek AC, Bice AN, Petronis J, Koller D, Loncaric S, et al. Short-axis circumferential profiles of the heart in healthy subjects: Comparison of T1-201 SPECT and two-dimensional echocardiography. Radiology. 1988 September 01;168(3):723-6.

94. Cerqueira MD, Weissman NJ, Dilsizian V, Jacobs AK, Kaul S, et al. Standardized myocardial segmentation and nomenclature for tomographic imaging of the heart. Circulation. 2002 January 29;105(4):539-42.

95. Hachamovitch R, Berman DS, Shaw LJ, Kiat H, Cohen I, Cabico JA, et al. Incremental prognostic value of myocardial perfusion single photon emission computed tomography for the prediction of cardiac death : Differential stratification for risk of cardiac death and myocardial infarction. Circulation. 1998 February 17;97(6):535-43.

96. Slomka PJ, Fish MB, Lorenzo S, Nishina H, Gerlach J, Berman DS, et al. Simplified normal limits and automated quantitative assessment for attenuation-corrected myocardial perfusion SPECT. Journal of Nuclear Cardiology. 2006 9;13(5):642-51.

97. Slomka PJ, Nishina H, Berman DS, Akincioglu C, Abidov A, Friedman JD, et al. Automated quantification of myocardial perfusion SPECT using simplified normal limits. Journal of Nuclear Cardiology. 2005 2;12(1):66-77.

98. DePuey EG, Rozanski A. Using gated technetium-99m-sestamibi SPECT to characterize fixed myocardial defects as infarct or artifact. Journal of Nuclear Medicine. 1995 June 01;36(6):952-5.

99. Lima RSL, Watson DD, Goode AR, Siadaty MS, Ragosta M, Beller GA, et al. Incremental value of combined perfusion and function over perfusion alone by

gated SPECT myocardial perfusion imaging for detection of severe three-vessel coronary artery disease. J Am Coll Cardiol. 2003 7/2;42(1):64-70.

100. Sharir T, Germano G, Kang X, Lewin HC, Miranda R, Cohen I, et al. Prediction of myocardial infarction versus cardiac death by gated myocardial perfusion SPECT: Risk stratification by the amount of stress-induced ischemia and the poststress ejection fraction. Journal of Nuclear Medicine. 2001 June 01;42(6):831-7.

101. Hashimoto J, Suzuki T, Nakahara T, Kosuda S, Kubo A. Preoperative risk stratification using stress myocardial perfusion scintigraphy with electrocardiographic gating. Journal of Nuclear Medicine. 2003 March 01;44(3):385-90.

102. Maruyama A, Hasegawa S, Paul A, Xiuli M, Yoshioka J, Maruyama K, et al. Myocardial viability assessment with gated SPECT tc-99m tetrofosmin % wall thickening: Comparison with F-18 FDG-PET. Ann Nucl Med. 2002;16(1):25-32.

103. Stollfuss JC, Haas F, Matsunari I, Neverve J, Nekolla S, Ziegler S, et al. 99mTc-tetrofosmin SPECT for prediction of functional recovery defined by MRI in patients with severe left ventricular dysfunction: Additional value of gated SPECT. Journal of Nuclear Medicine. 1999 November 01;40(11):1824-31.

104. Taki J, Higuchi T, Nakajima K, Matsunari I, Hwang E, Bunko H, et al. Electrocardiographic gated 99mTc-MIBI SPECT for functional assessment of patients after coronary artery bypass surgery: Comparison of wall thickening and wall motion analysis. Journal of Nuclear Medicine. 2002 May 01;43(5):589-95.

105. Akesson L. Operator dependent variability in quantitative analysis of myocardial perfusion images. Clinical Physiology and Functional Imaging. 2004;24(6):374-9.

106. Wolak A, Slomka PJ, Fish MB, Lorenzo S, Acampa W, Berman DS, et al. Quantitative myocardial-perfusion SPECT: Comparison of three state-of-the-art software packages. Journal of Nuclear Cardiology. 2008 2;15(1):27-34.

107. Grossman GB, Garcia EV, Bateman TM, Heller GV, Johnson LL, Folks RD, et al. Quantitative tc-99m sestamibi attenuation-corrected SPECT: Development and multicenter trial validation of myocardial perfusion stress gender-independent

normal database in an obese population. Journal of Nuclear Cardiology. 2004 6;11(3):263-72.

108. Hachamovitch R, Berman DS, Kiat H, Cohen I, Cabico JA, Friedman J, et al. Exercise myocardial perfusion SPECT in patients without known coronary artery disease : Incremental prognostic value and use in risk stratification. Circulation. 1996 March 1;93(5):905-14.

109. Nakajima K, Matsuo S, Kawano M, Matsumoto N, Hashimoto J, Yoshinaga K, et al. The validity of multi-center common normal database for identifying myocardial ischemia: Japanese society of nuclear medicine working group database. Ann Nucl Med. 2010;24(2):99-105.

110. Wolak A, Slomka PJ, Fish MB, Lorenzo S, Berman DS, Germano G. Quantitative diagnostic performance of myocardial perfusion SPECT with attenuation correction in women. Journal of Nuclear Medicine. June 2008 June 2008;49(6):915-22.

111. Guner L, Karabacak N, Cakir T, Akdemir O, Kocaman S, Cengel A, et al. Comparison of diagnostic performances of three different software packages in detecting coronary artery disease. European Journal of Nuclear Medicine and Molecular Imaging. 2010;37(11):2070-8.

112. Johansson L, Lomsky M, Marving J, Ohlsson M, Svensson S, Edenbrandt L. Diagnostic evaluation of three cardiac software packages using a consecutive group of patients. EJNMMI Research. 2011;1(1):22.

113. Grossman GB, Garcia EV, Bateman TM, Heller GV, Johnson LL, Folks RD, et al. Quantitative tc-99m sestamibi attenuation-corrected SPECT: Development and multicenter trial validation of myocardial perfusion stress gender-independent normal database in an obese population. Journal of Nuclear Cardiology. 2004 6;11(3):263-72.

114. Li D, Li D, Feng J, Yuan D, Cao K, Chen J. Quantification of myocardial perfusion SPECT studies in chinese population with western normal databases. J Nucl Cardiol. 2010 Jun;17(3):486-93.

115. Cuberas-Borros G, Aguade-Bruix S, Boronat-de Ferrater M, Muxi-Pradas MA, Romero-Farina G, Castell-Conesa J, et al. Normal myocardial perfusion SPECT database for the spanish population. Rev Esp Cardiol. 2010 Aug;63(8):934-42.

116. Nakajima K, Okuda K, Kawano M, Matsuo S, Slomka P, Germano G, et al. The importance of population-specific normal database for quantification of myocardial ischemia: Comparison between japanese 360 and 180-degree databases and a US database. Journal of Nuclear Cardiology. 2009;16(3):422-30.

117. Burrell S, MacDonald A. Artifacts and pitfalls in myocardial perfusion imaging. J Nucl Med Technol. 2006 Dec;34(4):193,211; quiz 212-4.

118. DePuey E. How to detect and avoid myocardial perfusion SPECT artifacts. J Nucl Med. 1994 04;35(4):699-702.

119. Germano G, Chua T, Kiat H, Areeda JS, Berman DS. A quantitative phantom analysis of artifacts due to hepatic activity in technetium-99m myocardial perfusion SPECT studies. J Nucl Med. 1994 Feb;35(2):356-9.

120. Germano G, Chua T, Kiat H, Areeda JS, Berman DS. A quantitative phantom analysis of artifacts due to hepatic activity in technetium-99m myocardial perfusion SPECT studies. J Nucl Med. 1994 Feb;35(2):356-9.

121. Goetze S, Brown TL, Lavely WC, Zhang Z, Bengel FM. Attenuation correction in myocardial perfusion SPECT/CT: Effects of misregistration and value of reregistration. J Nucl Med. 2007 Jul;48(7):1090-5.

122. Hendel RC, Berman DS, Cullom SJ, Follansbee W, Heller GV, Kiat H, et al. Multicenter clinical trial to evaluate the efficacy of correction for photon attenuation and scatter in SPECT myocardial perfusion imaging. Circulation. 1999 June 1;99(21):2742-9.

123. Singh B, Bateman TM, Case JA, Heller G. Attenuation artifact, attenuation correction, and the future of myocardial perfusion SPECT. Journal of Nuclear Cardiology. 2007 4;14(2):153-64.

124. Wheat JM, Currie GM. Recognising and dealing with artifact in myocardial perfusion SPECT. Internet J Cardiol. 2007;4(1).

125. Galt JR, Garcia EV, Robbins WL. Effects of myocardial wall thickness on SPECT quantification. Medical Imaging, IEEE Transactions on. 1990;9(2):144-50.

126. Dunn RF, Wolff L, Wagner S, Botvinick EH. The inconsistent pattern of thallium defects: A clue to the false positive perfusion scintigram. Am J Cardiol. 1981 8;48(2):224-32.

127. Johnson KM, Johnson HE, Dowe DA. Left ventricular apical thinning as normal anatomy. J Comput Assist Tomogr. 2009;33(3).

128. Links JM, Becker LC, Anstett F. Clinical significance of apical thinning after attenuation correction. Journal of Nuclear Cardiology. 2004 2;11(1):26-31.

129. DePuey EG, Guertler-Krawczynska E, Perkins JV, Robbins WL, Whelchel JD, Clements SD. Alterations in myocardial thallium-201 distribution in patients with chronic systemic hypertension undergoing single-photon emission computed tomography. Am J Cardiol. 1988 8/1;62(4):234-8.

130. Bartram P, Toft J, Hanel B, Ali S, Gustafsson F, Mortensen J, et al. False-positive defects in technetium-99m sestamibi myocardial single-photon emission tomography in healthy athletes with left ventricular hypertrophy. Eur J Nucl Med. 1998 Sep;25(9):1308-12.

131. Houghton JL, Frank MJ, Carr AA, von Dohlen TW, Prisant LM. Relations among impaired coronary flow reserve, left ventricular hypertrophy and thallium perfusion defects in hypertensive patients without obstructive coronary artery disease. J Am Coll Cardiol. 1990 Jan;15(1):43-51.

132. Cecil MP, Pilcher WC, Eisner RL, Chu TH, Merlino JD, Patterson RE. Absence of defects in SPECT thallium-201 myocardial images in patients with systemic hypertension and left ventricular hypertrophy. Am J Cardiol. 1994 7/1;74(1):43-6.

133. Jaber WA, DiFilippo FP, Cerqueira MD. Left ventricular hypertrophy and SPECT myocardial perfusion imaging: Finding the diamonds in the rough. Journal of Nuclear Cardiology. 2007 6;14(3):398-407.

134. Wackers FJT, Berman DS, Maddahi J, Watson DD, Beller GA, Strauss HW, et al. Technetium-99m hexakis 2-methoxyisobutyl isonitrile: Human biodistribution,

dosimetry, safety, and preliminary comparison to thallium-201 for myocardial perfusion imaging. Journal of Nuclear Medicine. 1989 March 01;30(3):301-11.

135. McQuaid SJ, Hutton BF. Sources of attenuation-correction artefacts in cardiac PET/CT and SPECT/CT. Eur J Nucl Med Mol Imaging. 2008 Jun;35(6):1117-23.

136. Nuyts J, Dupont P, Van den Maegdenbergh V, Vleugels S, Suetens P, Mortelmans L. A study of the liver-heart artifact in emission tomography. J Nucl Med. 1995 Jan;36(1):133-9.

137. van Dongen AJ, van Rijk PP. Minimizing liver, bowel, and gastric activity in myocardial perfusion SPECT. J Nucl Med. 2000 Aug;41(8):1315-7.

138. Pitman AG, Kalff V, Van Every B, Risa B, Barnden LR, Kelly MJ. Contributions of subdiaphragmatic activity, attenuation, and diaphragmatic motion to inferior wall artifact in attenuation-corrected tc-99m myocardial perfusion SPECT. Journal of Nuclear Cardiology. 2005 8;12(4):401-9.

139. Vandervoort E, Celler A, Harrop R. Scatter corrections, attenuation map quality and absolute quantitation in SPECT. Phys Med Biol. 2007;52:1527-1545.

140. Dewaraja YK, Ljungberg M, Fessler JA. 3-D monte carlo-based scatter compensation in quantitative I-131 SPECT reconstruction. Nuclear Science, IEEE Transactions on. 2006;53; 53(1):181-8.

141. Frey EC, Gilland KL, Tsui BMW. Application of task-based measures of image quality to optimization and evaluation of three-dimensional reconstruction-based compensation methods in myocardial perfusion SPECT. Medical Imaging, IEEE Transactions on. 2002;21(9):1040-50.

142. Dewaraja Y, Jia Li, Koral K. Quantitative ^{131}I SPECT with triple energy window compton scatter correction. Nuclear Science, IEEE Transactions on. 1998;45; 45(6; a pixel by pixel correction where the scatter fraction in the photopeak window is estimated by linear interpolation between two adjacent narrow sub-windows. For the phantom measurements performed in this work the TEW estimate of scattered cou(TRUNCATED)):3109-14.

143. Shcherbinin S, Celler A. An enhancement of quantitative accuracy of the SPECT/CT activity distribution reconstructions: Physical phantom experiments. Comput Med Imaging Graphics. 2010 7;34(5):346-53.

144. Da Silva AJ, Tang HR, Wong KH, Wu MC, Dae MW, Hasegawa BH. Absolute quantification of regional myocardial uptake of 99mTc-sestamibi with SPECT: Experimental validation in a porcine model. Journal of Nuclear Medicine. 2001 May 01;42(5):772-9.

145. Boening G, Pretorius PH, King MA. Study of relative quantification of tc-99 m with partial volume effect and spillover correction for SPECT oncology imaging. Nuclear Science, IEEE Transactions on. 2006;53; 53(3):1205-12.

146. DePuey EG. Artifacts in SPECT myocardial perfusion imaging. In: DePuey E, Garcia EV, Berman DS, editors. Cardiac SPECT Imaging. 2nd ed. Philadelphia, PA: Lippincott Williams and Wilkins; 2001.

147. Germano G, Slomka P, Bermana D. Attenuation correction in cardiac spect: The boy who cried wolf? Journal of Nuclear Cardiology. 2007;14(1):25-35.

148. Celler A, Shcherbinin S, Hughes T. An investigation of potential sources of artifacts in SPECT-CT myocardial perfusion studies. Journal of Nuclear Cardiology. 2010 -04-01;17(2):232-46.

149. Goetze S, Wahl RL. Prevalence of misregistration between SPECT and CT for attenuation-corrected myocardial perfusion SPECT. J Nucl Cardiol. 2007 Apr;14(2):200-6.

150. Boening G, Protorius PH, King MA. Study of relative quantification of tc-99m with partial volume effect and spillover correction for SPECT oncology imaging. Nuclear Science Symposium Conference Record, 2004 IEEE. 2004;5; 5:2705-9.

151. Meltzer CC, Kinahan PE, Greer PJ, Nichols TE, Comtat C, Cantwell MN, et al. Comparative evaluation of MR-based partial-volume correction schemes for PET. J Nucl Med. 1999 Dec;40(12):2053-65.

152. Meltzer CC, Zubieta JK, Links JM, Brakeman P, Stumpf MJ, Frost JJ. MR-based correction of brain PET measurements for heterogeneous gray matter radioactivity distribution. J Cereb Blood Flow Metab. 1996 print;16(4):650-8.

153. Muller-Gartner HW, Links JM, Prince JL, Bryan RN, McVeigh E, Leal JP, et al. Measurement of radiotracer concentration in brain gray matter using positron emission tomography: MRI-based correction for partial volume effects. J Cereb Blood Flow Metab. 1992 Jul;12(4):571-83.

154. Nuyts H, Maes A, Vrolix M, Schiepers C, Schelbert H, Kuhle W, et al. Three-dimensional correction for spillover and recovery of myocardial PET images. J Nucl Med. 1996 May;37(5):767-74.

155. Pretorius PH, King MA. Spillover compensation in the presence of respiratory motion embedded in SPECT perfusion data. Nuclear Science, IEEE Transactions on. 2008;55(1):537-42.

156. Tang HR, Da Silva AJ, Matthay KK, Price DC, Huberty JP, Hawkins RA, et al. Neuroblastoma imaging using a combined CT Scanner–Scintillation camera and 131I-MIBG. Journal of Nuclear Medicine. 2001 February 01;42(2):237-47.

157. Yang J, Huang SC, Mega M, Lin KP, Toga AW, Small GW, et al. Investigation of partial volume correction methods for brain FDG PET studies. Nuclear Science, IEEE Transactions on. 1996;43(6):3322-7.

158. Soret M, Koulibaly PM, Darcourt J, Buvat I. Partial volume effect correction in SPECT for striatal uptake measurements in patients with neurodegenerative diseases: Impact upon patient classification. Eur J Nucl Med Mol Imaging. 2006 Sep;33(9):1062-72.

159. Rousset OG, Ma Y, Evans AC. Correction for partial volume effects in PET: Principle and validation. J Nucl Med. 1998 May;39(5):904-11.

160. Du Y, Tsui BMW, Frey EC. Model-based compensation for quantitative 123 I brain SPECT imaging. Phys Med Biol. 2006;51(5):1269.

161. Hutton BF, Olsson A, Som S, Erlandsson K, Braun M. Reducing the influence of spatial resolution to improve quantitative accuracy in emission tomography: A

comparison of potential strategies. Nuclear Instruments and Methods in Physics Research Section A: Accelerators, Spectrometers, Detectors and Associated Equipment. 2006 12/20;569(2):462-6.

162. Soret M, Bacharach SL, Buvat I. Partial-volume effect in PET tumor imaging. Journal of Nuclear Medicine. June 2007 June 2007;48(6):932-45.

163. Matsuda H, Ohnishi T, Asada T, Li ZJ, Kanetaka H, Imabayashi E, et al. Correction for partial-volume effects on brain perfusion SPECT in healthy men. J Nucl Med. 2003 Aug;44(8):1243-52.

164. Kato H, Shimosegawa E, Oku N, Kitagawa K, Kishima H, Saitoh Y, et al. MRI-based correction for partial-volume effect improves detectability of intractable epileptogenic foci on 123I-iomazenil brain SPECT images. J Nucl Med. 2008 Mar;49(3):383-9.

165. Pretorius PH, King MA. Evaluation of spillover and partial volume effect compensation for quantitative accuracy in cardiac SPECT perfusion imaging. Nuclear Science Symposium Conference Record, 2006 IEEE. 2006;6; 6:3247-50.

166. Shcherbinin S, Celler A. Quantitative accuracy of SPECT reconstructions with a voxelized CT-based partial volume effect correction. Nuclear Science Symposium Conference Record, 2008 NSS '08 IEEE. 2008:4311-8.

167. Pretorius PH, King MA, Bruvant PP. Influence of mismatched CT anatomy on the accuracy of partial volume compensation in cardiac SPECT perfusion imaging. Nuclear Science Symposium Conference Record, 2004 IEEE. 2004;5; 5:3213,3216 Vol. 5.

168. Heiberg E, Sjogren J, Ugander M, Carlsson M, Engblom H, Arheden H. Design and validation of segment - freely available software for cardiovascular image analysis. BMC Medical Imaging. 2010;10(1):1.

169. S Shcherbinin and A Celler and T Belhocine and R Vanderwerf and,A.Driedger. Accuracy of quantitative reconstructions in SPECT/CT imaging. Phys Med Biol. 2008;53(17):4595.

170. Tsui BMW, Hu H-, Gilland DR, Gullberg GT. Implementation of simultaneous attenuation and detector response correction in SPECT. Nuclear Science, IEEE Transactions on. 1988;35(1):778-83.

171. DePuey E, Bommireddipalli S, Clark J, Thompson L, Srour Y. Wide beam reconstruction "quarter-time" gated myocardial perfusion SPECT functional imaging: A comparison to "full-time" ordered subset expectation maximum. Journal of Nuclear Cardiology. 2009;16(5):736-52.

172. DePuey E, Bommireddipalli S, Clark J, Leykekhman A, Thompson L, Friedman M. A comparison of the image quality of full-time myocardial perfusion SPECT vs wide beam reconstruction half-time and half-dose SPECT. Journal of Nuclear Cardiology. 2011;18(2):273-80.

173. Germano G, Kavanagh PB, Waechter P, Areeda J, Van Kriekinge S, Sharir T, et al. A new algorithm for the quantitation of myocardial perfusion SPECT. I: Technical principles and reproducibility. J Nucl Med. 2000 Apr;41(4):712-9.

174. Hughes T, Celler A, Shcherbinin S, Toennies K, Dornheim L, Kempe N. In: The effects of time reduced cardiac SPECT acquisitions with respect to left ventricle quantitation parameters using a dynamic mass spring model segmentation technique. Jul 21-24, 2009; Victoria, BC. . p. 298-300.

175. Hughes T, Shcherbinin S, Celler A. In: Improvement of myocardial perfusion defect severity quantitation in cardiac SPECT: A simulation study. Oct 25-29, 2009; Orlando, FL. . p. 2839-41.

176. Hughes T, Shcherbinin S, Celler A. In: A new approach in patient motion correction for cardiac SPECT: A simulation study. Oct 25-29, 2009; Orlando, FL. . p. 2839-41.

177. Hughes T, Celler A. In: A patient specific template-based quantitative analysis of SPECT myocardial perfusion imaging. ASNC annual meeting 2010; September 23-26, 2010; Philadelphia, PA. . p. 739.

178. Segars WP, Lalush DS, Tsui BMW. A realistic spline-based dynamic heart phantom. Nuclear Science, IEEE Transactions on. 1999;46(3):503-6.

179. Harrison RL, Haynor DR, Gillispie SB, Vannoy SD, Kaplan MS, Lewellen TK. A public-domain simulation system for emission tomography: Photon tracking through heterogeneous attenuation using importance sampling. Journal of Nuclear Medicine. 1993;34:60P.

180. Harrison RL, Vannoy SD, Haynor DR, Gillispie SB, Kaplan MS, Lewellen TK. In: Preliminary experience with the photon history generator module of A public-domain simulation system for emission tomography. Nuclear science symposium and medical imaging conference, 1993., 1993 IEEE conference record. ; 1993. p. 1154-8.

181. Holly TA, Abbott BG, Al-Mallah M, Calnon DA, Cohen MC, DiFilippo FP, et al. ASNC imaging guidelines for nuclear cardiology: Single photon-emission computed tomography. Journal of Nuclear Cardiology. 2010;17:941-73.

182. Frey EC, Gilland KL, Tsui BMW. Application of task-based measures of image quality to optimization and evaluation of three-dimensional reconstruction-based compensation methods in myocardial perfusion SPECT. Medical Imaging, IEEE Transactions on. 2002;21(9):1040-50.

183. Hughes T, Shcherbinin S, Celler A. In: Towards practical, quantitative, and patient-specific SPECT myocardial perfusion imaging. June 4-8, 2011; San Antonio, TX. ; 2011. p. 2041.

184. Hughes T, Celler A. Toward a practical template-based approach to semiquantitative SPECT myocardial perfusion imaging. Med Phys. 2012 March 2012;39(3):1374-85.

185. Sharir T, Germano G, Waechter PB, Kavanagh PB, Areeda JS, Gerlach J, et al. A new algorithm for the quantitation of myocardial perfusion SPECT. II: Validation and diagnostic yield. Journal of Nuclear Medicine. 2000 April 01;41(4):720-7.

186. Slomka PJ, Fieno D, Thomson L, Friedman JD, Hayes SW, Germano G, et al. Automatic detection and size quantification of infarcts by myocardial perfusion SPECT: Clinical validation by delayed-enhancement MRI. J Nucl Med. 2005 May;46(5):728-35.

187. Hanley JA, McNeil BJ. A method of comparing the areas under receiver operating characteristic curves derived from the same cases. Radiology. 1983 September 01;148(3):839-43.

188. Johnstone DE, Wackers FJ, Berger HJ, Hoffer PB, Kelley MJ, Gottschalk A, et al. Effect of patient positioning on left lateral thallium-201 myocardial images. J Nucl Med. 1979;20:183-8.

189. Wackers FJ. Diagnostic pitfalls of myocardial perfusion imaging in women. J Myocardial Ischemia. 1992;10:23-37.

Appendices

Appendix A: Details of the Segment Software

A description of Segment, the left ventricular segmentation software used to generate the boundaries of the heart compartment for TQPS was provided in Section 4.2.1. In this description, some details regarding its operation were omitted; thus, the following discussion attends to these points using the work performed by Soneson et al [91].

Thresholds used in the segmentation algorithm were established in a training set of MRI and SPECT MPI studies, which were ultimately based on four processes:

1. OPT length: optimal threshold based on left ventricular length.
2. MR: an optimal measure defined by MRI data.
3. OPT LVM: optimal threshold based on the left ventricular mass.
4. MPS: an optimal measured defined by SPECT data.

These thresholds are used throughout the segmentation process in order to aid the software in delineating an anatomically reasonable left ventricular myocardium. Overall, the segmentation process can be described by the flow chart shown in Figure A-1.

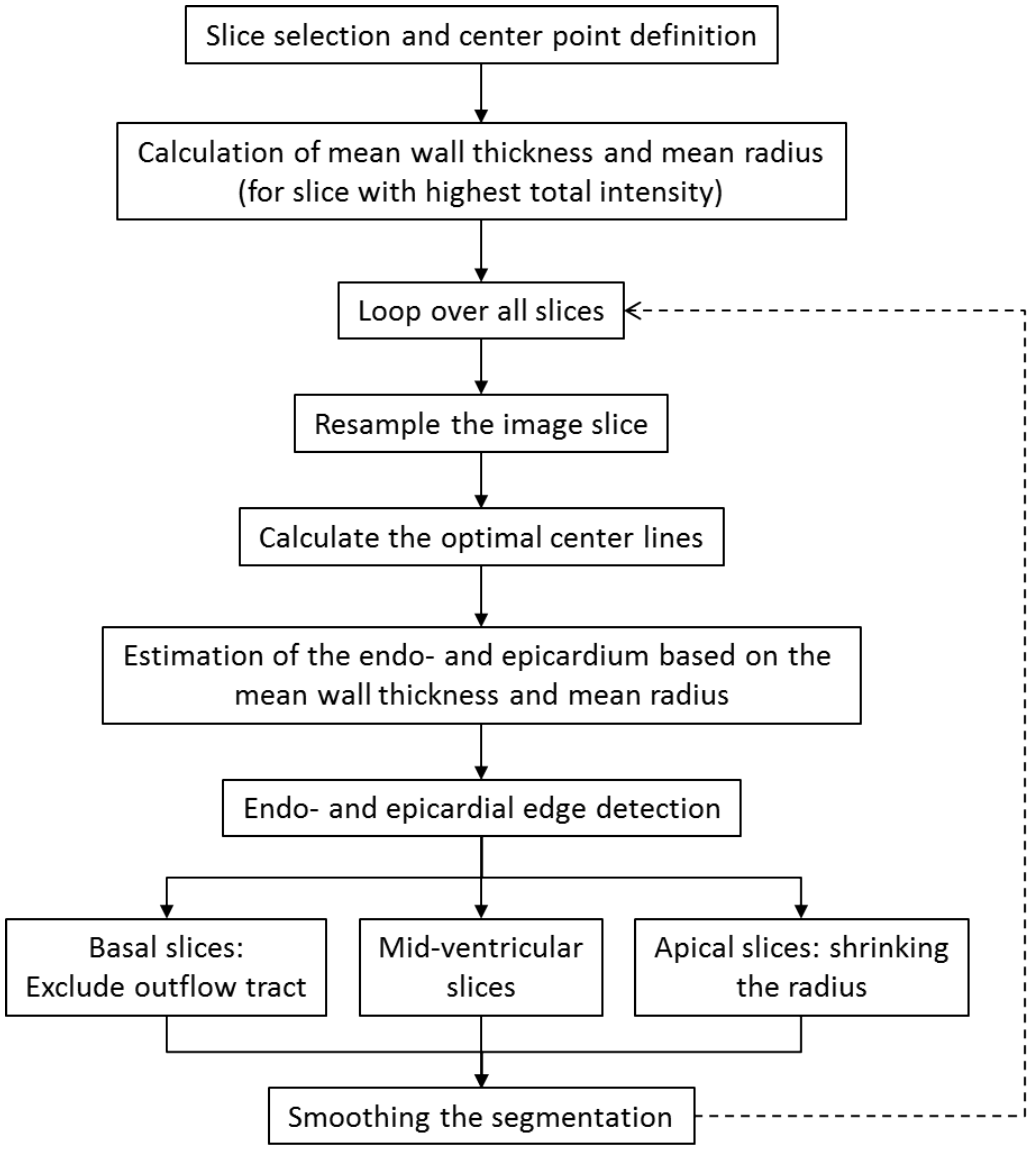

Figure A-1 A flow chart representing the operating step involved when segmenting the left ventricular myocardium using the Segment program.

In section 4.2.1, the slice selection and center point definition are described. With regard to the calculation of mean wall thickness and mean wall radius, a further description is provided here regarding Dijkstra's algorithm, which is used to find the midmural line in a short axis slice. The Dijkstra's algorithm is generally designed to find the optimal minimal cost path between a number of nodes. In this case, the algorithm is used to find the optimal midmural line of the myocardium using the maximum

intensities found in adjacent radial profiles for the resampled short axis slice. To achieve this, high intensity values and horizontal lines are given low cost as where low intensity and high slopes are given high cost. Specifically, the optimization problem could be stated as:

$$\min_f \int (-g\big(f(s)\big) + \alpha f'(s)^2 + \beta f''(s)^2) ds \qquad \text{Eq. A-1}$$

where g is the intensity value of the resample short axis image; f is the radius of the myocardium; and $\alpha$and β are the user defined elasticity and rigidity parameters, respectively. To solve this, using f as a discrete function $y(x)$, the problem can be approximated as:

$$\min_{y_i \in 1 \ldots M} -E_{image} + E_{int} \qquad \text{Eq. A-2}$$

$$E_{image} = \sum_{i=1}^{L} \sum_{j=y_{i-1}}^{y_i} \frac{|y_i - j|}{|y_{i-1} - y_i| + 1} g(i-1, j) + \frac{|j - y_{i-1}|}{|y_{i-1} - y_i| + 1} g(i, j) \qquad \text{Eq. A-3}$$

$$E_{int=} \sum_{i=1}^{L-1} \alpha (y_i - y_{i+1})^2 + \sum_{i=2}^{L-1} \beta (-y_{i-1} + 2y_i - y_{i+1})^2 \qquad \text{Eq. A-4}$$

where L and M are the number of columns and rows in the discrete resample short axis slice; E_{image} is the total intensity along the midmural line that is to be maximized; E_{int} is the slope of the line that is to be minimized. The rigidity and elasticity parameters come pre-determined in the Segment software and are established with the trade-off of flexibility to represent an accurate myocardial shape while being rigid enough to keep within reasonable anatomical bounds. Based on the training set study performed by Sonseon et al, the parameters were determined to be 0.015 for both α and β.

Appendix B: GE's Evolution for Cardiac versus the In-House Reconstruction Software

As mentioned in Section 7.2.4, the images for the QPS algorithm were processed using GE's Evolution for Cardiac software, while the TQPS images were processed using the In-house reconstruction software. In this study, the parameters for the two algorithms were match to produced nearly identical images. Specifically, both OSEM-based algorithms, with resolution recovery and without attenuation correction, were performed with 10 subsets and 4 iterations using a 5^{th} order Butterworth post-filter (0.52 cycles/cm cut-off frequency). This section of the Appendix provides an case study comparing the images produced by each algorithm. In this case, the mean absolute difference between the two normalized bulls-eye maps was 1.75% with a standard deviation of 0.6%, suggesting negligible differences between the two algorithms. Figure B-1 illustrates the results.

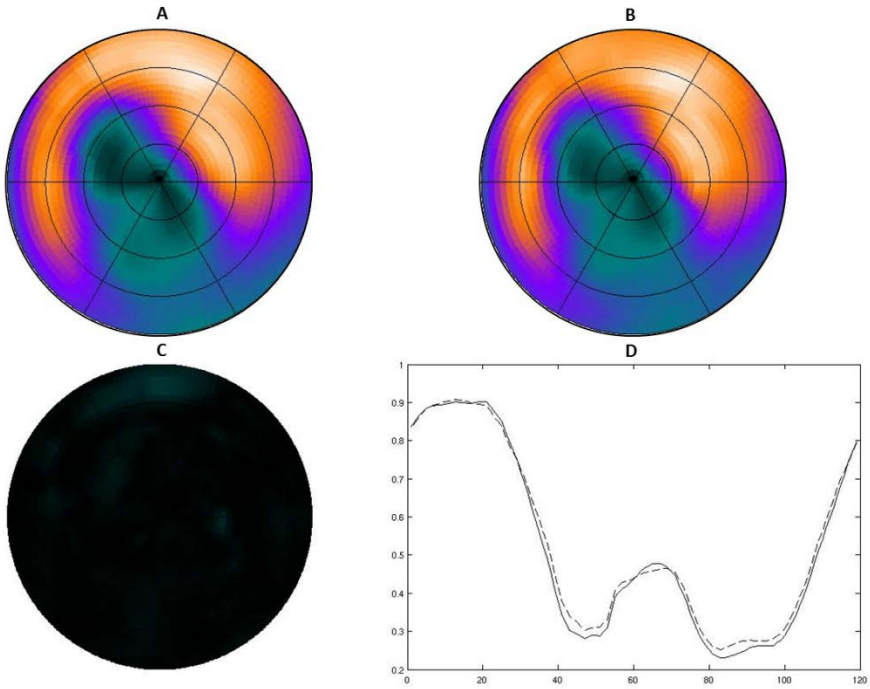

Figure B-1 An example patient case showing bulls-eye images produced by the In-house and Evolution for Cardiac software. Images (A) and (B) show the bulls-eyes from the In-house and Evolution for Cardiac software, respectively, each normalized to their respective global maximums. Image (C) is the absolute difference between images (A) and (B), normalized to unity. Image (D) shows a circumferential profile drawn in the mid-ventricular region for the In-house bulls-eye (solid line) and the Evolution for Cardiac bulls-eye (dashed line).